Development of a Small Satellite Remote Sensing Payload for Passive Limb Sounding of the Atmospheric Oxygen Emission

Michael Deiml

Dissertation

zur Erlangung des Grades

Doktor der Naturwissenschaften (Dr. rer. nat.)

vorgelegt der

Bergischen Universität Wuppertal

Fakultät für Mathematik und Naturwissenschaften

Wuppertal, 2017

Die Dissertation kann wie folgt zitiert werden:

Abstract

The Mesosphere/ Lower Thermosphere (MLT) is the region of the atmosphere in the altitude range from $60\,\mathrm{km}$ to $110\,\mathrm{km}$. This region becomes more and more important for climate predictions and weather forecasts with the extension of simulation models to higher altitudes. The global dynamics of the MLT is driven by gravity waves. Gravity waves are generated in the lower atmosphere and transport momentum to the MLT, where these waves break and dissipate. The resulting gravity wave drag influences the wind fields and, thus, the global circulation in this region. However, gravity waves are not yet sufficiently well represented in global circulation models, because their scales are often below the grid size of the simulation models, requiring that gravity waves are parameterized. The parameterization is one of the major uncertainties in current simulation models. Thus, observational data are required to better understand the underlying processes and to constrain gravity waves in the global circulation models. However, current gravity wave observing satellites for the MLT exceeded their operational lifetimes and succeeding missions are sparse. The observational gap in the near future is already conceivable.

The goal of this work is to propose a novel satellite mission with the corresponding remote sensing instrument that can reduce the data gap through a low-cost, agile, and scalable satellite. The satellite is based on the 3U CubeSat form factor that limits the mass to $4\,\mathrm{kg}$ and the launch volume to $34\,\mathrm{cm} \times 10\,\mathrm{cm} \times 10\,\mathrm{cm}$. CubeSats are nano satellites that can be launched on many different rockets through a standardized interface that eases the access to space. The here proposed AtmoCube-1 mission is described on a conceptual level. The focus of this work lies on the development of the remote sensing instrument that enables the characterization of gravity waves through temperature soundings in the MLT with a limb viewing geometry. The instrument measures the oxygen atmospheric band emission around $762\,\mathrm{nm}$ with a high spectral resolution in a small bandwidth to derive the kinetic temperature in the MLT from the temperature dependence of individual rotational fine structure lines. Thereby, the instrument uses a monolithic and temperature stabilized Fourier-transform spectrometer of the type Spatial Heterodyne Spectrometer that is characterized by a high resolving power and a high etendué at a small form factor. Thus, this instrument can be miniaturized to fit into the volume of a CubeSat.

The development of the instrument and of the satellite mission started with this work. Accordingly, the specification of the satellite instrument is a major part of this work, followed by the actual development of the instrument within the mission AtmoHIT. The Atmospheric Heterodyne Interferometer Test (AtmoHIT) is an experiment on-board the sounding rocket REXUS 22 that was launched in Kiruna, Sweden, in March 2017, within the Rocket/Balloon Experiments for University Students program. AtmoHIT had the goal to verify the satellite instrument under near-space conditions by measuring the oxygen atmospheric band. The temperature stabilized design of the spectrometer has been verified in a thermal vacuum chamber test before the flight, where also the operations in the temperature range from $-20\,^\circ\mathrm{C}$ to $46\,^\circ\mathrm{C}$ have been confirmed. Vibration tests indicated that the instrument can sustain the loads during the flight, which was demonstrated with the successful rocket flight campaign. The campaign showed also that the instrument operates under near-space conditions. The oxygen atmospheric band was measured, demonstrating the functionality of the instrument. An anomaly occurred during the separation of the payload module and the rocket motor that resulted in a strongly tumbling payload. Thus, the goal of temperature sounding in the MLT could not be fulfilled. Nevertheless, the sounding rocket campaign was deemed successful, because it showed that the instrument performed as expected.

This work concludes by a discussion of the major results from the instrument development and possible enhancements to the instrument. The here developed methods and design tools are already employed in the related projects AtmoSHINE and AtmoWINDS that eventually lead to the launch of the AtmoCube-1 satellite.

Zusammenfassung

Die Mesosphäre/ untere Thermosphäre (MLT) ist die Region in einer Höhe von $60\,\mathrm{km}$ bis $110\,\mathrm{km}$. Diese Region wird durch die Ausweitung von Simulationsmodellen hin zu größeren Höhen immer wichtiger für Klimaprognosen und Wettervorhersagen. Die globale Dynamik der MLT wird durch Schwerewellen angetrieben. Schwerewellen werden in der unteren Atmosphäre erzeugt und transportieren Impuls in die MLT, wo sie brechen. Die resultierende Kraft beeinflusst die Windfelder und somit die globale Zirkulation in dieser Region. Die Repräsentation von Schwerewellen in den globalen Modellen ist aber noch mit großen Unsicherheiten behaftet. Die Größenordnung von Schwerewellen befindet sich oft unterhalb der Gittergröße der Modelle, wodurch eine Parametrisierung notwendig wird. Diese Parametrisierung stellt eine der großen Unsicherheiten in aktuellen Simulationsmodellen dar. Daher werden Beobachtungsdaten benötigt, um die zugrundeliegenden Prozesse besser zu verstehen und Randbedingungen für Schwerewellen in globalen Zirkulationsmodellen zu erzeugen. Die momentan aktiven Satelliten zur Schwerewellenbestimmung in der MLT sind allerdings schon über ihrer operationellen Lebenszeit; ebenso existieren nur wenige Nachfolgemissionen. Eine Lücke in den Beobachtungsdaten ist daher für die nähere Zukunft bereits absehbar.

Ziel dieser Arbeit ist die Beschreibung einer neuartigen Satellitenmission mit dem dazugehörigen Erdbeobachtungsinstrument, um die Beobachtungslücke durch einen kostengünstigen, agilen und skalierbaren Satelliten zu reduzieren. Der Satellit basiert auf dem 3U CubeSat Formfaktor, welcher die Masse auf $4\,\mathrm{kg}$ und das Startvolumen auf $34\,\mathrm{cm} \times 10\,\mathrm{cm} \times 10\,\mathrm{cm}$ beschränkt. CubeSats sind Nanosatelliten, die mit vielen verschiedenen Raketen ins Weltall gebracht werden können, weil eine standardisierte Schnittstelle den Zugang zum Weltall vereinfacht. Die hier vorgeschlagene AtmoCube-1 Mission ist auf einem konzeptionellen Level beschrieben. Der Fokus dieser Arbeit liegt auf der Entwicklung des Erdbeobachtungsinstruments, mit dem Schwerewellen in der MLT durch Temperaturmessungen in einer Limb-Geometrie charakterisiert werden können. Das Instrument misst die Atmosphärenemission der Sauerstoffbande um $762\,\mathrm{nm}$ mit einem schmalbandigen, spektral hochauflösendem Spektrometer, um die kinetische Temperatur in der MLT durch die Temperaturabhängigkeit von verschiedenen Rotations-Feinstrukturlinien zu bestimmen. Dabei benutzt das Instrument ein monolithisches und temperaturstabilisiertes Fourier-Transformationsspektrometer vom Typ "Spatial Heterodyne Spektrometer", das eine hohe spektrale Auflösung und eine hohe Lichtempfindlichkeit bei einem kleinen Formfaktor ermöglicht. Daher kann dieses Instrument so miniaturisiert werden, dass es in das Volumen eines CubeSats passt.

Die Entwicklung des Instruments und der Satellitenmission begannen mit dieser Arbeit. Deshalb nimmt die Spezifikation eines Satelliteninstruments einen großen Teil der Arbeit ein, gefolgt von der eigentlichen Entwicklung des Instruments innerhalb der Vorreitermission AtmoHIT. Unter "Atmospheric Heterodyne Interferometer Test" (AtmoHIT) ist ein Experiment an Bord der Höhenforschungsrakete REXUS 22 zu verstehen, welche innerhalb des Programms für Raketen und Ballonexperimente für Universitätsstudenten in Kiruna, Schweden, im März 2017 startete. AtmoHIT hat die Verifikation des Satelliteninstruments durch die Messung vom Atmosphärenband des Sauerstoffs unter weltraumnahen Bedingungen zum Ziel. Die Temperaturstabilität des Spektrometers wurde in einem Thermalvakuumkammertest vor dem Flug verifiziert. Schwingungsversuche deuteten darauf hin, dass das Instrument der Belastung während des Raketenflugs standhalten kann. Dies wurde mit der erfolgreichen Raketenflugkampagne demonstriert. Die Kampagne zeigte, dass sich das Satelliteninstrument gegenüber den statischen Lasten und Vibrationslasten während des Flugs behaupten und unter weltraumnahen Bedingungen arbeiten kann. Das Atmosphärenband von Sauerstoff konnte mit dem Instrument gemessen werden, wodurch die Funktionalität des Instruments bestätigt wurde. Eine Anomalie während der Separation von Nutzlastsegment und Raketenmotor resultierte in einem stark taumelnden Nutzlast. Dadurch ließ sich das Ziel von Temperaturmessungen in der MLT nicht erreichen. Das Hauptziel der Kampagne, der Nachweis der Funktionalität unter Weltraumbedingungen, wurde aber erreicht.

Diese Arbeit schließt mit einer Diskussion über die wichtigsten Ergebnisse der Instrumentenentwicklung und möglichen Verbesserungen des Instruments ab. Die Methoden und Entwicklungswerkzeuge, die

innerhalb dieser Arbeit generiert wurden, werden schon jetzt in den Folgeprojekten AtmoSHINE und AtmoWINDS verwendet, wodurch schlussendlich der Weg für den Start des AtmoCube-1 Satelliten geebnet wird.

Contents

1. Introduction

The atmosphere is an essential system for life on Earth. We breathe its air and are influenced every day by the weather in the lower atmosphere (Troposphere). Oxygen and ozone in the middle atmosphere (Stratosphere and Mesosphere) protect life from harmful Ultra Violet (UV)-radiation, together with atomic oxygen in the upper atmosphere. The upper atmosphere (Thermosphere), with its ionized particles, also influences telecommunication and global positioning systems and protects life from solar winds. These are only a few examples; To understand in detail how humankind depends on the atmosphere and how we influence it, all aspects of it need to be well understood.

Specifically, climate change is a pressing topic that influences all of us. The Intergovernmental Panel on Climate Change (IPCC) has agreed on increasing global mean temperatures as most important finding, following detailed and extensive climate research (IPCC, 2014). After several decades of research, this field has matured considerably and provides compelling projections about the future of the Earth´s climate. However, the error bars in these projections are still partially high, which allows policymakers to argue instead of acting. Hence, the task of climate research is to reduce these error bars by investigating the underlying processes in more detail, by enhancing climate models, and by providing observational data to constrain these models.

Research on interactions between changes in large-scale atmospheric circulation and the climate is identified as a scientific challenge, within the Earth observation strategy of the European Space Agency (ESA)´s Living Planet Program (ESA, 2015). Several processes are not yet fully understood, especially in the Mesosphere/ Lower Thermosphere (MLT), due to a lack of observational data. The general circulation in the MLT is driven by waves generated in the lower troposphere, whereby the so called planetary waves are the most relevant waves in the stratosphere. In addition, gravity waves drive the circulation in the MLT. Gravity waves effect also the spatial and temporal variations of the MLT. However, it is not even understood which part of the gravity wave spectrum is most important for the momentum deposition in the MLT. The momentum deposition depends on the momentum flux, which is the vertical flux of horizontal momentum of gravity waves, that interacts with the background flow. Either a few large sporadic waves or many small waves can potentially provide the momentum flux (Vincent, 2015). Additionally, annual and inter-annual variations of the momentum flux need to be observed, to understand their temporal effects (Preusse et al., 2009).

Vincent (2015) argued that the MLT is a natural laboratory for investigating gravity waves and their effects, because there, waves dominate the wind and temperature fields (Vincent, 2015; Alexander et al., 2010; Kim et al., 2003). Thus, a satellite mission investigating gravity waves in the MLT would support the research of the gravity wave community. This work proposes a small satellite mission with the goal to characterize gravity waves in the MLT through temperature measurements. Thereby, the focus lies on the development of a small remote sensing instrument for atmospheric limb sounding. Limb sounding describes the vertical sampling of the atmosphere with a satellite instrument that looks tangentially towards the horizon of the Earth. Limb sounding together with tomographic retrieval allow to get spatially resolved data fields of the atmosphere that are useful to characterize a broad spectrum of gravity waves in the MLT. A small satellite, adhering to the CubeSat standard, shall be used for this mission. However, university built CubeSats still have failure rates around $60\,\%$ (Swartwout, 2016) and the remote sensing instrument is a novel system. Thus, a thorough mission concept and a precursor mission for the instrument with environmental tests are important steps towards a successful satellite mission.

The thesis begins with introducing the scientific research question and it establishes arguments to use small satellites and more specifically CubeSats for this application. Afterwards, the AtmoCube-1 CubeSat and its precursor mission AtmoHIT are being introduced as reference missions for the instrument development. The instrument and satellite bus concepts are described together with the measurement geometry and orbit parameters to show conceptual feasibility (Chapter 3). The satellite bus design stays on conceptual level for the remainder of this work. The subsequent Chapter 4 describes the measurement simulation which is used to link the most important instrument design parameters to the performance requirements.

It describes the simulation of the temperature retrieval and the corresponding forward model, including atmosphere, emission, observation, instrument, and data processing simulations. The results are used in the instrument development Chapter 5. This chapter describes in detail the optical design and analysis for the precursor mission AtmoHIT. The structural, thermal, and electrical designs are briefly described afterwards. A detailed description of the manufacturing and assembly of the instrument is not part of this thesis. A short chapter about characterization and calibration describes the required steps in the data processing and explains which of these steps are implemented in this work (Chapter 6). The next Chapter 7 outlines the verification of the instrument through multiple tests. The analysis of test results from laboratory tests, vibration tests, and a thermal vacuum chamber test show that the instrument fulfills its measurement requirements. The analysis of a sounding rocket flight campaign verifies that the instrument can survive and operate in its nominal environment. The discussion chapter reflects the results from the analysis sections and from the verification tests. This thesis concludes with a summary and a projection into future applications, showing where the developed design methods are being already applied. The appendix is used extensively to keep the main part concise and interesting, whilst providing detailed, especially technical, information for the interested reader.

2. Background and Scientific Justification

2.1. The Mesosphere/ Lower Thermosphere (MLT)

The atmosphere in the altitude range from approximately $60\,\mathrm{km}$ to $110\,\mathrm{km}$ is called Mesosphere/ Lower Thermosphere (MLT). It is an interface region that couples the lower atmosphere with the upper atmosphere. This region is strongly affected by radiative heat transfer and by different kinds of waves (gravity waves, planetary waves and tides). However, it was long not well understood that waves transport momentum and energy from the lower atmosphere to the MLT and are thus essential for driving the global circulation in this region:

Already in 1958, Murgatroyd and Goody (1958) analyzed the radiative heat balance in the MLT, which included heating by solar radiation and cooling by the $15\,\mathrm{\mu m}$ CO_2 band and the $9.6\,\mathrm{\mu m}$ O_3 band absorption as the main contributions. They showed that even with a balanced heating rate between $30°$ latitude in winter hemisphere and $60°$ latitude in the summer hemisphere, it deviated considerably from equilibrium outside this area. The temperature in this area would have been increasing or decreasing with time, which led to the assumption of heat transfer from the summer to the winter pole to sustain the thermodynamic equilibrium. Three years later, Murgatroyd and Singleton (1961) calculated a mean flow from the summer to the winter hemisphere in the MLT region. However, their model did not conserve the angular momentum at the poles. So, there was still an important process missing in their models.

McLandress (1998) used a simple mechanistic model of the MLT that shows very well why the radiative heat balance is not sufficient to describe the overall dynamics in this region. The MLT can be described by Navier-Stokes equations in latitude and altitude directions on a rotating sphere. Assuming hydrostatic equilibrium in the vertical and geostrophic equilibrium in the latitudinal direction, a simple set of partial differential equations emerges. For steady state conditions, the atmosphere needs to be in radiative equilibrium that results in a cold winter pole and a warm summer pole. Due to the temperature gradient from pole to pole (meridional direction) and the geostrophic equilibrium, zonal winds are generated that increase with height and are eastward directed (westerlies) for the winter hemisphere and westward directed (easterlies) for the summer hemisphere, with wind speeds of $60\,\mathrm{m/s}$ to $70\,\mathrm{m/s}$. This holds true for an altitude up to $70\,\mathrm{km}$ (Vincent, 2015). However, for the altitude region between $80\,\mathrm{km}$ and $110\,\mathrm{km}$, the radiative equilibrium is not longer fulfilled. The mean zonal wind reverses, with westward (eastward) winds in the winter (summer) hemisphere, reaching wind speeds of $10\,\mathrm{m/s}$ at the solstices and at the Mesopause ($90\,\mathrm{km}$) (Vincent, 2015). Thus, the MLT becomes coldest in the summer hemisphere and warmest in the winter hemisphere. Figure 2.1 shows the temperature as a function of altitude and latitude, with values between $150\,\mathrm{K}$ and $450\,\mathrm{K}$, whereby the coldest temperatures occur in the summer hemisphere at the Mesopause.
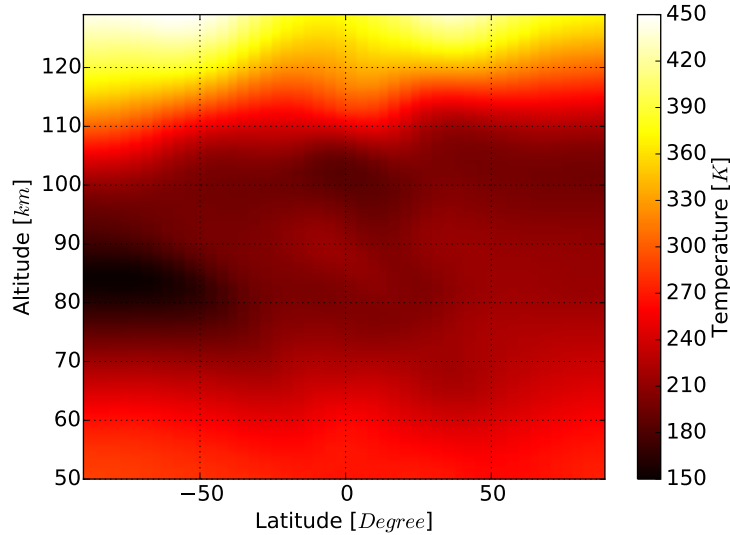
Figure 2.1.: Temperature field [K] in the MLT between an altitude range from $50\,\mathrm{km}$ to $130\,\mathrm{km}$ and latitudes from $-90°$ (summer) to $90°$ (winter) for January at midnight during solar minimum. Data from Hammonia simulations (Schmidt et al., 2006).

Leovy (1964) showed that the dynamics in the MLT could be explained by drag or mechanical friction in the model. Including a forcing term in the Navier-Stokes equations unequal to zero in the range between $80\,\mathrm{km}$ to $110\,\mathrm{km}$ generates a meridional wind from the summer to the winter pole. To conserve the mass balance, adiabatic cooling in the summer pole and adiabatic warming in the winter pole needs to occur, because air masses move upwards and downwards, respectively. Thus, the cooler summer hemisphere, the warmer winter hemisphere, and the reversal in mean zonal winds can be explained by a forcing term that describes drag or mechanical friction (McLandress, 1998). The source of this drag was not clear until Lindzen (1973) argued that dissipating gravity waves can cause it. Since these early studies, extensive research has been conducted to understand how gravity waves influence the MLT.

2.2. Gravity Waves

Gravity waves (also called buoyancy waves) are small scale atmospheric waves (Alexander et al., 2010) that are visible in density, pressure, wind, and temperature fluctuations. The restoring force for gravity waves is the difference in buoyancy of air parcels, adiabatically displaced in altitude compared to the mean background state (Fritts and Alexander, 2003), hence also the name buoyancy waves. Since the pioneering studies by Hines (1960), more than 50 years ago, knowledge about these phenomena has increased considerably. In the remaining part of this chapter, the mathematical background for gravity waves is briefly introduced, followed by a survey of sources and sinks for gravity waves, with the focus on the mechanisms relevant for the MLT. After discussing the simulation of gravity waves in General Circulation Models (GCMs), measurement strategies for observing these small-scale phenomena are discussed.

2.2.1. Mathematical Description

Gravity waves are a solution of the Navier-Stokes equations including mass and energy equilibrium for a three-dimensional rotating fluid in a Cartesian coordinate system, linearized around the mean background state. Equation 2.1 presents this particular solution with u, v, and w the winds speeds in zonal (x), meridional (y), and vertical direction (z), θ the potential temperature, p the pressure, ρ the density, and H the scale height. The wave is characterized by its wavenumbers in the horizontal directions k and l and in the vertical direction m. The frequency of the wave is ω. Variables with primes denote perturbations, tildes correspond to initial perturbation amplitudes, and bars refer to the background states.

$$\left(u', v', w', \frac{\theta'}{\bar{\theta}}, \frac{p'}{\bar{p}}, \frac{\rho'}{\bar{\rho}}\right) = \left(\tilde{u}, \tilde{v}, \tilde{w}, \tilde{\theta}, \tilde{p}, \tilde{\rho}\right) \exp\left[i(kx + ly + mz - \omega t) + \frac{z}{2H}\right] \qquad (2.1)$$

An important parameter of gravity waves is their intrinsic frequency $\hat{\omega}$. It is the frequency of the wave that a Lagrangian observer, moving with the background wind $(\bar{u}, \bar{v})$, would observe and is thus related to the wave frequency of an Earth stationary Eulerian observer by $\hat{\omega} = \omega - k\bar{u} - l\bar{v}$. Solving the Navier-Stokes equations results in the condition that the intrinsic frequency of the wave $\hat{\omega}$ needs to be between the buoyancy frequency $N = (g\partial ln(\theta)/\partial z)^{1/2}$ and the Coriolis parameter $f = 2\Omega \sin \Phi$, with g as gravitational constant, z the altitude, θ the potential temperature, Ω the rotation rate of the Earth, and Φ the latitude (Equation 2.2).

$$|f| < \hat{\omega} < N \tag{2.2}$$

This limit has implications for the existence of gravity waves in different areas of the atmosphere. For example, gravity waves with low intrinsic frequencies can only exist near the equator. The dispersion relation of Equation 2.3 is the incompressible solution for these linearized Navier-Stokes equations and relates the intrinsic frequency to the wavenumber, or wavelength, respectively.

$$\hat{\omega}^2 = \frac{N^2(k^2 + l^2) + f^2 \left(m^2 + \frac{1}{4H^2}\right)}{k^2 + l^2 + m^2 + \frac{1}{4H^2}} \tag{2.3}$$

The amplitude of gravity waves increases with altitude, because of the decrease of atmospheric density. It is expressed in Equation 2.1 with the exponential dependence of the amplitudes on the vertical coordinate z. The larger amplitude in higher altitudes eases the measurement of gravity waves, because they are more clearly visible against the background.

The final property of gravity waves introduced here is their phase speed c. In particular, the phase speed in horizontal direction $c_h = \omega/k_h$ is important. It can be expressed again for a Lagrangian observer and is called the intrinsic phase speed $\hat{c}_h = c_h - u_h$.

Polarization relations allow us to relate the wave amplitudes between different variables ($\tilde{u}, \tilde{v}, \tilde{w}, \tilde{\theta}, \tilde{p}, \tilde{\rho}$); see e.g. Fritts and Alexander (2003) for the set of equations. Ern et al. (2004) used these, together with the dispersion relation, to derive the vertical flux of horizontal pseudo-momentum (short: vertical flux) (Equation 2.4). The flux describes the energy/momentum transport from the lower atmosphere to the upper atmosphere,

$$F_{ph} = \frac{1}{2}\rho \frac{k_h}{m} \left(\frac{g}{N}\right)^2 \left(\frac{\tilde{T}}{\overline{T}}\right)^2 \tag{2.4}$$

with $k_h^2 = k^2 + l^2$ and $\tilde{T}$ the temperature amplitude relative to the mean background state. Ern et al. (2017) revisited the approximations used to derive this equation and showed that it is valid for the gravity waves considered here. This momentum flux is the key parameter that needs to be measured, because it describes the momentum deposition and, thus, the circulation in the MLT. Except for very high frequency waves, the vertical flux depends linearly on the horizontal wavenumber, on the reciprocal of the vertical wavenumber, and quadratically on the relative temperature fluctuation assuming that the density, the buoyancy frequency, and the specific gravitational constant are well known. This shows that the total momentum flux can only be measured, if the entire range of existing vertical and horizontal wavenumbers is being measured. Otherwise, only the partial momentum flux that belongs to a specific gravity wave spectrum, within a specific vertical and horizontal wavenumber range, can be measured. In any case, the vertical and the horizontal wavenumbers, as well as the relative temperature fluctuation need to be well known for accurate momentum flux estimates.

2.2.2. Sources and Sinks

Gravity waves are generated at their sources in the lower atmosphere and they are affected by various processes on their way up to the MLT. Kim et al. (2003) created an illustration of the major gravity wave processes including sources and sinks, which is reprinted in Figure 2.2. The main sources of gravity waves are the orography, convection, and wind shear instabilities, due to jet streams for example. Orographic gravity waves are also called mountain waves, because they are generated by adiabatic displacement of air parcels when they flow over mountains.

Gravity waves are filtered on their way further upwards, mainly in the Upper Troposphere/ Lower

Stratosphere (UTLS). If the phase speed c_h of a gravity wave approaches the background wind speed u_h, the intrinsic frequency approaches zero and the wave dissipates. Thus, this wave is filtered and cannot propagate further upwards. Additional information about this so called critical level filtering can be found in the relevant literature and references therein, e.g. Fritts and Alexander (2003) and Kim et al. (2003).

The remaining waves in the MLT dissipate, either because they reach their critical levels or due to non-linear instabilities caused by large wave amplitudes. These waves are saturated and break, thereby transferring momentum to the turbulent layers. The deposition of momentum is called gravity wave drag that can accelerate or decelerate the background flow. The background flow is dragged towards the same phase speed and direction as the dissipating gravity waves. This drag introduces a mean upwelling in the summer hemisphere and mean downwelling in the winter hemisphere and, consequently, a cooler summer and warmer winter Mesopause. Besides these main processes, other processes, such as secondary wave generation and wave reflection exist, that are discussed in detail in the relevant literature, see e.g. Kim et al. (2003) and Fritts and Alexander (2003) for an overview.

In conclusion, not all upward propagating gravity waves reach the MLT and a specific wavelength spectrum can be ascribed to this region. Knowing the spectrum is important for a satellite mission, because the satellite also needs to be sensitive to such gravity waves. The horizontal wavelength varies from a few tens of kilometers to several hundred kilometers and the vertical wavelength is of the order of several hundred meters to a few tens of kilometers for gravity waves in the MLT (Preusse et al., 2009).

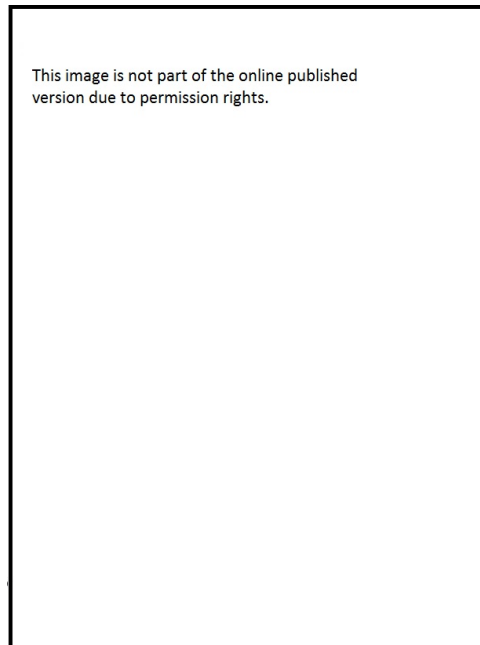This image is not part of the online published version due to permission rights.

Figure 2.2.: Overview of sources and sinks of gravity waves with their preferential propagation paths in the atmosphere. Reproduced from Kim et al. (2003) with permission.

2.2.3. Modeling

Modeling gravity waves in General Circulation Models (GCMs) is important for the MLT to correctly simulate mean zonal winds. However, due to the small scale of gravity waves, the grid size of GCMs also needs to be comparatively small to simulate them explicitly. This results in demanding computational requirements. Current GCMs resolve the MLT with a grid size of typically $1°$ to $2°$. But even with a grid size of $1°$, models cannot explicitly resolve gravity waves with a horizontal resolution smaller than approximately $220\,\mathrm{km}$ that still contribute significantly to the drag that reduces (or enhances) zonal mean wind speeds. For example, the high resolution GCM of Watanabe and Miyahara (2009) with an angular resolution of $0.52°$ cannot resolve gravity waves with a horizontal resolution smaller than $180\,\mathrm{km}$. Without parametrization of small scale gravity waves, the mean zonal winds in the MLT would be overestimated by the GCMs, rendering parametrization of gravity waves necessary.

For example, gravity waves are parametrized in the Whole Atmosphere Community Climate Model (WACCM) 3.5 (Richter et al., 2010), in the thermospheric extension WACCM-X (Liu et al., 2010), and also in the latest WACCM model (Marsh et al., 2013), with separate schemes for orographic gravity

waves and non-orographic gravity waves. However, only convection and frontal/baroclinic sources are considered for non-orographic gravity waves, because of a lack of understanding of the shear-generated gravity waves and other less relevant sources. The Hamburg Model of the Neutral and Ionized Atmosphere (HAMMONIA) (Schmidt et al., 2006) and ECHAM 6 (Stevens et al., 2013) models rely on the gravity wave parametrization scheme of Lott and Miller (1997) for orographic gravity waves and on a scheme from Hines (1997a,b) for all other gravity wave sources in their standard models. Other parametrizations have also been tested with these models and, depending on the model, the GCMs can yield significant differences in the results. For example, the study by Schirber et al. (2015) showed that the Quasi-Biennial Oscillation (QBO) properties in a warmer climate ($+4\,\mathrm{K}$) change as function of the chosen parametrization and the selected tuning parameters.

In summary, current GCMs and those in the near future require parametrization schemes for gravity waves. However, these GCMs lack constraints for the parametrization by observational data (Fritts and Alexander, 2003). For example, the parameters describing gravity waves in ECHAM 6 are tuned "to yield acceptable climate and a sufficiently stable model execution" (Giorgetta et al., 2013, p. 104). In addition, model-resolved gravity waves need to be validated by observations. For example, the amplitudes of resolved gravity waves with horizontal wavelengths larger than $150\,\mathrm{km}$ to $200\,\mathrm{km}$ are underestimated by a factor of two below $40\,\mathrm{km}$ altitude and by a factor of more than five above $50\,\mathrm{km}$ altitude in the European Centre for Medium-Range Weather Forecasts (ECWMF) model (Schroeder et al., 2009). Thus, there is a considerable gap in our understanding of gravity waves and how to describe them optimally in current climate models due to the lack of observational data.

The next section will, hence, describe how gravity waves have been, are being, and potentially will be observed to reduce the observational data gap, to better constrain GCMs, and to increase our understanding.

2.2.4. Observations

Gravity waves can be observed in wind and atmospheric temperature variations associated with the adiabatic movement of air parcels within the wave. From space, gravity waves are often observed in temperature variations that rely on the dispersion and polarization relations.

In-situ measurements with radiosondes, e.g. Wang and Geller (2003) and Allen and Vincent (1995), aircrafts (Chungu et al., 2005) and high altitude balloons (Schöch et al., 2004; Vincent et al., 2007), provide localized measurements on a restricted time scale and only in the troposphere and lower stratosphere. Balloons have the advantage that they fly with the background wind and are thus quasi-Lagrangian tracers, which allows them to directly observe the intrinsic frequencies of gravity waves (Alexander et al., 2010). Pioneering long-term gravity wave characterization flights with balloons were already performed in 1974/1975 and analyzed by Massman (1981).

Ground-based measurements with lidar (Schöch et al., 2004) and radar (Nakamura et al., 1996) have provided accurate measurements also in the MLT, but are localized and have a limited time scale. However, these measurement techniques are useful for cross-calibration and validation of satellite measurements. Research aircraft instruments, like the Gimballed Limb Observer for Radiance Imaging of the Atmosphere (GLORIA) (Riese et al., 2014), provide data of larger areas, but they cannot be used for research on a global scale. Satellite instruments are the only option to get a global view of the Earth´s atmosphere. Alexander et al. (2010) compared all these gravity wave measurement techniques and discussed their advantages and disadvantages in detail.

Preusse et al. (2008) created a survey of the vertical and horizontal wavelength ranges of gravity waves that can be expected to propagate to the MLT and compared it to the sensitivities of space-based remote sensing measurement techniques. Figure 2.3 reproduces the essence of this survey. The black dashed boundary lines constrain the area of gravity waves that can propagate to the MLT. The left curved boundary results from reflection and source evanescence in the lower atmosphere, whereas the right boundary describes the limit of the intrinsic frequency, relative to the Coriolis parameter. Thus, this limit depends on latitude and is shown for $25°$. The lower limit for short vertical wavelengths is a result of ray filtering in the lower atmosphere.
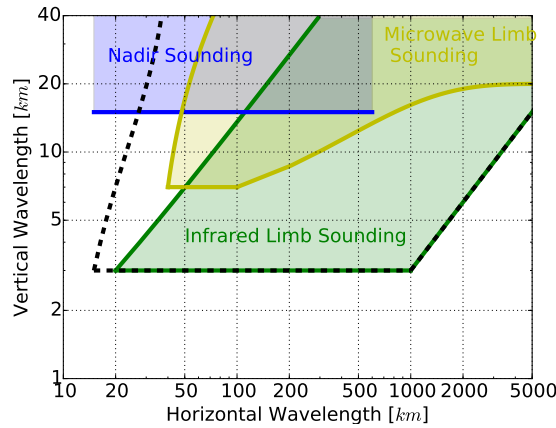
Figure 2.3.: Sensitivity to gravity waves of different measurement techniques. The dashed black lines represent the spectrum of gravity waves in the MLT. The blue area describes the sensitive area for nadir sounder; the yellow area, the sensitive area for microwave limb sounders; and the green area, the area for infrared limb sounders. After Preusse et al. (2008).

Space-based remote sensing instruments can be divided into nadir imagers and limb/ sub-limb sounders. Nadir imagers look down at the Earth´s surface and contribute to the majority of Earth observation instruments. These instruments have low vertical resolution, but high horizontal resolution. They are sensitive to gravity waves with vertical wavelengths down to $10\,\mathrm{km}$ and horizontal wavelengths down to $15\,\mathrm{km}$. Thus, the ratio between vertical and horizontal wavelengths is high, which means that nadir sounders are sensitive to waves with high intrinsic frequencies (Wu et al., 2006).

Limb sounders, on the contrary, look tangentially towards the horizon of the atmosphere. Relevant gravity wave limb sounders use microwave or passive infrared instruments. Microwave limb sounders have slightly worse resolving properties, compared to infrared instruments. The lowest vertical and horizontal wavelengths are approximately at $7\,\mathrm{km}$ and $40\,\mathrm{km}$, respectively, for optimal conditions. Similarly, passive infrared limb sounders are sensitive to vertical wavelengths longer than $2\,\mathrm{km}$ and horizontal wavelengths longer than $20\,\mathrm{km}$ for optimal conditions. The ratio between vertical and horizontal wavelengths is typically small for limb sounders, which means that they are sensitive to low intrinsic frequencies.

Figure 2.3 shows clearly the gap in the sensitivity of measurement techniques from space. Low horizontal wavelengths and low vertical wavelengths cannot be measured by established measurement principles. However, this gap can be minimized with specific gravity wave remote sensing missions.

2.3. Temperature Measurement Strategies for the MLT

Temperature measurements allow to characterize gravity waves. Typically, measurements of atmospheric emissions of CO_2 at $12.6\,\mathrm{\mu m}$ or at $15\,\mathrm{\mu m}$ are used for temperature retrieval, see e.g. Riese et al. (1999); García-Comas et al. (2014), but other methods can also be used. One option is to measure the emission of the atmosphere, the airglow, in the UV, visible, and near infrared regions.

Airglow exists because of fluorescence and chemiluminescence of atoms and molecules in the atmosphere, whereby light is emitted at different wavelengths. Some of the more important airglow emissions are (Brasseur and Solomon, 1986):

- the atomic oxygen green line at $558\,\mathrm{nm}$,
- the atomic oxygen red line at $630\,\mathrm{nm}$,
- the atmospheric band of molecular oxygen around $762\,\mathrm{nm}$,
- the infrared atmospheric band of molecular oxygen around $1270\,\mathrm{nm}$, and
- the Meinel bands of the hydroxyl radicals in the visible (VIS)/ near-infrared (NIR) region.

Not all of these lines are equally well suited for measuring temperature in the MLT. The intensity needs to be sufficiently strong in the relevant altitude range, which already eliminates the atomic oxygen red line. Additionally, the radiative lifetime should be sufficiently low that the dynamics in the atmosphere does not displace the emitting molecule considerably, which reduces the spatial resolution of the measurement.

This eliminates the infrared atmospheric band with its long radiative lifetime. However, the radiative lifetime should also be long enough for the molecules/atoms to reach thermodynamic equilibrium with the background state. Otherwise, only the temperature of the excited molecule/atom is measured, but not that of the atmosphere. Lastly, relying on the relative temperature dependence of different rotational transitions simplifies the measurement and the calibration (especially the in-orbit calibration) of the instrument, because an absolute calibration is not required. Thus, the measurement of the oxygen atmospheric band (A-band) has some advantages over the measurement of the atomic oxygen green line, because it allows the derivation of the temperature, based on the relative intensity of individual lines within the band. The oxygen A-band is an emission that extends between $60\,\mathrm{km}$ and $130\,\mathrm{km}$ during daylight and in a small range of about $10\,\mathrm{km}$ around $90\,\mathrm{km}$ altitude during nighttime. It is the emission of interest in this work.

2.4. Relevant Past, Current, and Future Remote Sensing Satellites

Limb sounders, that provided important data for gravity wave research, were the infrared instrument CRISTA (Offermann et al., 1999; Preusse et al., 2002), flown on two space shuttle missions in 1994 and 1997, the Limb Infrared Monitor of the Stratosphere (LIMS) instrument (Fetzer and Gille, 1994) on Nimbus-7, the High Resolution Dynamics Limb Sounder (HIRDLS) (Gille et al., 2008) on the Aura satellite, the Global Ozone Monitoring by Occultation of Star (GOMOS) instrument (Sofieva et al., 2007) onboard Envisat, the Microwave Limb Sounder (MLS) (Wu, 2001), and the WIND Imaging Interferometer (WINDII) instrument (Shepherd et al., 1993) onboard the Upper Atmosphere Research Satellite (UARS).

Instruments still in operation are MLS on Aura (Wu and Eckermann, 2008), the Sounding the Atmosphere using Broadband Emission Radiometry (SABER) instrument (Russell III et al., 1999), the TIMED Doppler Interferometer (TIDI) (Killeen et al., 1999) on the Thermosphere Ionosphere Mesosphere Energetics and Dynamics (TIMED) satellite, the Optical Spectrograph and Infrared Imager System (OSIRIS) and the Submillimeterwave Radiometer (SMR) on Odin (Llewellyn et al., 2004; Murtagh et al., 2002). All of these still operational instruments have been measuring for more than a decade, well above their design lifetimes and will most likely come to the end of their lives within the next few years. Placeholder missions to ensure data continuity are missing at the moment.

Nadir imagers are far more often used on satellites, but not many are useful for the characterization of gravity waves in the MLT. Indeed, nadir measurements of the MLT do not allow to resolve gravity waves with low vertical wavelengths, because atmospheric emissions begin to saturate in the stratosphere and below, which is a necessary condition for low vertical resolutions. The microwave nadir sounder Advanced Microwave Sounding Unit-A (AMSU-A) (Wu, 2004), an exemplary microwave sounder, can detect gravity waves up to approximately $30\,\mathrm{km}$ altitude, similar to the Atmospheric Infrared Sounder (AIRS) (Alexander and Barnet, 2007). They provide valuable data limited to the stratosphere.

The Michelson Interferometer for Global High-resolution Thermospheric Imaging (MIGHTI), onboard the Ionospheric Connection Explorer (ICON) satellite, should be launched in November 2017. It is a Michelson interferometer that measures winds and temperature in the thermosphere between $90\,\mathrm{km}$ and $300\,\mathrm{km}$ with a limb viewing geometry. They derive the temperature between $90\,\mathrm{km}$ and $150\,\mathrm{km}$ by measuring the oxygen A-band emission with narrow bandpass filters and use a Spatial Heterodyne Spectrometer (SHS) configuration called Doppler Asymmetric Spatial Heterodyne Spectrometer (DASH) to derive winds (Englert et al., 2013, 2017). Thus, temperature data from this instrument can also be used for gravity wave characterization, but only in the lower thermosphere and further up.

The Mesospheric Airglow/ Aerosol Tomography and Spectroscopy (MATS) satellite is a Swedish satellite, currently in development with an expected launch date in 2019 and a mission lifetime of two years. This satellite mission has the goal to characterize gravity waves in three dimensions by tomography. It uses four filters to derive temperatures from the oxygen A-band emission in a limb sounding configuration.

Even with the development of the MATS satellite, it is conceivable that there will soon be much less data available with a potential data gap in the temperature related observations of the MLT. In addition, none of the existing instruments are able to perform measurements of those atmospheric parameters that are relevant for characterizing gravity waves globally in three dimensions in the MLT, because it has never been their explicit mission objective.

In conclusion, contradicting trends exist around the scientific investigation of the MLT: Scientists extend their climate models to higher altitudes and acknowledge the relevance of small scale processes for the climate and on climate change. Scientists require observational data to constrain these models and processes. However, the number of operational MLT missions will decrease further in the future. New satellite missions need to be implemented to provide the required data to researchers. However, large satellite missions have long development times and with only "elderly", still operational satellites in orbit, data may soon not be available anymore at all. Fortunately, the recent trend in the aerospace industry that focuses on small satellites with short development times and frequent launch opportunities provides new perspectives for limb sounding missions. The following description of these so-called CubeSats, and in particular the AtmoCube-1 mission, details possible contributions in the area of gravity wave observation.

2.5. CubeSats and their Scientific Value

2.5.1. CubeSats

Satellites called CubeSats comply with the CubeSat standard. This standard was initiated at the California Polytechnic University by Prof. Jordi Puig-Suari and Prof. Bob Twiggs from Stanford University in 1999 (Mehrparvar, 2014). CubeSats are classified as nano satellites that typically have a mass between $1\,\mathrm{kg}$ and $10\,\mathrm{kg}$. For a general classification of small satellites refer to e.g. Doncaster and Shulman (2016). Thereby, the most common types of CubeSats are one unit (1U), two unit (2U) and three unit (3U) CubeSats. The smallest form factor is the 1U CubeSat, which has a volume of $10\,\mathrm{cm} \times 10\,\mathrm{cm} \times 10\,\mathrm{cm}$ and a mass of about $1\,\mathrm{kg}$ and maximum $1.33\,\mathrm{kg}$. A 3U CubeSat can be seen as three stacked 1U CubeSats. CubeSats are stowed within a deployer that releases them into space. The deployer is a box with a spring on one side and a door on the other side and it is mounted in the payload section of the launch vehicle. In orbit, the door opens and the CubeSat(s) is (are) pushed out by the spring. Deployers are currently qualified for many different launcher vehicles and, thus, CubeSats are quite regularly launched as secondary or tertiary payloads.

Initially, the goal of the CubeSat standard was to reduce costs and development time, while increasing the accessibility and launch frequency to space. Therefore, the standardized interface to the launch vehicle reduces risk for the launch provider and allows the launch of different CubeSats without a costly qualification campaign for each individual CubeSat for each rocket. Also, their small mass and volume makes the launch considerably cheaper compared to large satellites. Large satellites, like Envisat, carried multiple instruments with an expected reduction of cost per mass. However, the complexity of such large systems caused interference problems between instruments: Motions from scanning instruments influenced vibration sensitive instruments, Radio Frequency (RF) systems interacted with one another and already completed instruments had to wait for delayed ones. Thus, the synergistic advantages of a large satellite platform were significantly reduced by these disadvantages, leading to the increasing development of smaller satellites (Selva and Krejci, 2012). Overall, there is now a trend towards smaller spacecraft for Low Earth Orbit (LEO) satellites (Fuller et al., 2015).

The CubeSat standard became popular for small satellites and especially for educational programs; see for example the program of TU Delft (Bouwmeester et al., 2008). Since 2014, about 100 CubeSats have been launched each year, with an increasing trend (Swartwout, 2016). Whilst university-built CubeSats dominated the CubeSat sector for the last 15 years (Swartwout, 2013), the commercial sector will contribute more than $70\,\%$ of all nano/micro-satellites in the future, according to the market prognostics of Doncaster and Shulman (2016).

About two-third of all CubeSats missions are either partially or fully successful (Swartwout, 2016). However, this value depends strongly on the CubeSat developer. Hobbyist and new university groups have failure rates of around $60\,\%$, experienced smallsat builders have failure rates of about $20\,\%$ (the uncertainty of this value is higher, compared to the other values), and the traditional space industry has failure rates of about $12\,\%$. The differences in failure rates stem from significant delays in the development schedule for less experienced/professional teams that lead to little time and resource availability for environmental and functional testing, according to Swartwout (2016).

2.5.2. Science with CubeSats

At the beginning of the CubeSat era, these satellites were mainly built for demonstrator or technology missions and provided only little or no scientific value (Swartwout, 2013). In recent years, this aspect changed dramatically, because programs such as the Educational Launch of Nanosatellites (ELANA) program of the National Research Laboratory (US) (NRL) or the CubeSat flight opportunities provided by ESA require sound scientific objectives from the competing teams. Furthermore, the scientific and technological impact of CubeSat missions is increasing with the increasing interest of the industry. In particular, CubeSat-based constellations have seen large investments in recent years.

A prominent industrial example is the company PlanetLabs (now called Planet) with its 3U CubeSats, called Doves. The goal of this imaging satellite constellation is to provide daily global pictures of the Earth with a resolution of $3\,m$ to $5\,m$ in the visible band. Therefore, between 150 and 200 satellites need to operate in orbit simultaneously. The company has received more than $\$135$ million venture capital (Hand, 2015b) to set up this constellation and it has already launched more than 190 satellites (Krebs, 2016). Besides its impressive launch record, the company´s engineering philosophy also differs significantly, compared to established aerospace industry practices and shares similarities with Silicon Valley software start-ups (Boshuizen et al., 2014). However, PlanetLabs is generating pictures and whether these images are also suitable for scientific applications will become apparent in the future.

Atmospheric monitoring for weather forecasting is another area in which CubeSat constellations are being deployed, using Global Navigation Satellite System (GNSS) Radio Occultation (RO) measurements. This measurement technique became very important for the assimilation of water vapor and temperature profiles from near-surface up to approximately $40\,km$, with very high vertical resolution and high precision (Kursinski et al., 1997; Harnisch et al., 2013). A Global Positioning System (GPS) receiver measures the signal of a rising or setting GPS satellite, which propagates through the atmosphere. Having only a receiver on a single satellite limits the amount of vertical profiles per day, because of the observation geometry constraints. Thus, satellite constellations have been deployed and are currently in development to increase the data generation capabilities. For example, the successful small satellite, however not CubeSat, constellation COSMIC-1 (six satellites) and its successor, COSMIC-2 (12 satellites), provide approximately 1.7×10^3 profiles per day, respectively 10×10^3 profiles per day (Kramer, 2015). But nanosatellite constellations have also received considerable funding from investors such as the company Spire, with $\$80$ million for their 3U CubeSats (Lemur-X), or the 6U CubeSats from PlanetiQ, with $\$5$ million in funding. These constellations aim to provide 10×10^3 profiles per day, starting in 2016, or 34×10^3 occultations, starting in 2017 (Hand, 2015a). In summary, large numbers of tropospheric and stratospheric temperature measurements will be provided operationally in the near future. Nevertheless, still only a few satellites are measuring temperatures in the MLT.

2.5.3. CubeSats for Temperature Measurements in the MLT

Selva and Krejci (2012) conducted an extensive survey about the potential of CubeSats for scientific applications in Earth observation. They also discussed the use of the oxygen A-band and referred to the missions SwissCube and ION1. ION1 was a 3U CubeSat with an oxygen A-band photometer. However, it never reached orbit, due to a launch failure of the carrier Dnepr rocket. The goal of this mission was to measure wave structures of the oxygen A-band emission in the horizontal direction. SwissCube was a successful 1U CubeSat mission, which is still operational (2017). The satellite has the mission of studying the variability of the oxygen A-band emission as a function of time (Borgeaud et al., 2010). The mission website shows images taken by the camera (http://swisscube.epfl.ch/).

The paper of Selva and Krejci (2012) neglects the discussion of limb sounding as a niche for potential scientific measurements by CubeSats. Although it stated that limb sounders can achieve higher vertical resolutions than nadir sounders, the paper probably neglects limb sounders because of their stringent attitude knowledge and determination requirements. However, recent advances in this field make such types of missions possible. One of the first limb sounders on a CubeSat basis will probably be the Optical Profiling of the Atmospheric Limb (OPAL) satellite (Marchant et al., 2014), scheduled for launch in mid-2017.

In summary, the CubeSat and the small satellite markets exhibit a rapid development and they are changing the landscape in the aerospace industry. Especially with the advent of industry supported constellations,

this field will mature further. Scientific payloads are relatively rare in CubeSats. The oxygen A-band emission has already been used in CubeSat missions, but not yet for temperature measurements. The instrument for the satellite mission described here will fill this gap.

2.6. Scientific Objectives and Requirements of the Satellite Mission

The scientific objectives for the satellite mission proposed here evolve around the characterization of gravity waves and temperature measurements in the MLT. In particular, the following research objectives shall be addressed with the satellite mission:

- to improve the understanding of the importance of small scale gravity waves for the dynamics of the MLT.

- to improve the understanding of the temporal variation of the gravity waves and its impact on the dynamics of the MLT.

- to increase the number of global temperature measurements in the MLT.

These scientific objectives are addressed by observation requirements of

- Temperature measurement during day- and nighttime.
- Measurement in an altitude range from $60\,\mathrm{km}$ to $120\,\mathrm{km}$ during daytime.
- Measurement in an altitude range from $85\,\mathrm{km}$ to $95\,\mathrm{km}$ during nighttime.
- Measurement with a vertical resolution better than $1.5\,\mathrm{km}$.
- Measurement with a horizontal resolution better than $60\,\mathrm{km}$.
- Limb geo-location uncertainty better than $1.5\,\mathrm{km}$.
- Temperature measurement precision better than $2.5\,\mathrm{K}$.

The altitude ranges are restricted, because the oxygen A-band emission around $762\,\mathrm{nm}$ is used for the temperature retrieval. Nevertheless, the altitude range covers the complete MLT during daytime and a portion of it during nighttime. The vertical resolution is similar to existing limb sounders that were be used for gravity wave characterization. A limb geo-location uncertainty better than $1.5\,\mathrm{km}$ is similar to the vertical resolution and tolerable, if the altitude profiles are sampled in one step. Then, the total limb sounding profile is misplaced by the geo-location uncertainty, which has only minimal implications for gravity wave characterization.

3. AtmoCube-1 Mission Overview

The satellite mission, called AtmoCube-1, provides the main design drivers for the design of the remote sensing instrument, whereas an instrument test during a ballistic rocket launch campaign is used for verification and evaluation. The satellite mission AtmoCube-1 is first introduced followed by its precursor mission AtmoHIT (Atmospheric Heterodyne Interferometer Test). The main focus of this work lies on the remote sensing instrument and only a basic satellite bus concept is presented to demonstrate conceptual feasibility.

The design of the instrument is largely driven by the satellite mission AtmoCube-1 with the mission to perform temperature soundings in the MLT to provide data for climate models and for gravity wave characterization. This overall mission statement is supported by the four objectives based on the scientific objectives:

- to provide temperature data in the Mesosphere/ Lower Thermosphere (MLT),
- to characterize gravity waves,
- to demonstrate miniaturized remote sensing instrument technologies, and
- to provide a low-cost satellite to serve as a pathfinder for atmospheric swarm observations.

The first objective is in direct alignment with the mission statement and the scientific objectives. Temperature is measured, because gravity wave momentum flux can be derived thereof based on the polarization and dispersion relations. Thus, its measurement allows to globally derive the absolute gravity wave momentum flux and enables the second objective. The third objective is a technological objective and corresponds closely with the fourth objective. The cost of a satellite scales largely with its mass. Thus, the objective to provide a low-cost satellite requires the development of miniaturized remote sensing instrument technologies, which in itself is a demanding objective. The low-cost satellite can then serve as a pathfinder for a swarm of satellites.

Compared to typical scientific missions, where the payload mostly drives the satellite mission in its dimensions, mass, power production, and communication data rate, a CubeSat mission requires detailed assessment of the payload and its design based on the constraints set by the CubeSat form factor. Thus, some design choices encountered in the following might not seem optimal from the scientific perspective, but are needed trade-offs within the available design space. This situation is different to most scientific missions and is thus emphasized here, specifically.

3.1. Scientific Measurement

A limb viewing near Infra-Red (IR) measurement concept is selected for the AtmoHIT instrument, because it has the potential to be highly miniaturized while providing a fair Signal-to-Noise (S/N)-ratio. Specifically, the instrument measures emission of excited molecular oxygen centered around $762\,\mathrm{nm}$ wavelength. The emission is produced in various processes related to the photolysis of molecular oxygen and ozone as well as chemiluminescence. Five production mechanisms have been identified which produce oxygen in the required excited state. Figure 3.1 shows the emission rate in $\mathrm{photon/s/cm^3}$ as a function of altitude between $50\,\mathrm{km}$ and $130\,\mathrm{km}$ with a distinction between day and night emission. The day emission is up to two orders of magnitude larger compared to the nighttime emission as multiple additional production mechanisms contribute to the emission rate. It is intended to measure the emission during day and night by using different exposure/integration times of the sensor. Further information about these mechanisms is provided in Chapter 4.1.2.
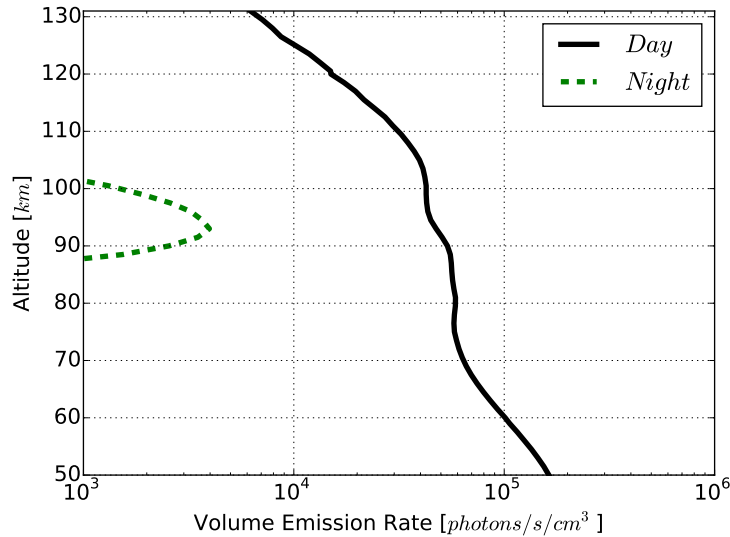
Figure 3.1.: Oxygen A-band volume emission for day and night.

The A-band emission stems from a rotational-vibrational transition from an excited state to the ground state $(O_2(b^1\Sigma, v = 0)$ to $O_2(X^3\Sigma, v = 0))$ (Figure 3.2). The rotational distribution within the band depends on ambient temperature and individual lines have different temperature dependencies. Thus, the temperature can be derived by measuring the intensity of multiple lines without an absolute calibration. This simplifies the instrument considerably and allows it to be flown on a CubeSat. Analysis shows that the measurement of six fine structure lines, which are marked red in Figure 3.2, provides most information within the trade-off of spectral resolution versus spectral bandwidth. Appendix B.3 provides further information.
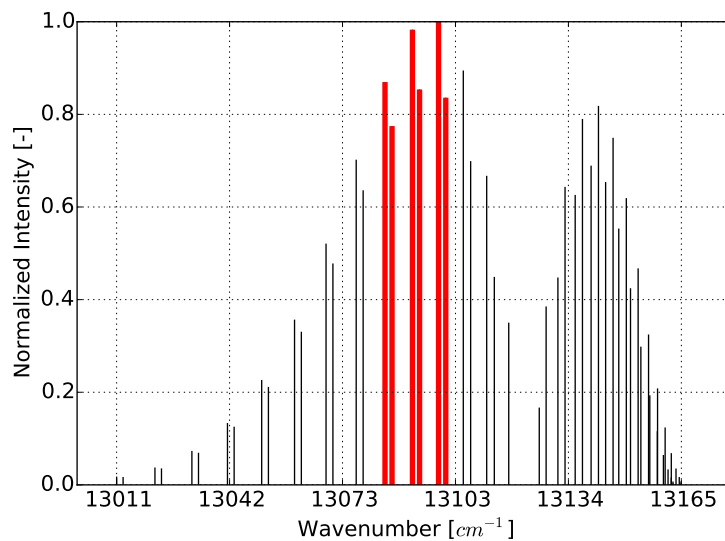
Figure 3.2.: Fine structure of the oxygen A-band emission resulting from different rotational quantum numbers. Lines have different temperature dependencies, allowing temperature derivation without absolute calibration. The six marked red lines are measured by the instrument.

Measuring the emissions at this wavelength has also the advantage that background noise from surface emissions and scattered Sun and Moon light gets absorbed by the oxygen in the lower atmosphere.
The instrument profiles the atmosphere in one step, which provides data between $60\,km$ and $120\,km$ with a vertical resolution of $1.5\,km$. The atmosphere gets opaque for this band below approximately $60\,km$, because the oxygen density is so high that the emission from an excited oxygen molecule is absorbed by the surrounding oxygen in ground state. Emitted radiation above $60\,km$ starts to reach the outer edge of the atmosphere and can therefore be detected with a satellite. At around $95\,km$, the remaining oxygen molecules are so sparsely spread that no absorption is effectively present anymore. Figure 3.3 shows the

average band transmission factor of the atmosphere for an oxygen molecule at an specific tangent altitude. It is discussed again in more detail in section 4.2.2.
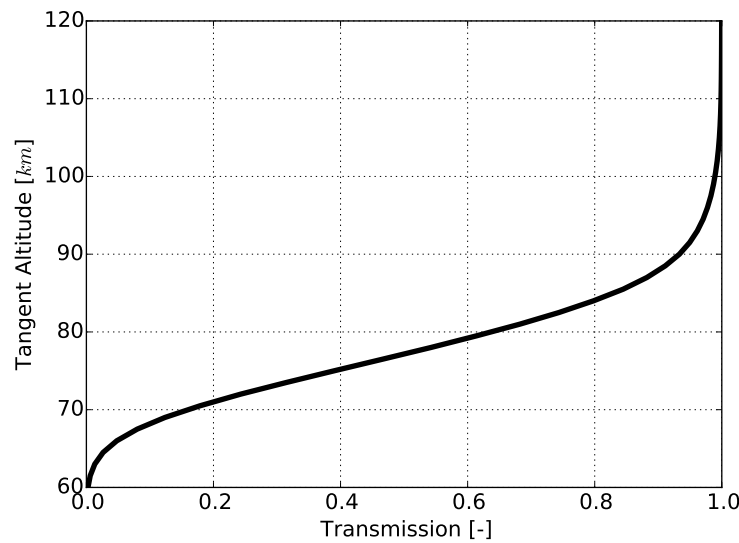
Figure 3.3.: Transmission of the oxygen A-band emission from air parcels to a limb viewing satellite as a function of air parcel tangent height.

3.2. Measurement Geometry

The temperature measurement between $60\,\mathrm{km}$ and $120\,\mathrm{km}$ tangent altitudes requires a vertical full Field of View (FOV) of $1.3°$ for the selected nominal orbit altitude of $600\,\mathrm{km}$, see Chapter 3.3.2. The horizontal full FOV is chosen equally to the vertical FOV, because it represents a trade-off between sensitivity, cross-track horizontal resolution, and instrument complexity.

3.2.1. Limb Measurement

The nominal observation mode for AtmoCube-1 is limb observation, viewing opposite to the flight direction, similar to the CRISTA experiment (Offermann et al., 1999; Preusse et al., 2002), see Figure 3.4. The opposing direction is chosen, because it reduces the degradation of the first optical element by atomic oxygen.

The retrieval of one-dimensional temperature profiles from limb observations includes errors due to horizontal inhomogenities, see e.g. Steck et al. (2005). Two dimensional retrievals along the line of sight and in dependence of altitude can reduce this error. In addition, a two-dimensional limb retrieval scheme also increases the sensitivity of the instrument to a broader spectrum of gravity waves, see e.g. Preusse et al. (2009).
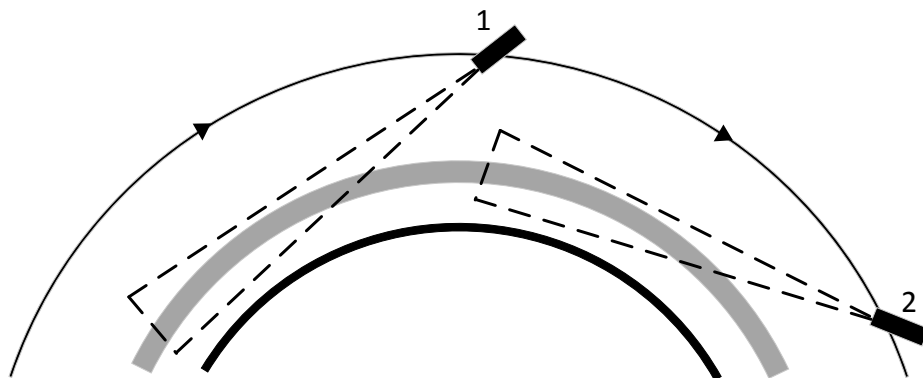
Figure 3.4.: Limb measurement geometry for AtmoCube-1.

3.2.2. Momentum Flux Error Estimations for MLT Limb Measurements

For the limb sounding configuration of AtmoCube-1, the sampling in along-track direction depends on the integration time of the instrument and on the weighting function of the limb retrieval, which describes where the radiation from the atmosphere originates. The Full-Width Half-Maximum (FWHM) resolution along the Line-of-Sight (LOS) of a limb sounder is approximately $500\,\mathrm{km}$ for optically thin conditions (Preusse et al., 2009), which corresponds to the horizontal along-track FWHM resolution for AtmoCube-1. The integration of the signal over $500\,\mathrm{km}$ along LOS cannot be avoided. By sampling multiple times along-track, however, a higher resolution can be recovered by a two-dimensional tomographic retrieval. Then, the integration time is the theoretical limit for the tomographic retrieval, because of the smearing of the signal in horizontal direction. The AtmoCube-1 satellite moves with $7.6\,\mathrm{km/s}$ for a typical Low Earth Orbit (LEO). Thus, the instrument integrates over an along-track sample smaller $50\,\mathrm{km}$, if the integration time is less than $6.5\,\mathrm{s}$ for this orbital velocity. So as an interim conclusion, an integration time less than $6.5\,\mathrm{s}$ is achieved during daytime conditions, which will be discussed in Chapter 3.3.3. The low integration time cannot be achieved for nighttime conditions. However, other tomographic measurement modes are planned for the nighttime, which are the topic of the next chapter.

The goal of the remainder of this chapter is to get an estimate over the absolute momentum flux error that can be expected in the MLT for the AtmoCube-1 satellite instrument. It is simplified and relies on Equation 2.4 to estimate the error. The analysis includes the error due to the approximate nature of this equation, an uncertainty in horizontal wavelength of $200\,\%$, in vertical wavelength of $20\,\%$, and in a temperature measurement precision of $2.5\,\mathrm{K}$. The horizontal wavelength has a factor of two uncertainty similar to Ern et al. (2004), due the pure along-track sampling. It is assumed that the gravity wave temperature amplitude is $10\,\mathrm{K}$ and that aliasing effects can be neglected. The $10\,\mathrm{K}$ temperature amplitude is a typical value for gravity waves at the Mesopause. Preusse et al. (2002) showed that the retrieval uncertainty of vertical wavelengths from CRISTA data is approximately $20\,\%$. CRISTA data has the same vertical sampling as AtmoCube-1, which allows this analogy for the vertical wavelength uncertainty. The temperature measurement precision of $2.5\,\mathrm{K}$ corresponds to the precision of the SABER instrument at an altitude of approximately $85\,\mathrm{km}$ (Remsberg et al., 2008). SABER was already used for gravity wave analysis, e.g. (Preusse et al., 2006), and is therefore useful as a reference for the required temperature measurement precision to characterize gravity waves.

Figure 3.5 shows the error in absolute momentum flux as a function of the horizontal and vertical wavelengths. For three exemplary points, the error budgets are shown in the bar chart to the right of the figure. The contour in the plot represents the boundary of the gravity wave spectrum in the MLT. The figure shows that the momentum flux approximation is appropriate for gravity waves in the MLT and that the highest gravity momentum flux error is due to the horizontal wavelength measurement error. The measurement error can increase up to $208\,\%$.

The analysis shows already the importance of a high temperature measurement precision and a good characterization of vertical and horizontal wavelengths of gravity waves. The first aspect is addressed in detail in this work and the second aspect is the topic of another PhD research (Song, 2018, in preparation).
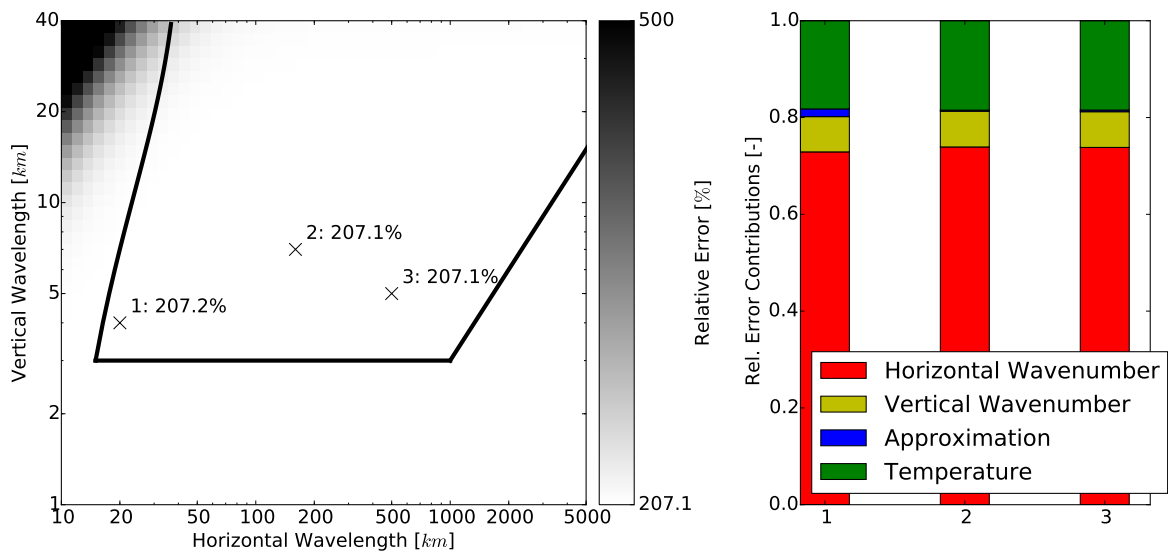
Figure 3.5.: Gravity wave measurement errors. Left figure: Measurement error of absolute vertical flux of horizontal momentum in dependence of vertical and horizontal wavelengths. Boundary lines describe the existing spectrum in the MLT, inspired by Preusse et al. (2008). Right figure: Relative measurement error contributions of the four considered error terms including the momentum flux approximation error, the vertical and horizontal relative wavelengths measurement errors, and the temperature measurement precision for three points in the right figure.

3.2.3. Tomographic Measurement

Besides the nominal limb measurement mode, other tomographic measurement modes are planned to be performed. These measurement modes are specifically tailored to characterize a broad spectrum of gravity waves. AtmoCube-1 houses only one dedicated instrument. Thus, it is possible to perform maneuvers for tomographic observations without interfering with other payload operations. One of these maneuvers is shown in Figure 3.6. A pre-selected volume of the atmosphere is first observed while the satellite rises and when it sets. Therefore, the satellite needs to continuously rotate. The individual measurements are combined in the post-processing for the three-dimensional characterization of gravity waves. Song et al. (2017) describe this measurement mode and its sensitivity in detail.
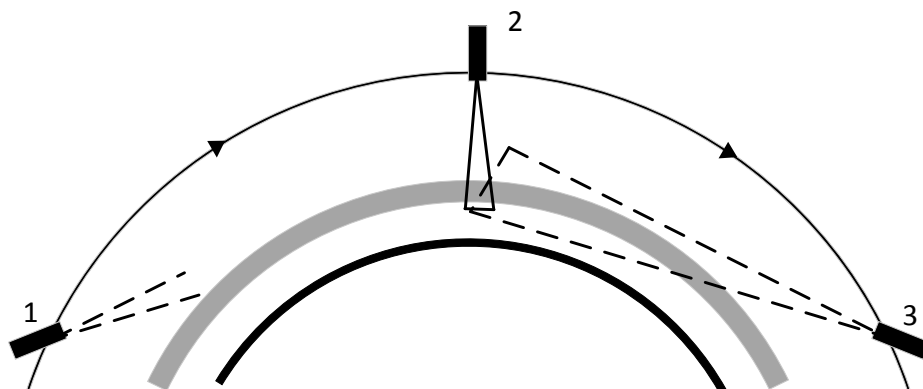
Figure 3.6.: Pointing tomographic measurement geometry for AtmoCube-1.

3.3. Mission Design

3.3.1. Science Payload

Remote sensing satellites typically use filters and gratings to record spectral information. Fabry-Perot Spectrometers (FPSs) and Michelson Interferometers (MIs) are complex instrument types, which can

provide high light sensitivity - they have a high etendué or throughput. The TIDI (Killeen et al., 1999) on the TIMED satellite is stated exemplary for an FPS. FPSs can be built very small and with the use of for example piezo-actuators, they can measure a spectrum with high resolution. The Aalto-1 CubeSat is a satellite with an FPS to measure multiple spectral channels in the visible spectrum (Kestilä et al., 2013). The Michelson Interferometer for Passive Atmospheric Sounding (MIPAS) (Fischer et al., 2008) onboard ENVISAT and WINDII (Shepherd et al., 1993) for wind measurements have been successfully flown in space as MIs. MIs are relatively complex instruments, because they usually require moving parts, especially if a large etendué (light sensitivity) is required. However, the etendué of so called field-widened MIs exceeds the etendué of FPSs. The application of the AtmoCube-1 satellite mission requires a spectrometer with high etendué at a small form factor to measure the faint oxygen A-band emission and without any moving parts at interferometric accuracy. Thus, a so called Spatial Heterodyne Spectrometer (SHS) was selected due to its favorable attributes.

The SHS is a relatively new type of spectrometer, which was originally proposed by Pierre Connes in 1958 in a configuration which he called "Spectromètre interférential à selection par l'amplitude de modulation (SISAM)" (Connes, 1958). This spectrometer was impractical to use until the development of imaging detectors. Due to the advent of detector technology, it was re-invented by Harlander and Roesler at the University of Wisconsin (Harlander et al., 1992) and called SHS. Since then, this spectrometer type has been successfully demonstrated in space during a Space Shuttle mission (Harlander et al., 2002). Afterwards, it was shown that such a spectrometer can be built as a monolithic block (Harlander et al., 2002; Doe et al., 2011). The monolithic design is of particular interest, as it reduces the size and mass of the instrument considerably and makes it quite rigid and fault tolerant, e.g. to vibrations. Additionally, it can be field-widened, which increases the etendué by approximately one to two orders of magnitude compared to a standard MI and by five orders of magnitude compared to a conventional grating spectrometer, see appendix B.2.4. Thus, it is possible to build a small instrument which fits into a CubeSat, while still being able to provide data with high precision for scientific applications. Englert et al. (2007) and Solheim et al. (2015) demonstrated that a variant of the SHS can also be used for wind measurements - the Doppler Asymmetric Spatial Heterodyne Spectrometer (DASH) configuration.

Similar to the MI, the SHS is a Fourier-transform spectrometer, but with gratings instead of mirrors in the two arms. Figure 3.7 shows the schematic of the most basic SHS. It consists of a beamsplitter to divide the incoming collimated beam into two arms. Two identical reflective diffraction gratings in each arm with the equal distance from the beamsplitter reflect the light back towards the beamsplitter. The beams get combined and half of the incoming intensity leaves the beamsplitter towards the detector, where an interferogram appears. One dimension on the focal plane array (detector) describes the spectral domain, whereas the second dimension can image spatial information, depending on the optical configuration. Fourier-transformation allows to retrieve the spectrum. Field-widening is not included in the most basic SHS schematics of Figure 3.7. It can be achieved by including prisms in the arms of the SHS. They virtually rectify the image of the grating relative to the optical axis. An in-depth discussion of the SHS principles is provided in the appendix B.2.
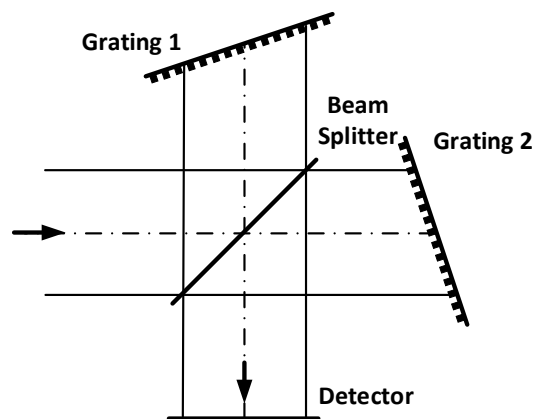

Figure 3.7.: Schematic of the most basic SHS with two diffraction gratings, a beamsplitter, and a detector.

Figure 3.8a shows the schematic of the actual SHS with beamsplitter, field-widening prisms, and two

gratings. The position of these elements is controlled by spacers (Spacer 1 and Spacer 2). The spacers are hollow and do not interfere with the light paths. Figure 3.8b shows the actual SHS with the two gratings shining with different colors due to the illumination during the photography.
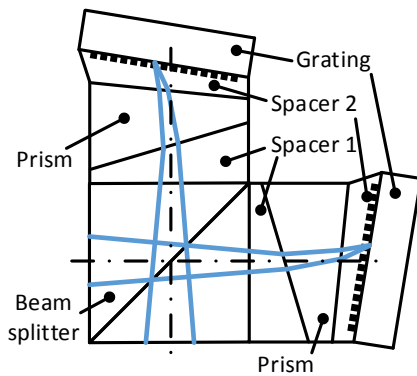
(a) Schematic of the SHS.　　　　(b) Assembled SHS for the precursor mission.

Figure 3.8.: The SHS consists of two diffraction gratings, a beamsplitter, and the field-widening prisms. The relative position between these parts is controlled by spacers (Spacer 1 and Spacer 2). The blue lines in Figure 3.8a show the ray paths for the central beam, focusing on the gratings.

The spectrometer alone does not suffice to fulfill the observational requirements and additional optics is required. Figure 3.9 shows the overall optical concept for the instrument. The heart of the instrument builds the SHS. In front of the SHS, the fore-optics focuses light onto the SHS gratings. A bandpass filter in front of the fore-optics selects the spectral band. The baffle reduces straylight by reducing the Sun exclusion angle. The gratings of the SHS are imaged onto the detector by the detector optics. The blue lines in Figure 3.9 show the ray paths for the central incoming collimated light beam, which gets imaged onto one pixel of the detector. A detailed description of the optical system is provided in Chapter 5.2.
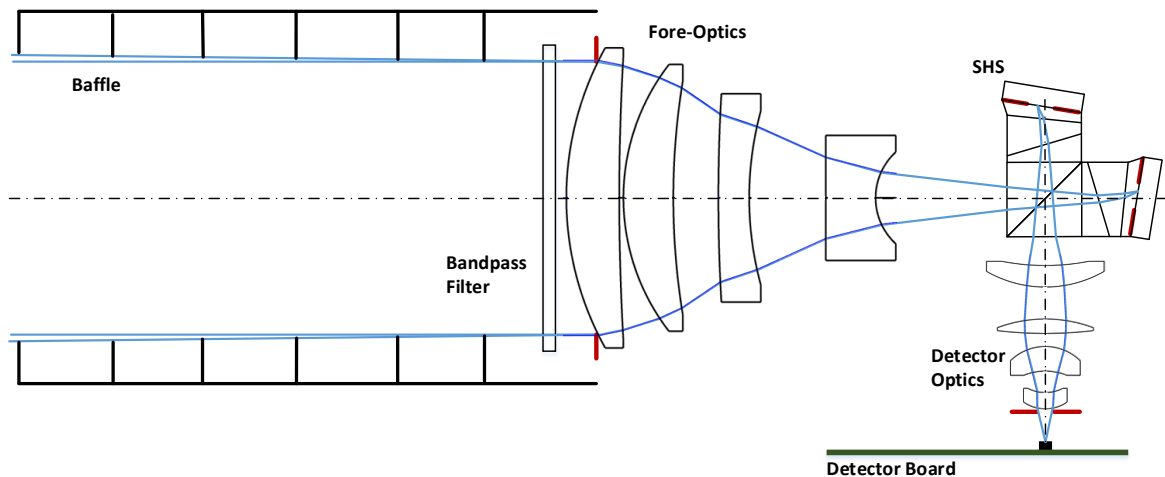
Figure 3.9.: Concept of the optical system with straylight baffle, bandpass filter, fore-optics, SHS, detector optics, and detector board. The red thick lines describe aperture stops and field stops, respectively. The thin blue lines show ray paths for the center field.

A detector optics images the gratings onto the detector, where fringe patterns are recorded. Figure 3.10 shows a simulated fringe pattern for an altitude range from $60 \, \text{km}$ to $120 \, \text{km}$. The interferogram is recorded with 420 pixels in spectral direction and the altitude range is resolved with 41 pixels, resulting in a vertical resolution of $1.5 \, \text{km}$. Performing a Fourier-transformation of the interferogram retrieves the spectrum. Figure 3.11 shows an example spectrum in detector recorded electrons e^- for an altitude of $80 \, \text{km}$ and during daylight with a mean spectral resolution $(\lambda/\Delta\lambda)$ of 9100. Six emission lines between $13\,100 \, \text{cm}^{-1}$ and $13\,080 \, \text{cm}^{-1}$ are used for temperature measurement. The second abscissa with label 'Spatial Frequency' is instrument related and will be formally introduced in Chapter 4.3.2.

To achieve the desired measurement precision of $2.5 \, \text{K}$, the S/N-ratio needs to be higher than approx-

imately 17 on average for the whole spectrum. Figure 3.12 shows the temperature retrieval precision in dependence of S/N-ratio. The required S/N-ratio is achieved with an integration time of $2\,s$ during daylight conditions. During nighttime, the integration time needs to be $10\,s$. A detailed analysis of the temperature measurement precision for day- and nighttime conditions is provided in Chapter 4.5.
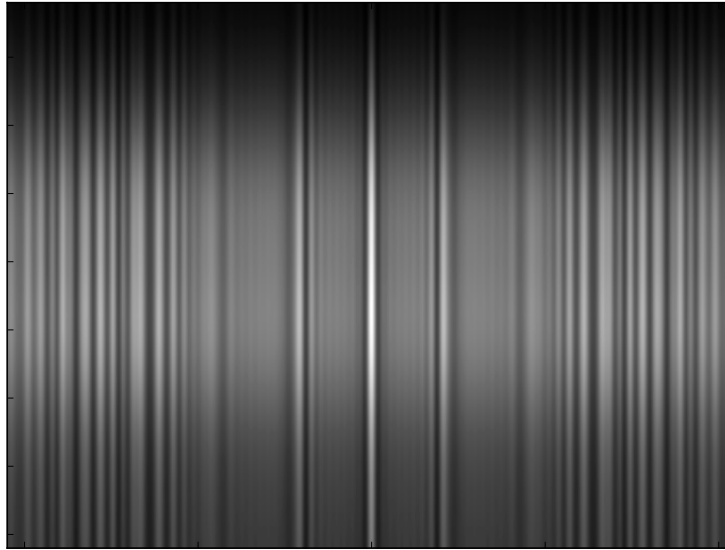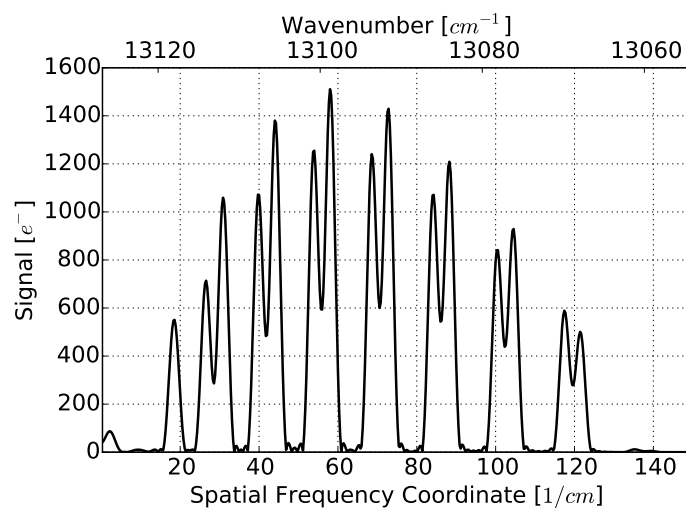

Figure 3.10.: Simulated interferogram at the detector.

Figure 3.11.: Simulated spectrum retrieved from the interferogram.
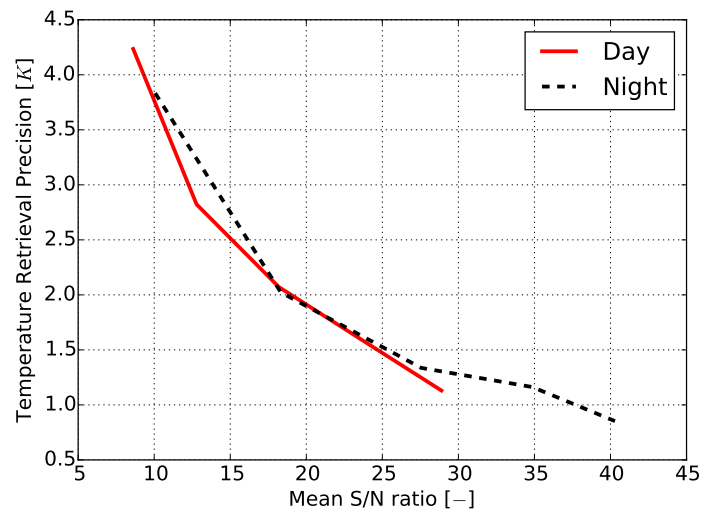
Figure 3.12.: Temperature retrieval precision in dependence of mean S/N ratio for day- and nighttime measurements. The integration time is varied to achieve different S/N-ratios and temperature retrieval precisions within a Monte-Carlo analysis.

3.3.2. Orbit Selection

CubeSats are usually launched piggy-back as secondary payloads on rockets. Thus, their orbits cannot be selected in advance and is dependent on the primary payload. However, two orbits are relatively common for CubeSats (Selva and Krejci, 2012): They are carried by rockets for re-supply missions of the International Space Station (ISS), where they are either deployed before docking to the ISS or are launched from the ISS through the Japanese J-POD deployer. The circular ISS orbit has an average altitude of $400\,\mathrm{km}$ and an inclination of $51.4°$. Thus, these CubeSat orbits have low lifetimes from days to a few months maximum. Nevertheless, they are useful for technology demonstrations due to the frequent launch opportunities.

The second common CubeSat orbit is a $600\,\mathrm{km}$ Sun-Synchronous Orbit (SSO). This orbit is a trade-off between orbit lifetime while still fulfilling the space debris mitigation guidelines. Depending on the exact altitude, the CubeSat shape, and the space weather, the orbit lifetime approaches 25 years and is therefore still within the maximum allowable orbit lifetime. An SSO is useful for Earth observation missions, because it allows to image the Earth under similar sunlight conditions. Different light conditions can be chosen depending on the Right Ascension of the Ascending Node (RAAN) angle of the orbit. With a RAAN angle corresponding to a local time of 6 o'clock or to 18 o'clock, the satellite is 'riding the terminator', providing almost continuous illumination for power generation. Despite its advantage, this particular SSO cannot be selected for the AtmoCube-1 satellite, because the atmosphere is in a transition phase between day and night at the terminator per definition, increasing the complexity and uncertainty in the temperature retrieval. However, other SSOs are useful for this mission. For the design of the instrument, the SSO is used as baseline orbit, because it will be the most likely orbit for an operational AtmoCube-1 satellite. The instrument performance for the ISS orbit is slightly higher compared to the SSO, because the orbit altitude is lower and, therefore, the FOV of the instrument covers a smaller altitude range. The smaller observation altitude range is also the only drawback of the ISS orbit. The satellite bus concept is discussed with having both the ISS orbit and the SSO in mind.

The satellite should be able to characterize gravity waves with short horizontal wavelengths that are typically generated by deep convection or as a result of the orography (Preusse et al., 2008). The deep convection mechanism mainly exists in the tropics and, thus, a satellite mission covering the tropics and extratropics can be used for characterization of such gravity waves. Orographic mountain waves appear globally and can be, at least partially, detected by a satellite covering the tropics and the extratropics. However, if a satellite also covers higher latitudes, the number of detectable localized sources increases accordingly. Indeed, the gravity wave hotspot world maps of Hoffmann et al. (2013) show that a satellite in a SSO can cover all gravity waves hotspots of convective and orographically generated gravity waves and that a satellite in ISS orbit covers most hotspots, except in the Antarctica and in Northern Europe.

The hotspot map was generated with data from AIRS. The AIRS instrument is only sensitive to gravity waves with long vertical wavelengths above 15 km. Thus, it is expected that the AtmoCube-1 satellite can also detect convectively generated gravity waves in the tropics that are not visible in the hotspot maps.

3.3.3. Concept of Operations (ConOps)

The satellite is intended to work in different operational modes, depending on the scientific objective addressed. The standard measurement mode will be altitude resolved temperature sounding in limb viewing geometry. The satellite will operate in tomography mode to support and complement coordinated measurement campaigns with ground based airglow instruments or aircraft campaigns. It is planned to allow scientific users to operate the satellite depending on their special needs for measurement modes and data acquisition. A web service for the scientific community will allow to specify the to-be-measured data, by selecting the geographic region, the type of measurement, the desired S/N-ratio, the spatial, spectral, and time resolution besides other parameters.

The generated power of the satellite is not sufficient to sustain continuous operations of the satellite with full performance of the instrument with the conservative assumptions for worst case conditions in this document. Two different schemes show how the instrument could be operated. The first scheme focuses on maximum operational time and the second on highest spatial resolution. The following values are a trade-off between scientific return, power, and communication requirements and show two examples of instrument operation schemes. For the first scheme, the instrument takes pictures every 10 s with an integration time of 2 s during daytime. During nighttime, the instrument takes measurements every 20 s with an integration time of 10 s. The satellite can sustain this operational mode nominally for 98 % of the time, see appendix A.1. For the second scheme, the instrument takes consecutive measurements with an integration time of 2 s during daytime and of 10 s during nighttime. However, this scheme can only be active for 34 % of the time per orbit in worst case conditions. It has the advantage that the sampling is fast enough to achieve high horizontal resolution with tomographic retrieval routines.

The remainder of the time, the satellite is in communication mode to transmit data and to receive commands from the Ground Station (GS). Thereby, the communication mode is divided into scientific data transmission mode (Com Data Mode), control and housekeeping communication mode (Com Control Mode), and a combination of both. Besides these modes, the ConOps includes an idle mode, a save mode, and an antenna deployment mode. Figure 3.13 summarizes these modes and the relations between them.
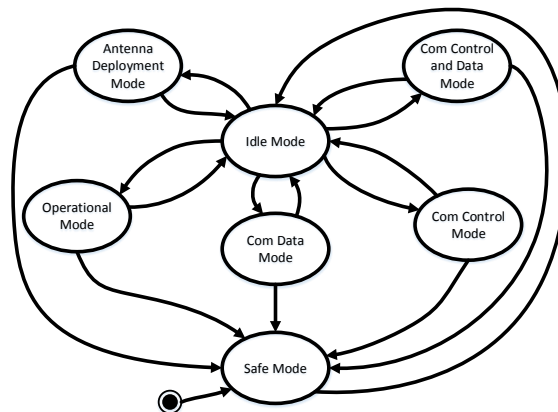

Figure 3.13.: Operational Modes of AtmoCube-1. The black dot symbolizes the initial state.

3.3.4. Satellite Technology

The optical payload requires a volume of approximately 1.5U, which is in accordance with typical remote sensing payloads of 3U CubeSats, like the MicroMas (Blackwell et al., 2012), the Opal satellite (Marchant et al., 2014), or the PolarCube (Deiml et al., 2014). However, a baffle is also required to reduce straylight, taking up considerable volume. Therefore, the baffle of AtmoCube-1 is designed that it can slide over the instrument into its stowed position to comply with the 3U form factor. During release of the CubeSat from the deployer, the baffle extends into its final position. In orbit, the instrument volume increases to

approximately 3U and the whole satellite has a size of approximately 4.5U with the remaining 1.5U being occupied by the satellite bus.

The satellite bus consists only of off-the-shelf components with a custom made structure for the following conceptual design. Components from established CubeSat component providers are utilized if their specifications meet the requirements. A detailed trade-off analysis has not been performed and better combinations of off-the-shelf components may exist. In addition, complete satellite bus subsystems can be bought already fully integrated from companies, which may be also a viable alternative.

Figure 3.14 shows the complete satellite in its deployed configuration and a 3D printed volume model. The sides are covered with solar panels and only the side of the instrument with the detector is left uncovered and acts as radiator. The instrument is mounted onto the Attitude Determination and Control System (ADCS), which is clearly visible with its star camera opening in the middle of Figure 3.14. The remaining 1U volume is occupied by the batteries, the Electrical Power Subsystem (EPS)-board, the Command and Data Handling (CDH)-board, the GPS-board, the Ultra-High Frequency (UHF)/Very-High Frequency (VHF)-radio, and the S-band radio. The last element is the UHF/VHF antenna subsystem, consisting of four dipole-antennas (yellow) that are deployed after release. The green circle in the lower left of the satellite is the S-band patch antenna as secondary communication subsystem. Figure 3.15 shows a cut through the satellite, visualizing the boards within the bus and the optical system of the instrument.
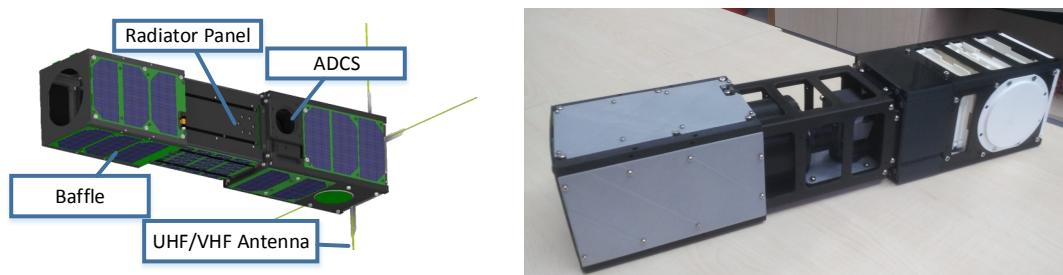
Figure 3.14.: Illustration (left) and 3D-printed model (right, without solar panels) of AtmoCube-1.
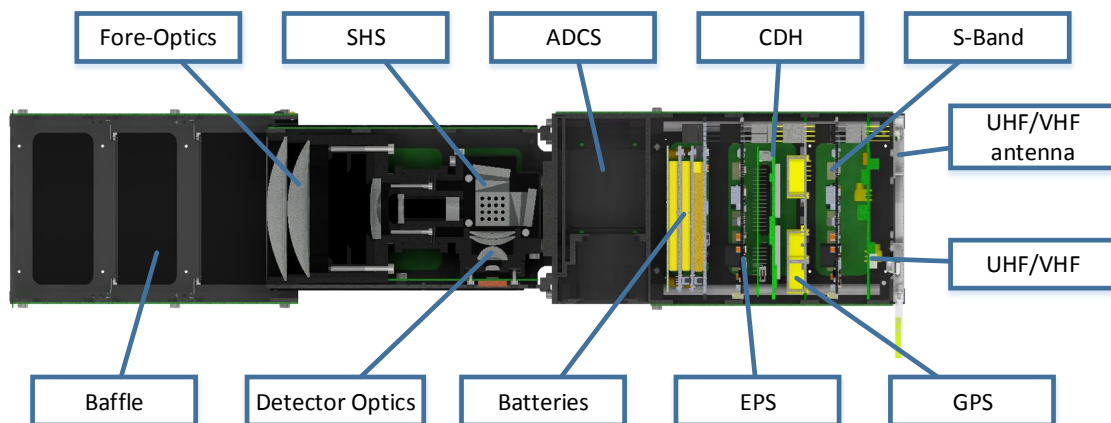
Figure 3.15.: Illustration of AtmoCube-1 with a cut through its side.

The design lifetime for the satellite is one year. Compared to a statistical analysis of nano-satellites, this lifetime is met with a reliability of 25% (Guo et al., 2014) and is larger than the average CubeSat lifetime of 200 days, according to Swartwout (2013). Increasing the design lifetime further would require the use of radiation hardened components and custom electronics instead of commercial of-the-shelf electronics. Components with high Technology Readiness Levels (TRLs) are selected for the satellite bus.[1] Thus, the

---

[1] "TRLs are a set of management metrics that enable the assessment of the maturity of a particular technology and the consistent comparison of maturity between different types of technology — all in the context of a specific system, application and operational environment." (ESA TEC-SHS, 2008, p. 7) A TRL of one describes the basic principles and a TRL of nine describes the actual successful flight proven system.

mission can rely on a mature satellite bus system and development and risk mitigation can focus on the instrument. A detailed list of the TRLs of all subsystems is provided in the appendix A.7.

3.3.4.1. Attitude Determination and Control System (ADCS)

The ADCS has the task to determine the attitude of the spacecraft and to point it towards the limb for temperature sounding or to the ground station for communication. The limb slant range is long with about $2650\,\text{km}$ for the SSO as design orbit. The limb position should be held with $1.5\,\text{km}$ uncertainty, which drives the ADCS requirements. The pointing and determination uncertainty needs to be lower than $116''$. Such a low attitude determination uncertainty can only be achieved with star sensors. Sun sensors, horizon sensors and magnetometer cannot provide this precision. The requirement for attitude control results in the need for reaction wheels, because magnetometers alone are not precise enough. The system XACT from Blue Canyon Technologies builds the baseline for AtmoCube-1. It has a TRL of nine, a design lifetime of three years in LEO, and the volume and mass of half a unit. It uses two sun sensors and a star camera for orbit determination. Three reaction wheels control the attitude with $33''$ ($3\,\sigma$) error for the pitch and yaw axis and $76''$ ($3\,\sigma$) for the roll axis. Three magneto-torquers are used to dump the momentum of the reaction wheels (Blue Canyon Technologies, 2016; Mason et al., 2017).

3.3.4.2. Electrical Power Subsystem (EPS)

The EPS generates power, distributes it to the other subsystems of the satellite, and stores excessive energy. It uses solar cells with $28\,\%$ efficiency mounted on the outside of the satellite structure to generate approximately $5.2\,\text{W}$ to $7.4\,\text{W}$ of constantly available power depending on the sun angle for worst case conditions. A battery pack with $30\,\text{W h}$ capacity stores the $2\,\text{W h}$ electrical energy that is required for operations during eclipse. The power is distributed with an EPS board to the other bus subsystems and the instrument. The power budget closes with a $98\,\%$ duty cycle of the instrument: The instrument is always on except when communicating with the GS. A detailed discussion of the power subsystem is provided in appendix A.1. The baseline solar cells are triple-junction GaAs cells from Azurspace with TRL nine, the EPS board and the battery pack are offered by ClydeSpace, also with a TRL of nine. Figure A.2 in the appendix shows the internal power distribution architecture.

3.3.4.3. Command and Data Handling (CDH)

The CDH subsystem stores the scientific data from the instrument together with GPS attitude and housekeeping data to send it to the GS via the communication system. Thus, the CDH board builds the data interface between all subsystems. On-board processing of the data is not performed and the requirement on processing power is low. The memory needs to store all housekeeping and science data till the satellite passes over the GS. This requires a storage of at least $13\,\text{MB}$ per orbit. The CDH board from ISIS is a flight proven (TRL 9) on-board computer with an ARM 9 $400\,\text{MHz}$ processor, $64\,\text{MB}$ SDRAM and redundant 2x8 GB SD card data storage. The two redundant $8\,\text{GB}$ storage provide sufficient memory to store data for more than a month. Nevertheless, the data is transmitted to the GS whenever a stable communication link is established. Figure A.2 in the appendix shows the internal communication architecture of AtmoCube-1.

3.3.4.4. Global Positioning System (GPS)

Besides the attitude of the satellite, its position in space is important for geo-locating the remote sensing measurements. A GPS board calculates its position based on the US GNSS and provides reference time for the internal clocks. The GPS board from SSBV is used as baseline. It provides a position measurement accuracy of $20\,\text{m}$ ($2\,\sigma$) with $1\,\text{Hz}$ measurement frequency.

3.3.4.5. Communications

The communication subsystem sends data packages provided by the CDH subsystem to the GS. The largest data generation unit on-board AtmoCube-1 is the instrument. It provides approximately $13\,\text{MB}$ per orbit under nominal limb-viewing operations. These data together with housekeeping data of the

instrument and bus need to be send down to the GS, which is assumed to be located near Wuppertal or Jülich. Two different technologies are used for communication to increase the reliability of the system, while providing high downlink data rates. The UHF/VHF radio is a communication method dominantly used for CubeSats, because of its relative simplicity, space heritage, and fault tolerance. The data rate of these radios is low and cannot be used to downlink all the generated scientific data. However, it is sufficient to downlink housekeeping data and to receive commands from the GS. The antennas are omni-directional and can establish a communication link even with a tumbling satellite. The power consumption of the UHF/VHF system is low. It is also continuously operated in burst mode to provide a beacon signal.

The second communication system is based on an S-band transmitter with patch antenna to transmit the scientific data to the GS. The S-band communication system can send down up to $2\,\mathrm{Mbit/s}$, but the antenna needs to be pointed towards the GS. Thus, during communication with the GS, the instrument cannot perform measurements.

All communication components have flown in space and have a TRL of nine. The UHF/VHF transceiver and the corresponding antenna are offered by ISIS, whereas the S-band transmitter and the patch antenna are offered by ClydeSpace. Further details about the communication subsystem are provided in appendix A.3.

3.3.4.6. Structure and Thermal

The structure of the satellite is custom made using aluminum as main material. It consists of three parts: the deployable baffle, the instrument structure, and the bus structure. The instrument is connected through the ADCS to the bus structure. The satellite has a total mass of below $4\,\mathrm{kg}$ and its volume is $340\,\mathrm{mm} \times 100\,\mathrm{mm} \times 100\,\mathrm{mm}$. Some parts extend over the $100\,\mathrm{mm}$ by a maximum of $3\,\mathrm{mm}$ to use the available space between deployer and satellite. A detailed mass budget is stated in table A.6 in the appendix. Solar panels are mounted on top of the structural parts. The thermal subsystem is designed to be passive with exception of a heater for the batteries, as a standard component in the ClydeSpace battery pack. The thermal subsystem is similar to the subsystem of the PolarCube satellite (Deiml et al., 2014). In addition, the instrument has two main passive control mechanisms, because the spectrometer is a thermally sensitive component and the dark current noise of the detector is an exponential function with temperature. Thus, even a small temperature increase has a large influence on the S/N-ratio:

- The detector chip is cooled down to reduce the dark current by using one panel of the instrument as radiator plate, which continuously points to deep space and has a high thermal conductivity to the chip.

- The SHS is designed to be thermally stable by selecting appropriate materials.

3.3.5. Alternative 6U CubeSat Concept

AtmoCube-1 is desgined as a 3U CubeSat and uses a deployment system to increase its size to approximately 4.5U. An alternative concept for future AtmoCube satellites is based on a 6U CubeSat. Using the volume of two 3U CubeSats stacked together on one long side increases the maximum allowable mass and allows to add additional subsystems. It follows that the power generation increases and the system becomes more tolerant to additional operational scenarios. Including a deorbiting system is advisable, especially for a constellation satellite, to cope with future potential space debris mitigation policies currently in discussion (IADC Steering Group, 2016). Using a 6U CubeSat also allows to include a secondary star camera to increase the redundancy in altitude determination. However, the 3U platform was chosen as reference for the AtmoCube-1 swarm precursor mission, because launch opportunities are more frequent and the mission is less complex, which lowers the mission costs and reduces development risks.

3.4. The Precursor Mission

A variant of the instrument for the AtmoCube-1 satellite was verified in a precursor mission within the sounding rocket experiment Atmospheric Heterodyne Interferometer Test (AtmoHIT). This test was

performed within the Rocket/ Balloon Experiments for University Students (REXUS/BEXUS) program and had the verification of the instrument under near-space conditions as goal.

The REXUS/BEXUS program is realized under a bilateral agency agreement between the Deutsches Zentrum für Luft- und Raumfahrttechnik (DLR) and the Swedish National Space Board (SNSB). The goal of this program is to support university students from ESA member states to carry out science and technology experiments on balloons or ballistic rockets. Each year up to 20 student teams can participate and learn to know the complete cycle of an aerospace mission.

The AtmoHIT experiment was conducted by a group of ten students (six PhD candidates, three graduate students and one undergraduate student), working mostly on the project within their thesis work. Throughhout this work, references are provided to their respective work. Figure 3.16a shows the mission logo of AtmoHIT and Figure 3.16b shows the Computer Aided Design (CAD) model of the experiment. Two windows are cut in the outer hull of the rocket. The AtmoCube-1 instrument looks through the larger window and the smaller window allows a secondary visible camera (VisCAM) to observe the same scene. A power supply unit besides the instrument provides power to all components. A detailed description of AtmoHIT can be found in the Student Experiment Documentation (SED) (Deiml et al., 2017a). This document and other AtmoHIT specific documents may not be accessible to everyone and can be requested from the author.

| (a) | (b) |
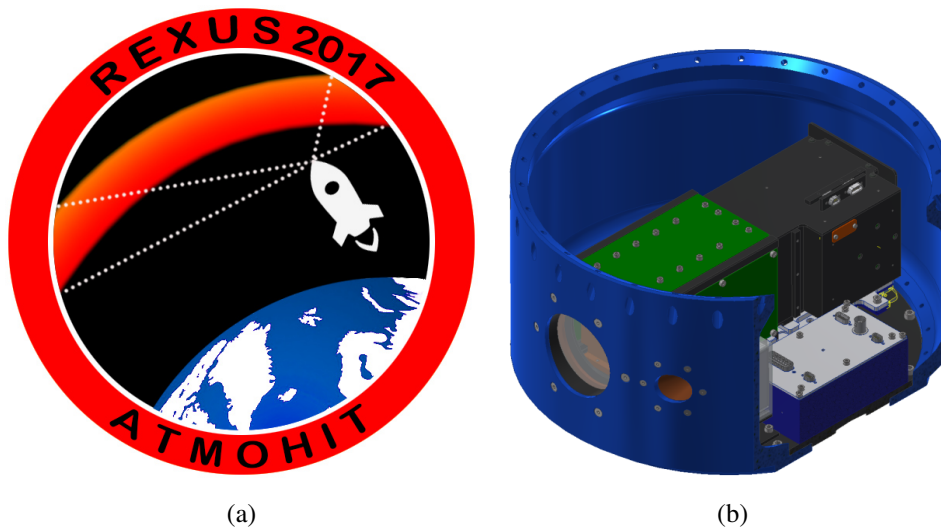
Figure 3.16.: The mission logo (3.16b) and an illustration of AtmoHIT with a cut through the rocket hull (3.16a).

The AtmoHIT experiment had the mission

to verify the AtmoCube-1 remote sensing instrument under space conditions by measuring temperatures in the middle atmosphere from a REXUS rocket.

Three objectives were derived from this mission statement:

- Instrument precursor mission for the satellite mission AtmoCube-1: verification of the instrument under near space conditions.

- Verification of the data processing and retrieval routines.

- Temperature measurement in the MLT with a remote sensing spectrometer.

The ballistic rocket reached a ceiling altitude of approximately $85\,\mathrm{km}$ and the experiment experienced micro-gravity and vacuum conditions for several minutes. Thus, the instrument could be verified under near space conditions. Also, the static and dynamic loads during launch were similar and even partially exceeded the loads from larger rockets, which allows to verify launch survivability. From a scientific point of view, the images taken from the atmosphere help in the verification of the data processing and retrieval routines. This is only possible from above $60\,\mathrm{km}$, because the atmosphere gets opaque for the oxygen A-band emission below this altitude, as already stated in Chapter 3.1. The last objective corresponds with

the satellite objective, however with limited scope. The anomaly that occurred during the rocket flight hindered to derive scientifically useful temperature data. But overall, the sounding rocket experiment significantly increased the maturity of the system and built up heritage.

4. Measurement Simulation

The mission objectives require a detailed simulation to specify the instrument parameters. The focus of the measurement simulation is put on the worst case to analyze the minimum satellite performance. It includes scenarios for temperature measurements in limb observation during daylight and nighttime. The retrieval of gravity waves in these modes and tomographic measurements in general are not considered. The goal of this simulation is also not to establish an operational retrieval code.

Figure 4.1 shows a comprehensive summary of the simulation, which is described in detail in the following Chapters. The simulation includes a forward model that simulates the atmosphere, the oxygen atmospheric band (A-band) emission, the observation through an atmosphere transfer model, the satellite/ instrument, and the data processing. The forward model is inverted by a retrieval routine, allowing the derivation of atmospheric properties from measured and post-processed signals. The temperature measurement precision is estimated with a Monte-Carlo analysis, including the error contributions of the retrieval process, instrument uncertainties, and noise sources. The description in the following Chapters is depicted with simulation results from limb observation during daytime and only retrieval results are shown for nighttime emissions.

This chapter uses index notation for equations to ease the understanding of the dimension of the tensors. To differentiate between variable names (including subscript) and indices, all characters after the comma in the subscript are indices.
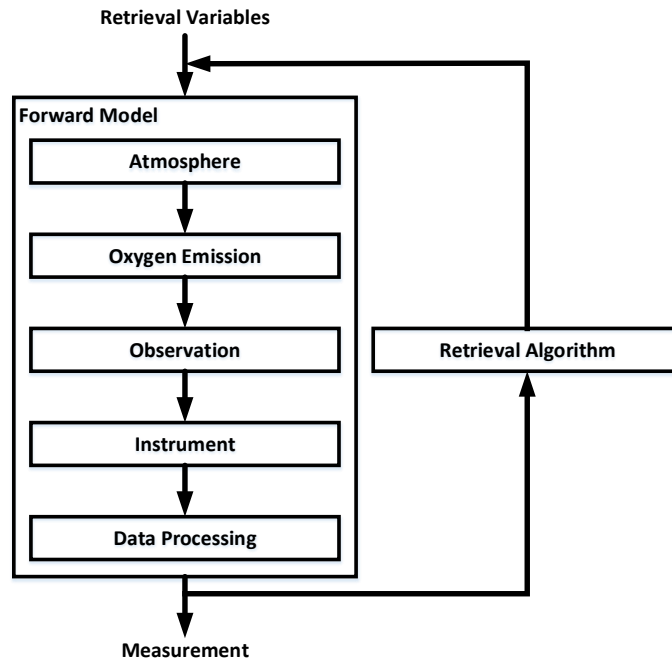
Figure 4.1.: Process of the measurement simulation and the temperature retrieval.

4.1. Atmosphere Simulation

The atmosphere simulation uses atmospheric data to simulate the oxygen A-band emission. The simulation processes information about the densities of relevant species and the temperature and uses this data to calculate the volume emission rate. The model is one dimensional with the geometric altitude as grid variable. The following subsections describe the atmosphere, the chemistry behind the oxygen A-band

emission, and provide an error analysis for the volume emission rate.

4.1.1. Atmosphere

The simulation of the atmosphere is based on data from Hammonia simulations (Schmidt et al., 2006). The simulation results contain data of total density, oxygen, ozone, atomic oxygen, nitrogen densities, and of temperature data. The carbon dioxide amount is approximated with $400\,\mathrm{ppm}$ over the whole altitude range. It is an upper limit approximation that is sufficient for the instrument parameter optimization. The data is mapped onto a geometric grid in altitude beginning at $0.5\,\mathrm{km}$ to $180\,\mathrm{km}$ in $0.5\,\mathrm{km}$ steps. It is available in $1°$ latitude steps from $-90°$ to $90°$, $15\,\mathrm{min}$ local time steps from $0\,\mathrm{h}$ to $24\,\mathrm{h}$ and for each monthly mean. Data for the solar minimum is used, because it provides lower emission values.

For the simulation, the daytime operation is approximated with a test scenario at noon and the nighttime operation with midnight as local time. Analysis suggests that the emission in both cases is minimal at solar minimum and equatorial latitude for a day in January. Figures 4.2 and 4.3 show the molecule density distribution of the five relevant species for the model (oxygen, ozone, atomic oxygen, carbon dioxide, and nitrogen), together with the total density at an altitude range from $60\,\mathrm{km}$ to $120\,\mathrm{km}$ in their zonal mean. Both figures show an approximately exponential decrease in total density. The relevant difference between day and night lies in the atomic oxygen abundance in lower altitudes. At approximately $75\,\mathrm{km}$ the atomic oxygen density decreases fast for nighttime simulation, whereas it stays approximately constant during daytime. This influences two excitation processes, as further described in Chapter 4.1.2.

The temperature field from Hammonia is used as background temperature for the analysis. It was already shown in Figure 2.1 for latitudes from $-90°$ (Summer) to $90°$ (Winter) at midnight and solar minimum in January.
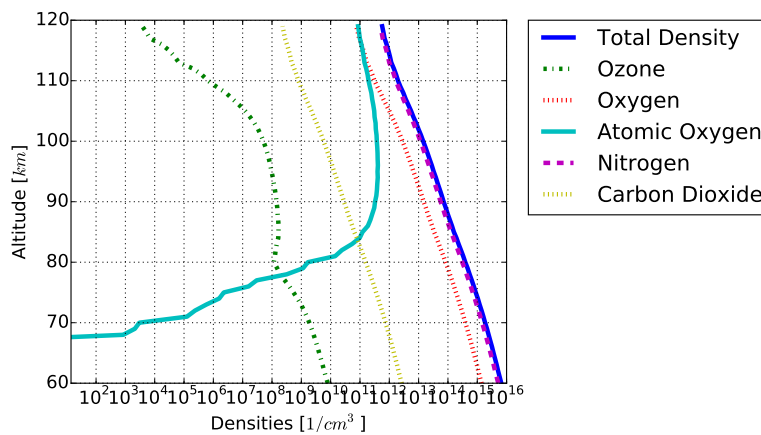
Figure 4.2.: Distribution of zonal mean total density, oxygen, ozone, atomic oxygen, nitrogen and carbon dioxide in $[\mathrm{cm}^{-3}]$ in an altitude range from $60\,\mathrm{km}$ to $120\,\mathrm{km}$ at **midnight** for a January day at $0°$ latitude in solar minimum. Data from Hammonia simulations (Schmidt et al., 2006).
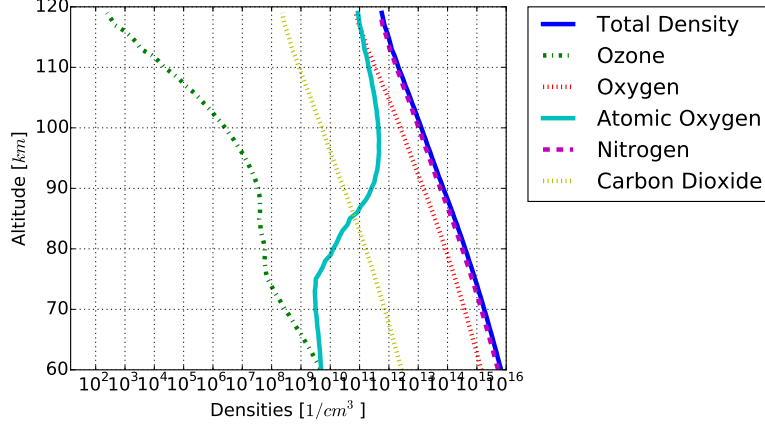
Figure 4.3.: Distribution of zonal mean total density, oxygen, ozone, atomic oxygen, nitrogen, and carbon dioxide in [cm^{-3}] in an altitude range from $60\,\mathrm{km}$ to $120\,\mathrm{km}$ at **noon** for a January day at $0°$ latitude in solar minimum. Data from Hammonia simulations (Schmidt et al., 2006).

4.1.2. Oxygen A-Band Emission Production

The model behind the A-band emission of oxygen is similar to the model of Sheese (2009). It takes the part relevant for the A-band emission from the model by Yankovsky and Manuilova (2006) and includes the process responsible for nightglow emission. All models extend the model of Mlynczak et al. (1993).

4.1.2.1. Chemistry

Five relevant mechanisms produce the excited oxygen state $O_2(b^1\Sigma_g^+, \nu = 0)$, necessary for A-band emission. The first mechanisms describe the production of $O_2(b^1\Sigma_g^+, \nu = 0)$ through A-band photons ($762\,\mathrm{nm}$), of $O_2(b^1\Sigma_g^+, \nu = 1)$ through B-band photons ($689\,\mathrm{nm}$), and of $O_2(b^1\Sigma_g^+, \nu = 2)$ through photons with $629\,\mathrm{nm}$ wavelength from ground state oxygen, respectively (process 4.1).

$$O_2 + h\nu(762\ nm; 689\ nm; 629\ nm) \rightarrow O_2(b^1\Sigma_g^+, \nu = 0, 1, 2) \tag{4.1}$$
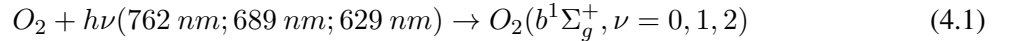
The excited oxygen molecules in states $O_2(b^1\Sigma_g^+, \nu = 0, 1, 2)$ are quenched by other oxygen molecules, nitrogen, atomic oxygen, ozone, and carbon dioxide to the lower energy state $O_2(a^1\Delta_g)$ by an electronic-vibrational energy exchange, see process 4.2.

$$O_2(b^1\Sigma_g^+, \nu = 0, 1, 2) + M(= O_2, N_2, O, O_3, CO_2) \rightarrow O_2(a^1\Delta_g) + M \tag{4.2}$$
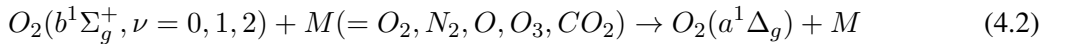
The excited oxygen molecules with vibrational states 1 and 2 are fast quenched to vibrational state 0 (Bucholtz et al., 1986). The process is two to three orders of magnitude faster than quenching to $O_2(a^1\Delta_g)$ according to Yankovsky and Manuilova (2006), because it is an intramolecular near resonance electronic-electronic exchange process (process 4.3). Thus, the production mechanism of excited oxygen by B-band photons has to be fully accounted for in the A-band emission. The production of excited oxygen with vibrational level 2 is neglected, because its photochemical reaction coefficient is two orders of magnitude lower than the production of $O_2(b^1\Sigma_g^+, \nu = 1)$ (Bucholtz et al., 1986). Vibrational levels up to $\nu = 15$ have been observed by Hwang et al. (1999), but $\nu = 0$ is the strongest due to the inefficient collisional removal.

$$O_2(b^1\Sigma_g^+, \nu \geq 1) + O_2(X^3\Sigma_g^-, \nu = 0) \rightarrow O_2(X^3\Sigma_g^-, \nu \leq 2) + O_2(b^1\Sigma_g^+, \nu = 0) \tag{4.3}$$
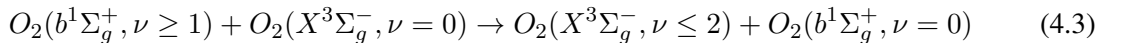
The next process is the collisional excitation of ground state oxygen by highly excited atomic oxygen $O(^1D)$, process 4.4. The atomic oxygen state $O(^1D)$ is produced by the photolysis of molecular oxygen and ozone (Processes 4.5 and 4.6). The Lymann-α line and the Schumann Runge Continuum (SRC) are mainly responsible for the photolysis of oxygen and the Hartley band for the photolysis of ozone.

$$O(^1D) + O_2(X^3\Sigma_g^-) \to O(^3P) + O_2(b^1\Sigma_g^+, \nu \leq 1) \tag{4.4}$$

$$O_2 + h\nu(\lambda \leq 175nm) \to O(^1D) + O(^3P) \tag{4.5}$$

$$O_3 + h\nu(\lambda \leq 310nm) \to O(^1D) + O_2(\alpha^1\Delta) \tag{4.6}$$
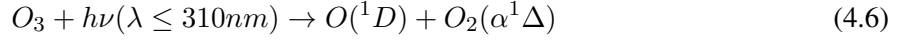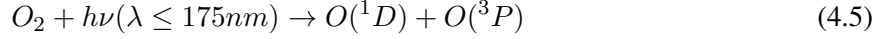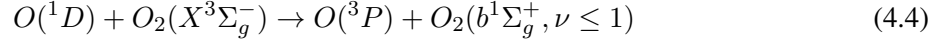
The last relevant process was proposed by Barth (1961) and is established nowadays (Bucholtz et al., 1986; McDade et al., 1986). The two-step Barth process is the only excitation process, which is active during night and day, because it is independent of solar radiation. Because it is the only process that is active during night, it is of high relevance for nighttime operations of the instrument. The Barth process describes the creation of excited oxygen O_2^* by atomic oxygen (Process 4.7), which is afterwards quenched to $O_2(b^1\Sigma_g^+, \nu \leq 1)$ (Process 4.8).

$$O + O + M \to O_2^* + M \tag{4.7}$$

$$O_2^* + O_2 \to O_2(b^1\Sigma_g^+, \nu = 0) + O_2 \tag{4.8}$$
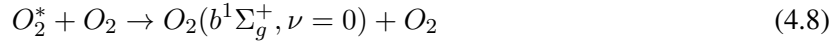
4.1.2.2. Kinetics

The calculation of the volume emission rate as function of altitude requires the oxygen density $[O_2]_{,i}$, the atomic oxygen density $[O]_{,i}$, the nitrogen density $[N_2]_{,i}$, the ozone density $[O_3]_{,i}$, and the carbon dioxide density $[CO_2]_{,i}$ for each altitude level h_i with $i \in 0, ..., N$. The data is provided by the atmosphere simulation.

The calculation is separated into the five different mechanisms described above. The emission through A-band absorption is calculated by Equation 4.9, using the photochemical reaction coefficient g_A. Its value is dependent on altitude and solar zenith angle. Chapter 4.1.3 addresses its calculation.

$$P_{A,i} = g_{A,i}[O_2]_{,i} \tag{4.9}$$

The emission through B-band absorption includes the photochemical reaction coefficient and the quenching of $O_2(b^1\Sigma_g^+, \nu = 1)$. Quenching through atomic oxygen, oxygen, and nitrogen is considered, described by the corresponding quenching parameters k_{Ob}, k_{O_2b}, and k_{N_2b}. The value of k_{Ob} is taken from Pejaković (2005) and the value of k_{O_2b} from Pejaković et al. (2005). The quenching through nitrogen is of minor relevance to the emission and an upper limit is considered to be 5×10^{-13} cm^3/s by Hwang et al. (1999). The effective quenching rate $k_{b,i}$ is calculated by Equation 4.10. With this parameter, the volume emission rate due to oxygen B-band absorption is calculated by Equation 4.11. Thereby, $g_{B,i}$ is the altitude dependent photochemical reaction rate of B-band absorption with N altitude levels. The Einstein coefficient A_{771} defines the spontaneous emission of $O_2(b^1\Sigma, \nu = 1)$ resulting in $O_2(X^3\Sigma_g^+, \nu = 1)$ ground state oxygen and emitting radiation at 771 nm, (Krupenie, 1972, p.486). The quenching factor k_{O_3b} describes quenching by ozone and the value is taken from Yankovsky and Manuilova (2006).

$$k_{b,i} = k_{Ob}[O]_{,i} + k_{O_2b}[O_2]_{,i} + k_{N_2b}[N_2]_{,i} \tag{4.10}$$

$$P_{B,i} = k_{b,i}\frac{g_{B,i}[O_2]_{,i}}{A_{771} + k_{b,i} + k_{O_3b}[O_3]_{,i}} \tag{4.11}$$

Process 4.5 describes the photolysis of oxygen to produce atomic oxygen by solar UV radiation. Its density $[O(^1D)]_{O_2,i}$ is calculated by Equation 4.12. Thereby, $J_{O_2,i}$ is the altitude dependent photolysis frequency of oxygen. Its derivation is described in Chapter 4.1.4. The two quenching parameters $k_{O_2,i}$ and $k_{N_2,i}$ are dependent on temperature at a specific altitude and describe the deactivation of exited oxygen to $O(^1D)$ with the help of another oxygen and a nitrogen molecule, respectively (Sander et al., 2006, page 1-5). The Einstein coefficient A_{1D} describes the self-deactivation of atomic oxygen in state $O(^1D)$ (Kernahan and Pang, 1975).

$$[O(^1D)]_{O_2,i} = \frac{J_{O_2,i}[O_2]_{,i}}{A_{1D} + k_{O_2,i}[O_2]_{,i} + k_{N_2,i}[N_2]_{,i}} \qquad (4.12)$$
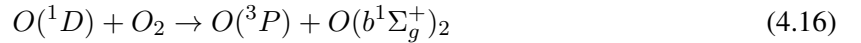
The same principle applies for the atomic oxygen production through photolysis of ozone, see Equation 4.13. The photolysis frequency $J_{O_3,i}$ is described further in Chapter 4.1.4. The Einstein coefficient A_{1D} and the quenching parameters $k_{O_2,i}$ and $k_{N_2,i}$ are the same as in Equation 4.12.

$$[O(^1D)]_{O_3,i} = \frac{J_{O_3,i}[O_3]_{,i}}{A_{1D} + k_{O_2,i}[O_2]_{,i} + k_{N_2,i}[N_2]_{,i}} \qquad (4.13)$$

With the atomic oxygen densities of state $O(^1D)$, the production rate of the relevant excited oxygen state $O_2(b^1\Sigma_g^+, \nu = 0)$ is calculated for the two different sources of atomic oxygen. The production rates are described by Equations 4.14 and 4.15, respectively. Thereby, $k_{O_2,i}$ is the quenching factor of atomic oxygen $O(^1D)$ by molecular oxygen. The quenching factor describes both the deactivation to ground state oxygen and to the relevant excited oxygen state. As these could not be distinguished, the parameter φ describes the branching ratio between the reaction coefficients of processes 4.16 and 4.17. It is measured at $298\,\text{K}$ and is assumed as temperature independent due to lack of data. The parameter is taken from Green et al. (2000), where it is called B_2. The production rates are proportional to this branching ratio.

$$P_{Oxygen,i} = \varphi k_{O_2,i}[O(^1D)]_{O_2,i}[O_2]_{,i} \qquad (4.14)$$

$$P_{Ozone,i} = \varphi k_{O_2,i}[O(^1D)]_{O_3,i}[O_2]_{,i} \qquad (4.15)$$

$$O(^1D) + O_2 \rightarrow O(^3P) + O(b^1\Sigma_g^+)_2 \qquad (4.16)$$

$$O(^1D) + O_2 \rightarrow O(^3P) + O_2 \qquad (4.17)$$

McDade et al. (1986) adjusted their model of the Barth process to rocket observations, which is used in this simulation. The production rate is calculated by Equation 4.18. It includes quenching of highly excited oxygen O_2^* to various states and quenching of $O_2(b^1\Sigma_g^+)$ to ground state oxygen by oxygen, nitrogen, and atomic oxygen. This is expressed by the two fitting parameters C^{O_2} and C^O in the equation. Four sets of parameters for C^{O_2} and C^O are stated in a paper of McDade et al. (1986). In here, the values and errors are used for MSIS-83 atmosphere and for an atomic oxygen quenching factor $k_6 = 8 \times 10^{-14}\ cm^3/s$ (in paper k_2). The quenching factor k_5 describes the recombination of atomic oxygen $O(^3P)$ to highly excited oxygen O_2^* by nitrogen and oxygen. Thus, the density of the deactivation partners $[M]_{,i}$ is the sum of nitrogen $[N]_{,i}$ and oxygen $[O_2]_{,i}$ densities.

$$P_{Barth,i} = \frac{k_{5,i}[O]_{,i}^2[O_2]_{,i}[M]_{,i}}{C^{O_2}[O_2]_{,i} + C^O[O]_{,i}} \qquad (4.18)$$

The total volume emission rate is calculated by the summation of all $O_2(b^1\Sigma_g^+, \nu = 0)$ sources and with considering the self-deactivation through the Einstein coefficient A_{762}, and by quenching through nitrogen $k_{0,i}$, ozone $k_{3,i}$, oxygen $k_{4,i}$, atomic oxygen k_6, and carbon dioxide k_7. Equation 4.19 reflects these relations. The value of parameter k_6 is calculated for $298\,\text{K}$. For lower temperatures, the value is decreasing, which increases the A-band emission. Thus, for a worst case scenario, it is sufficient to use the value for a temperature of $298\,\text{K}$. The Franck-Condon factor F_c describes the probability of the vibrational transition and the calculated value from Nicholls (1965) is used. The volume emission rate for individual $O_2(b^1\Sigma_g^+, \nu = 0)$ sources is calculated with the same expression, but by neglecting all other source terms. A summary of all parameters and how their errors are calculated is provided in Appendix B.1.

$$\eta_{total,i} = F_c \frac{A_{762}(P_{A,i} + P_{B,i} + P_{Oxygen,i} + P_{Ozone,i} + P_{Barth,i})}{A_{762} + k_{0,i}[N_2]_{,i} + k_{3,i}[O_3]_{,i} + k_4[O_2]_{,i} + k_6[O]_{,i} + k_7[CO_2]_{,i}} \qquad (4.19)$$

4.1.2.3. Volume Emission Rate

The volume emission rate is calculated using the equations from above. Figure 4.4 shows the volume emission rate in $\mathrm{photons/cm^3/s}$ of the total A-band emission in dependence of altitude between $50\,\mathrm{km}$ and $130\,\mathrm{km}$, divided in total emission (solid, black line) and emission due to the Barth process (green, dashed line), A-band absorption (red, dashed line), B-band absorption (blue, dotdashed line), oxygen photolysis (magenta, dotted line), and ozone photolysis (yellow, dotdashed line). All processes are active during day, but only the Barth process is active during night. The figure shows that oxygen photolysis is the major contributor for altitudes above $100\,\mathrm{km}$. Ozone photolysis and A-band absorption are the main contributors for altitudes below $100\,\mathrm{km}$. The order of magnitude of B-band excited emission is similar to the Barth process, but their respective altitude emission regions are different. The Barth process emission is narrowly centered around $95\,\mathrm{km}$ and the B-band absorption is only relevant for altitudes below approximately $95\,\mathrm{km}$. The areas around the lines represent the 1σ model uncertainties.

The A-band volume emission rates in $\mathrm{photons/cm^3/s}$ are plotted in dependence of altitude between $50\,\mathrm{km}$ and $130\,\mathrm{km}$ for all months in the equatorial plane during solar minimum in Figures 4.5 and 4.6. Figure 4.5 shows a simulation at midnight, where the maximum emission lies at approximately $95\,\mathrm{km}$ with sharp decrease and negligible emission above $100\,\mathrm{km}$ and below $85\,\mathrm{km}$. The emission is at a maximum during summer and in a minimum during winter. In the daytime simulation at noon (Figure 4.6), the volume emission rate decreases constantly with increasing altitude in general, but the emission is one order of magnitude larger compared to the nighttime emission. The seasonal dependence of the emission is minimal. In summary, these results show that the emission is minimal during nighttime and in winter, as it is used in the measurement simulation.
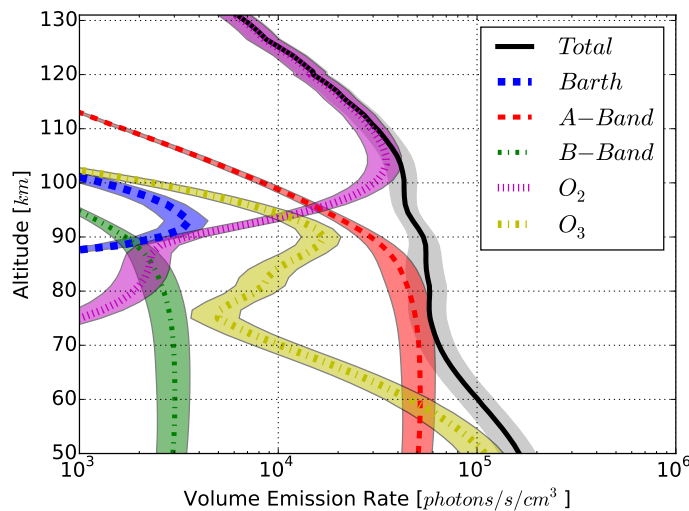
Figure 4.4.: Oxygen A-band volume emission rate and contributions of the five mechanisms (Barth process, A-band absorption, B-band absorption, O_2 photolysis, and O_3 photolysis) to the total volume emission rate $[photons/cm^3/s]$ of the oxygen A-band in the altitude between $50\,\mathrm{km}$ and $130\,\mathrm{km}$ and with 1σ model uncertainties for each production mechanism.
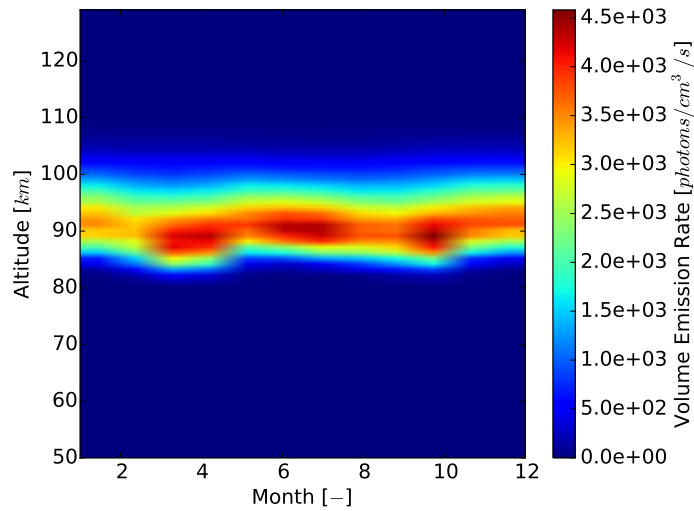
Figure 4.5.: Volume emission rate $[photons/cm^3/s]$ in an altitude range from $50\,\mathrm{km}$ and $130\,\mathrm{km}$ and for January till December at a latitude of $0°$ and at midnight for solar minimum.
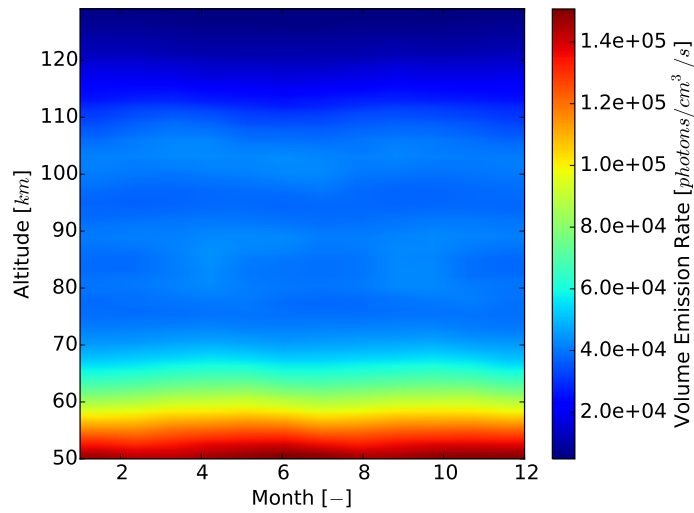
Figure 4.6.: Volume emission rate $[\mathrm{photons/cm^3/s}]$ in an altitude range from $50\,\mathrm{km}$ and $130\,\mathrm{km}$ and for January till December at a latitude of $0°$ and at noon for solar minimum.

4.1.3. Photochemical Reaction Coefficient Calculation (g-Factor)

The production of excited oxygen in state $O_2(b^1\Sigma_g^+, \nu = 0)$ from the ground state due to resonance scattering for the A-band emission and $O_2(b^1\Sigma_g^+, \nu = 1)$ for the B-band emission is described with the altitude dependent photochemical reaction coefficients (g-factors) $g_{A,i}$ and $g_{B,i}$, with $i \in 0, ..., N$ altitude levels. The reaction coefficient specifies how many molecules are transformed per second into the relevant state for the whole band by external radiation. The external radiation is the solar spectral flux for a specific altitude $\phi_{,ij}$ with $j \in 0, ..., M$ as wavenumber coordinate. It is derived from the flux at the top of the atmosphere in Chapter 4.1.5. The fine structure of the band is characterized by the line strength S_{ik} for line k and altitude i. The altitude dependence comes from a temperature dependence of the line strength. Each line strength k is convoluted with an altitude dependent line shape D_{ijk} with j as wavenumber coordinate. It is approximated by a Doppler profile, because temperature broadening is the dominating effect in the relevant altitude range and pressure broadening can be neglected (Bucholtz et al., 1986). The reaction coefficient is then the integral over all wavenumbers j of the solar spectral flux and the convoluted line strength, as in Equation 4.20.

$$g_{,i} = \int \phi_{,ij} \sum_{k=0}^{k=N} S_{,ik} D_{,ijk} d\nu_{,j} \tag{4.20}$$

The line shape function is expressed by a Doppler profile with Equation 4.21. Thereby, $\sigma_{0,k}$ is the center wavenumber for line k and $\sigma_{,j}$ the wavenumber at wavenumber coordinate j. The width $\alpha_{,ik}$ of line k is temperature dependent, see Equation 4.22. The altitude dependent temperature $T_{,i}$ is the background temperature or the current temperature retrieval value. In the equation, c is the vacuum speed of light, k_B the Boltzmann-Constant and m the molecular mass of the absorber oxygen.

$$D_{,ijk} = \frac{1}{\alpha_{,ik}\sqrt{\pi}} \exp\left(\frac{-(\sigma_{,j} - \sigma_{0,k})^2}{\alpha_{,ik}^2}\right) \tag{4.21}$$

$$\alpha_{,ik} = \frac{\sigma_{0,k}}{c}\sqrt{\frac{2k_B T_{,i}}{m}} \tag{4.22}$$

The line strength $S_{,ik}$ is calculated with an expression from Bucholtz et al. (1986), which approximates the temperature dependence of the line strength relative to a baseline line strength $S_{0,k}$ at temperature T_0, Equation 4.23. The parameter $E_{,k}$ describes the energy of the lower state for line k. The line strength and lower energy data are taken from the HIgh Resolution TRANsmission (HITRAN) database for a reference temperature $T_0 = 296$ K.

$$S_{,ik} = \frac{S_{0,k} T_0}{T_{,i}} \exp\left(\frac{1.439 E_{,k}(T_{,i} - T_0)}{T_{,i} T_0}\right) \tag{4.23}$$

Using these equations, the g_A and g_B photochemical reaction coefficients can be calculated. Figures 4.7a and 4.7b show the coefficients for the A-band and B-band in dependence of altitude and for specific solar zenith angles. The solar zenith angle dependence propagates from the solar spectral flux dependence. In this work, the temperature dependence of the coefficients is considered in the retrieval process, which reduces the error compared to the model of Sheese (2009). The A-band value on top of the atmosphere is approximately 30% lower and the B-band value is approximately 0.3% higher than the value from Sheese (2009), when a constant atmosphere with a temperature of 296 K is assumed. Then, the shapes of the curves can also be reproduced.

(a) A-band   (b) B-band
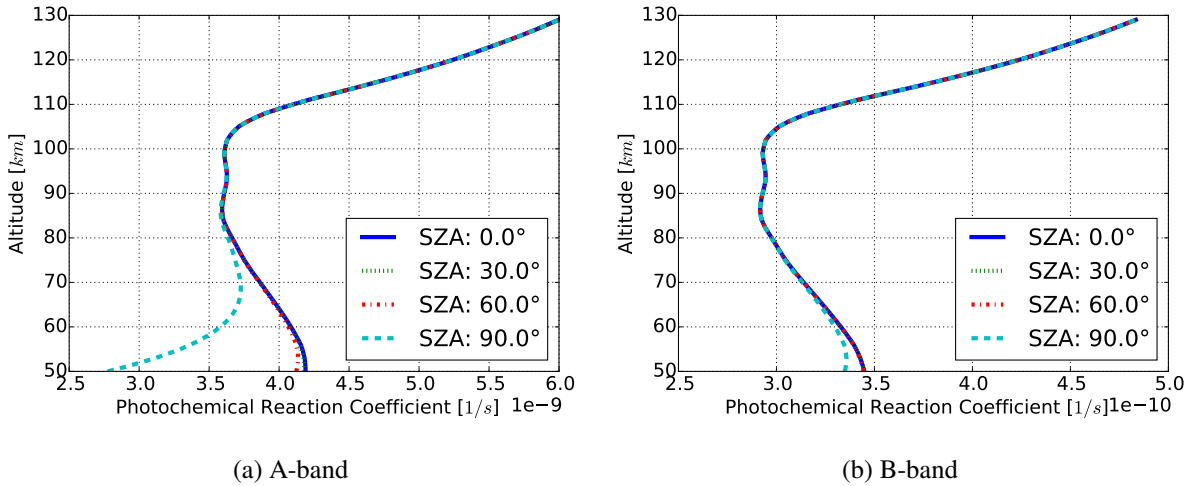
Figure 4.7.: Photochemical reaction coefficients [1/s] for the A-band and the B-band in an altitude range between 50 km and 130 km as a function of Solar Zenith Angle (SZA) between $0°$ and $90°$.

4.1.4. Photolysis Frequency Calculation

The photolysis frequencies describe the production of $O(^1D)$ from O_2 and O_3 through solar radiation. Thus, they are relevant for two production mechanisms of the oxygen in the relevant excited state. The photolysis frequencies are the integrals over the corresponding spectral regions of the products of quantum yield, absorption cross-section, and solar spectral flux ϕ. In particular, the oxygen photolysis frequency

$J_{2,k}$ for altitude k is calculated with the quantum efficiency Φ_{ly}, the absorption cross-section of oxygen σ_{A-ly} for the Lymann-α line, and with Φ_{src}, $\sigma_{A-src,j}$ for the SRC, respectively. The solar spectral flux $\phi_{src,kj}$ and the absorption cross-section $\sigma_{A-src,j}$ for the SRC are wavenumber dependent. Thus, after elementwise multiplication, integration along the wavenumber coordinate is necessary to get the total oxygen photolysis frequency. The integration is performed by an trapezoidal rule as in Equation 4.24. The ozone photolysis frequency $J_{O_3,k}$ is similarly calculated by integration over the spectral range of the quantum yield $\Phi_{hartley,j}$, the absorption cross-section $\sigma_{A-hartley,j}$, and the altitude dependent solar spectral flux $\phi_{hartley,kj}$, see Equation 4.25.

$$J_{O_2,k} = \Phi_{ly}\sigma_{A-ly}\phi_{ly,k} + \sum_{j} 0.5(\Phi_{src,j+1}\sigma_{A-src,j+1}\phi_{src,k(j+1)} - \Phi_{src,j}\sigma_{A-src,j}\phi_{src,kj})\Delta\sigma_{,j} \quad (4.24)$$

$$J_{O_3,k} = \sum_{j} 0.5(\Phi_{hartley,j+1}\sigma_{A-hartley,j+1}\phi_{hartley,k(j+1)} - \Phi_{hartley,j}\sigma_{Ahartley,j}\phi_{hartley,kj})\Delta\sigma_{,j}$$
$$(4.25)$$

A quantum yield $\Phi_{ly} = 0.55$ is used for the Lymann-α line, which represents an average value for the middle atmosphere (Reddmann and Uhl, 2003). The SRC quantum yield is estimated to be $\Phi_{src} = 1$ by Lee et al. (1977). The quantum yield in the Hartley band is patched together from data by Nishida et al. (2004), Talukdar et al. (1998), and Takahashi (2002). The absorption cross-section data is the same as in the solar spectral flux calculation Chapter 4.1.5.

Figure 4.8a shows the calculated oxygen photolysis frequency J_2 in $1/s$ between $50\,km$ and $130\,km$ for solar zenith angles between $0°$ and $90°$. The photolysis frequency decreases with decreasing altitude. The hump at an altitude of approximately $80\,km$ comes from the Lymann-α absorption. The photolysis frequency decreases faster for higher solar zenith angles. The ozone photoylsis frequency J_3 in $1/s$ is shown in Figure 4.8b for equal conditions. The ozone photolysis frequency is almost constant for the whole altitude range and for all zenith angles. The coefficient deviates below $65\,km$ from its nominal value only for large solar zenith angles. The comparison of the oxygen photolysis frequency J_2 with Sheese (2009) shows very good agreement. It also verifies the solar spectral flux calculation of the next chapter. The ozone photolysis frequency J_3 at the top of the atmosphere agrees with the values from Yankovsky and Manuilova (2006) and Sheese (2009).

(a) Oxygen   (b) Ozone
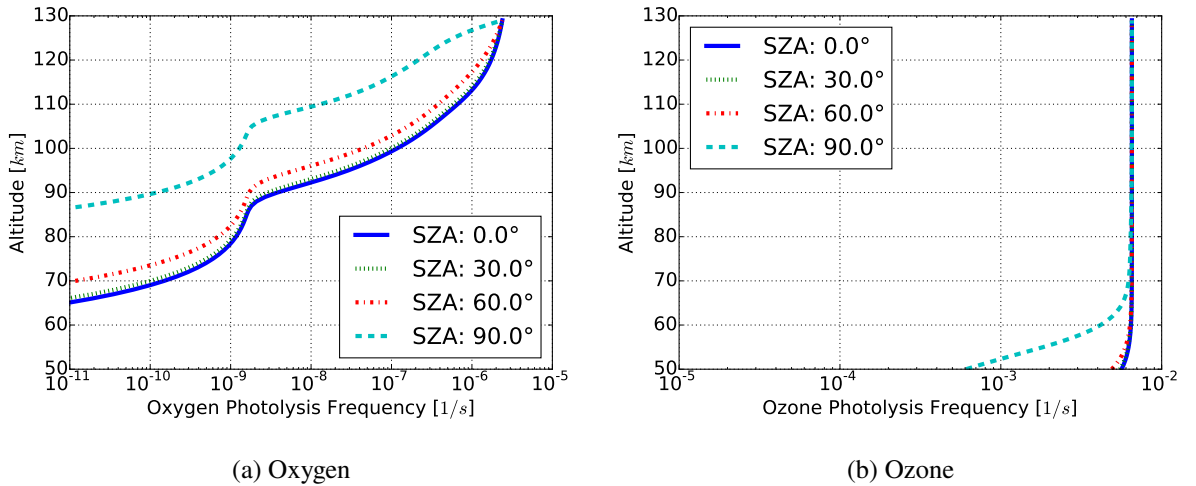
Figure 4.8.: Photolysis frequencies $[1/s]$ of oxygen and ozone in dependence of altitude between $50\,km$ and $130\,km$ and of Solar Zenith Angle (SZA) between $0°$ and $90°$.

4.1.5. Solar Spectral Flux Calculation

The production of atomic oxygen in state $O(^1D)$ through photolysis of oxygen and ozone requires solar radiation. Similarly, the photochemical reaction coefficients for the A-band $g_{A,i}$ and the B-band $g_{B,i}$ depend on solar radiation. The transmission of solar radiation through the atmosphere is dependent on

the solar irradiance on top of the atmosphere, on the absorber molecule density, and the cross-section σ_A. First, information on solar irradiance at the top of the atmosphere is provided, followed by the derivation of solar irradiance at a certain altitude level.

Solar radiation with wavelengths lower than 175 nm allows the production of atomic oxygen in the state $O(^1D)$ through dissociation of oxygen in the SRC between 137 nm and 175 nm and through the Lymann-α line at 121.6 nm. The instrument Solar Stellar Irradiance Comparison Experiment (SOLSTICE) within the Solar Radiation and Climate Experiment (SORCE) mission provides solar spectral irradiance data in the wavelength region between 115 nm and 180 nm (Rottman et al., 2006) on a daily basis from 2005 to 2013. This data is available at http://lasp.colorado.edu/home/sorce/data/. Figure 4.9a shows the maximum and minimum solar spectral irradiance between 115 nm and 180 nm in photons/cm^2/s/nm. In the Hartley-band between 198 nm and 310 nm, solar radiation dissociates ozone, which results in atomic oxygen in state $O(^1D)$. Spectral irradiance data on top of the atmosphere is also available from the instrument SOLSTICE. The maximum and minimum irradiance data is shown in Figure 4.9b. The Spectral Irradiance Monitor (SIM) instrument of the SORCE mission measures solar spectral flux on top of the atmosphere (130 km) at wavelengths of 689 nm and 762 nm. Table 4.1 states the minimum and maximum values in photons/cm^2/s/nm.

Table 4.1.: Minimum and maximum solar spectral flux values on top of the atmosphere for the A-band and B-band, as measured by SIM. Data from http://lasp.colorado.edu/home/sorce/data/.

	Minimum photons/cm^2/s/nm	Maximum photons/cm^2/s/nm
762 nm	4.67×10^{23}	4.70×10^{23}
689 nm	5.02×10^{23}	5.05×10^{23}
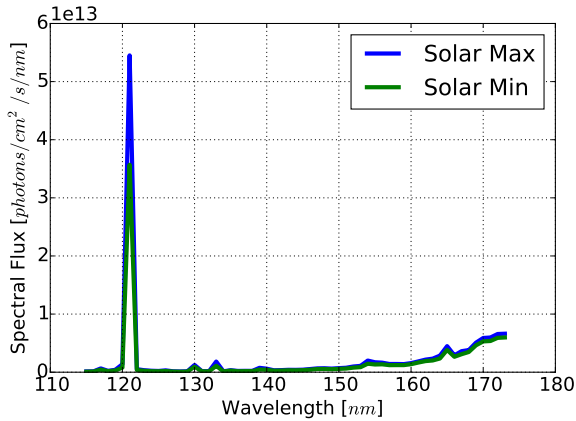
(a) Incoming solar irradiance between 115 nm and 180 nm.
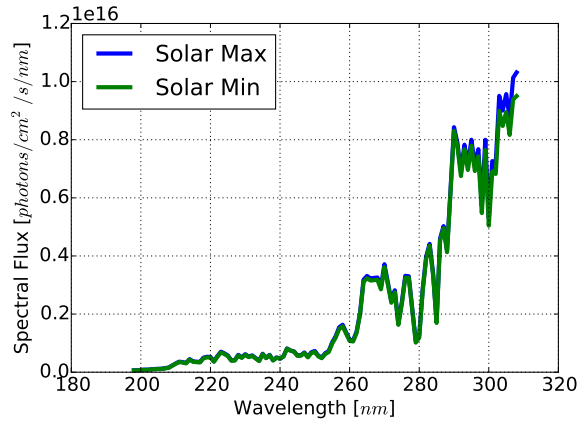
(b) Incoming solar irradiance between 198 nm and 310 nm.

Figure 4.9.: Maximum and minimum incoming solar irradiance [photons/cm^2/s/nm] between 2005-05-13 and 2013-07-15 as measured by SOLSTICE. Data from http://lasp.colorado.edu/home/sorce/data/.

The first step in calculating the oxygen photolysis frequency is to calculate the solar flux at a certain altitude. Therefore, two approaches are considered. The first approach uses the absorption cross-sections of the absorbers and is used for the calculation of solar spectral flux in the Hartley band, in the SRC, and for the Lymann-α line. The second approach relies on the line strength and is used for the photochemical reaction coefficient calculation. The transmissivity $\tau_{,kj}$ for altitude k and a wavelength j is calculated by Equation 4.26 and with $\Delta h_{,m} \in 0, ..., N$ as altitude segment lengths and $I_{,mj}$ as wavenumber and altitude dependent integrand with $m \in 0, ..., N$ and $j \in 0, ..., M$. The equation represents a trapezoidal cumulative integration with having a transmission exponent $\tau_{,k=N} = 0$, because $I_{,(N+1)j}$ is not defined anymore. For the first approach, the integrand $I_{,mj}$ is calculated with Equation 4.27. Thereby, $[A]_{,m}$ represents the absorber molecule density [molecules/cm^3] in dependence of altitude, which is oxygen and ozone in this forward model. The wavenumber dependent parameter $\sigma_{A,j}$ is the absorption cross-section of the absorber. The solar zenith angle dependence is represented by the factor $g_{\chi,m}$, which is also dependent on altitude. Equation 4.28 calculates the integrand with the line strength $S_{,mk}$ and the

line width $D_{,mjk}$, which have been defined in Chapter 4.1.3.

$$\tau_{,kj} = \sum_{m=k}^{N} 0.5 \left(I_{,(m+1)j} - I_{,mj} \right) \Delta h_{,m} \tag{4.26}$$

$$I_{,mj} = \sigma_{A,j} g_{\chi,m} [A]_{,m} \tag{4.27}$$

$$I_{,mj} = g_{\chi,m} [A]_m \sum_{k=0}^{k=N} S_{,mk} D_{,mjk} \tag{4.28}$$

This solar zenith angle factor $g_{\chi,m}$ is calculated by the Chapman function. In general, this function is computational intensive to evaluate and an approximation is used instead, see Equation 4.29 (Smith and Smith, 1972). Thereby, the variable $X_{p,i}$ represents a dimensionless altitude, calculated by $X_{p,i} = (h_{,i} + R_E)/H_{,i}$ with $h_{,i}$ being the geometric altitude, R_E the Earth radius, and $H_{,i}$ the pressure scale height. The pressure scale height calculates to $H_{,i} = kT_{,i}/mg = RT_{,i}/Mg$ with k the Boltzmann constant, $T_{,i}$ the absolute temperature at altitude level i, m the molecular or atomic weight, M the molar mass, and g the gravitational acceleration at the Earth´s surface. It is valid for solar zenith angles $\chi < 90°$. It can be further approximated by $g_\chi = 1/\cos(\chi)$ for solar zenith angles between $0°$ and $70°$, which results in an error below 1% for this application.

$$g_{\chi,i} = \left[\frac{\pi}{2} X_{p,i} \right]^{\frac{1}{2}} \exp\left(\frac{1}{2} X_{p,i} \cos^2(\chi) \right) \left[1 - erf\left(\left(\frac{1}{2} X_{p,i}\right)^{\frac{1}{2}} \| \cos(\chi)\| \right) \right] \tag{4.29}$$

The solar flux $\phi_{,kj}$ in $\mathrm{photons/cm^3/s/nm}$ at altitude level k and wavenumber j is calculated with an exponential decrease of solar irradiance on top of the atmosphere by the transmission exponent from Equation 4.26. It is described by Equation 4.30, where $\phi_{\infty,j}$ being the solar spectral flux on top of the atmosphere in dependence of wavenumber j.

$$\phi_{,kj} = \phi_{\infty,j} \exp(-\tau_{,kj}) \tag{4.30}$$

The Equations above are used to calculate the solar flux for the SRC and the Lymann-α line, which is required for oxygen photolysis. Furthermore, the solar flux is calculated in the Hartley band for the ozone photolysis and at $762\,\mathrm{nm}$ and $689\,\mathrm{nm}$ for the A-band and B-band, respectively. In all five cases an absorber is required, which is ozone for the Hartley band solar flux calculation and oxygen in all other cases. The absorber molecule density is taken from the atmosphere simulation module and changes depending on the simulation configuration. The absorption cross-section has a value of $(1.0 \pm 0.2) \times 10^{-20}\,\mathrm{cm^2}$ for the Lymann-α line that represents an average value for the middle atmosphere (Reddmann and Uhl, 2003). Data for the SRC absorption cross-section is taken from Yoshino et al. (2005). Similarly, the ozone absorption cross-section data between $198\,\mathrm{nm}$ and $310\,\mathrm{nm}$ is taken from Sander et al. (2006) for a temperature between $293\,\mathrm{K}$ and $295\,\mathrm{K}$.

4.1.6. Oxygen A-Band Emission Fine Structure

The volume emission, rate calculated in Chapter 4.1.2, has a fine structure that depends on the rotational quantum number. Thereby, individual emission lines have different rotational temperature dependencies. The rotational temperature is derived by relative comparison of intensities from multiple lines. In general, the rotational temperature does not need to equal the kinetic temperature. However, it is the case for the oxygen A-band emission, as shown experimentally by Touzeau et al. (1991). The lifetime of oxygen in state $O_2(b^1\Sigma_g^+, \nu = 0)$ is approximately $12\,\mathrm{s}$.

The Σ-Σ transition of the A-band is a forbidden transition, which means that the change in rotational quantum number $\Delta J = 0$ is not allowed (zero gap) and the two branches R and P exist, but not the Q branch. The rotational quantum numbers of each branch increase with distance from the zero gap. The intensity maximum for each branch shifts towards higher rotational quantum numbers for increasing temperature (Herzberg, 1950).

The used fine structure distribution is based on HITRAN data (Rothman et al., 2013). HITRAN provides for all A-band fine structure lines $m \in 0...M$ the energy $E'_{,m}$ of the excited, upper state $O_2(b^1\Sigma_g^+, \nu = 0)$,

the weighting function $g_{,m}$, and the Einstein coefficient $A_{,m}$. Furthermore, the Einstein coefficient for the whole A-band emission A_{762} and the temperature $T_{,i}$ in dependence of altitude for $i \in 0...N$ are required. The Einstein coefficient is the same as in the oxygen A-band emission production Chapter 4.1.2 and is taken from Burch and Gryvnak (1969).

The line strength is calculated by Equation 4.31, see e.g. Herzberg (1950); Burch and Gryvnak (1969). The temperature dependence is exponential and depends on the energy of the upper state. The constant c_2 is defined as $c_2 = hc_0/k$ with h being the Planck constant, c_0 the vacuum light speed, and k the Boltzmann constant. The rotational partition function $Q_{,i}$ is the sum over all lines of the weighting function multiplied with the temperature dependence term, see Equation 4.32. The output is the weighting matrix $d_{,mi}$, which splits up the total intensity into individual lines m for each altitude i. The weighting matrix is further normalized to the sum of all lines to conserve the energy of the total A-band emission.

$$d_{,mi} = \frac{A_{,m}}{A_{762}} \frac{g_{,m}}{Q_{,i}} \exp\left(-c_2 \frac{E'_{,m}}{T_{,i}}\right) \tag{4.31}$$

$$Q_{,i} = \sum_m g_{,m} \exp\left(-c_2 \frac{E'_{,m}}{T_{,i}}\right) \tag{4.32}$$

The resulting fine structure distribution, here also normalized to one, between the wavenumbers $13\,010\,\mathrm{cm}^{-1}$ and $13\,170\,\mathrm{cm}^{-1}$ is shown in Figure 4.10. The left series of lines is the P-branch and the right series the R-branch. The lines are modeled without broadening. Pressure broadening is of minor relevance in altitudes above approximately $40\,\mathrm{km}$ (Bucholtz et al., 1986) and temperature broadening is the main source of line broadening in the relevant altitude range. However, the linewidth for purely temperature-broadened lines lies between $22.1 \times 10^{-3}\,\mathrm{cm}^{-1}$ and $22.4 \times 10^{-3}\,\mathrm{cm}^{-1}$ for typical temperature conditions in the atmosphere and is much smaller than the resolution of the instrument. Thus, it is neglected in the following.

The six broader, red lines in the figure and their temperature dependence are analyzed in the following: Each line has a specific temperature dependence, which overlaps with the temperature dependence of the total A-band emission. The overall temperature dependence of the emission is non-linear and is shown for the six selected lines in the left plot of Figure 4.11. The plot shows the volume emission rate per line in $\mathrm{photons/s/cm}^3/\mathrm{cm}^{-1}$ in a temperature range from $150\,\mathrm{K}$ to $300\,\mathrm{K}$. Lines with similar temperature dependencies, e.g. lines $13\,084\,\mathrm{cm}^{-1}$ and $13\,086\,\mathrm{cm}^{-1}$ are less useful for relative temperature retrieval compared to lines with differing temperature dependencies. However, measuring such lines together increases the S/N-ratio and, thus, can still be helpful for temperature retrieval.

The plot in the middle shows the absolute intensity change of the volume emission rate per line in $\mathrm{photons/s/cm}^3/\mathrm{cm}^{-1}/\mathrm{K}$ in dependence of temperature, which is the first derivative of the left plot. It is divided into total absolute intensity change (solid lines), volume emission rate temperature dependence change (dotted lines), and rotational temperature dependence change (dashed lines). For relative temperature retrieval, the rotational temperature dependence change of the lines should be as different as possible, which means that individual lines should be far apart from each other in the plot in the middle and optimally the temperature dependence of the total volume emission rate should be low. The plot to the right side shows the relative temperature change of the six lines, also divided into the total relative change and the contributions of rotational dependency and total volume emission rate dependency. All total emission dependencies fall together to a single dotted line, as it is expected. Three curves are visible for the rotational temperature dependence, because every two neighboring lines form a pair with equal temperature dependence. Thus, it is necessary to measure more than two closely related lines to retrieve temperature information from their relative temperature change. The graph also shows that the change in volume emission rate is only approximately -2 to $4\,\text{‰}/\mathrm{K}$ for the rotational temperature change.

A goal of the analysis is to select a set of lines that increases the measurement precision. Therefore, it is important to select lines, that have different temperature dependencies, but have also high intensities. This trade-off is further discussed in Appendix B.3.
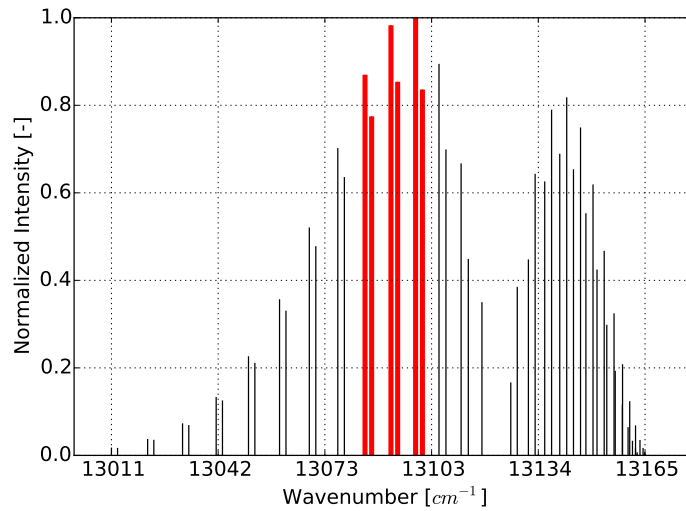
Figure 4.10.: Normalized fine structure distribution of the oxygen A-band emission. The temperature dependence of the marked, red lines is shown in Figure 4.11.
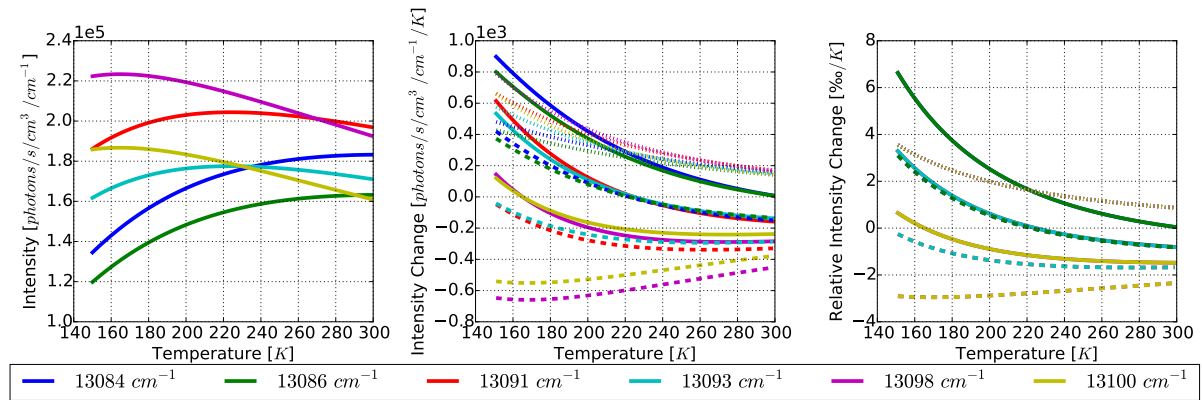

Figure 4.11.: **Left**: Volume emission rate per line in $\mathrm{photons/s/cm^3/cm^{-1}}$ of six oxygen A-band lines in dependence of temperature from $150\,\mathrm{K}$ to $300\,\mathrm{K}$. **Middle**: Absolute volume emission rate change per line in $\mathrm{photons/s/cm^3/cm^{-1}/K}$ of the same lines in dependence of temperature, divided into total (solid), volume emission temperature dependence (dotted), and rotational temperature dependence (dashed). **Right**: Relative volume emission rate change per line in $‰/\mathrm{K}$ in dependence of temperature and division in total (solid), volume emission temperature dependence (dotted), and rotational temperature dependence (dashed).

4.2. Observation

The observation module simulates the transmission of the emitted radiation through the atmosphere for different tangent altitudes. The atmosphere simulation provides the input for the module. Its output is the radiant flux at the entrance pupil of the satellite instrument.

This module consists of a transfer model to calculate the transmission through the atmosphere. It requires the segment lengths of the optical path from the tangent points in the atmosphere to the satellite. In the following two Chapters, the optical path calculation and the transfer model are described.

4.2.1. Optical Path
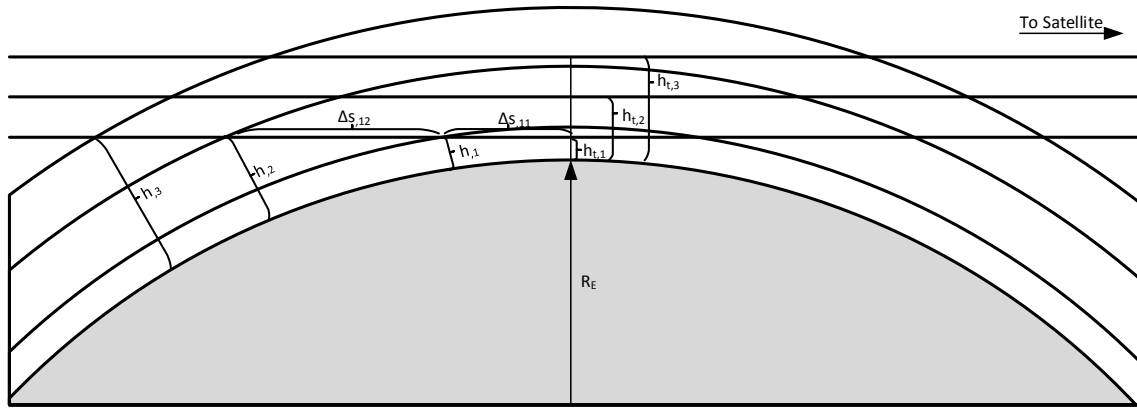
Figure 4.12.: Optical paths for the transfer model. The altitude coordinate is described with $h_{,i}$ and the tangent altitude with $h_{t,j}$.

The total segment lengths $s_{,ji}$ are calculated for each altitude i and tangent altitude j by using the Pythagorean theorem, Equation 4.33. The difference of total segment lengths for two following altitudes i and $i + 1$ is the segment lengths $\Delta s_{,ji}$, see Equations 4.34 and 4.35. By taking the real part, the physically valid optical path differences can be extracted.

$$s_{,ji} = \sqrt{-(h_{t,j} + R_E)^2 + (h_{,i} + R_E)^2} \tag{4.33}$$

$$\Delta s_{,ji} = \mathrm{Re}(s_{,ji} - s_{,j(i+1)}) \tag{4.34}$$

$$\Delta s_{,jN} = \mathrm{Re}(s_{,jN} - s_{,j(N-1)}) \tag{4.35}$$

4.2.2. Transfer Model

An air parcel in the atmosphere at a specific altitude emits radiation, which is transferred through the atmosphere and a portion of it reaches the satellite. The radiation is partly absorbed by oxygen in the path between air parcel and satellite. The transfer model calculates for a specific optical path segment the transmission factor through all remaining path segments until the radiation reaches the satellite. This process is repeated for all optical path segments. The total irradiance at the satellite is then calculated by integration over all path segments.

Here, the transfer model from Sheese (2009) is used. The transfer model requires information about the atmosphere, the volume emission rate, and the instrument observation geometry as input. The altitude coordinate $h_{,i}$ with $i \in 1, ..., N$ describes the atmosphere grid on which the oxygen density $[O_2]_{,i}$ is defined. The tangent altitude coordinate $h_{t,j}$ defines the altitudes on which the atmosphere properties are retrieved. The optical path segment length $\Delta s_{,ji}$ maps the altitude coordinate of the atmosphere to the tangent altitude coordinate of the observation.

The transmission of radiation by an air parcel at tangent altitude j through the atmosphere is described by an exponential decrease. The exponent τ depends on the oxygen density in the atmosphere, the optical path length, and the absorption cross-section as in Equation 4.36. It depends on the wavenumber of the emitted radiation and the absorption cross-section $\sigma_{A,ki}$ with $k \in 0, ..., P$ wavenumber points, which is taken from HITRAN (Rothman et al., 2013).

$$\tau_{,kji} = -[O_2]_{,i} \Delta s_{,ji} \sigma_{A,ki} \tag{4.36}$$

The transmission factor T through the atmosphere is divided into a portion before (T_{near}) and after (T_{far}) the tangent point, relative to the satellite. The near transmission factor $T_{near,jl}$ for tangent altitude j and atmosphere shell at altitude l is calculated by Equation 4.37. The transmission factor is the product of

all optical path segment transmission terms from the edge of the atmosphere with $i = N$ to the current altitude $i = l$. A single optical path segment transmission term is the sum over all wavenumbers k of the relative path strength w_{ki} and the transmission $\tau_{,kji}$. The relative band strength is defined by Equation 4.38.

$$T_{near,jl} = \prod_{i=N}^{i=l} \sum_{k} w_{ki} \exp(\tau_{,kji}) \tag{4.37}$$

$$w_{,ki} = \frac{\sigma_{A,ki}}{\sum_{k} \sigma_{A,ki}} \tag{4.38}$$

The transmission factor for the far side $T_{far,segments,jl}$ is similarly calculated (Equation 4.39). Here, the product of segment transmission terms goes from the lowest altitude $i = 0$ to the current altitude $i = l$, whereby only transmission factors are considered, where the optical path actually intersects with the atmosphere shell at altitude i.

$$T_{far,segments,jl} = \prod_{i=0}^{i=l} \sum_{k} w_{ki} \exp(\tau_{,kji}) \tag{4.39}$$

So far, the transmission factor for the far side $T_{far,segments,jl}$ does not consider the absorption by oxygen on the near side. By multiplication with the tangent altitude transmission factor $T_{t,j}$, Equation 4.40, the far side transmission factor $T_{far,jl}$ includes the whole optical path beginning at the optical path segment in the far side, via the tangent altitude to the satellite.

$$T_{far,jl} = T_{far,segments,jl} T_{t,j} \tag{4.40}$$

Figure 4.13 shows the tangent transmission through the atmosphere between $60\,\mathrm{km}$ and $120\,\mathrm{km}$. Above $100\,\mathrm{km}$, the atmosphere is fully transparent. The transmissivity decreases constantly and becomes opaque at approximately $60\,\mathrm{km}$. This is also the reason, why the A-band emission in the middle atmosphere cannot be observed from ground. For space-born middle atmosphere limb observations, the opacity of the lower atmosphere has the advantage that surface emissions get mostly absorbed, reducing the noise in the measurement.
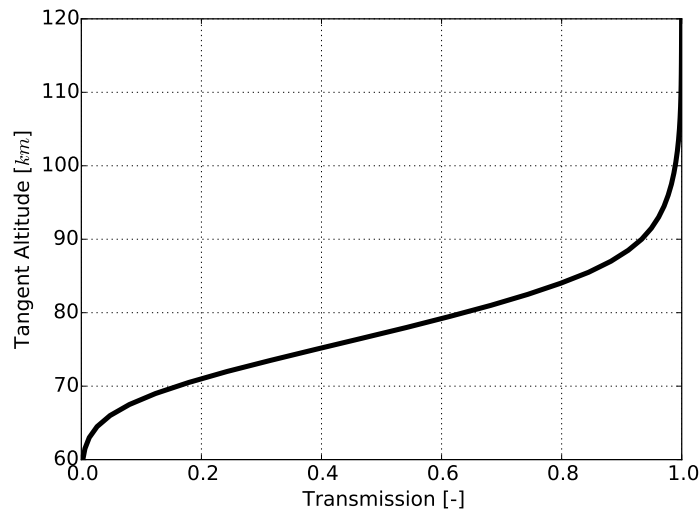
Figure 4.13.: Transmission through the atmosphere for air volumes at tangent altitudes from $60\,\mathrm{km}$ to $120\,\mathrm{km}$.

The radiance $L_{,mj}$ at the entrance pupil for a tangent altitude j and for fine structure line m is the integral of volume emission rate for each fine structure line $\eta_{total,i}d_{,im}$ weighted by the combined far and near transmission factors $(T_{near,ji} + T_{far,ji})$ over the optical path $\Delta s_{,ji}$. The altitude index of the transmission factor is now named i, because i equals l. The integral is approximated with a midpoint integration by summation over all altitude levels $i \in 1, ..., N$, as in Equation 4.41. The factor $1/(4\pi)$ normalizes the uniform irradiance to radiance.

$$L_{,mj} = \sum_i \frac{1}{4\pi} \eta_{total,i} d_{,im} (T_{near,ji} + T_{far,ji}) \Delta s_{,ji} \tag{4.41}$$

The index j describes the tangent altitude coordinate, which corresponds with the first field coordinate (vertical field coordinate). The radiance is expanded along the second, horizontal field axis n, because it is assumed for the measurement simulation that the variation of emission intensity is negligible in horizontal direction for the observation geometry used here. This aspect is further discussed in Chapter 5.2.1.1. Thus, the radiance $L_{,mjn}$ represents a three dimensional tensor with spectral dimension m, field 1 dimension j and field 2 dimension n. It is multiplied with the instrument FOV Ω and entrance pupil area A to derive the spectral radiant flux at the entrance pupil $R_{,mjn}$, see Equation 4.42.

$$R_{,mjn} = \Omega A L_{,mjn} \tag{4.42}$$

The instrument FOV $\Omega = 4.1 \times 10^{-4}$ sr corresponds to an half-field angle of $0.65°$ that allows to image the tangent altitude range from $60\,\text{km}$ to $120\,\text{km}$ for a $600\,\text{km}$ orbit. The entrance pupil area A of $34\,\text{cm}^2$ corresponds to an entrance aperture diameter of $66\,\text{mm}$.

4.3. Instrument

The instrument model uses the spectral radiant flux output from the observation model. The radiant flux is transformed by the fore-optics, filtered with the optical bandpass filter and Fourier-transformed by the SHS. The Fourier-transformed radiant flux is converted to an electric signal by the detector model, after it has been transformed by the detector optics. The fore- and detector-optics are not simulated in detail but only reduce the intensity of the signal by a specific transmission factor. Hence, the two optical components are not further discussed for the measurement analysis.

4.3.1. Bandpass Filter

The bandpass filter reduces the accepted wavenumber range of the instrument and influences the intensity of the radiation. It is described by the transmission filter function $T_{,m}$, which transforms the incoming radiant flux $R_{,mjn}$ with wavenumber coordinate $m \in 0, ..., M$ to filtered spectral radiant flux $R_{filtered,mjn}$, Equation 4.43.

The filter can be modeled with two options in the measurement simulation. One being the actual filter function as calculated in detail by the filter manufacturer and the other a modified Lissberger filter (Lissberger, 1968) for preliminary analysis (Equation 4.44). The equation calculates the transmission for each wavenumber $\sigma_{,m}$. The difference to the filter function as derived in the paper of Lissberger (1968) is that the exponent in the denominator is defined as a variable N_{cav}, describing the number of cavities of the filter, instead of having a constant exponent of two. Other filter parameters are the maximum transmission at normal incidence τ_{max}, the wavenumber at peak transmittance and normal incidence σ_0, the spectral half-width $\Delta\sigma$, and the effective refractive index μ_e. The transmission of the filter is also dependent on the incidence angle of the incoming light θ.

$$R_{filtered,mjn} = T_{,m} R_{,mjn} \tag{4.43}$$

$$T_{,m} = \frac{\tau_{max}}{1 + \left(\frac{2(\sigma_{,m} - \sigma_0)}{\Delta\sigma} + \frac{\sigma_0}{\Delta\sigma} \frac{\theta^2}{\mu_e^2} \right)^{N_{cav}}} \tag{4.44}$$

Figure 4.14 shows the filtered A-band radiant flux at an altitude of $90\,\text{km}$ between wavenumbers $13\,040\,\text{cm}^{-1}$ and $13\,160\,\text{cm}^{-1}$ as an example. The radiant flux is overlayed with the manufacturer provided filter function (thick solid line). The transmission of the filter is above $95\,\%$ in the relevant wavenumber range and has sharp edges. The goal in the filter selection is to maximize the transmission for the six emission lines between $13\,081\,\text{cm}^{-1}$ and $13\,101\,\text{cm}^{-1}$ and to minimize the influence of all the other lines. A detailed trade-off analysis of the filter parameters is provided in Chapter 5.2.5.
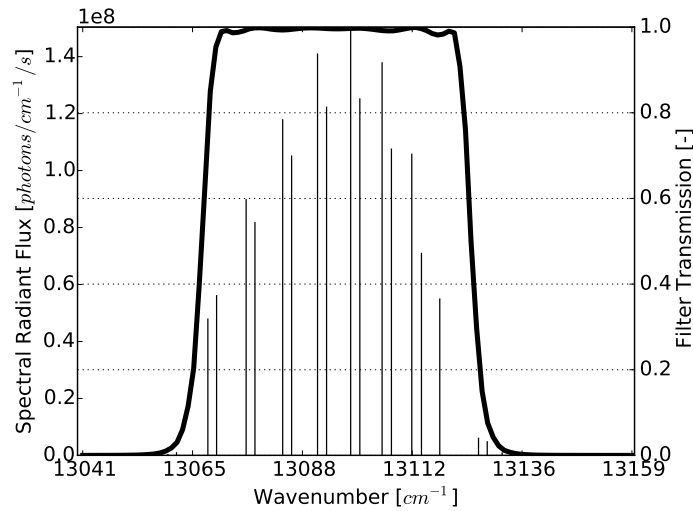
Figure 4.14.: Filtered spectral radiant flux in $\mathrm{photons/cm^{-1}/s}$ in dependence of wavenumber from $13\,040\,\mathrm{cm^{-1}}$ to $13\,160\,\mathrm{cm^{-1}}$ for an altitude of $90\,\mathrm{km}$ and integrated over horizontal field (spectral direction) with filter transmission function.

4.3.2. Spatial Heterodyne Spectrometer (SHS)

The SHS is selected as spectrometer due to the advantages discussed in Chapter 3.3.1. In this chapter the basic concept is introduced, before the SHS simulation model is described. A detailed description of its resolving power, the off-axis analysis, and the description of field widening is provided in Appendix B.2 and references therein.

4.3.2.1. Basic Concept

The SHS can be described as a combination of grating spectrometer and Fourier Transform Spectrometer (FTS). It visually appears to be similar to the MI, where the mirrors in the arms are replaced by tilted gratings. Figure 4.15 illustrates the basic concept of the SHS. Light enters the system from the left and gets divided by a beam splitter. Each beam is diffracted and reflected by a grating (Grating 1, Grating 2).
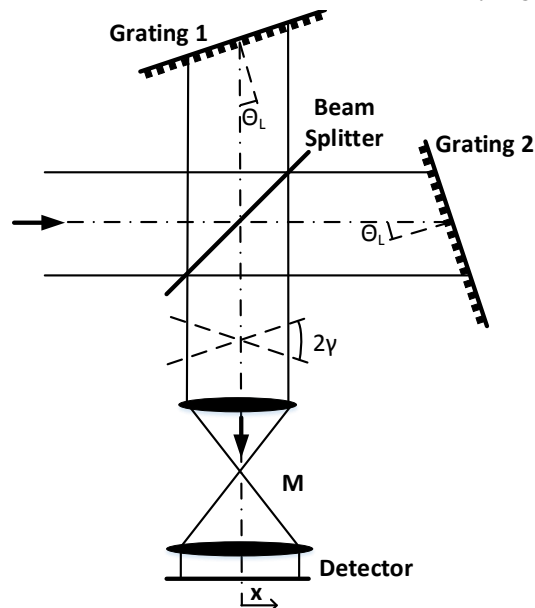
Figure 4.15.: Schematic of an SHS with beamsplitter, gratings, detector optics and detector. The two tilted dashed lines represent the wavefronts from the two arms with a wavenumber different from the Littrow wavenumber. The detector optics has a magnification of M.

Both gratings are tilted by the Littrow angle θ_L. The incoming light is refracted according to Equation

4.45,

$$\sigma\left(\sin(\theta_L) + \sin(\theta_L - \gamma)\right) = m/d \tag{4.45}$$

where σ is the wavenumber of the incoming light in cm^{-1}, θ_L the Littrow angle, γ the angle of deviation from the Littrow angle for the exiting beam, m the diffraction order, and $1/d$ the grating groove density. As illustrated in Figure 4.15, the Littrow angle is chosen that the reflected radiation exits parallel to the incoming radiation for a specific wavenumber, the Littrow wavenumber σ_L. This Littrow condition is expressed by Equation 4.46.

$$\sin \theta_L = \frac{m}{2d\sigma_L} \tag{4.46}$$

The two beams are recombined at the beam splitter and parallel wavefronts propagate to the detector (Focal Plane Array (FPA)) for the Littrow wavenumber. For other wavenumbers, the refracted and reflected wavefronts from the two arms are slightly tilted with respect to the incoming wavefront. This results in interference patterns after recombination, caused by the phase differences between the two beams. Figure 4.15 shows the wavefronts of these two beams after recombination in dashed lines. The phase difference equals zero in the center of the detector and increases with the distance x. At a specific distance from the center, the phase difference becomes $\pi/2$, which results in destructive interference. With further increasing distance, maximum constructive interference is observed. Overall, a striped interference pattern (in x-direction) is registered by the FPA (Detector in Figure 4.15). This interferogram is described by Equation 4.47, which represents an inverse Fourier-Transformation of the incoming radiant flux spectrum $R(\sigma)$. Its basic derivation is provided in Appendix B.2. The number of intensity maxima and minima for a spectral line depends on the difference of the spectral line´s wavenumber σ to the Littrow wavenumber σ_L. This describes the heterodyning aspect of the SHS. The spatial frequency is expressed by Equation 4.48 for a specific spectral line with wavenumber σ .

The interference equation includes also the visibility or contrast factor V. This value varies between zero and unity and is defined by Equation 4.49 (Shepherd, 2002). It describes the difference between intensity maxima and minima relative to the mean intensity. A higher visibility factor is advantageous, because it increases the S/N-ratio. Signal that is not modulated by the cosine term of the interference equation contributes to the intensity offset. Thus, it decreases the usable signal and increases the shot noise.

$$I_g(x) = \int_0^\infty 0.5 L(\sigma)((2 - V) + V\cos(8\pi \tan\theta_L x(\sigma - \sigma_L)) d\sigma \tag{4.47}$$

$$\nu_F = 4\tan\theta_L(\sigma - \sigma_L) \tag{4.48}$$

$$V = \frac{I_{max} - I_{min}}{I_{max} + I_{min}} \tag{4.49}$$

The spatial frequency on the detector does not necessarily equal the spatial frequency at the SHS (More specifically, on the later introduced localization plane of the SHS, see Chapter 5.2.1.3). The magnification factor of the detector optics M transforms the frequency by multiplication. Thus, the spatial frequency is named fringe frequency, when referred relative to the detector. However, the spatial frequency is most often referred to the SHS in the remainder of the document and only referenced to the detector, when necessary.

4.3.2.2. SHS Simulation Model

The simulation model of the SHS uses Equation 4.51 to generate the interferogram, which is derived from Equation 4.47. The radiant flux $R_{,imn}$ is the main input for the model. It is dependent on the wavenumber coordinate $\sigma_{,q}$, the horizontal and vertical field coordinates $f_{1,m}$, and $f_{2,n}$. Furthermore, the instrument is characterized by its Littrow wavenumber σ_L, the grating groove density $1/d$, the diffraction order m, its transmissivity t_{shs}, and the grating width $w_{grating}$.

The Littrow angle is calculated with Equation 4.46 from the input parameters and the spatial coordinate $x_{,j}$ ($j \in 0, ..., N$) goes from x_{min} to x_{max} with $N + 1$ samples and $x_{min} = -0.5 w_{grating}$ and $x_{max} = +0.5 w_{grating}$.

The spatial frequency $\nu_{F,i}$ is calculated for each wavenumber $\sigma_{,i}$, Equation 4.50. It replaces the wavenumber coordinate for the signal, after it is transformed by the interference Equation, 4.51.

The radiant flux is formally integrated along the first field coordinate (summation along m) and along the wavenumber coordinate i. The result is a two dimensional radiant flux field $R_{fshs,jn}$ with spectral coordinate j as first field coordinate. The second field coordinate n stays unchanged. The index f states that the radiant flux is now defined in the frequency domain.

$$\nu_{F,i} = 4\tan\theta_L(\sigma_{,i} - \sigma_L) \tag{4.50}$$

$$R_{fshs,jn} = \sum_i \sum_m t_{shs} R_{,imn}((2-V) + V\cos(2\pi x_{,j}\nu_{F,i})) \tag{4.51}$$

The SHS is modeled in the measurement simulation with a Littrow wavenumber of $13\,127\,\mathrm{cm}^{-1}$, a grating groove density of $1200\,\mathrm{lines/mm}$, and a grating width of $0.7\,\mathrm{mm}$. The visibility is set to $50\,\%$ and the transmissivity to $22\,\%$. These parameters are a trade-off between multiple aspects and are further discussed in Chapter 5.2.2. Figure 4.16 shows an exemplary Fourier-transformed radiant flux distribution along the spectral coordinate. The highest intensity is visible in the center. It corresponds to the position of zero-Optical Path Difference (OPD) and is called barber pole.
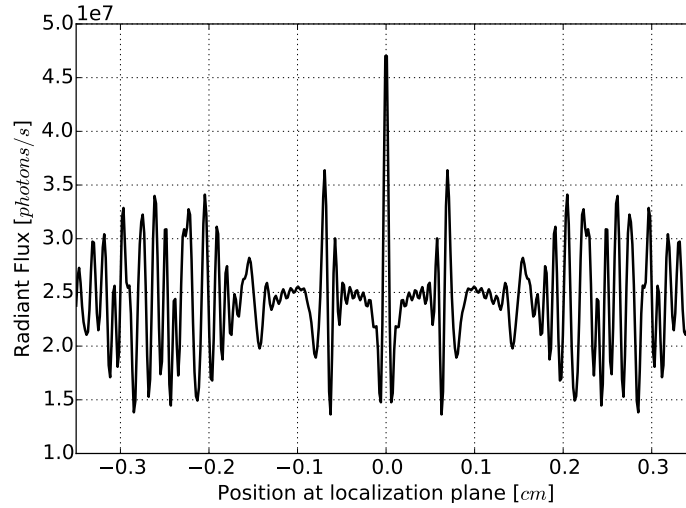
Figure 4.16.: SHS radiant flux distribution in spectral direction at $90\,\mathrm{km}$ altitude during daytime observation.

4.3.3. Detector

The detector model has the task to convert the radiant flux into an electric signal and to add detection noise to it. The detector consists of an array of bins. Each bin is identified by a pixel coordinate in direction 1 (horizontal) $p_{1,k}$ with $k \in 0, ..., K$ and direction 2 (vertical) $p_{2,p}$ with $p \in 0, ..., P$. The radiant flux after the detector optics $R_{fdo,jn}$ is defined along the field coordinates 1 $x_{,j}$ with $j \in 0, ..., J$ and 2 $f_{2,n}$ with $n \in 0, ..., N$, whereby the field coordinate 1 corresponds with the spectral coordinate. The number of field samples and the number of pixels in both directions are the same in the model ($R_{fdo,kp} = R_{fdo,jn}$). The radiant flux is converted to an electric signal $S_{d,kp}$ by multiplication with the quantum efficiency q = 0.4. The signal is assumed to be time independent and thus, the radiant flux is multiplied by the integration time Δt, as in Equation 4.52.

Three detector noise sources contribute to the signal. The noise sources are approximated by random Gaussian distributed noise. The shot noise $S_{shot,kp}$ is calculated from the square root of the integrated radiant flux, see Equation 4.53. It is proportional to the radiant flux and, thus, classified as a multiplicative noise. The two other noise sources dark current $S_{dark,kp}\Delta t$ and readout noise $S_{readout,kp}$ are additive noise terms, see Equation 4.52. The dark current increases with increasing integration time and is temperature dependent, while the readout noise is constant. All noise terms are defined for each bin and differ from bin to bin in general. The dark current is $S_{dark,kp} = 0.3\,\mathrm{e^-/s/pixel}$, which corresponds to a detector temperature of $-10\,°\mathrm{C}$ (Deiml et al., 2017a). The readout noise $S_{readout,kp}$ is better than

$1\,\mathrm{e^-/pixel}$ according to the detector datasheet. These factors are multiplied with a binning factor of 40, resulting in the bin relative noise terms.

$$S_{d,kp} = qR_{fdo,kp}\Delta t + S_{shot,kp} + S_{dark,kp}\Delta t + S_{readout,kp} \tag{4.52}$$

$$S_{shot,kp} = \sqrt{qR_{fdo,kp}\Delta t} \tag{4.53}$$

The output of the detector model is a two dimensional array of the signal $S_{d,kp}$ with $k \in 0, ..., K$ and $p \in 0, ..., P$. Noise sources are included in the measurement model and are excluded from the retrieval model. A typical detector image without noise is shown in Figure 4.17. The image consists of 420 pixel in spectral direction and 41 pixel in spatial direction ranging from an tangent altitude of $60\,\mathrm{km}$ to $120\,\mathrm{km}$ with $1.5\,\mathrm{km}$ resolution. The integration time is $2\,\mathrm{s}$ and the picture simulates the interferogram during daytime observation.
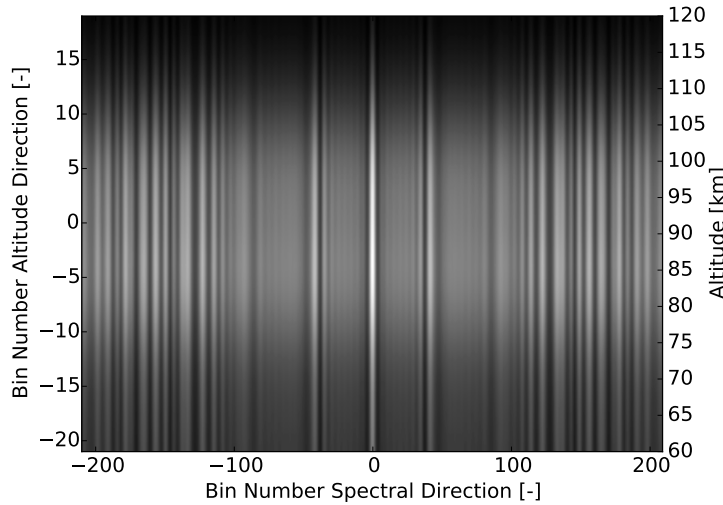
Figure 4.17.: Simulated detector image with 420 pixels in spectral (horizontal) direction and 41 pixels in spatial (vertical) direction. The vertical direction corresponds to a tangent altitude from $60\,\mathrm{km}$ to $120\,\mathrm{km}$ with $1.5\,\mathrm{km}$ resolution.

4.4. Data Processing

The data processing module simulates the actual signal processing after it is sent down to Earth. It includes processes for bias removal, apodization, zero padding, and Fourier transformation. The data processing module does not contain all steps relevant for calibration, like flat-fielding, pixel non-uniformity correction, or phase-correction, because their causes are not simulated. The detailed post-processing and calibration scheme is introduced in Chapter 6. In the following, the relevant methods are described and their algorithmic implementation is explained.

4.4.1. Bias Removal

The process of bias removal subtracts the constant offset from the signal $S_{d,lp}$ by subtracting the arithmetic mean of it along the spectral direction for each altitude, as specified in Equation 4.54. It has the effect that the zero frequency after Fourier transformation is approximately zero. Otherwise, it would be much larger than the actual signal of the emission lines in the spectrum. Bias removal helps to clearly identify the emission lines.

$$S_{br,lp} = S_{d,lp} - \frac{1}{K+1}\sum_{l=0}^{K} S_{d,lp} \tag{4.54}$$

4.4.2. Apodization and Zero-Padding

Apodization is the process of applying a digital filter to the signal to reduce sidelobes and to increase the spectral quality. Harris (1978) discussed in detail the use of different window functions for discrete Fourier transformations. The classic Hann window is used in this implementation as it provides a compromise between sidelobe reduction and loss in spectral resolution. The signal is multiplied with the Hann function along the spectral coordinate (Equation 4.55).

$$S_{a,lp} = S_{br,lp} \left(0.5 - 0.5 \cos \left(\frac{2\pi l}{K} \right) \right)$$ (4.55)

Figure 4.18 shows the signal after the apodization function is applied. The red line shows thereby the Hann function scaled with the highest value of the apodized signal.
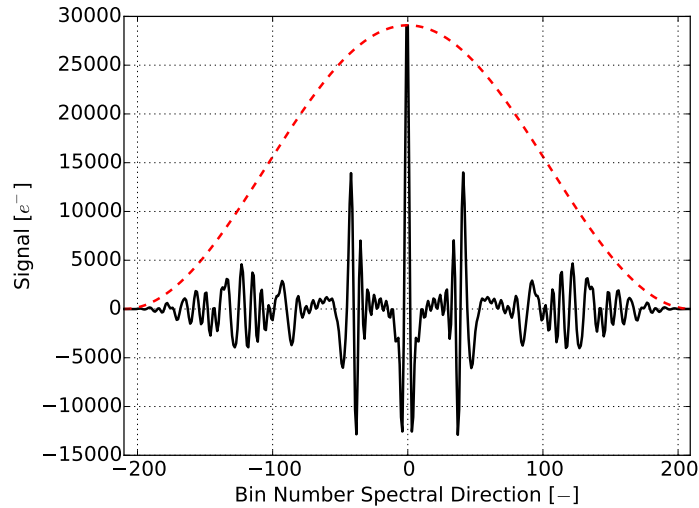
Figure 4.18.: Signal apodized with Hann function in black for a tangent altitude of $90\,\mathrm{km}$. The dashed red line shows the apodization function scaled with the highest apodized signal.

The apodized signal is further zero-padded to increase the sampling of the interferogram and to achieve smoother spectral peaks which enhance retrieval convergence. On both sides of the interferogram in spectral direction, an array with zeros is inserted which has a length of interferogram samples or multiples thereof. The spatial frequency coordinate after Fourier-transformation is scaled accordingly to keep the spatial frequency independent of zero-padding.

4.4.3. Fourier Transformation

The SHS performs an inverse Fourier transformation on the signal from the spectral to the spatial space. For the retrieval of atmospheric properties, spectral information is necessary, because of the individual temperature dependencies of A-band lines, as discussed in Chapter 4.1.6. The Fourier transformation, implemented as a Fast Fourier Transformation (FFT), transforms the interferogram $S_{a,lp}$ with $l \in 0, ..., K$ and $p \in 0, ..., P$ back into the spectral space. The spatial coordinate is transformed to the spatial frequency coordinate. The transformation is performed along the first pixel coordinate l. The symbol j in the exponent stands for the imaginary unit and i is an index, Equation 4.56.

$$S_{fft,ip} = \sum_{l=0}^{K-1} S_{a,lp} \exp \left(-2\pi j \frac{li}{K} \right)$$ (4.56)

The output of the FFT is a complex signal $S_{fft,ip}$, which is symmetric around $i = K/2$ for the first dimension. The signal at $i = K/2$ represents the zero frequency and all values from $i = K/2 + 1$ to $i = K$ represent positive frequencies. The absolute values from $i = K/2, .., K$ are extracted from the Fourier-transformed signal and correspond to the spectrum of the transformed and processed spectral radiant flux. Equation 4.57 summarizes the process, which has as output the signal $S_{spec,jp}$ with $j \in 0, ..., K$ and $p \in 0, ..., P$.

$$S_{spec,jp} = \|S_{fft,(i=K/2,...,K)p}\| \tag{4.57}$$

Important for the retrieval of atmospheric properties is that the peaks are well resolved in the spectrum, because it allows the distinction between different lines with individual temperature dependencies. Figure 4.19a shows an exemplary interferogram for a tangent altitude of $90\,\mathrm{km}$. All six lines are resolved and the temperature dependence of each peak is shown in Figure 4.19b for temperatures between $150\,\mathrm{K}$ and $500\,\mathrm{K}$. The dependence is similar to the temperature dependence of the volume emission rate for the same six lines in Figure 4.11, as expected. The curves do not have exactly the same form, due to the transmission through atmospheric layers with different temperatures. Be aware that a lower spatial frequency corresponds to a higher wavenumber. Thus, also the second abscissa 'wavenumber' is decreasing from left to right.

(a) Spectrum   (b) Temperature dependence
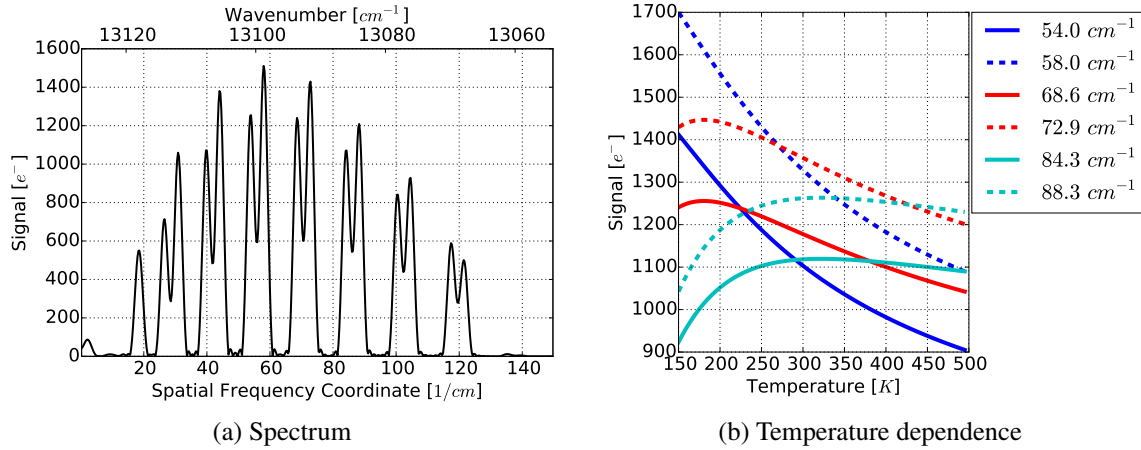
Figure 4.19.: **Left (a)**: Spectrum after data processing and Fourier transformation at $90\,\mathrm{km}$ altitude and noon. **Right (b)**: Temperature dependence of the six peaks identified by their spatial frequency in cm^{-1} for a temperature between $150\,\mathrm{K}$ and $500\,\mathrm{K}$.

The spectrum is also analyzed regarding its resolving power. Gauß fits on the individual peaks allow to calculate their standard deviations σ_s (half-width of the peaks), which are transformed to the FWHM by using the relation $FWHM = 2\sqrt{2ln(2)}\sigma_s$. The resolving power is then calculated by $R = \sigma/FWHM$ to 9260 ± 253 as mean over all spectral peaks. The resolving power is expected to decrease, because the wavenumber gets smaller for larger spatial frequencies. However, this decrease is in the permille range and within the error of the resolving power calculation. The resolving power is sufficient to separate individual peaks of the fine structure. But even without separation of peak pairs, the temperature can still be retrieved as their relative temperature dependencies are similar.

4.5. Retrieval

All modules so far model individual aspects of reality. The atmosphere module provides data and calculates the oxygen A-band volume emission. This data is used by the observation module to calculate the amount of radiation, which reaches the satellite. The satellite/ instrument module represents the physical manipulation and signal detection of the radiation at the FPA. The signal is processed in the data processing module, which provides spectral information about the measured radiation. All these modules comprise the forward model.

The retrieval module has the task to estimate properties of the atmosphere from the measured radiation. This can be described as an inversion of the forward model and is implemented as an optimization problem. The following analysis picks the altitude levels $85\,\mathrm{km}$ and $90\,\mathrm{km}$ to analyze the S/N-ratio during day- and nighttime measurements, respectively. The resulting temperature retrieval precision is also shown for these retrieval points.

4.5.1. Variables and Errors

The retrieval variables are the temperature at the specific altitude and a multiplicative factor. These variables are retrieved from the spectrum as calculated by the forward model.

Noise is introduced into the system at various places and it is statistically distributed. It is assumed that every noise source can be described by a Gaussian distribution and is statistically independent from the others, reasonable for a first estimation without cross-correlation of detector pixels. The vector $\epsilon_{,j}$ with $j \in 0, ..., Q$ summarizes all noise sources. It includes the shot noise $S_{shot,lp}$, the dark current $S_{dark,lp}$, and the readout noise $S_{readout,lp}$ of the detector. Each detector bin has own independent noise sources. Thus, the number of noise variables increases quadratically with detector size. Details about the detector noise sources were discussed in Chapter 4.3.3.

Two types of straylight are considered as noise variables. External straylight originates from reflection at the Earth's surface or at clouds, which are not in the observation scene. It is dependent on the lighting conditions and it is considerably stronger during daylight compared to the nighttime. The external straylight during the daytime is approximated with $1 \times 10^{12}\,\text{photon/s}$ for the whole illuminated detector area as worst case approximation during operations. During nighttime it reduces to $1 \times 10^{7}\,\text{photon/s}$ as worst case. Internal straylight results from unwanted reflections and scattering of radiation within the FOV of the instrument. Therefore, it is proportional to the atmospheric emission. More specifically, the analysis uses a value of $3.5\,\%$ (1σ) ghost reflections to account for this noise source. The origin of these values is derived and discussed in Chapter 5.2.8 about straylight analysis.

The last error source is the optical bandpass filter temperature measurement error of $0.1\,\text{K}$. It is of little influence on the temperature retrieval precision, due to the temperature stabilized bandpass filter design, which is further discussed in Chapter 5.2.5.

4.5.2. S/N-Ratio Analysis

The resulting S/N-ratio is calculated in a Monte-Carlo analysis with 200 samples. These samples are sufficient to get a smooth statistics about the S/N-ratio in dependence of spatial frequency. Figure 4.20 shows the result for daytime observations. The analysis reproduces the spectrum very well. The S/N-ratio is high at the spectral peaks and becomes very small in the spectral gaps. There, the additive noise sources (readout-noise, external straylight) have proportionally stronger influence. The S/N-ratio increases also with increasing integration time Δt.
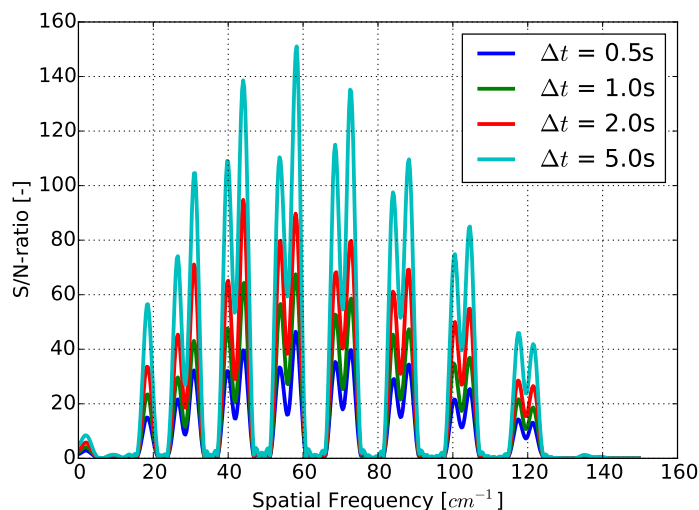
Figure 4.20.: S/N-ratio in dependence of spatial frequency $[\text{cm}^{-1}]$ for different integration times and for an altitude of $85\,\text{km}$ during daytime observations. See Figure 4.19a for a correlation between spatial frequency and wavenumber.

As the S/N-ratio is strongly dependent on spatial frequency/ wavenumber, the mean S/N-ratio between $0\,\text{cm}^{-1}$ and $150\,\text{cm}^{-1}$ is used as a characteristic performance indicator in this analysis. The oxygen A-band emission intensity is significantly higher during daytime compared to nighttime observations. The mean S/N-ratio is also considerably lower for equal integration times during nighttime. Therefore,

the integration time during nighttime needs to be longer to achieve a similar temperature measurement precision. Figure 4.21 shows the mean S/N-ratio in dependence of integration time for day- and nighttime observations.
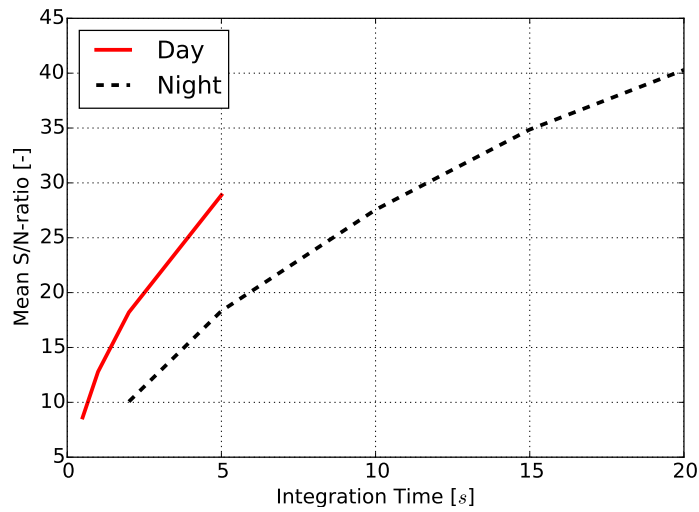
Figure 4.21.: Mean S/N-ratio in dependence of integration time [s] for an altitude of $85\,\mathrm{km}$ for daytime and for an altitude of $90\,\mathrm{km}$ for nighttime observations.

4.5.3. Temperature Retrieval

The temperature retrieval precision analysis is also performed with a Monte-Carlo analysis. Thereby, the noise variables are randomly varied 200 times and each time the temperature is retrieved in an optimization problem. The standard deviation of the retrieved temperature value distribution is the quantity of interest. This analysis is performed for day- and nighttime conditions and for varying integration times. The resulting Figure 4.22 shows the temperature retrieval precision in dependence of mean S/N-ratio, as defined in Chapter 4.5.2. The temperature retrieval precision is similar for the same mean S/N-ratios for day- and nighttime operations, which means that multiplicative noise dominates the noise sources in both cases.

The graph shows that a temperature measurement precision of $2.5\,\mathrm{K}$ can be achieved with a S/N-ratio higher than approximately 17. It corresponds to an integration time larger than $1.5\,\mathrm{s}$ for daytime operations and larger than $5\,\mathrm{s}$ during nighttime operations. The selected integration times of $2\,\mathrm{s}$ and $10\,\mathrm{s}$ fulfill the temperature measurement requirement for this altitude with margin.
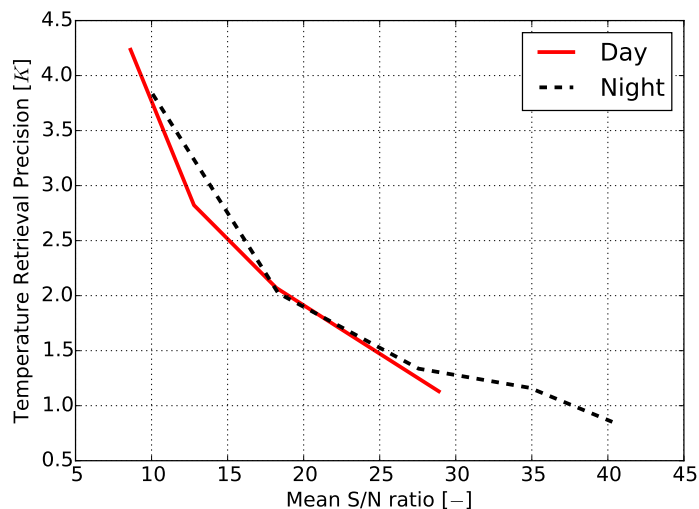
Figure 4.22.: Temperature retrieval precision (1σ) in [K] in dependence of mean S/N-ratio for an altitude of $85\,\mathrm{km}$ for daytime and for an altitude of $90\,\mathrm{km}$ for nighttime observations.

In summary, the measurement simulation, with the resulting temperature measurement precision uncertainties, shows that the instrument fulfills its measurement performance requirements with the selected

set of parameters for conservative and worst-case assumptions.

The selection of all parameters is also strongly dependent on the instrument design in the highly constraint design solution space of a CubeSat form factor. Therefore, the following chapters about the instrument design will further discuss these parameters.

5. Instrument Development

5.1. Instrument Design Parameter

First, the requirements are described on which the development of the instrument is based upon, before the detailed description of the design starts. The requirements are divided into functional, performance, design, and operational requirements as well as constraints. In the following, only the most important requirements are discussed and an extended list can be found in the Appendix C.1.

5.1.1. Functional Requirements

Temperature profiles in the middle atmosphere shall be obtained from observations of relative spectral flux. The measurement shall be performed with an SHS. These core requirements describe the main functionality of the experiment. In addition, important housekeeping data like integration time and temperatures within the instrument shall be recorded with each measurement. Specifically, the temperature of the SHS, of the optical filter, and of the detector shall be measured due to their temperature dependent characteristics. Furthermore, the AtmoHIT experiment shall include, in addition to the CubeSat instrument, a visible camera (VisCAM) to record an image of the observed scene in the atmosphere. These images help to identify and to geo-locate the measurements performed by the instrument. The scientific measurement data, consisting of interferograms and housekeeping data shall be stored on-board the instrument. This is not necessary for a satellite instrument as it includes a CDH system, but necessary for the AtmoHIT experiment. The science data shall also be sent down to the GS for redundancy in the AtmoHIT experiment.

5.1.2. Performance Requirements

Most of the performance requirements are based on the AtmoCube-1 instrument nominal limb viewing scenario. This nominal limb viewing scenario describes the satellite at $600 \, \text{km}$ altitude during daylight to observe the limb of the atmosphere. The main requirement is to achieve a temperature measurement precision better than $2.5 \, \text{K}$ within an altitude range from $60 \, \text{km}$ to $120 \, \text{km}$. Therefore, the FWHM spatial resolution in vertical direction shall be better than $1.5 \, \text{km}$ and in horizontal direction better than $60 \, \text{km}$. The temperature in this altitude range varies approximately between $130 \, \text{K}$ to $500 \, \text{K}$. Thus, this temperature measurement range shall be retrievable. Besides these main instrument performance requirements, additional requirements on the precision, accuracy, and range of the housekeeping data, the radiometric resolution, the geo-location precision/accuracy, and on the performance of the VisCAM can be found in Appendix C.1.

5.1.3. Design Requirements

A number of design requirements provide additional limits to the design trade space. Due to the more refined nature of design requirements, many of them are AtmoHIT specific. The following requirements are relevant for the description of the instrument design and therefore discussed explicitly. Please refer to the Appendix C.1 for the full list of requirements.

The REXUS rocket, which houses AtmoHIT, is a spin stabilized solid fuel ballistic rocket. Its initial acceleration is high compared to typical satellite launch vehicles. Thus, the AtmoHIT experiment shall withstand the structural loads during flight. It also includes the centrifugal forces from spin stabilizing the rocket. The detailed dynamic and static loads are defined in the REXUS user manual (Schüttauf et al., 2016). Another relevant requirement is that the experiment shall be able to handle an input voltage range between $24 \, \text{V}$ to $36 \, \text{V}$. This is significantly different compared to the AtmoCube reference bus, as described in Appendix A.2, and thus results in additional design considerations.

5.1.4. Operational Requirements

The operations of the instrument, both for the satellite and the rocket instrument, require that it operates completely autonomous during flight and that it operates under variable settings of the detector. Thus, parameters like gain or integration time need to be able to be set via tele-commanding. For testing, it is also important that the experiment survives several power-on-off cycles.

5.1.5. Constraints

Besides these requirements, constraints need to be adhered. Three of them are specifically defined for AtmoHIT. The first constraint states that the experiment shall comply with the requirements as specified in the REXUS user manual. The relevant requirements from the user manual have already been introduced in the requirements sections. The next constraints require that the mission adheres to the deadlines set by the REXUS program and that the entrance aperture of the instrument shall have a diameter of at least 66 mm. However, the CubeSat form factor does not need to be fulfilled. Thus, the final design of AtmoHIT differs from the CubeSat instrument to account for these additional constraints. Nevertheless, the design can be readily adopted for the CubeSat and AtmoHIT can act as a verification mission for the instrument of AtmoCube-1.

5.2. Optical Design and Analysis

The instrument is built around the optics. The structural and electrical designs are strongly influenced by it. Therefore, the first focus of the instrument development chapter lies on the optical design and analysis. The optics, including the spectrometer, the mechanics, and the electronics for the entire instrument are developed, assembled, tested, and verified in-house. Thus, all optical and structural components/ functions need to be well understood.

This chapter first discusses the heart of the instrument, the spectrometer. The SHS was introduced in Chapter 3.3.1, its basic concept was described in Chapter 4.3.2, and a detailed derivation of its properties is provided in Appendix B.2. Thus, the following sections focus on the applied aspects of the SHS design. At first, its basic design and the field-widening performance are described, followed by the SHS temperature stability analysis and the analysis of the influence of aliasing and filter effects. A chapter about tolerances concludes the SHS specific aspects. The fore- and detector optics' designs are discussed afterwards, which includes a performance and tolerance analysis. The straylight analysis for the complete setup concludes the optical design chapter. But before the in-depth discussion starts, the following description summarizes the most important properties and aspects of the optical system and uses Figure 5.1 as illustration.

The SHS has a Littrow wavenumber of $13\,127\,\mathrm{cm}^{-1}$ (vacuum) and a grating groove density of 1200 lines/mm. In front of the SHS, the fore-optics focuses light onto the gratings of the SHS. To observe the specified scene in the atmosphere, a FOV of $0.65° \times 0.65°$ is required, which is enforced by field stops in the two SHS arms. Together with an entrance aperture of 66 mm diameter, the FOV defines the etendué of the system. The fore-optics has a $F/\#$ of 4.16 and a focal length of 273 mm. A bandpass filter in front of the fore-optics selects the spectral band of 3.8 nm width around the center wavelength of 763.8 nm. The baffle reduces straylight with an attenuation factor of 1×10^{-3} above the Sun exclusion angle of $26°$. The gratings of the SHS are imaged onto the detector by the detector optics. This relay optics has a paraxial magnification of 0.6 with an object focal length of 28.2 mm and a $F/\#$ of 2.17. The last element of the detector optics is a pupil stop with 3.2 mm diameter, slightly vignetting the entrance aperture and thus acting as a Lyot-stop.
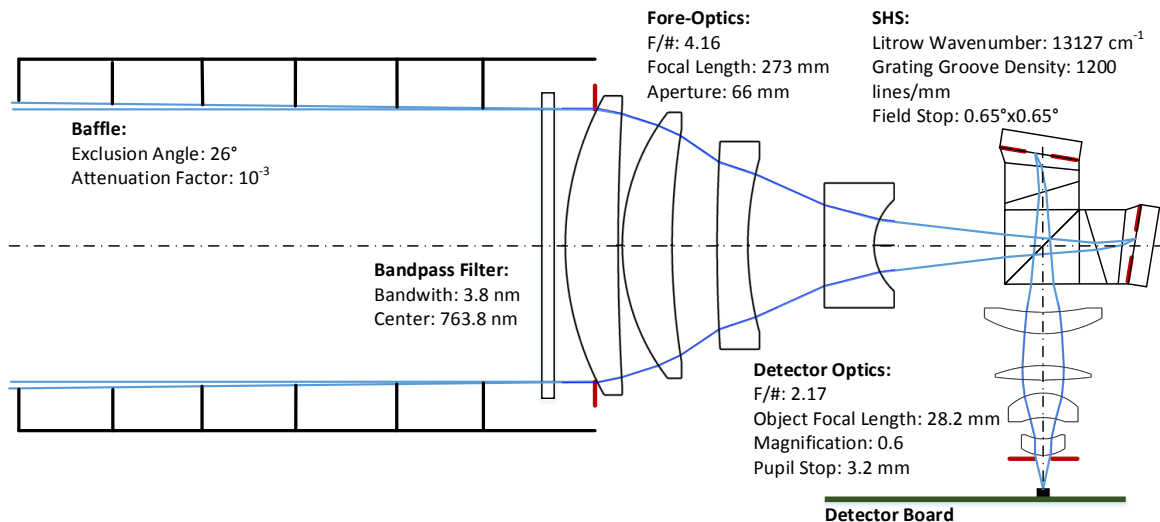
Figure 5.1.: Concept of the optical system with straylight baffle, bandpass filter, fore-optics, SHS, detector optics, and detector board. The most important properties of each optical element are stated with the element name.

5.2.1. SHS Design

5.2.1.1. Imaging Concept

An SHS can be operated in a collimated or focused light beam. The light beam needs to be at least partially focused for this application, otherwise it is challenging to resolve altitude information. Englert et al. (2005) demonstrated that the detector dimension, orthogonal to the spectral direction, can be used as spatial dimension when imaging a scene with an anamorphic telescope onto the gratings. Thus, the SHS can detect the vertical intensity distribution of an atmospheric emission in limb viewing geometry. However, an anamorphic telescope requires more volume compared to a standard lens system focusing in both, the spatial and spectral direction.

An afocal system operates in a collimated light beam and a beam steering mechanism is required to sample different altitude levels. Such a complex mechanism does not fit within the mass and volume constraints of a CubeSat and is thus not further discussed. However, the two principal optical concepts are further described to increase the understanding of the system.

Figures 5.2 and 5.3 show these two concepts for an SHS optics. The detector optics is similar in both concepts: The gratings need to be imaged onto the FPA, which is performed with a transfer optics having the appropriate magnification and imaging quality. The detector optics could also be viewed as a telescope with the gratings in the entrance pupil and the FPA at the exit pupil.

This view of the detector optics is particularly useful for the afocal imaging concept of Figure 5.2. The figure shows an SHS between two telescopes. The fore-optics telescope has its exit pupil on the grating, which is also the position of the entrance pupil of the detector optics. For a particular field point, as for example for the center field point in Figure 5.2 (dashed rays), the afocal property of the fore-optics telescope does not image the scene at infinity onto the gratings. Rather, light from every field point contributes to every location on the gratings. However, the detector optics images the gratings onto the detector. Thus, each detector pixel sees light from every field point and the system exhibits overall no imaging functionality.

The focused design does not lack the imaging functionality. The detector optics is the same, but it is more intuitive to think of it as transfer optics that images every point of the grating onto the FPA. As shown in Figure 5.3, the fore-optics consists of a lens system that images infinity onto the gratings. Thus, every field point in the atmosphere can be mapped onto a position on the detector and spatial information can be retrieved. The focused design has the disadvantage that spherical wavefronts traverse through the SHS for each field point in contrast to planar wavefronts in the afocal design. This results in larger aberrations or a more complex/ expensive design.

Another disadvantage of the focused design is that inhomogeneities in the horizontal direction of the atmosphere are visible in the spectra and thus potentially introduce noise. This inhomogeneity is of little relevance for the AtmoCube-1 instrument, because it influences the measurement only if its oscillatory component with the highest horizontal wavelength in the atmosphere overlaps with the spatial frequency of the emission at the detector. The spatial frequencies of the relevant emission lines lie between $40\,\mathrm{cm}^{-1}$ and $100\,\mathrm{cm}^{-1}$, which will be further discussed in Chapter 5.2.2. This means that an aliasing oscillatory component in the atmosphere requires a horizontal wavelength lower than $2.1\,\mathrm{km}$, by using a grating width of $0.7\,\mathrm{cm}$ and a horizontal field width in the atmosphere of $60\,\mathrm{km}$. As explained in Preusse et al. (2009), the weighting function for standard limb retrieval in along track direction has a FWHM of approximately $500\,\mathrm{km}$ for optical thin conditions. Thus, oscillations with a horizontal wavelengths of less than $2.1\,\mathrm{km}$ average out without impact on net radiance. With sophisticated tomographic limb retrieval routines, the horizontal wavelengths of still resolvable oscillations in along track direction can be reduced. In theory, they approach two times the distance the satellite moves during a measurement (Nyquist limit). With an orbital velocity of $7.6\,\mathrm{km\,s}^{-1}$ and an integration time of $2\,\mathrm{s}$ for worst case (daytime) conditions, the maximum resolvable horizontal wavelength along track calculates to $30.4\,\mathrm{km}$. Even in this worst case, oscillations with horizontal wavelengths of less than $2.1\,\mathrm{km}$ average out and do not influence the temperature retrieval. This analysis assumed that the horizontal wavelengths are similar in both horizontal directions.
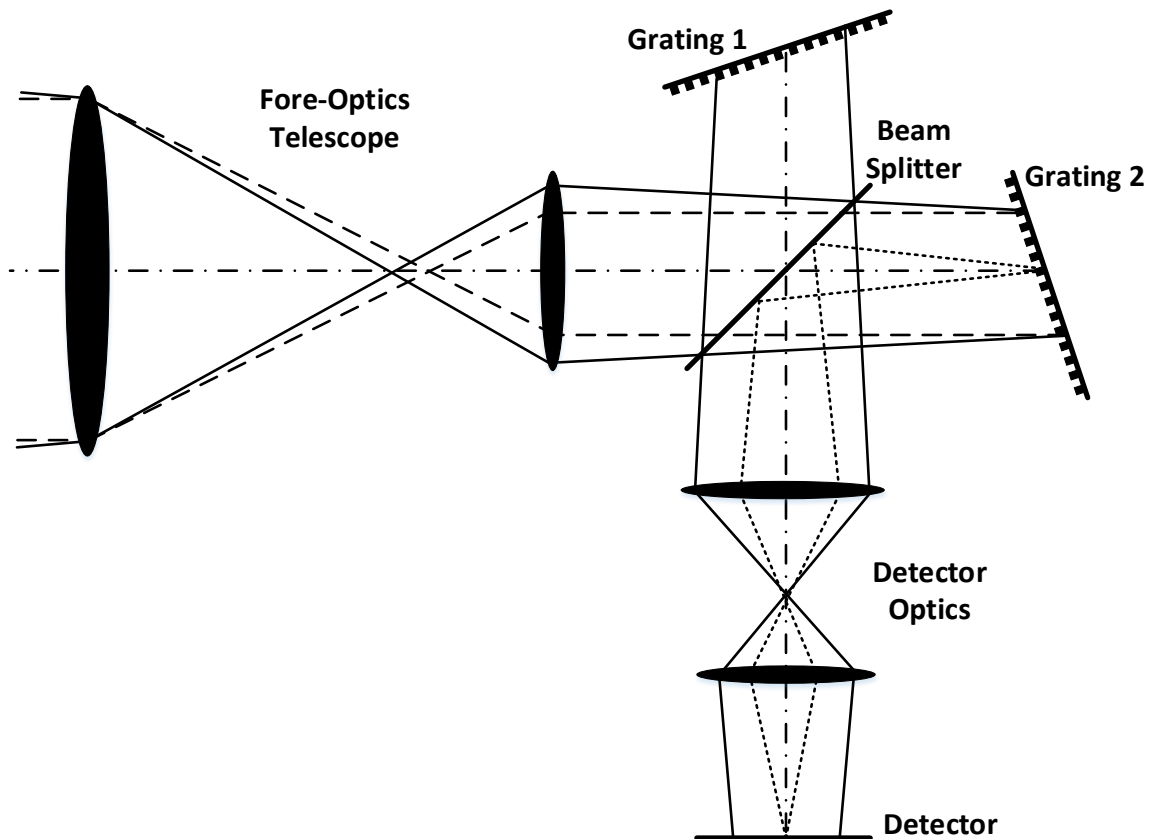
Figure 5.2.: Imaging concept of the SHS with an afocal telescope. Only outer rays are shown for the upper arm of the SHS.
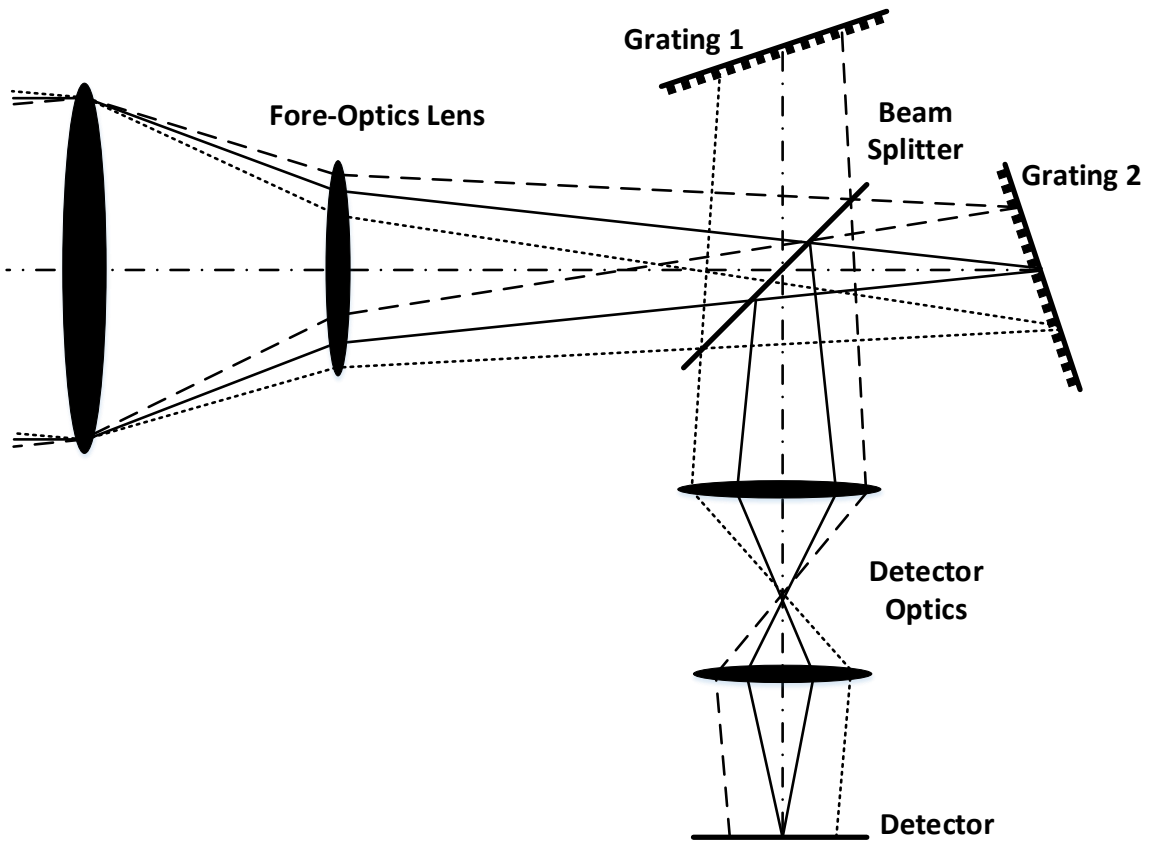
Figure 5.3.: Imaging concept of the SHS with fore-optics lens focusing onto the gratings. Only outer rays are shown for the upper arm of the SHS.

5.2.1.2. Components

The SHS is a complex optical subsystem. It consists of 13 or 15 individual parts and six different elements. All their properties need to be controlled to achieve the desired performance of the spectrometer. The following elements assemble a field-widened SHS:

- Beamsplitter
- Spacer 1
- Field-widening Prism (Short: Prism)
- Spacer 2
- Grating
- Side Plate (optional)

The beam splitter is in the center and has a cubic form. The two arms are mounted on two side surfaces of it. Figure 5.4a shows the front view of the SHS with the individual element angles and labels of the elements. The overall depth of the SHS is $27\,\mathrm{mm}$. Spacer 1 consists of two prisms in each arm with apex angles β and depths of $6\,\mathrm{mm}$. Thus, an air gap exists between the two spacer 1 prisms that these parts do not interfere with the light beam. It is visible in the three dimensional illustration of the CAD model in Figure 5.4b. The air gap between the two parts is also needed for calibration. The field-widening prisms extend over the full depth and have the apex angles α. The spacers 2 again are hollow and have the apex angles η. Optional side plates can be mounted on the front and back surfaces of the SHS to increase its structural stability. The technical drawings in the Appendix C.5.2 provide more detailed information and specify also all other dimensions.

(a) Front view of the SHS with labels for elements.   (b) Three-dimensional view of the SHS.
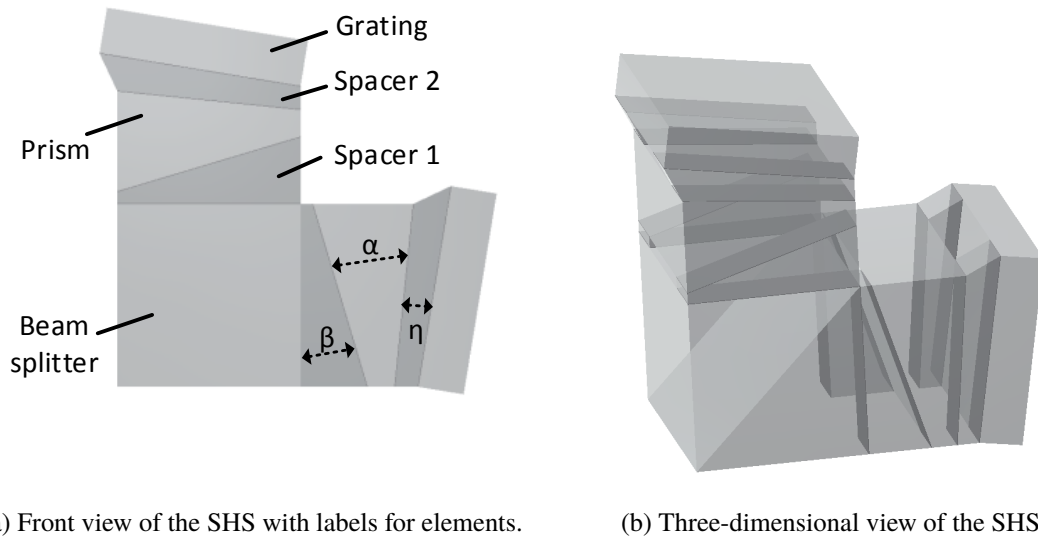
Figure 5.4.: Illustration of the SHS with different views of a CAD model.

In the following, these elements are described in more detailed. In addition, the bandbass filter in front of the SHS is specified as it has major influence on the performance of the SHS. The filter is also further discussed in Chapter 5.2.5.

Beam Splitter   The cubic beam splitter is used to split unpolarized light with an efficiency of $(50 \pm 5)\,\%$ for transmission and reflection in the relevant wavelength range. It is made out of N-BK7 with the overall dimensions of $18\,\text{mm} \times 18\,\text{mm} \times 27\,\text{mm}$. The catheti of the beam splitter prisms are coated with an Anti-Reflection (AR) coating. The front and back sides are not polished and coated, because they are used for glueing the SHS into its housing.

Gratings   The gratings are holographically blazed gratings with a high efficiency ($> 70\,\%$) at $762\,\text{nm}$ for the first diffraction order. Holographic instead of ruled gratings are used, because of their generally lower straylight. The gratings are being replicated from master gratings due to cost considerations. The substrate material is the Fused Silica Corning 7980 and the grating surface is coated with gold. All other sides are not coated. The grating groove density was chosen to $1200\,\text{lines/mm}$, because it fits to the spectral resolution/ bandwidth requirement and is a standard density, therefore commonly available.

Field-widening Prisms   The field-widening prisms consist of the material N-SF11, which provides acceptable field-widening performance and temperature stability, see Chapters 5.2.1.3 and 5.2.4. The most important feature of the prism is its apex angle, because it influences the Littrow wavenumber and the field-widening performance. The two working surfaces of a field-widening prism are coated with an Anti-Reflection (AR)-coating.

Spacers   Two types of spacers are used for the SHS and from each type four pieces are required. The spacers between beamsplitter and field-widening prisms (spacer 1) are made out of N-SF11, whereas the spacers between field-widening prism and grating (spacer 2) consist of Fused Silica.

Side Plates   The SHS is further stabilized by side plates. These L-shaped N-BK7 glass plates are glued on the front and back side of the SHS to increase the resilience against shear forces. They extend from the beamsplitter via the spacers and the field-widening prisms to the gratings. These optional components have been used for the AtmoHIT experiment to ensure higher structural stiffness.

Bandpass Filter   The bandpass filter has a narrow bandpass and uses a hard coating. It is specified to be temperature stable within the operational temperature range of the instrument. The main filter properties are stated in the Appendix C.2 and Chapter 5.2.5 discusses the selection of these properties.

Glue   The glue Norland Optical Adhesive 88 (NOA 88) is used for bonding of the individual glass elements. It is developed as low-outgassing glue with a Total Mass Loss (TML) of $1.07\,\%$ and a Collected Volatile Condensable Material (CVCM) below $0.01\,\%$. The glue has a refractive index equivalent to N-BK7, when it is cured. Thus, it can also be used for the beamsplitter. For the arm elements, the refractive index is not relevant as the glue areas are not within the optical path.

The fully assembled SHS is glued to the aluminum housing to simplify the optical alignment and to have a slightly flexible connection. Therefore, the single compound and low outgassing silicone MasterSil 922-LO was selected. Its paste-like consistency and one part system makes it convenient to handle during the gluing process. It is a humidity curing system that requires a seven day cure time at room temperature to achieve full strength and the low outgassing properties.

Microspheres   Microspheres with a diameter between $47\,\mu m$ to $50\,\mu m$ ($4\,\sigma$) are used to control the bond line thickness between the elements. The glue is loaded with $10\,\%$ volume ratio of these microspheres. By using microspheres from the same batch, the bond line thickness error should be below $\pm 0.5\,\mu m$ (Brian Gobrogge, cospheric.com, personal communication). Thus, the bond line thickness angle uncertainty calculates to $11.5''$ ($4\,\sigma$) for a height of $18\,mm$. Performing a statistical analysis with a Gaussian distribution and a standard deviation of $3\,\mu m$ ($4\,\sigma$), as specified in the datasheet, the uncertainty is $15.6''$ ($4\,\sigma$). This larger value is used in the tolerance assessment of Chapter 5.2.6.1 to calculate the Littrow wavenumber uncertainty.

Coatings   Three different coatings are used for the SHS, without considering the bandpass filter coating:

1. The gratings are covered with a gold coating, which has a higher reflection than aluminum in the relevant wavelength range.

2. The splitter surface of the beam splitter uses a $(50 \pm 5)\,\%$ coating with low dependence on polarity.

3. All other optically relevant surfaces are coated with an AR-coating with a maximum reflection lower than $0.5\,\%$ in the wavelength range from $763\,nm$ to $765\,nm$.

5.2.1.3. Field-Widening

Field-widening is achieved by introducing two stationary prisms between the gratings and the beam splitter. This allows to increase the FOV by approximately two orders of magnitude by virtually rotating the image of the gratings perpendicular to the optical axis. A monolithic design of a field-widened SHS is shown in Figure 5.5. The two arms need to be geometrically identical and thus can be transformed to one another by rotating by $\pi/2$. The three arm elements have slanted angles as shown in Figure 5.5. The figure shows also the optical axis with dash-dotted lines and a ray bundle for the center field point.
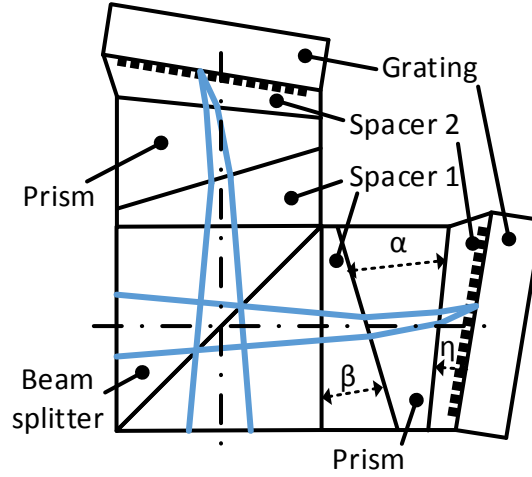
Figure 5.5.: Schematic of a field-widened Spatial Heterodyne Spectrometer (SHS) with beam splitter, spacer 1, field-widening prism, spacer 2, and gratings (Side View).

Harlander et al. (2002) state that optimal field-widening is achieved by a minimum deviation prism for an astigmatism limited SHS. The prism incidence angle (β) depends on the Littrow angle θ_L and the field-widening prism refractive index (Equation 5.1) (Harlander et al., 2002). The prism apex angle is calculated as for a minimum deviation prism, see Equation 5.2. The spacer 2 angle η is calculated by Equation 5.3, which tilts the grating such that an incoming beam, parallel to the optical axis, hits the grating at the Littrow angle θ_L. This equation can be easily derived by analytically tracing a ray through a prism and demanding that the ray hits the grating surface at the Littrow angle.

$$\frac{n^2 - 1}{n^2} \tan \beta \frac{2n^2 - \sin^2 \beta}{n^2 - \sin^2 \beta} = \tan \theta_L \tag{5.1}$$

$$n \sin \left(\frac{\alpha}{2} \right) = \sin \beta \tag{5.2}$$

$$\eta = \theta_L - \arcsin \left(n \sin \left(\alpha - \arcsin \left(\frac{1}{n} \sin \beta \right) \right) \right) \tag{5.3}$$

Equation 5.1 is used to calculate an initial angle for the ray tracing simulation. Through this simulation, the angles are further optimized while still regarding Equation 5.3. Overall, six Degrees of Freedom (DOF) are available to optimize the SHS. The three angles have the largest influence on the performance, but also the center thickness of each prism has slight influence on the performance. The constraint of Equation 5.3 reduces the effective number of DOFs to five, because one angle is dependent on the two other angles. The refractive index of the field-widening prism glass provides in theory another DOF. However, the glass type is used in the temperature stabilization of the SHS and is not further regarded in this chapter. The SHS optimization is conducted with a simplified and perfect fore-optics simulated by one paraxial lens. The lens has the entrance aperture and the focal length of the actual fore-optics. This results in an entrance angle of the SHS of 6.9°. Figure 5.6 shows the complete setup. The maximum and minimum entrance fields with incidence angles of 0.65° together with the center field are simulated in the analysis and shown by different colors in the image. Only one arm of the SHS is simulated, because this is sufficient to perform the analysis on imaging quality of the system, when considering that both arms are aligned to have the exact same optical path difference in the center.
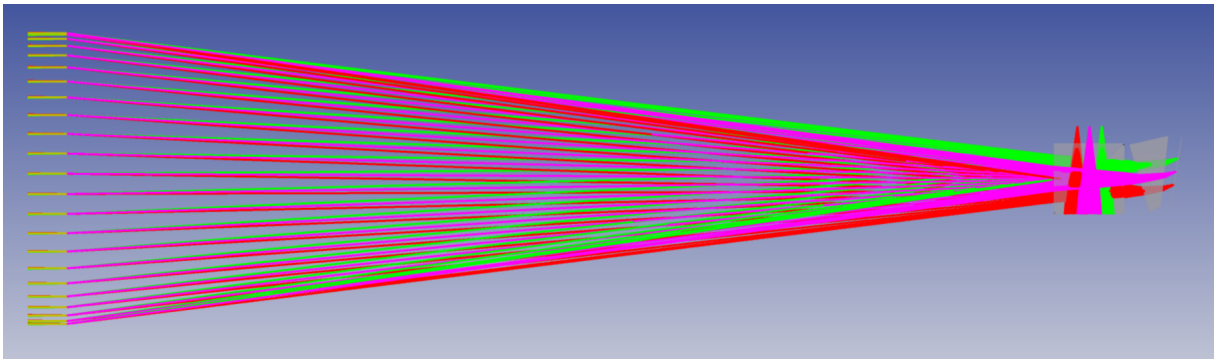
Figure 5.6.: Setup for the field-widening performance analysis including a perfect paraxial lens as imaging optics and one arm of the SHS.

Zooming into the relevant part of the setup, the rays hit the optical elements in the following order: The beam splitter is simulated with two prisms, where the splitter surface is set to transmit all rays. Of the arm elements, only the field-widening prism and the grating are simulated as the spacers do not interfere with the optical path. The grating is a reflection grating and diffracts rays in the first order. The distance between paraxial lens and SHS is adjusted that the beam is focused onto the gratings. After a ray hits the grating, it is reflected back and travels from the right to the left, where it hits again the field-widening prism and the left part of the beamsplitter. The splitter surface is now set to reflect all rays downwards. The rays would leave the SHS at the bottom of the beam splitter. However, a retro-reflective surface is added through which the rays are focused onto the virtual localization plane of the gratings for performance analysis reasons. The beam splitter is not considered anymore for this path. The properties at the localization plane can be used as performance metric for the SHS, because the localization plane is imaged with the detector optics onto the detector.

The virtual image at the localization plane is spanned up by the outermost fields, which are represented by rays in red (left) and green (right) color. The virtual image has a size of approximately $6.5\,\text{mm} \times 6.5\,\text{mm}$.
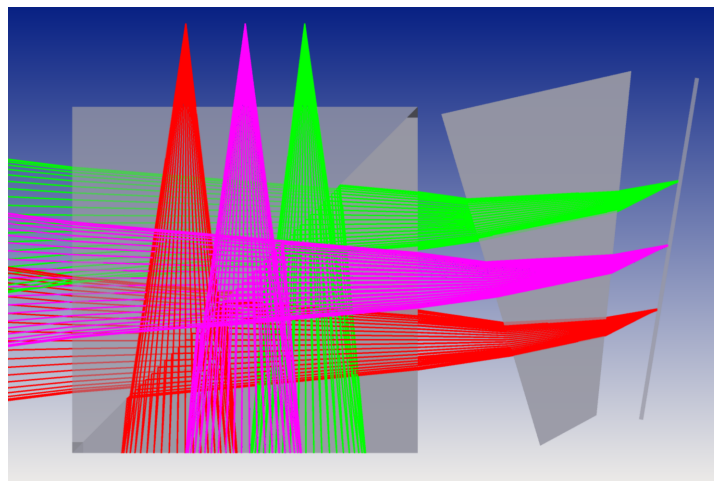
Figure 5.7.: Detailed view of the setup for the field-widening performance analysis of the SHS.

The field-widening prism angle, the spacer angles and their positions are optimized to minimize the Optical Path Difference (OPD) for five characteristic field points. The goal of the optimization of the SHS is to keep the OPD below approximately 0.5 wavelengths. This holds true for the center field point as shown in Figure 5.8. The image shows the OPD in spectral and spatial direction for two different wavelengths. Here, the OPD in wavelengths is described as function of the normalized pupil coordinate. For other field points, the OPD increases to values below 0.6 wavelengths at the corners for marginal rays, showing that the field-widening ability of the SHS is on its limit at an entrance angle of $6.9°$. It is accepted, because a lower OPD would require a slower fore-optics (larger focal lengths). Furthermore, Figure 5.9 demonstrates that the Root-Mean-Square (RMS) OPD for the whole field is below 0.2 wavelengths.

(a)   (b)
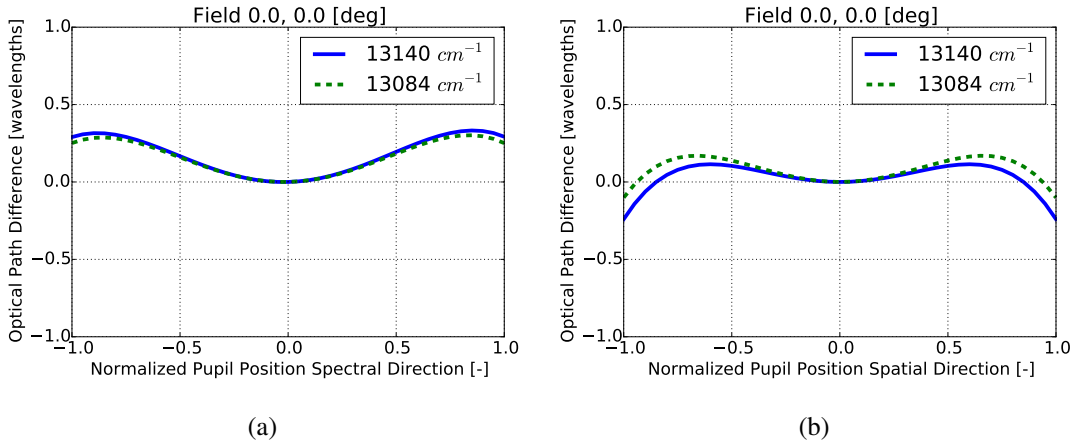
Figure 5.8.: OPD in spectral (5.8a) and spatial (5.8b) direction for the center field point at the virtual image of the SHS for two different wavelengths.
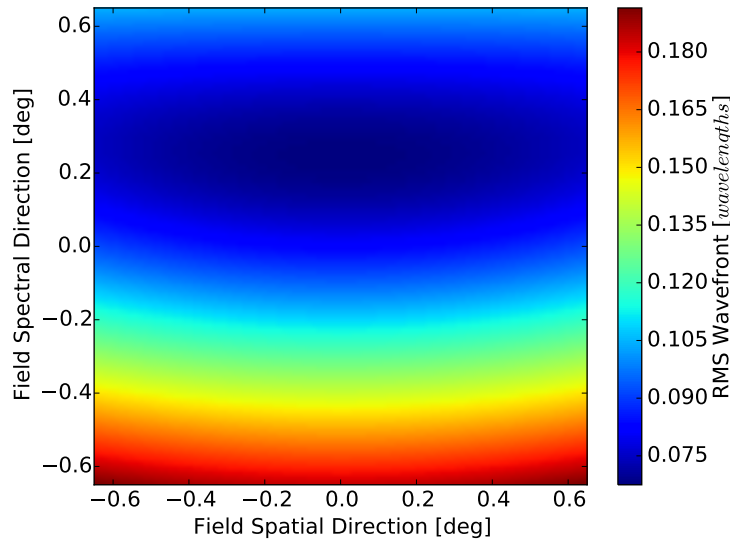
Figure 5.9.: RMS OPD [$wavelengths$] for the whole field [deg] of the SHS.

5.2.2. Maximum allowable Littrow Wavenumber Deviation

For further analysis of the SHS, it is important to establish the maximum allowable deviation from the design Littrow wavenumber. This knowledge helps to set the effects of ambient air pressure, SHS temperature, aliasing, and filter effects in the next sections into context. Multiple aspects need to be considered to specify these constraints:

One aspect describes the Nyquist-Shannon criteria (Shannon, 1998). If an emission line has a fringe frequency at the detector larger than half of the number of pixel bins on the detector, this emission line cannot be retrieved anymore by Fourier-transformation. This fringe frequency translates to spatial frequency by considering the detector size and the magnification factor of the detector optics. More specifically, the detector has 420 pixel bins over a detector size of $0.42\,\mathrm{cm}$ in spectral direction. The resulting maximum fringe frequency of $500\,\mathrm{cycles/cm}$ corresponds to a maximum spatial frequency of $300\,\mathrm{cm}^{-1}$ with a magnification factor of 0.6 The relevant emission lines need to stay below this maximum spatial frequency. Emission lines with high spatial frequencies, that are not used for temperature retrieval, should also be resolved. Otherwise, they may alias with the relevant emission lines.

The second aspect in consideration relates to the SHS as heterodyning system. The fringe frequency is dependent on the distance of the emission line wavenumber from the Littrow wavenumber. This dependency is symmetric. For a certain distance from the Littrow wavenumber, the spatial frequency is the same, independent whether the emission wavenumber is left or right of the Littrow wavenumber. In the AtmoCube-1 specific case, emission lines right of the Littrow wavenumber can alias with the relevant

emission lines if their corresponding spatial frequencies are not far enough apart. Hence, the Littrow wavenumber can only deviate a certain distance, otherwise this aliasing occurs.

Figure 5.10 shows the spatial frequencies for the two outer wavenumbers, which shall be detected by the SHS, as a function of Littrow wavenumber deviation. With positive deviation from the design Littrow wavenumber, the spatial frequencies are increasing as expected. The maximum and minimum allowable spatial frequencies are shown with thick solid lines as defined by the Nyquist-Shannon criteria.

In addition to these two relevant emission lines, also two boundary emission lines are plotted. The emission line with wavenumber $13\,059\,\mathrm{cm}^{-1}$ has the highest spatial frequency of all lines with a relative intensity larger than $5\,\text{\textperthousand}$ compared to the highest emission peak within the filter bandwidth. Its spatial frequency is also increasing with increasing Littrow wavenumber. The spatial frequency should be below the Nyquist-Shannon criteria to avoid aliasing effects, which is the case within a wide range of Littrow wavenumber deviations.

For lower spatial frequencies, the heterodyning aspect of the SHS is the limiting factor. The emission line with the greatest distance to the right of the Littrow wavenumber and a relative intensity larger than $5\,\text{\textperthousand}$ has a wavenumber of $13\,133\,\mathrm{cm}^{-1}$. Because the emission line is on the other side of the Littrow wavenumber, an increase in Littrow wavenumber decreases the spatial frequency. To avoid aliasing, the emission line should have a spatial frequency lower than the relevant emission lines. With a deviation larger than approximately $-10\,\mathrm{cm}^{-1}$ from the Littrow wavenumber, aliasing will start to occur. Including margin, the maximum negative allowable Littrow wavenumber deviation shall be therefore below $-6\,\mathrm{cm}^{-1}$.

In summary, a maximum allowable Littrow wavenumber deviation of $\pm 6\,\mathrm{cm}^{-1}$ is used for the following analysis. These two limits are also depicted in Figure 5.10 with two vertical black lines.
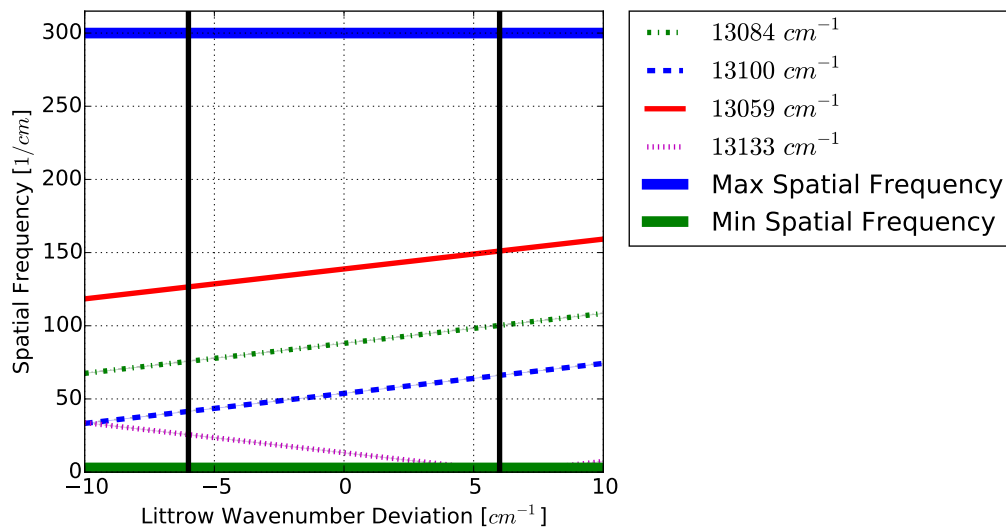
Figure 5.10.: Allowable Littrow wavenumber deviation. Spatial frequency in dependence of deviation from the design Littrow wavenumber $13\,127\,\mathrm{cm}^{-1}$ for the two outer relevant emission lines and two boundary emission lines. The thick solid lines show the maximum and minimum detectable spatial frequencies.

5.2.3. Pressure Dependence of the SHS

The Littrow wavenumber of the SHS is pressure dependent, because the volume between the spacers is filled with air or is evacuated in vacuum. The pressure dependent refractive index of air needs to be considered for detailed analysis of the Littrow wavenumber, because it changes in the same order of magnitude as its allowable tolerance.

This dependence can be calculated with Equations 5.5 and 5.4. The first equation reflects Equation 5.3, but with considering that the refractive index of air $n_{air}(p)$ is dependent on pressure and not unity. The second equation originates from Equation 4.46 with the difference that the Littrow wavenumber is also indirectly proportional to the refractive index of air $n_{air}(p)$. This dependence on refractive index of air results from the diffraction equation. Appendix C.3 provides additional information.

$$\theta_L(p) = \eta + \arcsin\left(\frac{n}{n_{air}(p)}\sin\left(\alpha - \arcsin\left(\frac{n_{air}(p)}{n}\sin\beta\right)\right)\right) \tag{5.4}$$

$$\sigma_L(p) = \left(\frac{1}{d}\right)\frac{m}{2n_{air}(p)\sin(\theta_L(p))} \tag{5.5}$$

Figure 5.11 shows the analytically calculated pressure dependence of the Littrow wavenumber relative to its design Littrow wavenumber of $13\,127\,\mathrm{cm}^{-1}$ in vacuum (parameter b). The Littrow wavenumber increases with rising pressure. This result is experimentally validated in Chapter 7.3. The graph shows that the Littrow wavenumber deviates by about $1.3\,\mathrm{cm}^{-1}$ between ambient air and vacuum conditions for a temperature of $43\,°\mathrm{C}$ (parameter a). This temperature was selected to keep the analysis comparable to the experiment, because the gradient of the pressure dependence is also temperature dependent.
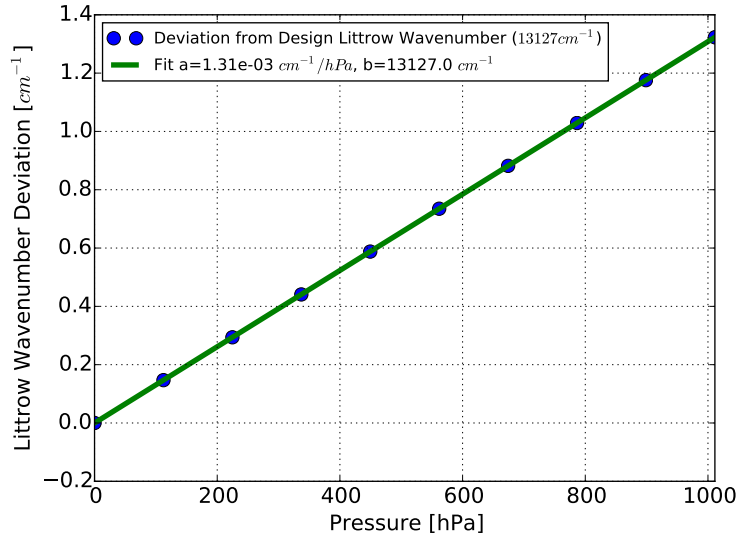
Figure 5.11.: Analytically calculated deviation of the Littrow wavenumber from the design wavenumber in dependence of pressure. The fit errors for both parameters lie within the numerical error.

5.2.4. SHS Temperature Stability

The Littrow wavenumber is also temperature dependent besides the pressure dependence. This relation is analyzed and strategies are developed to thermally stabilize the SHS. A preliminary ZEMAX analysis shows that the temperature dependence analysis of the aberrations is of minor influence. Thus, it is not further described. The Littrow wavenumber dependence can be further separated into the refractive index temperature dependence of the field-widening prism, the grating groove density temperature dependence, and the thermal expansion that changes the element angles and, thus, the Littrow angle and the Littrow wavenumber. All aspects are analyzed and discussed in the following sections.

The underlying equations to describe the Littrow wavenumber temperature dependence are Equations 5.6 and 5.7. Both equations follow directly from Equations 5.3 and 4.46. The diffraction order represents the only constant parameter, because it is selected when the SHS is designed.

$$\theta_L(T) \quad = \quad \eta(T) \quad + \quad \arcsin\left(n(T)\sin\left(\alpha(T) - \arcsin\left(\frac{1}{n(T)}\sin(\beta(T))\right)\right)\right) \tag{5.6}$$

$$\sigma_L(T) = \left(\frac{1}{d}(T)\right)\frac{m}{2\sin(\theta_L(T))} \tag{5.7}$$

Throughout this analysis, it is assumed that the temperature is distributed uniformly in the SHS - the block capacity assumption. This assumption can be accepted only if the internal thermal conductivity significantly exceeds the heat transfer coefficient to the surrounding. In the following, the SHS is supposed to be mounted on the top and back face of the beam splitter to an aluminum casing, which encloses it

completely except at the entrance and exit ports. The SHS housing is mounted to the outer structure of the satellite, but most of its surface faces vacuum. The structural connection is assumed to be thermally isolated that radiative heat transfer between SHS housing and satellite resembles the major heat flow path to the SHS. The heat transfer coefficient between satellite and SHS housing needs to be smaller than the thermal conductivity of the SHS glass for verification of the block capacity assumption. The conductivity of the aluminum housing can be neglected as it considerably exceeds that of glass. Thus, if the block capacity assumption for the SHS glass block is valid, it is also permissible for the SHS housing. The assumption can be verified with the Biot number Bi, as defined in Equation 5.8 (Incropera, 2007, p. 261),

$$Bi = \frac{\alpha_{str} L}{\lambda} \tag{5.8}$$

with L as characteristic length, α_{str} the heat transfer coefficient through radiation, and λ the thermal conductivity of the glass. The characteristic length depends on the boundary conditions, for example whether the SHS is thermally isolated on one side. The characteristic length is defined as half of the SHS thickness for this mounting configuration of the SHS. A typical requirement for the block capacity assumption describes $Bi < 0.1$ (Incropera, 2007, p. 261). The heat transfer coefficient is extracted from the Stefan-Boltzmann law for black body radiative transfer (Incropera, 2007, p. 830) and is defined by Equation 5.9,

$$\alpha_{str} = \sigma_S \Sigma_{12} (T_1 + T_2)(T_1^2 + T_2^2) \tag{5.9}$$

with the Stefan-Boltzmann-Constant $\sigma_S = 5.67 \times 10^{-8} \, \text{W m}^{-2} \, \text{K}^{-4}$ and Σ_{12} as radiation exchange factor, which includes the emissivity and absorptivity of the warmer and colder body, respectively, as well as the view factor between them. The worst case equals a radiation exchange factor of one and corresponds to two black bodies where the emitted radiation from the warmer body is completely absorbed by the colder body. The temperature of the SHS is T_1 and T_2 of the satellite structure. The assumption of block capacity is justified, when Equation 5.10 is true for a specific temperature T_2 of the satellite structure.

$$\frac{0.1\lambda}{L} > \sigma_S (T_1 + T_2)(T_1^2 + T_2^2) \tag{5.10}$$

Evaluating the equation shows that if the temperature of the satellite structure is larger than $T_2 > 366 \, \text{K}$ for the worst case, the block capacity assumption is no longer valid. Here, the characteristic length equals $L = 13.5 \, \text{mm}$, the SHS temperature is $T_1 = 293.15 \, \text{K}$, and the conductivity is $\lambda = 1.114 \, \text{W m}^{-1} \, \text{K}^{-1}$, representing the glass N-BK7 as a typical optical glass. This means that the temperature difference between the satellite structure and SHS must not exceed 73 K, which is deemed reasonable for a CubeSat.

5.2.4.1. Influence of Refractive Index Temperature Dependence

The refractive index of a glass can be calculated by the Sellmeier Equation 5.11 (Advanced Optics, 2016). Thereby, n describes the refractive index in dependence of wavelength λ. The six parameters B_1, B_2, B_3, C_1, C_2, and C_3 are provided by the glass manufacturer.

$$n^2(\lambda) = 1 + \frac{B_1 \lambda^2}{\lambda^2 - C_1} + \frac{B_2 \lambda^2}{\lambda^2 - C_2} + \frac{B_3 \lambda^2}{\lambda^2 - C_3} \tag{5.11}$$

The absolute temperature dependence of the refractive index for a specific wavelength in vacuum is calculated with Equation 5.12. It equals the integrated refractive index temperature dependence equation in Advanced Optics (2016) and it describes the change of refractive index $\Delta n_{abs}(\lambda, T)$ relative to the refractive index at reference temperature T_{ref}. The parameters D_0, D_1, D_2, E_0, E_1, and λ_{TK}^2 are provided by the glass manufacturer.

$$\Delta n_{abs}(\lambda, T) = \frac{n^2(\lambda, T_{ref}) - 1}{2n(\lambda, T_{ref})} C(T) \tag{5.12}$$

$$C(T) = \left(D_0 \Delta T + D_1 \Delta T^2 + D_2 \Delta T^3 + \frac{E_0 \Delta T + E_1 \Delta T^2}{\lambda^2 - \lambda_{TK}^2} \right) \tag{5.13}$$

The temperature dependent refractive index $n(T, \lambda) = n(\lambda) + \Delta n_{abs}(\lambda, T)$ at the design Littrow wavelength λ_L is used in Equation 5.6 to calculate the temperature dependent Littrow angle and the Littrow wavenumber. Figure 5.12 shows the temperature dependence of the Littrow wavenumber on the refractive index change for the three glasses F-Silica, N-SF11, and N-BK7. The reference temperature of $293\,\mathrm{K}$ corresponds to a Littrow wavenumber of $13\,127\,\mathrm{cm}^{-1}$ and the temperature varies between $263.15\,\mathrm{K}$ and $323.15\,\mathrm{K}$. The glass F-Silica changes the Littrow wavenumber by more than $4\,\mathrm{cm}^{-1}$ in either direction within the temperature range. Whereas, the temperature dependence of N-BK7 and N-SF11 is lower with about a $0.5\,\mathrm{cm}^{-1}$ change in either direction.

All glasses in the SCHOTT and INFARED optical glass catalogs, that are shipped with ZEMAX, are analyzed by calculating the SHS properties for each glass type with the default values for Littrow wavenumber, grating groove density, and diffraction order. Then, the Littrow wavenumber temperature dependence analysis is performed for each SHS design individually and the resulting curve is approximated with a linear fit. Routines from the program ZEMAXGlass v.1.0 (Hagen, 2014) are utilized for reading data from the glass catalogs.

Figure 5.13 shows the gradients of the linear fits for all glasses. They are plotted against the refractive index of the field-widening prism glass, as it qualifies as performance indicator for the SHS. The higher the refractive index, the smaller the apex angle of the field-widening prism and the lower the optical aberrations. Thus, the figure helps in the selection process of the optimal field-widening glass by selecting a glass with low temperature gradient and high refractive index. However, it only shows the refractive index temperature dependence. The selection of a prism glass with near zero Littrow wavenumber temperature gradient might not be optimal in other aspects. The glass N-SF11 is marked in the figure due to its importance in the temperature stabilization Chapter 5.2.4.5.
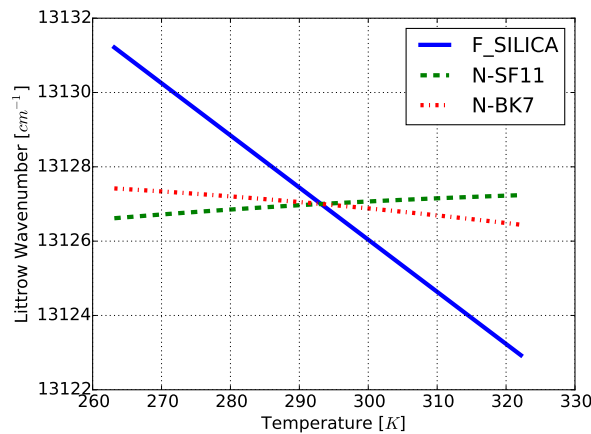
Figure 5.12.: Littrow wavenumber $[\mathrm{cm}^{-1}]$ in dependence of temperature [K] for refractive index change of the glasses F-Silica, N-SF11, and N-BK7.
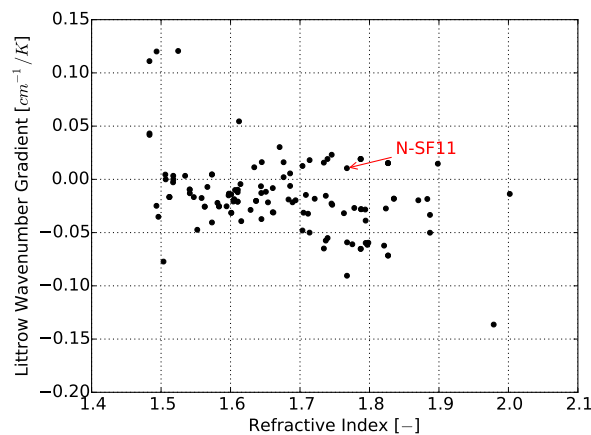
Figure 5.13.: Littrow wavenumber gradient $[\mathrm{cm}^{-1}/\mathrm{K}]$ due to refractive index temperature dependence versus refractive index [-] for all standard and preferred glasses in the SCHOTT optical glass catalog. The maximum standard deviation of the Littrow wavenumber gradient fits of all glasses is $4 \times 10^{-4}\,\mathrm{cm}^{-1}/\mathrm{K}$.

5.2.4.2. Influence of Grating Groove Density Temperature Dependence

The second analysis aspect investigates the grating groove density change due to thermal expansion. The example spectrometer design contains two gratings with a groove density of $1200\,\text{lines/mm}$. A decrease in grating groove density of $1\,\%$ decreases the Littrow wavenumber also by $1\,\%$, as directly visible from Equation 5.7. With increasing temperature, the grating glass expands and the grating height changes relatively by $\delta d > 0$, Equation 5.14.

$$1 + \delta d = \frac{\frac{d}{\cos(\eta+\alpha-\beta)} + \alpha_T \Delta T \frac{d}{\cos(\eta+\alpha-\beta)}}{\frac{d}{\cos(\eta+\alpha-\beta)}} = 1 + \alpha_T \Delta T \tag{5.14}$$

In the equation, d describes the image height perpendicular to the optical axis. The grating height h is calculated by dividing the field height with the cosine of the grating angle $(\eta + \alpha - \beta)$. The linear thermal expansion coefficient of the grating glass is defined by α_T. The temperature expansion is modeled that the upper edge of the grating is displaced by $\Delta = 0.5\alpha_T \Delta T h$ and the lower edge by the same amount but in the opposite direction. The model assumes that the displacement equals zero at the center of the grating and that the SHS expands symmetrically. Section 5.2.4.4 shows that this assumption is approximately valid. A positive temperature difference ΔT increases the grating height. Hence, the number of lines per length decreases, see Equation 5.15.

$$\left(\frac{1}{d}(T)\right) = \frac{\left(\frac{1}{d}\right)(T_{ref})}{1 + \delta d} \tag{5.15}$$

The temperature dependence of the grating groove density is used in Equation 5.7 to calculate the Littrow wavenumber change. For the remainder of the analysis, it is assumed that the glass of the gratings is the same as the glass of the spacers 2 or at least that their thermal expansion coefficients are similar enough to approximate the grating expansion with the spacer 2 expansion.

Figure 5.14 shows the gradient of the Littrow wavenumber temperature dependence over a temperature range of $\pm 30\,\text{K}$ around the reference temperature versus refraction index of the grating glass for all standard and preferred glasses in the INFRARED glass catalog. The refractive index of the gratings has no influence on the optical SHS performance. However, it provides an intuitive glass sorting. The gradient is negative for all glasses, because of the positive thermal expansion coefficient α_T. The glass F-Silica is marked due to its importance in the temperature stabilization Chapter 5.2.4.5.
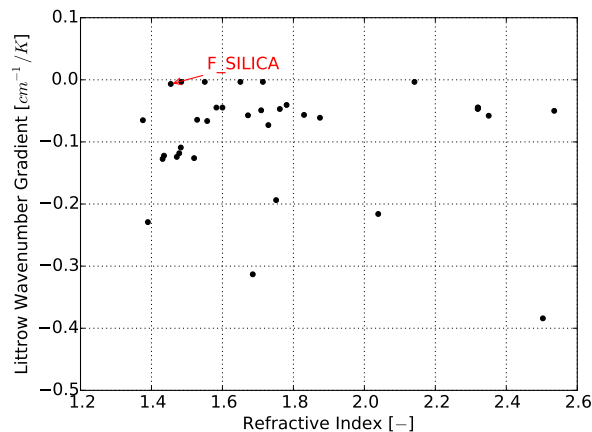
Figure 5.14.: Littrow wavenumber gradient $[\text{cm}^{-1}/\text{K}]$ due to grating groove density temperature dependence versus refractive index [-] for glasses from the INFRARED optical glass catalog. The maximum Littrow wavenumber temperature gradient standard deviation of fits of all glasses is smaller than $3 \times 10^{-5}\,\text{cm}^{-1}/\text{K}$.

5.2.4.3. Influence of Thermal Expansion on Element Angle Change

All elements of the SHS are influenced by thermal expansion. The size of the beam splitter and the center distances of the arms elements have no influence on the Littrow wavenumber, according to Chapter

5.2.1.3. Thus, changes of these properties can be neglected. However, the element angles depend on the temperature in general and change the Littrow wavenumber, which is analyzed in the following. Thereby, only a single arm is considered, as both arms of an SHS are identical.

The change of the angle of, for example, spacer 1 can be approximated with a linear model. The change of angle β is described by the displacement in x-, and y-direction of two prism corners (B, C) to (B', C'), as in figure 5.15. The other two corners (A,D) and the side in between them (d) are held fixed, as the change in apex angle is fully described by considering one side of the prism. The displacement in x-direction is u_1 and in y-direction it is v_1 for corner C. The corner B side is displaced by u_2 in x-direction and v_2 in y-direction.
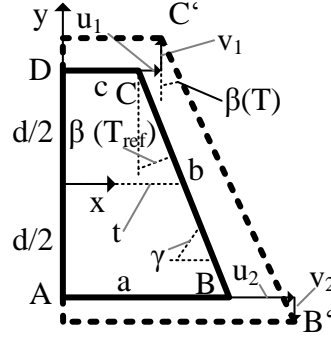
Figure 5.15.: Schematic of the deformation of the spacer 1 element.

Equation 5.16 is derived through basic geometric calculus, for details consult the Appendix C.4. It describes how the prism angle $\beta(T)$ depends on the undeformed angle $\beta(T_{ref})$ at reference temperature T_{ref}, the temperature dependent displacements (u, v), and the height of the prism d. The equation represents an identity transformation for zero displacements, as expected.

$$\beta(T) = \frac{\pi}{2} - \arctan\left(\frac{d - (v_2(T) - v_1(T))}{d\tan\beta(T_{ref}) + u_2(T) - u_1(T)}\right) \tag{5.16}$$

The displacements can either be provided by a numerical simulation or approximated by analytic expressions. For the analytic approximation applies: In x-direction, both corners (B, C) expand proportional to the edge lengths to the fixed corners. The difference in length between short (c) and long (a) edge effectively changes the prism angle. This can be described by $u_2(T) - u_1(T) = \alpha_T \Delta T d \tan\beta$, with α_T as linear thermal expansion coefficient, $\Delta T = T - T_{ref}$ as the temperature difference to reference temperature and $d\tan\beta$ as the difference in edge length. Similarly in y-direction, the displacement of the upper corner C is deduced to $v_1(T) = \alpha\Delta T 0.5d$ and for the lower corner B, it is expressed by $v_2(T) = -\alpha_T\Delta T 0.5d$. Only half of the height is used, because the displacement approximately equals zero in y-direction in the middle of the prism. This assumption is also confirmed by the numerical simulation, described in Chapter 5.2.4.4. Equation 5.17 results by replacing the displacements in Equation 5.16 with their analytical temperature dependent expressions. As expected, the apex angle of the prism is not changing in dependence of temperature. However in a real instrument, the mounting of the SHS and the use of different materials influence the deformation. Their influence is discussed in the next chapter.

$$\beta(T) = \frac{\pi}{2} - \arctan\left(\frac{d + \alpha_T\Delta T d}{d\tan\beta + \alpha_T\Delta T d\tan\beta}\right) \overset{\beta\in[0,\frac{\pi}{2}]}{=} \beta \tag{5.17}$$

5.2.4.4. Numerical Simulation of the Spectrometer

The numerical simulation of an example spectrometer shall demonstrate that the analytical model approximates a more detailed model of reality. Therefore, a Finite Element Method (FEM) analysis is performed in Autodesk Simulation Mechanical 2016, based on an Autodesk Inventor Professional 2016 model of the SHS. The beamsplitter has an edge length of 18 mm by 18 mm with a depth of 27 mm. It is made out of N-BK7. The spacers 1 and the field-widening prisms are made out of N-SF11. Spacer 2 and the gratings consist of F-Silica. This particular glass selection is further discussed in Chapter 5.2.4.5 regarding temperature stabilization. The SHS is connected at front and back face to its aluminum housing

with a $1\,\mathrm{mm}$ thick silicone layer, which is also modeled with a low elastic modulus of $30\,\mathrm{N\,mm^{-2}}$ and an assumed Poisson's ratio of 0.3. Overall, the model consists of twelve parts, which have bonded contacts between them.

A static stress analysis is performed with a linear material model. These material models are based on data from the glass catalogs. The model consists of 222k nodes and 52k elements in a mix of hexahedra, wedges, pyramids, and tetrahedra with quadratic element and fourth order integration formulation. Structural loads are not applied to the model. However, deformations are simulated by deviating from the stress free reference temperature of $293.15\,\mathrm{K}$. Each temperature deviation is described by a separate load case. Overall, 17 load cases approximate the change in deformation for temperature differences between $-40\,\mathrm{K}$ to $40\,\mathrm{K}$ from the reference temperature.

Figure 5.16 shows the meshed simulation model in its reference coordinate system. The green color in the front face of the beam splitter silicone layer symbolizes a constraint of the model. A similar constraint is applied at the back face of the beam splitter silicone layer. There, all six degrees of freedom (three translations and three rotations) are constrained. On the front face, also all degrees of freedom are fixed, except the translation in y-direction. The additional degree of freedom simulates a mounting of the SHS, which reduces deformations in x- and z-direction by allowing deformations in y-direction. This is possible as deformations in y-direction have no influence on instrument performance. The arms are free from constraints to reduce stresses and, thus, possible stress birefringence.
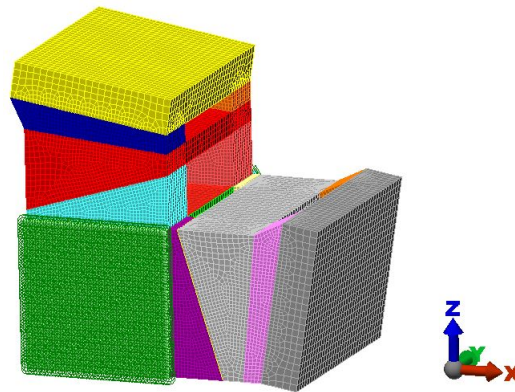
Figure 5.16.: Structural model of the example Spatial Heterodyne Spectrometer (SHS). Its mesh consists of approximately 222k nodes and 52k quadratic elements (mix of hexahedra, wedges, pyramids, and tetrahedra) for linear stress analysis. The silicone layer at the back face of the beam splitter is fixed. Similar, the silicone layer at the front face of the beam splitter is fixed except in y-direction.

An example result for a temperature deviation of $+20\,\mathrm{K}$ from reference temperature is presented in Figure 5.17. It shows the displacements in x-direction in a cut through the SHS center. The color red corresponds to maximum deformation ($4.5\,\mathrm{\mu m}$). Similarly, the minimum deformation (blue) calculates to $-1.7\,\mathrm{\mu m}$. Zero deformation exists at the transition from green to light blue. The inherent symmetry of the SHS allows to qualitatively view the displacements in z-direction by mentally rotating the picture. It shows that the assumption of zero deformation in the middle of the arm height is approximately correct, as assumed in the analytical model. The figure magnifies the actual deformations by a factor of 300.

The FEM software simulation is not capable of calculating the Littrow wavenumber temperature dependence. To compare the element angle changes, the displacements of eight nodes are monitored for each load case. The displacements in x- and z-direction are used to calculate the temperature dependent angles and thus the Littrow wavenumber temperature dependence in Equation 5.16. The eight nodes are located in the middle of the spectrometer in depth direction (y-direction). Always two nodes sit on the outer surfaces of beam splitter, field-widening prism, and grating, respectively. These pairs are $10\,\mathrm{mm}$ apart in height in the undeformed state. Only one arm is considered due to the instrument symmetry. Figure 5.17 shows the eight nodes with purple points.
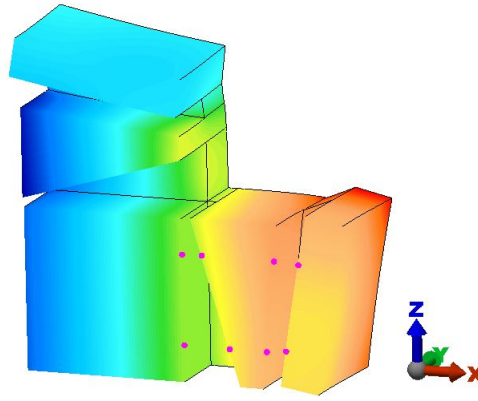
Figure 5.17.: Deformation in x-direction for a temperature difference of $+20\,\mathrm{K}$ to the reference temperature. The deformation is scaled by a factor of 300. The maximum deformation (red) is $4.5\,\mu\mathrm{m}$ and the minimum deformation (blue) is $-1.7\,\mu\mathrm{m}$. The green to blue color transition corresponds to zero deformation.

Equations 5.6 and 5.7 are used to calculate the Littrow wavenumber from the node displacements. To estimate the error of the analytical model, the temperature dependence of the element angles is compared with the reference angle. This comparison is shown in Figure 5.18, where the relative errors between numerically calculated element angles and reference element angles are shown for spacer 1, prism, and spacer 2 as a function of temperature.
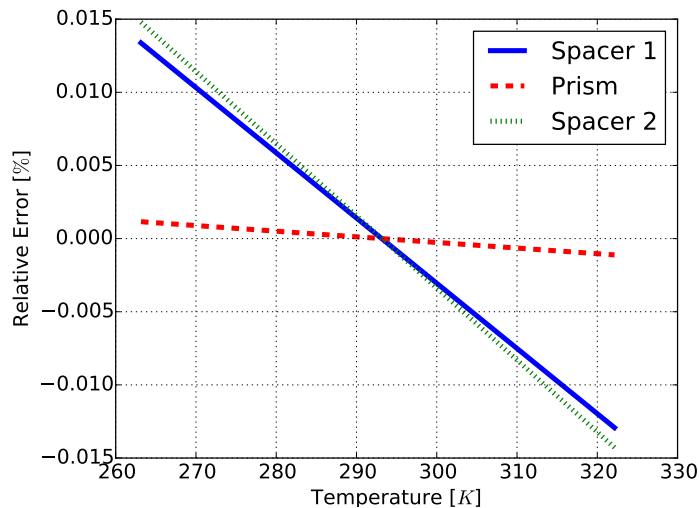
Figure 5.18.: Relative element angle errors [%] of spacer 1 (solid), field-widening prism (dashed) and spacer 2 (dotted) in dependence of temperature [K] for the numerical simulation relative to reference angles.

The errors of the temperature dependence gradients between analytical model and numerical simulation are summarized in Table 5.1 for the three elements and also for the resulting Littrow wavenumber gradient. The Table 5.1 and the Figure 5.18 show that the changes in element angles are very small, however not negligible for extremely precise temperature stabilization. Actually, the Littrow wavenumber change is dominated by the thermal expansion for an analytically optimized SHS, which will be discussed in the following chapter.

Table 5.1.: Absolute error in temperature gradient for the spacer 1, prism, and spacer 2 angles and the resulting Littrow wavenumber temperature gradient error.

	Absolute error in temperature gradient $[°/K; cm^{-1}/K]$
Spacer 1 Angle	$9.1 \cdot 10^{-5}$
Prism Angle	$8.7 \cdot 10^{-6}$
Spacer 2 Angle	$3.4 \cdot 10^{-5}$
Littrow Wavenumber	$1.8 \cdot 10^{-2}$

5.2.4.5. Temperature Stabilization

Temperature stabilization of an SHS becomes possible by selecting an optimal glass combination of spacer 1, field-widening prism, spacer 2, and grating, as already mentioned above. In the following, combinations of glasses in the SCHOTT optical glass catalog are evaluated. Overall, 120 glasses are used, which are all standard and preferred glasses in the catalog. The spacer 1/ prism and spacer 2/ grating glasses are assumed to be identical, which leaves overall 120^2 possible combinations. Since numerical simulation of all of these combinations costs too much computation time, the analytical model is chosen for the optimization.

The optimal glass combination is distinguished by a low Littrow wavenumber temperature dependence and a large refractive index of the field-widening prism. The gradient $\frac{d\sigma_L}{dT}$ should ideally be zero and the refractive index as large as possible. The glass combinations are compared by ranking Equation 5.18. It describes an ellipsoid where the z-dimension represents the ranking value χ. The other two dimensions are the refractive index and the gradient $\frac{d\sigma_L}{dT}$. The ellipse that results in cutting the ellipsoid with the x-y-plane has its center at zero gradient and at the maximum refractive index of all evaluated glasses. Thus, the best ranking value would be given to a glass combination with highest refractive index for the field-widening prism and zero Littrow wavenumber temperature gradient. The semi-major and semi-minor axis are scaled such that glasses with the lowest prism refractive index can have a ranking value unequal to zero and that glass combinations above a certain gradient $\left(\frac{d\sigma_L}{dT}\right)_{max}$ are excluded from the ranking. For these glass combinations, the ranking value χ becomes imaginary and, thus, set to zero.

$$\chi = 10^2 \sqrt{1 - \left(\left(\frac{n_{max} - n}{n_{max} - 0.95 n_{min}} \right)^2 + \left(\frac{\frac{d\sigma_L}{dT}}{\left(\frac{d\sigma_L}{dT} \right)_{max}} \right)^2 \right)} \tag{5.18}$$

Figure 5.19 provides an overview over the performance of all possible combinations for the SCHOTT/ INFRARED glass catalogs. The Littrow wavenumber temperature gradient in $\mathrm{cm}^{-1}/\mathrm{K}$ is shown in dependence of refractive index of the field-widening prism. The glasses of spacer 2/ grating are reflected in the vertical distribution of points for a specific prism glass. The graph shows that the gradient lies approximately between $-0.5\,\mathrm{cm}^{-1}/\mathrm{K}$ and $0.5\,\mathrm{cm}^{-1}/\mathrm{K}$. The red, dashed ellipse section represents the area in which the glass combination ranking value χ exceeds zero. Its center lies at a refractive index of approximately 2.35 and the maximum allowable absolute temperature gradient is specified to $\left| \left(\frac{d\sigma_L}{dT} \right)_{max} \right| = 0.03\,\mathrm{cm}^{-1}/\mathrm{K}$.
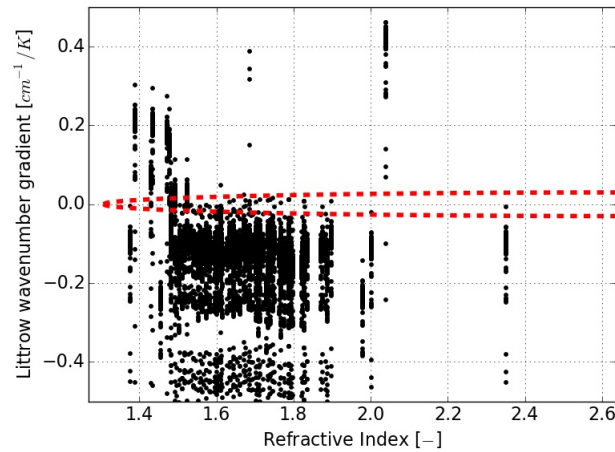
Figure 5.19.: Temperature stability evaluation of all 120^2 possible combinations of standard and preferred glasses in the SCHOTT/ INFRARED optical glass catalog. The change in Littrow wavenumber $[\mathrm{cm}^{-1}/\mathrm{K}]$ is shown in dependence of refractive index of the field-widening prism. The maximum standard deviation of the Littrow wavenumber temperature gradient of all glass combination fits is $4 \times 10^{-4}\,\mathrm{cm}^{-1}/\mathrm{K}$. The red dashed ellipse shows the area in which the ranking is unequal to zero. The ranking value increases with decreasing distance of the glass combination value from the center point of the ellipse.

Most of the combinations do not lie within the acceptable glass combination space when considering only the SCHOTT glass catalog. However, the best eight glasses are presented in Table 5.2 with prism and grating glass, refractive index of the prism, and Littrow wavenumber gradient. For further analysis, the combination **C5** is selected as best glass combination for temperature stabilization, because of the lowest Littrow wavenumber temperature dependence and still a high refractive index. The grating glass was already restricted to F-Silica, because this glass is well known to grating manufacturers.

Table 5.2.: Optimal glass combinations for all standard and preferred glasses in the SCHOTT/ INFRARED glass catalogs based on the implemented ranking system for the SHS temperature stabilization with the analytical model and restricting the grating glass to F-Silica.

	Prism	Grating	Index [-]	$\frac{\partial \sigma_L}{\partial T}\ [cm^{-1}/K]$
C1	SRTIO3	F-SILICA	2.35	-0.0067
C2	IRG2	F-SILICA	1.87	-0.0067
C3	N-SF66	F-SILICA	1.90	0.0080
C4	IRG3	F-SILICA	1.83	-0.0067
C5	N-SF11	F-SILICA	1.77	0.0038
C6	N-SF57HTultra	F-SILICA	1.83	0.0085
C7	N-SF57	F-SILICA	1.83	0.0085
C8	N-SF57HT	F-SILICA	1.83	0.0085

For the optimal glass combination **C5**, the maximum and minimum Littrow wavenumbers calculate to $13\,127.04\,\mathrm{cm}^{-1}$ and $13\,126.82\,\mathrm{cm}^{-1}$ (Numerical model: $13\,127.36\,\mathrm{cm}^{-1}$ and $13\,126.52\,\mathrm{cm}^{-1}$) for a temperature range of $\pm 30\,\mathrm{K}$. Thus, the spectrometer design can be described as temperature stabilized. Figure 5.20 shows the Littrow wavenumber in dependence of temperature. The graph distinguishes between total change, independent element thermal expansion contributions from the numerical simulation, grating groove density variations, and field-widening prism refractive index change. The negative gradient of the grating groove density temperature dependence is balanced with the positive gradient of the refractive index temperature dependence of field-widening prism. However, the thermal deformations of the arm elements have large influence on the temperature stability. Including thermal deformations, the Littrow wavenumber dependence increases by an order of magnitude. This Littrow wavenumber gradient is probably still suitable for most applications, but too high for extremely precise temperature stabilization. The difference between analytical and numerical model stems mostly from spacer 1 and spacer 2 deformation. A numerical simulation of a SHS with solid spacer elements showed that the Littrow wavenumber gradient reduces by a factor of approximately 2. However, this cannot explain the

major part of the deviation from the analytical model. It is concluded that the difference in thermal expansion coefficients between the glass types and the mounting of the SHS are the major factors of uncertainty in the model. To account for these effects, each glass combination would need to be modeled and simulated in an FEM tool, which is time consuming. For example the solution space would span 120^3 combinations for the SCHOTT/ INFRARED glass catalogs and a detailed simulation takes at least ten minutes, taking overall about 200 days.
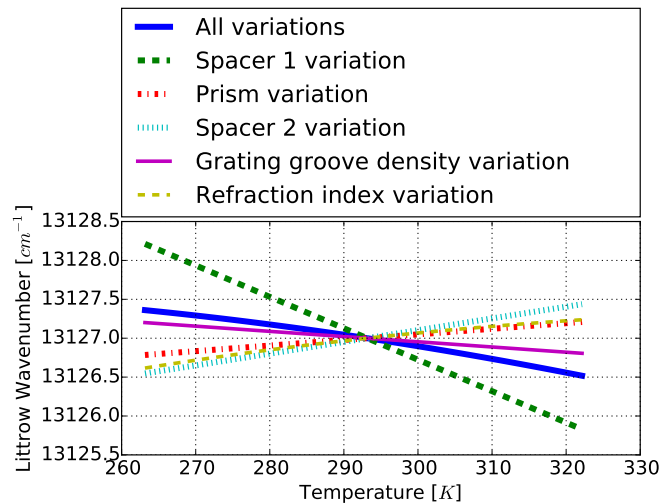
Figure 5.20.: Littrow wavenumber $[\text{cm}^{-1}]$ in dependence of temperature [K] for an optimal spacer 1, field-widening prism, and spacer 2/ grating glass combination **C5**. Results from the numerical simulation are used to describe the arm element deformations.

So far, the analysis in this work has only considered glasses from the SCHOTT/ INFRARED glass catalogs. Including other glass catalogs, for example the OHARA catalog, the optimization space increases further and allows the selection of additional well suited glass combinations. For example, the glass combination of OHARA S-PHM52 for spacer 1/ prism glass and LAFN7 for spacer 2/ grating also temperature stabilizes the SHS, with similar refractive index for the field-widening prism, but with an even lower temperature gradient using the analytic deformation formulation. Overall, many combinations exist that are suitable for temperature stabilization. Hence, it is possible to base the final decision on glass combination selection on other requirements, like manufacturability. For example, it was already done for Table 5.2 by restricting the grating glass to F-Silica.

This chapter addressed the problem of how to temperature stabilize the SHS by minimizing the Littrow wavenumber temperature gradient. But, Figure 5.19 shows also glass combinations that allow to quite considerably tune the Littrow wavenumber with up to $0.5\,\text{cm}^{-1}/\text{K}$ by changing the temperature. This property makes it possible to scan through a larger spectral region compared to a basic SHS or to measure multiple separate atmospheric emission bands.

5.2.4.6. Conclusion

Temperature stabilization is achieved if the Littrow wavenumber temperature dependence lies within an acceptable range for the particular application. Ideally, it equals zero. Then, the spatial frequencies of relevant spectral lines are detectable for a wide temperature range. The Littrow wavenumber temperature gradient depends on the refractive index temperature dependence of the field-widening prism, the grating groove density change, and the arm element angle changes due to thermal expansion.

An analytical model was developed to simulate all these dependencies to predict the Littrow wavenumber temperature dependence. With this model, all standard and preferred glasses in the SCHOTT glass catalog were evaluated and compared against each other. This design was also simulated with a thermal-structural Finite Element Method (FEM) analysis. It showed that the influence of differing thermal expansion coefficients and of the SHS mounting influence the deformations in the sub-permille level, which in turn increases the Littrow wavenumber gradient to an order of magnitude of $10^{-2}\,\text{cm}^{-1}/\text{K}$ for a temperature stabilized SHS. Lower temperature gradients can only be achieved by a very time-consuming coupled SHS temperature and FEM structural-thermal analysis for a large number of glass combinations.

The temperature stabilization analysis was performed based on the analytical model and showed that there are many glass combinations within the SCHOTT/ INFRARED glass catalogs to temperature stabilize the SHS. Finally, the glasses N-SF11 for spacer 1/ field-widening prism and F-Silica for spacer 2/ grating have been selected.

5.2.5. Aliasing and Filter Effects

Emission lines on both sides of the Littrow wavenumber can have similar spatial frequencies, as already discussed in Chapter 5.2.2. The peaks in the spectrum may interfere with each other and reduce the temperature retrieval precision especially if the intensity of one emission line is not well characterized. This holds typically true for lines in the filter edges, because the edge position is dependent on the filter temperature and only a small temperature measurement error of the filter temperature changes already significantly the transmissivity in the filter edge.

In this SHS design, the relevant emission lines lie below of the Littrow wavenumber in the wavenumber domain. Thus, the SHS should be designed that the emission lines with higher wavenumbers do not alias with the relevant emission lines. This can be achieved by using a filter with a narrow bandpass and by adjusting the Littrow wavenumber.

Figure 5.21 shows the transmission of all emission lines through the filter and an ideal SHS in dependence of spatial frequency. In addition, the filter function, transformed into the spatial frequency domain, is plotted with a dotted line.

The aliasing effect of the SHS can be seen by the filter function close to zero spatial frequency. The filter is broad enough that the theoretical transmission is approximately 10% for zero spatial frequency, which corresponds exactly with an emission wavenumber equal to the Littrow wavenumber. Transmission values lower than approximately 10% influence emission lines right of the Littrow wavenumber (essentially negative spatial frequencies). However, these lines are aliased into the positive spatial frequencies. It shows in the filter function as a knee where it is mirrored into the positive spatial frequency domain at zero spatial frequency.

The emission lines are scaled by the strongest emission line in Figure 5.21. The six red colored emission lines are the relevant emission lines that are used to retrieve the atmospheric temperatures. Thus, other emission lines should not alias into the spatial frequency region of these lines. Another important aspect is that emission lines with higher spatial frequencies should also be resolved by the Fourier-transformation. Otherwise, "traditional" aliasing appears and reduces the temperature measurement precision. Figure 5.21 shows for example that the highest resolvable spatial frequency should be above approximately $140\,\mathrm{cm}^{-1}$.
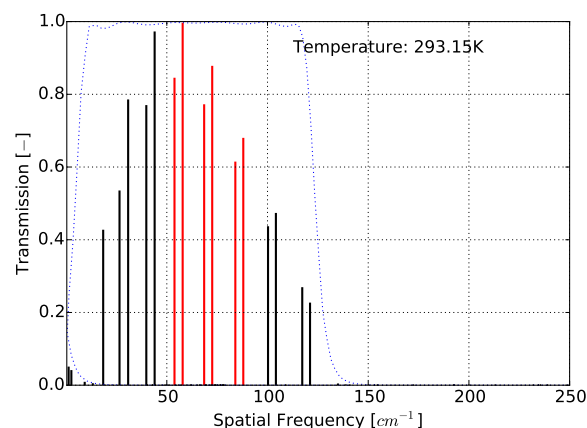
Figure 5.21.: Aliasing and filter effects analysis showing the relative transmission [-] for all emission lines in dependence of spatial frequency $[\mathrm{cm}^{-1}]$ and the filter function (dotted line), projected into the spatial frequency domain for an instrument temperature of $20\,\mathrm{°C}$. The six red emission lines are the relevant lines for temperature retrieval. The temperature value describes the filter and the SHS temperature.

The analysis can be extended by including the aspect of instrument temperature. Both, the filter center wavelength and the Littrow wavenumber exhibit temperature dependencies. Through the filter center wavenumber shift, the relevant emission lines can get into the filter edges. Their relative intensities to each other are then strongly dependent on the filter transmissivity and thus on the filter temperature.

To minimize this dependency, it is desirable to keep the relevant emission lines within the plateau of the filter for the whole temperature range. The Littrow wavenumber temperature dependence needs to be considered as well, because the spatial frequencies of the emission lines change with the Littrow wavenumber. Figures 5.22a and 5.22b show the aliasing analysis for the maximum and minimum operating temperatures. Together with the previous Figure 5.21, these plots show that the six relevant emission lines are not aliased by other emission lines in the whole temperature range and that they stay within the plateau of the filter function.
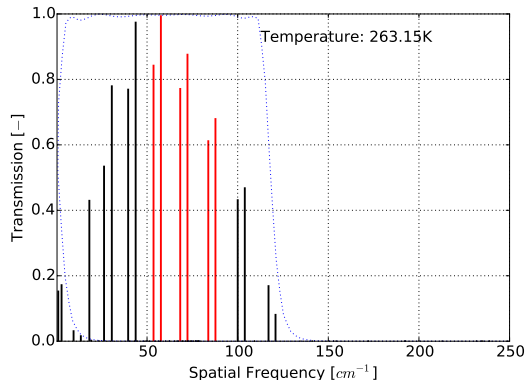
(a) Similar to Figure 5.21 but for an instrument temperature of $-10\,^\circ\mathrm{C}$.
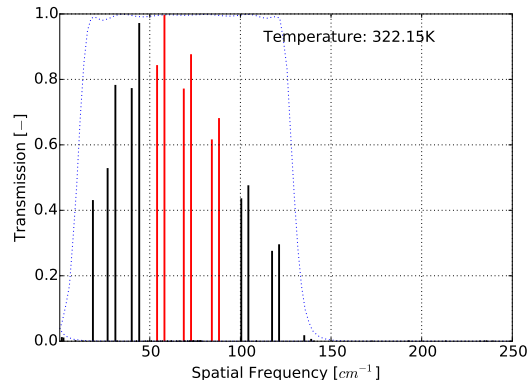
(b) Similar to Figure 5.21 but for an instrument temperature of $50\,^\circ\mathrm{C}$.

5.2.6. SHS Tolerancing

This chapter describes the tolerance assessment of the SHS. Manufacturing tolerances influence the Littrow wavenumber and the field-widening performance of the SHS. This analysis is based on the vacuum conditions in space. The reference temperature is 293.15 K and it is assumed that the temperature of the filter and of the SHS are equal.

5.2.6.1. Influence of Tolerances on Littrow Wavenumber

The Littrow wavenumber can be calculated with Equations 5.6 and 5.7 from the SHS element angles, α, β, and η, the diffraction order m, and the grating groove density $1/d$, as discussed in Chapters 5.2.3 and 5.2.4. Thereby, the element angles correspond to the field-widening prism, spacer 1, and spacer 2 angles, respectively.

All angles have tolerances and also the refractive index of the field-widening prism differs from the nominal design value (absolute error) and varies within the glass (refractive index inhomogeneity). The refractive index inhomogeneity locally varies the Littrow wavenumber over the pupil. However, this variation is an order of magnitude smaller than the absolute refractive index and thus has only minor influence (Advanced Optics, 2004). In addition, the grating groove density is manufactured with a certain tolerance and the grooves may be tilted by a certain angle relative to the reference surface. This essentially changes the grating groove density with the cosine of the tilt angle. For this analysis, it is assumed that all tolerance values, except the grating groove density tolerance, describe three times the standard deviation (3σ) of a normal distribution. For the grating groove density tolerance, a 6σ tolerance is used. The analysis is performed with a Monte-Carlo analysis by randomly varying the element angles, the refractive index, the grating groove density, and the grating groove tilt and considering their influence on the Littrow wavenumber. The element angle errors include the element angle manufacturing error and also the error due to bond line thickness variations.

Table 5.3 shows the influence of the element angles and the refractive index with considering each tolerance separately. The relation between Littrow wavenumber error (3σ) and element tolerance is linear in the relevant range and, therefore, only the slopes with the fit errors are stated. The influence of the grating groove tilt tolerance on Littrow wavenumber is non-linear in the relevant range. Figure 5.23 shows this relation.

Table 5.3.: Littrow wavenumber error (3σ) in dependence of element tolerance (3σ, angles and refractive index).

Element	Slope linear fit	Standard deviation (1σ) linear fit
Spacer 1	$7.7 \times 10^{-2}\,\mathrm{cm^{-1}/arcsec}$	$2 \times 10^{-4}\,\mathrm{cm^{-1}/arcsec}$
Prism	$1.4 \times 10^{-1}\,\mathrm{cm^{-1}/arcsec}$	$3 \times 10^{-4}\,\mathrm{cm^{-1}/arcsec}$
Spacer 2	$7.5 \times 10^{-2}\,\mathrm{cm^{-1}/arcsec}$	$1 \times 10^{-4}\,\mathrm{cm^{-1}/arcsec}$
Refractive Index	$6.5 \times 10^{3}\,\mathrm{cm^{-1}}$	$1 \times 10^{1}\,\mathrm{cm^{-1}}$
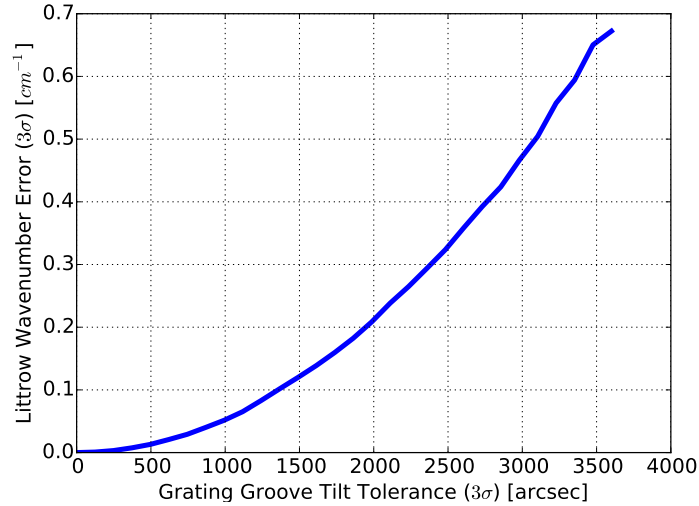
Figure 5.23.: Littrow wavenumber error (3σ) in [$\mathrm{cm^{-1}}$] in dependence of grating groove tilt tolerance (3σ) in [arcsec].

The table and the graph show only the independent errors that provide a good understanding of the sensitivity of the Littrow wavenumber to the individual tolerances. For example, the field-widening prism angle has stronger influence than the spacer element angles. However, the combined analysis of these error provides more precise estimations of the actually expected deviations. This is especially important for the grating groove density and tilt error, as these magnify the influence on Littrow wavenumber for the other errors, refer to Equation 5.7.

Figure 5.24 shows the probability [%] for a specific Littrow wavenumber error [cm^{-1}] with assuming the following manufacturing and assembly tolerances:

- Element angle tolerances (3σ): $15''$
- Index of refraction tolerance (3σ): 3×10^{-5}
- Grating groove density (6σ): $0.05\,\%$
- Grating groove tilt tolerance (3σ): $20'$
- Bond line thickness tolerance (3σ): $11.7''$

The requirement of achieving a maximum allowable Littrow wavenumber lower than $6\,\mathrm{cm^{-1}}$ is fulfilled with almost $100\,\%$ probability.
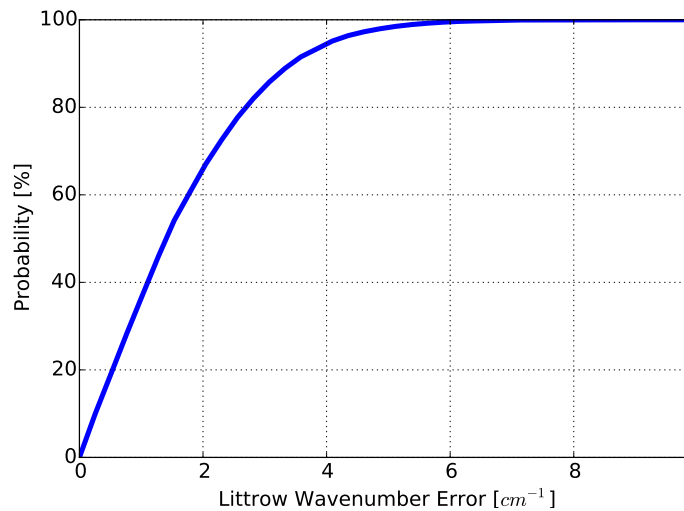
Figure 5.24.: Probability [%] of a maximum Littrow wavenumber error [cm^{-1}].

5.2.6.2. Influence of Tolerances on Field-widening Performance

In addition to the influence of tolerances on the Littrow wavenumber, the tolerances also influence the field-widening performance of the SHS. Its analysis is performed on the model from Chapter 5.2.1.3 with ZEMAX OpticStudio and is divided into the following steps:

1. Tolerances are applied to the undisturbed model.
2. The distance between fore-optics (ideal lens) and SHS acts as compensator to achieve optimal focus on the grating.
3. The distance to the localization plane acts as compensator to achieve optimal OPD at the image.
4. The image RMS OPD is evaluated for five fields as tolerance metric.

The following parameters are considered in the tolerance analysis:

- Distances:
    - Beamsplitter all sides
    - Spacer 1
    - Field-widening prism
    - Spacer 2
- Angles (X, Y):
    - Beamsplitter input
    - Beamsplitter splitting surface
    - Beamsplitter exit
    - Spacer 1
    - Field-widening prism
    - Spacer 2

- Index of Refraction:
    - Beamsplitter (both parts separate)
    - Field-Widening prism
- Abbe Number:
    - Beamsplitter (both parts separate)
    - Field-widening prism
- Surface Irregularity:
    - Beamsplitter (input, exit)
    - Field-widening prism (input, exit)

A few other errors are not directly considered in the tolerance analysis and are addressed in the following: The striae class of the glass materials is the standard SCHOTT manufacturing tolerance, which means that the wavefront deviation is smaller than 30 nm for a thickness of 50 mm. The striae are directly proportional to the glass thickness. With a prism thickness of 6 mm, the resulting striae is smaller than 4 nm. It is acceptable for the application, as it corresponds to 5×10^{-3} wavelengths. Similarly for the beamsplitter, the striae results in an OPD of 10.8 nm, which corresponds to 14×10^{-3} wavelengths. Stress birefringence is lower than 10 nm cm^{-1} for the selected glass materials. Thus, the stress birefringence in the field-widening prism is below 6 nm and about 18 nm for the beamsplitter. These imperfections result in acceptable OPD errors below 24×10^{-3} wavelengths and 8×10^{-3} wavelengths, respectively.

The tolerance analysis is performed with two methods. The Root-Sum-Square method calculates the sensitivity for each parameter separately and assumes a Gaussian distribution to calculate the estimated

change. The resulting performance metric shows that the RMS wavefront error increases to approximately 0.16 wavelengths from 0.13 wavelengths. Thereby, the worst offenders are the refractive index tolerances of the beamsplitter parts. However, these results are very conservative, because the beamsplitter parts will be aligned to each other that the actual error is minimized. Thus, the errors due to beamsplitter manufacturing tolerances should be much smaller than assumed in this analysis. Even with these tolerances, the estimated wavefront error is still acceptable. A summary of the results is provided in Table 5.4.

Table 5.4.: Estimated performance of SHS based upon the Root-Sum-Square tolerance analysis method.

	RMS OPD [wavelengths]
Nominal Wavefront	0.133
Estimated Change	0.023
Estimated Wavefront	0.156

The second method for analysis of the tolerances is based on a Monte-Carlo-Simulation with 100 samples. The mean wavefront error is 0.14 wavelengths with a standard deviation of 0.01 wavelengths. For 90 % of the samples the wavefront error is lower than 0.15 wavelengths. Additional information is provided in Table 5.5.

Table 5.5.: Estimated performance of SHS based upon the Monte-Carlo tolerance analysis method (100 samples).

	RMS OPD [wavelengths]
Nominal Wavefront	0.133
Best Wavefront	0.105
Worst Wavefront	0.160
Mean Wavefront	0.135
Standard Deviation Wavefront	0.012
> 90%	0.145

In the tolerance analysis, two optimization steps are used to reduce the wavefront error. The first compensator changes the distance between fore-optics lens and SHS to have a minimal spot size at the gratings. The second compensator changes the distance to the focal plane. These compensators are also implemented in the actual fore- and detector optics. The maximum adjustment range is $\pm1.00\,\mathrm{mm}$. The compensator statistics for the Monte-Carlo simulation shows that both distances change less than $\pm0.15\,\mathrm{mm}$ (Table 5.6). This is well within the adjustment range.

Table 5.6.: Compensator statistics for the SHS tolerance analysis based upon the Monte-Carlo method.

Compensator	ΔD_{min} [mm]	ΔD_{max} [mm]
SHS distance to image lens	-0.09	0.15
SHS distance to focal plane	-0.09	0.13

Further information about the tolerances can be found in Appendix C.5, where a summary of all properties and tolerances of the SHS is presented.

5.2.7. Optics

5.2.7.1. Fore-Optics

The fore-optics has the function to image the scene in the atmosphere onto the gratings. It consists of four spherical lenses with different glasses to achieve sufficient imaging performance. The most important properties of the fore-optics are stated in Table 5.7. The challenge in designing the fore-optics lies in achieving a long effective focal length to minimize the entrance angle for the SHS and to sustain an acceptable image height on the localization plane, while keeping it as short as possible and with sufficient imaging performance. Hence, the fore-optics has an effective focal length of 273 mm and a length of 128 mm. The back focal length needs also to be large to accompany all elements of the SHS in the optical path.

The fore-optics is shown in Figure 5.25. The first lens surface acts as aperture stop with 66 mm diameter.

All lenses except the last lens are convex-concave. The last lens is planar on its front side. The lenses are designed "bulky" to some degree to sustain the vibration loads during rocket launch. Figure 5.25 shows also field points which span up the image on the localization plane.

Table 5.7.: Optical properties of the fore-optics.

Property	Value	Unit
F/#	4.16	[-]
Effective Focal Length	273	[mm]
Back Focal Length	53.7	[mm]
Entrance Pupil Diameter	66	[mm]
Length	128	[mm]
AR-coating	<0.5	[%]
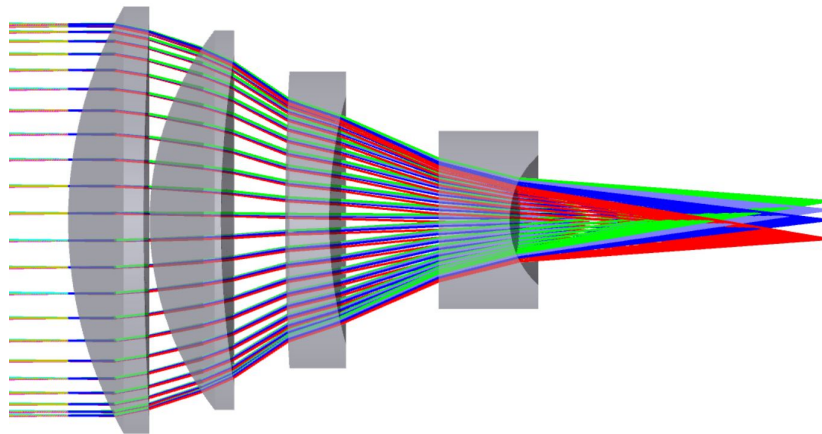
Figure 5.25.: Schematic of the fore-optics with four field points.

The performance requirements on the fore-optics are moderate. It shall distinguish 41 altitude levels over the grating localization plane height of 6.5 mm. Thus, the Modulation Transfer Function (MTF) should be larger than 0.5 for a spatial frequency of approximately 7 cycles/mm. The spectral direction has no specific imaging requirement, because the worse the imaging gets in spectral direction, the more the spectral signatures in horizontal direction are averaged out over the interferogram. Figure 5.26 shows its FFT for three representative field points. For two of the three field-points, the spectral (tangential) and spatial (sagittal) direction fall onto the same line and are therefore not discernible. The modules of the Optical Transfer Function (OTF) is larger than 0.7 for the worst case, which means that different altitude levels are separated.
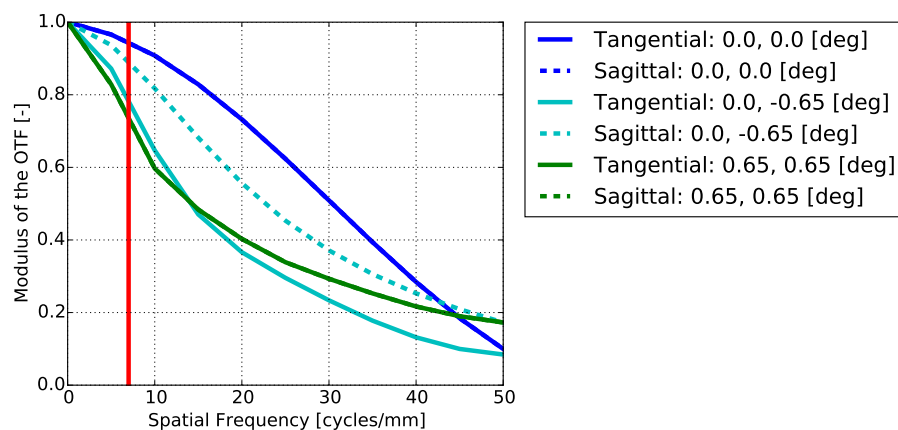
Figure 5.26.: Diffraction MTF of the fore-optics calculated by FFT for three characteristic field points. The red vertical line shows the spatial frequency that corresponds to 41 altitude levels. They can be distinguished if the MTF is larger than 0.5.

5.2.7.2. Detector Optics

The detector optics images the gratings onto the detector. It is a transfer optics with a magnification of 0.6 and an object focal lengths of 16.4 mm. It is a fast system with a F/# of 2.17 and a length of 41 mm. As for the fore-optics, the challenge in the design of the detector optics is the small available volume. The detector optics has a pupil stop as last element before the detector with a diameter of 3.2 mm that acts as a Lyot-stop. Its influence is further described in Chapter 5.2.8 regarding the straylight analysis. Table 5.8 summarizes the most important properties.

Figure 5.27 shows the layout of the detector optics. The left focal points of four field points lie at the localization plane of the SHS and have a distance of 16.4 mm (object focal length) to the first lens. The lenses are made out of different glasses and have only spherical surfaces. The first lens almost collimates the beams and the other three lenses focus on the detector with the desired magnification.

Table 5.8.: Optical properties of the detector optics.

Property	Value	Unit
F/#	2.17	[-]
Object Focal Length	16.4	[mm]
Entrance Pupil Diameter	18.7	[mm]
Length	41	[mm]
Magnification	0.6	[-]
Pupil Stop	3.2	[mm]
AR-coating	<0.5	[%]
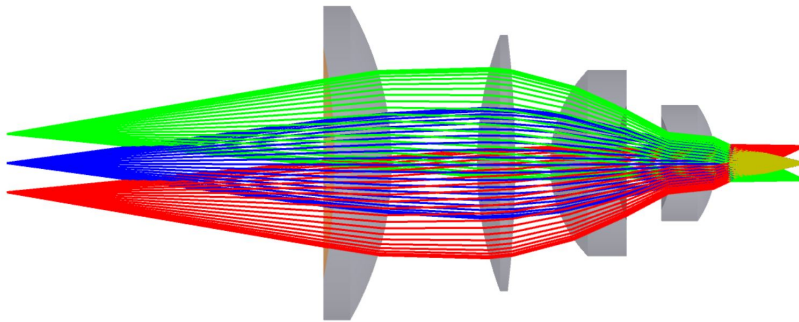
Figure 5.27.: Schematics of the detector optics with four field points.

The fringe frequency of a specific emission line on the detector is dependent on the magnification factor of the detector optics. It equals 0.6 by design. But the distances between SHS and detector optics and between detector optics and detector can vary by ± 1.0 mm to compensate for manufacturing and alignment tolerances. This results in a change of the magnification factor between 0.58 and 0.62 and, thus, also changes the fringe frequency on the detector. The magnification factor needs to be characterized in laboratory tests to establish the relation between spatial frequency and wavenumber for the actual SHS.

In spatial direction, 41 individual altitude levels need to be resolvable, corresponding to a spatial frequency of approximately 10 cycles/mm at the detector. As Figure 5.28 shows, the MTF of the detector optics is above 0.9 for this spatial frequency. However, an individual fore- and detector optics analysis is to some extent misleading, because the detector optics compensates partially aberrations of the fore-optic, for example. Thus, the following chapter discusses the overall optical performance, which allows to predict the performance more accurately.
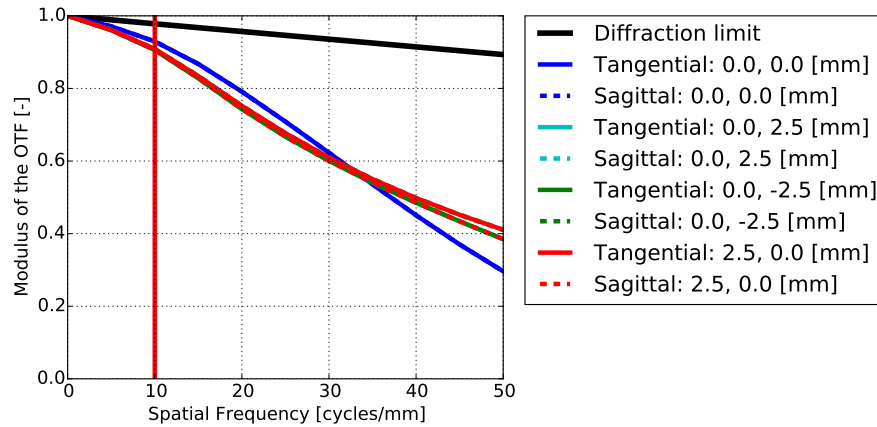
Figure 5.28.: Diffraction MTF of the detector optics calculated by FFT for four characteristic field points. The red vertical line shows the spatial frequency that corresponds to 41 altitude levels. They can be distinguished if the MTF is larger than 0.5.

5.2.7.3. Optical Assembly

The optical system´s performance is analyzed with an integrated simulation, including the fore-optics, SHS, and detector optics. Both arms of the SHS are analyzed separately in different configurations. This is necessary, because the sequential mode, with most analysis tools in ZEMAX, does not allow ray splitting. Hence, the interferogram can not be directly simulated and other performance metrics need to be used to determine the suitability of the optical design. The simulation setup is shown in Figure 5.29. Overall, six characteristic field points are evaluated in the analysis and optimization. The distances between fore-optics/ detector optics and SHS are iterated with the opto-mechanical design. The following analysis shows the results for the arm depicted in Figure 5.29 and the differences to the second arm are pointed out in the text.
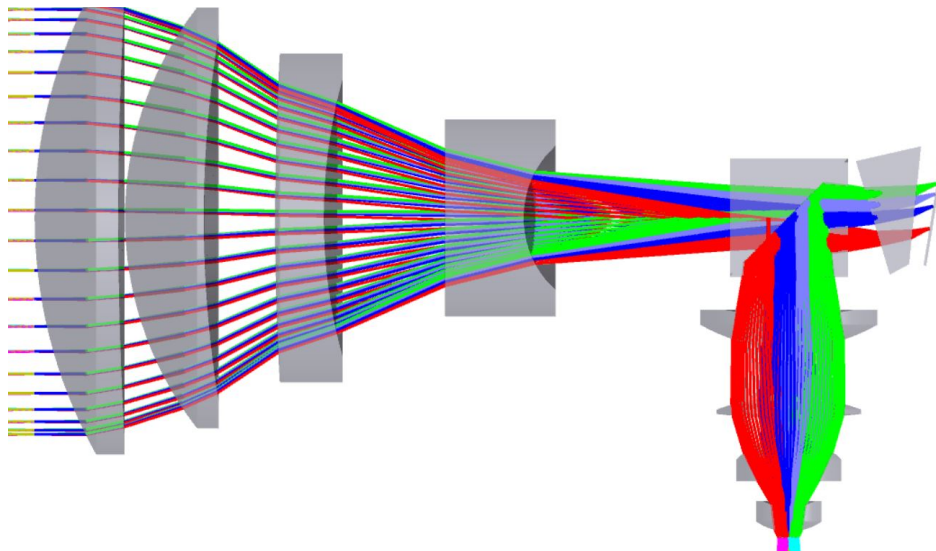
Figure 5.29.: Complete optics analyzed with ray bundles from six field points for one SHS arm.

Initially, the design goal was to keep the OPD to a value below 0.5 wavelengths. This design goal is derived from Equation B.38 in the appendix and is used in the calculation of the maximum acceptable FOV. It was loosened due to limited resources and it was deemed sufficient to not strictly comply with it. This design choice results in a reduced contrast of the fringes and a reduced resolving power. The analysis of the aberration influence on the contrast is not within the scope of this work, because it is performed by the Max Planck Institute for the science of light. The final design of the optical assembly has nevertheless high performance and the OPD is below 1.5 wavelengths for all field points and pupil positions. For the central field point, the OPD is at a maximum of approximately 0.5 wavelengths for both directions,

see Figure 5.30. These graphs show the OPD in dependence of normalized pupil coordinate and for two boundary wavenumbers in the relevant spectral range. For the other relevant wavenumbers, the OPD lies within these two boundary lines. The OPD is equal in both arms in spatial direction. In spectral direction, the OPD lines are mirrored in the center. This relation holds true for the center point, but is not valid for every field point.

(a)   (b)
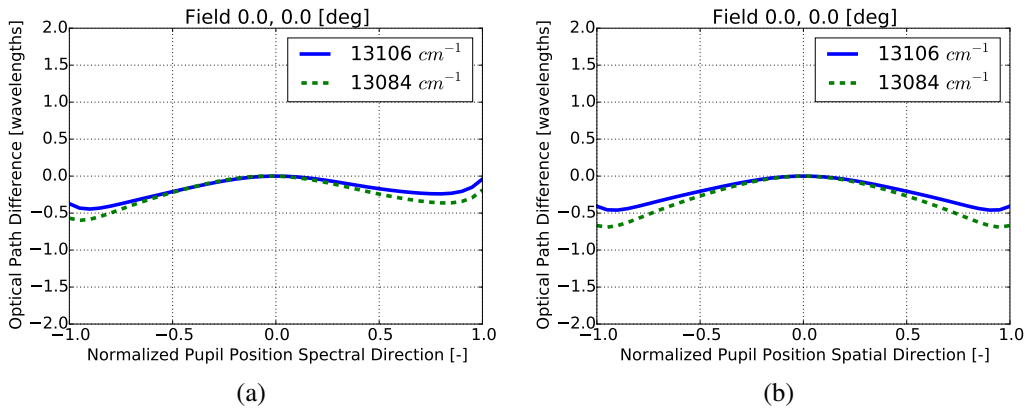
Figure 5.30.: OPD in spectral (5.30a) and spatial (5.30b) direction for the center field point at the detector. and for two different wavelengths.

The RMS OPD is below 0.2 wavelengths for all field points, as shown in Figure 5.31. The asymmetry in spectral field direction is introduced by the spectrometer arm with lowest aberrations on the narrow field-widening prism side. Therefore, the field map is approximately mirrored for the simulation with the second interferometer arm at the center of the spectral direction.
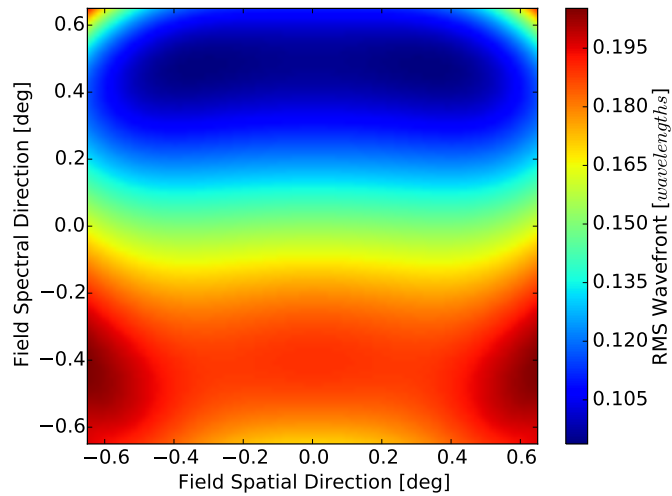
Figure 5.31.: RMS OPD field map for the complete optics for one interferometer arm. The field map for the second interferometer arm is a similar image, but mirrored at the zero spectral field line.

The required high optical performance in the small volume has the disadvantage that geometric image distortion is pronounced in the system. More specifically, Figure 5.32 shows the image of a theoretical rectangular grid and the simulated image with dots. The image depicts clearly that geometric image distortions appear with a maximum distortion of 7.1% in the corners of the image relative to the reference image. The distortion bends the fringes on the outer side, which effectively decreases the spectral resolution. Deiml et al. (2017a) describe methods to reduce the influence of image distortion in the post-processing.
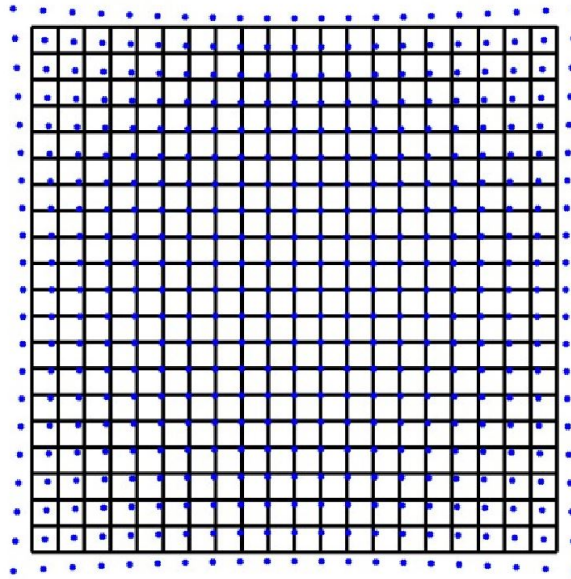
Figure 5.32.: Image distortion at the detector for the complete optics system. The maximum image distortion is 7.1 %.

5.2.7.4. Tolerance Analysis

The tolerance analysis is performed similar to the analysis of the SHS with focus on the lenses of fore- and detector optics. The difference in the process is that the ideal optical components (paraxial fore-optics lens and retro-reflective surface) are replaced with the actual optical components:

1. Tolerances are applied to the undisturbed model.
2. The distance between fore-optics and SHS acts as compensator to achieve optimal focus on the gratings.
3. The distances between detector optics/ SHS and detector optics/ detector act as two additional compensators to achieve optimal OPD at the image.
4. The image RMS OPD is evaluated for five fields as tolerance metric.

The following parameters are tolerated in the process:

- Center thickness of lenses
- Distance between lenses
- Tilt of individual lens surfaces relative to local optical axis of each lens in both directions
- Decenter of individual lens surfaces relative to optical axis of each lens in both directions
- Irregularity of each lens surface
- Radius of curvature of each lens surface
- Tilt of lens relative to optical axis in both directions
- Decenter of lens relative to optical axis in both directions
- Index of refraction of each lens
- Abbe number of each lens
- Tilt of fore-optics relative to SHS in both directions
- Decenter of fore-optics relative to SHS in both directions
- Tilt of detector optics relative to SHS in both directions
- Decenter of detector optics relative to SHS in both directions

The Master thesis of Wagner (2017) shows the lens drawings with the actual tolerances of the lenses. The resulting performance metric based on the Root-Sum-Square method shows that the RMS wavefront error increases to approximately 0.33 wavelengths from 0.18 wavelengths. A summary of the results is provided in Table 5.9.

Table 5.9.: Estimated performance of the complete optics based upon the Root-Sum-Square tolerance analysis method.

	RMS OPD [wavelengths]
Nominal Wavefront	0.178
Estimated Change	0.151
Estimated Wavefront	0.329

The second method for analysis of the tolerances is based on a Monte-Carlo-Simulation with 100 samples. The mean wavefront error is 0.18 wavelengths with a standard deviation of 0.01 wavelengths. For 90 % of the samples the wavefront error is lower than 0.38 wavelengths. Additional information is provided in Table 5.10.

Table 5.10.: Estimated performance of the complete optics based upon the Monte-Carlo tolerance analysis method (100 samples).

	RMS OPD [wavelengths]
Nominal Wavefront	0.178
Best Wavefront	0.194
Worst Wavefront	0.523
Mean Wavefront	0.294
Standard Deviation Wavefront	0.062
> 90%	0.379

The same compensators are utilized for the complete tolerance analysis as for the SHS tolerancing. The minimum and maximum compensator values have larger deviations from the nominal position in this analysis. More specifically, the fore-optics compensator may need to adjust the position by more than 2 mm in both directions. This adjustment range can be achieved by a combination of shims and positioning of the SHS within its housing. Table 5.11 summarizes the results of the compensator statistics. The compensators for the detector optics can be used interchangeably, which only influences the magnification of the system. So, the detector can be adjusted to the SHS with shims at these two compensation positions.

Table 5.11.: Compensator statistics for the tolerance analysis based upon the Monte-Carlo method.

Compensator	ΔD_{min} [mm]	ΔD_{max} [mm]
Distance between fore-optics and SHS	-2.46	2.29
Distance between SHS and detector optics	-1.46	0.77
Distance between detector optics and detector	-0.22	0.28

5.2.8. Straylight

This last chapter in the optics chapter analyzes the expected straylight at the detector. Straylight can be divided into in-field and out-of-field straylight. In-field straylight corresponds to straylight which origins from sources within the intended FOV. For example, every refractive optical element, like a lens, also partially reflects light. This light can reach via unintended optical paths the detector and, thus, contributes to straylight. Out-of-field straylight describes the influence of light sources outside the intended FOV that finds an optical path towards the detector. Typical out-of-field straylight sources in aerospace applications are the Sun, the Moon or the surface/ clouds of the Earth. The following four contributors in the optical system influence straylight:

- Surface Coatings
- Surface Roughness
- Surface Contamination
- Aperture Diffraction

Coatings of refractive surfaces, like lenses or prisms, influence straylight. For example, an uncoated surface reflects approximately 5 % of the incoming light. This does not only reduce the transmissivity of the whole optical system, but can also contribute to 'ghosts', if the reflected light finds an optical path

to the detector. Also, the surface of structural components contributes to straylight. Polished aluminum acts like a mirror in a large wavelength range and can enable unwanted optical paths to the detector. By coating structural parts with a highly absorbing material such straylight can be minimized. Thereby, the coating material should ideally absorb as much light as possible in the relevant spectral range.

The roughness of optical surfaces is a result of the polishing process and is typically around $1\,\mathrm{nm}$ for standard optical materials and polishing mechanisms (Fest, 2013, p. 69). This unisotropy in the surface scatters light not only in specular, but also in other directions. If the scattered light finds a path to the detector, it contributes to straylight.

A similar mechanism is scattering by surface contamination. Depending on the clean room level and the cleanliness of the optical elements, particles on the surface of optical elements scatter light by Mie-scattering.

Aperture diffraction describes straylight from the side-lobes of the Airy disc for circular apertures, respectively from spikes for other aperture types. Aperture diffraction gets relevant if a very sharp transition between in-field transmittance and out-of-field rejection is required. It is typically important for systems with narrow FOVs.

Overall, all contributors to straylight should be kept low within the given constraints of time and money to achieve a sufficient straylight behavior of the optical system. Thus, the next chapter will discuss the potential straylight radiation from the atmosphere. It is followed by a chapter about the optical setup for the analysis, including a description of stops, coatings, and scattering models. Afterwards, the analysis results are discussed with respect to the different straylight contributors.

5.2.8.1. Radiance from the Atmosphere

The main source of external straylight is the Sun. Its radiance is detected by the instrument via multiple straylight paths. This chapter analyzes these paths and calculates the expected radiance at the entrance aperture of the instrument. This information is used in the remaining sections of the analysis to verify that the straylight reduction mechanisms are sufficient for the instrument.

Figure 5.33 shows a schematical diagram of the relevant paths for external straylight. The radiance from the Sun can propagate to the entrance aperture directly if the Sun is not obstructed by the Earth (nighttime) or is behind the instrument. Radiance from the Sun can also be reflected by the Earth´s surface and by clouds at lower altitudes. During nighttime, Moon reflected sunlight may either directly illuminate the entrance aperture or via clouds in the lower atmosphere.

The Sun is represented by a $5800\,\mathrm{K}$-hot blackbody in this analysis. Its radiance calculates to $L_{Sun,inband} = 3 \times 10^{19}\,\mathrm{photons/s/cm^2/sr}$ in a wavelength range of $4\,\mathrm{nm}$ around $762\,\mathrm{nm}$, which is transmitted by the filter. In the detector sensitive wavelength range of $300\,\mathrm{nm}$ to $1200\,\mathrm{nm}$, the radiance of a blackbody is $L_{Sun,outofband} = 5.3 \times 10^{21}\,\mathrm{photons/s/cm^2/sr}$. The out-of-band rejection of the bandpass filter is lower than 1×10^{-4} on average. Thus, the out-of-band radiance is in the percent range of the in-band radiance and can further be neglected.

The Sun has a solid angle of $\Omega = 6.8 \times 10^{-5}\,\mathrm{sr}$, when viewed from Earth´s vicinity. Thus, the direct irradiance from the Sun equals $I_{Sun} = L_{Sun}\Omega_{Sun}cos(\theta_{Sun})$, which includes the projection of the Sun onto the entrance aperture with Sun angle θ_{Sun}.

The reflected irradiance from the Earth´s surface is approximated with an isotrop, Lambertian, and an infinite large plane. The Lambertian approximation may not be valid for a localized area on the surface, but it is regarded useful as an average over the completely visible surface. The exitance $M_{EarthSun}$ from the surface and clouds can then be calculated as $M_{Earth-Sun} = L_{Sun}\Omega_{Sun}sin(\theta_{Sun})\alpha/\pi$ with α being the average albedo value (Fest, 2013, p. 199). The sine is used instead of the cosine, because it is referred relative to the instrument viewing direction. The isotropy assumption is reasonable, because the albedo averages over a larger area of the Earth´s surface and the distance between Sun and Earth is so large that the irradiance from the Sun can be assumed to be constant. Specular reflection of the Sun in the Earth´s surface/ clouds is also considered. The instrument is viewing the Sun via the Earth´s surface/ clouds with an albedo α. Therefore, the exitance of the Sun $M_{Sun-reflected}$ can be calculated by Equation 5.19,

$$M_{Sun-reflected} = L_{Sun}\Omega_{Sun}\alpha \sin(\theta_{Sun})cos(\beta) \qquad (5.19)$$

with $\beta = \pi/2 - \theta_{Sun}$ to fulfill the specular reflection condition.

The Moon may also reflect sunlight towards the instrument during nighttime. The worst case condition is the illumination of the entrance aperture during full moon and for a low incidence angles θ_{Moon}. The exitance of the Moon M_{Moon} depends on the irradiance from the Sun, the Moon albedo $\alpha_{Moon} = 0.12$ (Fest, 2013, p. 199), and the solid angle of the Moon $\Omega_{Moon} = 6.4 \times 10^{-5}$ sr by $M_{Moon} = I_{Sun}\alpha_{Moon}\Omega_{Moon}\cos(\gamma)/\pi$. The factor $1/\pi$ shows that the Moon is approximated as a Lambertian radiator.

The moon reflected sunlight can also be specularly reflected by clouds and the surface. As before, the exitance calculates to $M_{Moon-reflected} = M_{Moon}\alpha\sin\theta_{Moon}$ by considering the specular reflection condition ($\gamma = \pi/2 - \theta_{Moon}$) and the albedo of the Earth.

The last considered mechanisms are moonlit clouds that illuminate the entrance aperture. Thus, this is a three step mechanism. The irradiance from the Sun gets reflected by the Moon and then reflected by clouds and the Earth´s surface towards the instrument. The mechanism is treated as above with two Lambertian radiators (Moon and clouds) and considering the albedo of both. The same view factors as above are used to calculate the incidence dependent exitance $M_{EarthMoon}$ of this pathway.
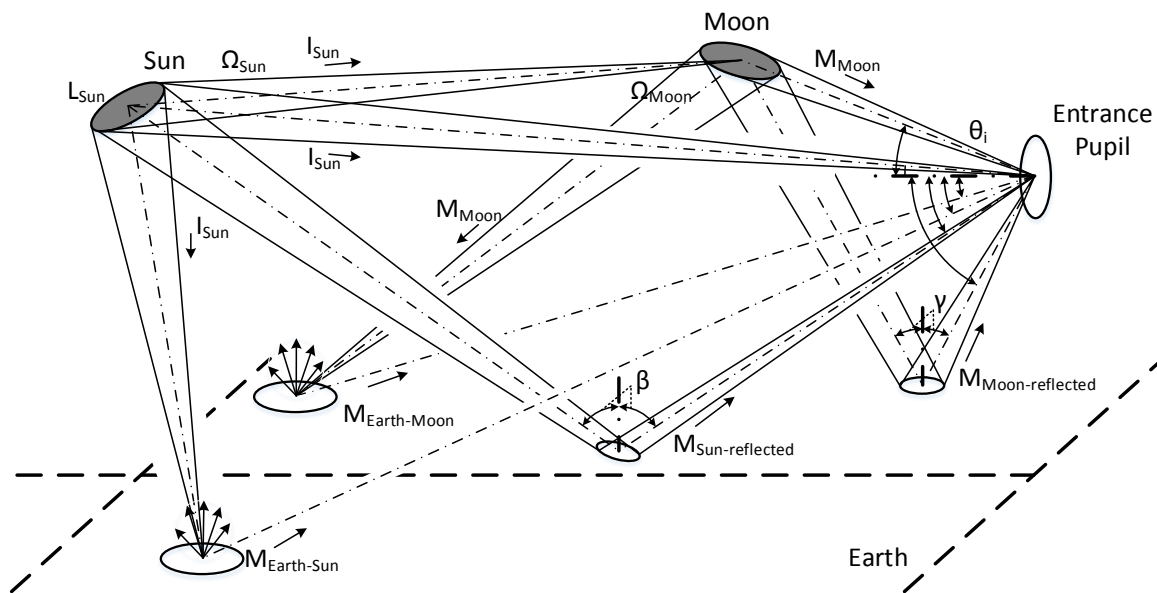
Figure 5.33.: Schematic diagram of straylight sources and paths for the measurement geometry.

One goal of the following analysis is to calculate the radiant flux on the detector in dependence of incidence angle θ of Sun and Moon. The radiant flux on the entrance aperture for the direct and specular reflection paths is only dependent on incidence angle. The radiant flux on the detector is therefore calculated by multiplication with the Point Source Transmittance (PST) of the instrument. The calculation of the radiant flux for the Lambertian reflected radiant flux is more complex. For every incidence angle of the Sun/Moon, the radiant flux is the area integral over the Earth´s surface of the surface exitance weighted by the PST. The area integral is substituted by a numerical view factor calculation. The Earth´s surface is approximated with an infinite plane in this calculation. The view factor between a patch of the plane and the entrance aperture of the instrument needs to be calculated in dependence of incidence angle to correctly account for the incidence dependent PST of the optics. The calculation of the view factor is further discussed in the Appendix C.6. The calculation of the PST of the instrument is subject of the following chapters.

5.2.8.2. Optical Setup

All optical components and the structural parts that influence the straylight behavior are included in the analysis. The structural components are imported in their original shape. As in Figure 5.34, the structural parts consist of the baffle, the fore-optics assembly, the SHS housing, and the detector optics assembly. The optical components are directly modeled in ZEMAX, including the lenses for detector and fore-optics, and the SHS. The SHS is modeled with all spacers, even if they are not within the nominal light path. Two field-stops close to the SHS gratings are modeled with planes, similar to the aperture stop

between last lens and detector.

Figure 5.34 shows the light path colored by segment for a collimated light beam with the extent of the entrance aperture. The beam is focused in the center of the gratings and then imaged onto the detector. This light source is used for ghost analysis, because it allows to show the different ghost mechanisms and their influence on the detector. For the other types of analysis, extended light sources are used to illuminate the full detector.
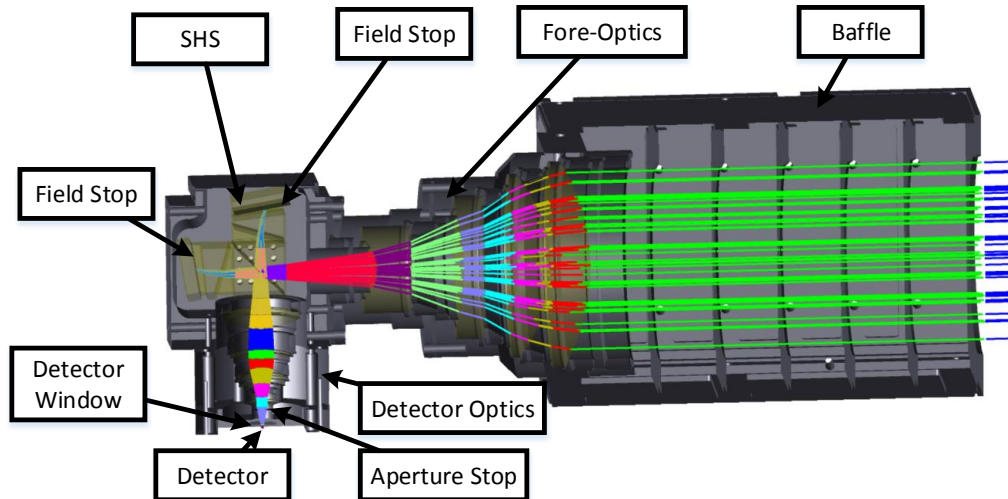
Figure 5.34.: Optical setup for the straylight analysis with rays of the center field point.

Baffle The baffle is designed using geometric ray tracing considerations, described in Fest (2013). The overall length of the baffle is determined by the CubeSat form factor. The entrance aperture size and the FOV are determined by the performance analysis. Thus, the overall performance is already largely determined by these geometric constraints. Figure 5.35 shows a conceptual drawing of the baffle. Rays, relevant for dimensioning of the baffle vanes, are also shown with dashed lines. The lower part of the baffle is fully modeled, whereas the upper part is only sketched. The exclusion angle of $26°$ describes the angle above which the entrance aperture cannot be directly seen anymore at all. Thus, only scattered rays can hit the entrance aperture for larger incidence angles. Additional baffle vanes are placed that this first-order straylight is also blocked. At least two reflections are required to hit the entrance aperture. The out-of-field straylight is therefore reduced by at least three orders of magnitude using a black coating with an absorption of $97\,\%$. The performance of the baffle can be analyzed with the attenuation factor (PST), which describes the ratio between irradiance at the entrance aperture and at the illumination source as a function of incidence angle (Fest, 2013). A detailed analysis of the baffle performance is discussed in Chapter 5.2.8.4.
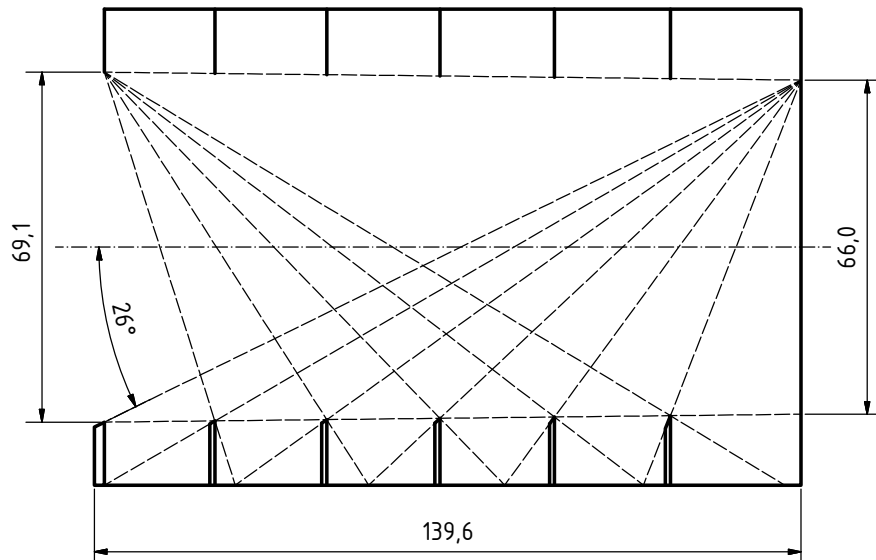
Figure 5.35.: Conceptual drawing of baffle with rays (dashed lines) relevant for the baffle vane dimensioning.

Field Stop   Two field stops are mounted onto the gratings of the SHS, because the gratings represent an intermediate image. These field stops restrict the acceptable field and thus reduce out-of-field straylight. In addition, these field stops eliminate unwanted ghost paths between gratings and field-widening prisms. A field stop, as shown in Figure 5.36, is a very thin plate (0.1 mm) with a rectangular cutout and coated with the same coating as all other structural surfaces, see Chapter 5.2.8.2. Dedicated field stops are available, but have not been included in the AtmoHIT experiment. However, due to their importance for the satellite instrument, they are considered in the straylight analysis. The detector surface is the field stop for the AtmoHIT experiment.

Figure 5.36.: Field stop mounted on the diffraction grating.

Aperture Stop   The aperture stop is the last element before the detector, rendering it very efficient for straylight reduction. The stop is in the position of the exit pupil with the first lens being the entrance pupil. Thus, it can also be used as a Lyot stop to reduce aperture diffraction. Figure 5.37 shows the aperture stop in blue color as it is mounted onto the detector optics. The alignment and manufacturing tolerances are relatively high to control the performance of the stop.
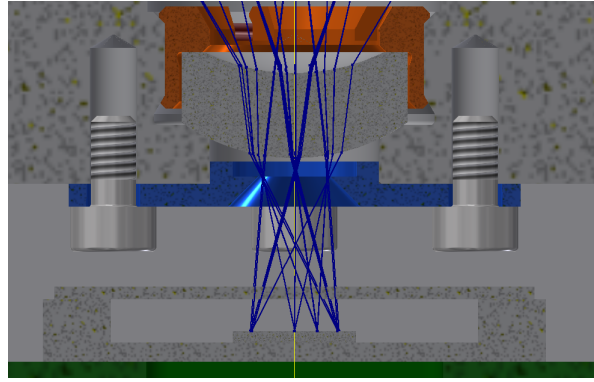
Figure 5.37.: Aperture stop (blue) between detector optics and detector. The thin blue lines illustrate rays for four characteristic fields.

Noll (1973) and Johnson (1987) analyzed the performance of a Lyot stop based on the Huygens-Fresnel principle and derived approximations for the straylight reduction ratio due to diffraction. The approximation from Noll (Equation 5.20) describes the reduction ratio in dependence of wavelengths, entrance aperture diameter, FOV, and Lyot stop reduction ratio,

$$R = \frac{2}{\pi^2 (ka\theta)^2 (1 - \alpha^2)^2} \tag{5.20}$$

with $k = 2\pi/\lambda$ with λ as wavelength, a the radius of the entrance aperture, θ the angular radius of a circular field stop, essentially $FOV/2$ for small angles, and α the reduction ratio of the Lyot stop. This equation is evaluated for an estimation of the Lyot stop performance and the results are shown in Chapter 5.2.8.4.

Optical Surface Coating The optical surfaces are coated with an idealized AR coating. This simulates the requirement to the manufacturers of having reflections in refractive elements lower than $0.5\,\%$ for the relevant wavelength range. Thereby, the coating performance is seen independent of wavelength and incidence angle. Thus, the surface coatings simulate the worst case and can be considered as conservative.

Optical Surface Scattering Model A Bi-Directional Scatter Distribution Function (BSDF) is utilized to describe the scattering due to surface roughness, based on the ABg model. The parameters are calculated according to Fest (2013), using a surface roughness value of $1\,\mathrm{nm}$, the K-correlation model parameters $C = 1.5$ and $B = 200\,\mu\mathrm{m}$, and a dispersion difference at the interface regions of 0.5 as standard values. The values for the ABg model then calculate to $A = 1.44 \times 10^{-6}\,\mathrm{sr}^{-1}$, $B = 2.36 \times 10^{-4}$, and $g = 1.5$. The BSDF function is calculated with these values, see Equation 5.21. Here, θ_s equals the angle of the scattered ray to the surface normal and θ_i the angle between incidence ray and surface normal.

$$BSDF = \frac{A}{B + |sin(\theta_s) - sin(\theta_i)|^g} = \frac{1.44 \times 10^{-6}}{2.36 \times 10^{-4} + |sin(\theta_s) - sin(\theta_i)|^{1.5}} \tag{5.21}$$

The BSDF in dependence of the direction vector magnitude $|\vec{x}| = |sin(\theta_s) - sin(\theta_i)|$ is shown in Figure 5.38. The function is in its plateau of almost constant values below 10×10^{-2} and decreases afterwards by $1.5\,\mathrm{dB/decade}$, which is a moderate decrease and consistent with a conservative approach.
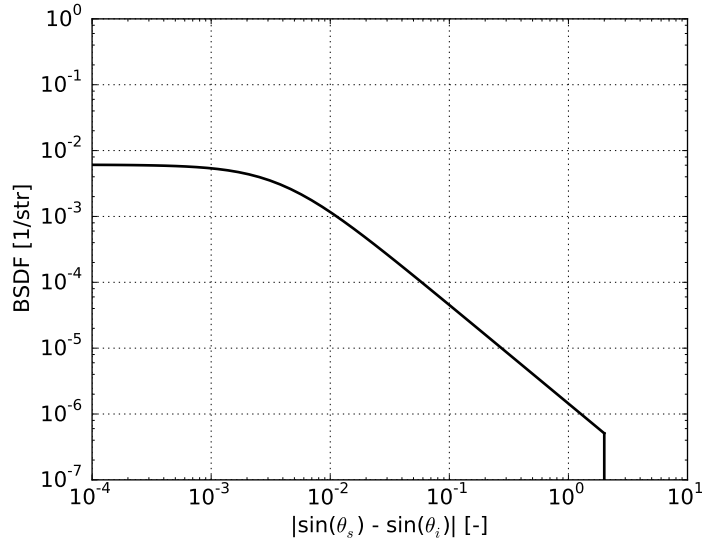
Figure 5.38.: BSDF [$1/str$] as a function of magnitude of direction vector $|\vec{x}| = |sin(\theta_s) - sin(\theta_i)|$ [-] used for all refractive surfaces to describe a surface roughness less than $1\,\mathrm{nm}$.

Optical Surface Contamination Model The surface contamination model is also based on an ABg model, which is derived from a Harvey model (Harvey, 1976; Fest, 2013). The parameters for the Harvey model are calculated from the Cleanliness Level (CL) by Equation 5.22,

$$PAC = 10^{K+|S|log_{10}^2(CL)} \tag{5.22}$$

with $K = -7.245$ and $S = -0.926$ for a freshly cleaned surface (Fest, 2013). The slope $S = -0.926$ is based on experimental data for precision cleaned optics (Hamberg and Shon, 1984). Using this equation, the Percent Area Coverage (PAC) for a CL of 200 (only particles smaller than $200\,\mu\mathrm{m}$) is 4.5×10^{-3}, resulting in a Total Integrated Scatter (TIS) of $4.5 \times 10^{-3}/100$ The PAC value, together with standard values for the $l = 0.01\,\mathrm{rad}$ and $s = -1.5$ parameters for the Harvey model, allows to calculate the remaining parameter b_0 with Equation 5.23.

$$b_0 = \frac{(PAC/100)l^s(s+2)}{2\pi\left((1+l^2)^{(s+2)/2} - (l^2)^{(s+2)/2}\right)} \tag{5.23}$$

As in Chapter 5.2.8.2, the parameters of the ABg model can be computed from the Harvey model, resulting in $A = 4.02 \times 10^{-6}\,1/\mathrm{sr}$, $B = 1 \times 10^{-3}$, and $g = 1.5$. This BSDF is shown in Figure 5.39. The order of magnitude of the BSDF is slightly lower for particle contamination compared to the BSDF for surface roughness scattering. Thus, precision cleaning the optics is necessary to take advantage of the low surface roughness of the optical elements.
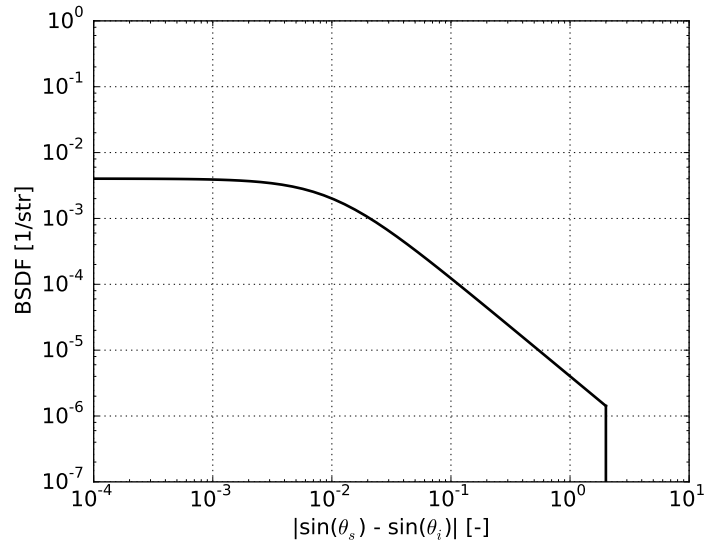
Figure 5.39.: BSDF [1/sr] in dependence of magnitude of direction vector $|\vec{x}| = |sin(\theta_s) - sin(\theta_i)|$ [-] used for all refractive surfaces to describe particle scattering with a CL level of 200.

Model of Structural Surfaces All structural surfaces are coated with Nextel Velvet Coating 811-21. This black paint absorbs more than 97 % of the incoming radiance (Tang-Kwor and Matteï, 2001). Of the remaining amount of 3 %, 98 % is diffusely scattered, while the rest is specularly reflected (Mankiewicz, 2017). The surfaces are modeled with an idealized coating with these properties and the scattering is Lambertian.

Diffraction Grating Model The diffraction gratings are modeled within ZEMAX to include multiple orders of diffraction. Only the diffraction orders 0 and 1 can exist (see grating diffraction Equation B.6). For a specific wavelength and a constant incidence angle, energy over all diffraction orders is conserved (Palmer, 2014). As the input angle does not vary for the SHS configuration, the grating can be described by two diffraction efficiencies. The efficiency of the gratings is higher than the conservative value of 70 % for the first diffraction order in Littrow condition. Thus, the zeroth diffraction order has an efficiency of 30 % in worst case conditions. Absorption and scattering is not modelled for the gratings, due to a lack of information.

Aperture Diffraction Model Aperture diffraction is simulated with a Bi-Directional Diffraction Distribution Function (BDDF) on the entrance aperture (first lens) of the system. As the optics uses a circular aperture, the far-field diffraction pattern can be approximated by Equation 5.24. This equation is valid if the aperture is the entrance pupil and the evaluating surface is the focal plane, even if it is within the Fraunhofer distance, according to Fest (2013).

$$BDDF = \frac{D^2}{\lambda^2} \left[\frac{\pi J_1(\pi|sin\theta_d - sin\theta_i|/\lambda)}{\pi D|sin\theta_d - sin\theta_i|/\lambda} \right]^2 \tag{5.24}$$

In the equation, D is the aperture diameter, λ the wavelength, J_1 a Bessel function, and $|sin\theta_d - sin\theta_i|$ the magnitude of the direction vector. Thereby, θ_d describes the diffraction angle. The resulting curve is highly oscillatory and an approximation is used instead, Equation 5.25. This function decreases by $3\,\mathrm{dB/decade}$, which is much steeper than for particle contamination and surface roughness scatter. Thus, scattering by aperture diffraction gets significant for rays close to the specular beam.

$$BDDF = \frac{\lambda}{\pi^3 D|sin\theta_d - sin\theta_i|^3} \tag{5.25}$$

Figure 5.40 shows the BDDF due to aperture diffraction of the entrance aperture using the far-field approximation for a circular aperture (solid blue line) and its approximation (green dashed line). The approximation is used in ZEMAX for performance estimation by converting it into ABg data with $A =$

3.73×10^{-8} 1/sr, $B = 1 \times 10^{-14}$, and $g = 3$. The value of B is larger than zero, because otherwise the function is not integratable and cannot be used in ZEMAX. This value results in a relative error of the TIS lower than $0.01\,\%$ and is, thus, acceptable.
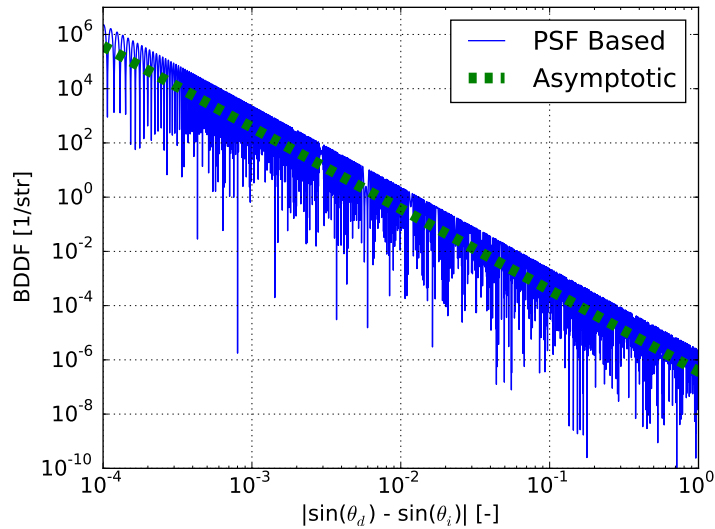
Figure 5.40.: BDDF [$1/str$] in dependence of magnitude of direction vector $|\vec{x}| = |sin(\theta_s) - sin(\theta_i)|$ [-] for aperture diffraction of the entrance pupil. The solid blue line shows the BDDF based on the PSF. The green dashed line illustrates its asymptotic approximation.

5.2.8.3. Analysis Method

The optical setup described above is used to perform the straylight analysis on the system. Different models have been created that focus on individual aspects of the analysis. A straylight analysis program like FRED, ASAP, or TracePro was not available and thus, it needed to be performed with the optical design software ZEMAX 16SP2. Data was post-processed with a program written in Python 2.7, Numpy 1.9.2 and Scipy 0.14.0 and PyZDDE 2.0.2 (Indranil Sinharoy et al., 2016). The professional version of ZEMAX only allows to use forward ray-tracing. Thus, usually a large number of rays needs to be traced to predict the straylight with sufficient accuracy, especially for large incidence angles of external straylight. The baffle performance analysis was conducted using only the structural baffle model. The first lens is replaced by a detector surface to simulate the entrance aperture. The baffle performance is evaluated against this surface. A Lambertian scene is used as light source providing rays with different incidence angles.

The ghost reflection analysis was performed with the complete opto-structural system. Scattering is not included, but rays are allowed to split. The beam is focused on the central point of the detector, making ghost reflections clearly visible.

The aperture diffraction analysis is divided into an analytic approximation, see Equation 5.20, and a vignetting analysis. The vignetting analysis was performed with the sequential analysis tool of ZEMAX. The external straylight analysis combines all mechanisms and is the simulation which approximates reality closest. The complete opto-structural design was used with all considered straylight mechanisms, including scattering through surface roughness, surface contamination, and aperture diffraction. It is also the most computational expensive analysis as many rays need to be traced to achieve adequate performance for large off-axis angles. Importance sampling was included for scattered rays to improve the raytracing efficiency. As for the baffle performance analysis, a Lambertian light source launched rays from different incidence angles.

5.2.8.4. Results

In the following, the results of the baffle performance and the ghost analysis are presented. The individual contributions of surface roughness, surface contamination, out-of-field straylight, and aperture diffraction are analyzed.

Baffle Analysis   The baffle is analyzed analytically with the cold shield efficiency and with numerical raytracing. The cold shield efficiency is defined as the ratio of intensity at the detector that comes directly from an uniform Lambertian scene to the total power, which includes scattering and other straylight mechanisms (Fest, 2013). For this baffle, the cold shield efficiency is 96%. More important for the performance is the baffle attenuation in dependence of incidence angle. Thus, Figure 5.41 shows the attenuation factor in dependence of incidence angles in horizontal (spectral) and vertical (spatial) direction. The Sun exclusion angle of $26°$ marks a cut in baffle attenuation. For larger angles, the attenuation reaches 1×10^{-3}. This is also visible in a vertical cut through this image, showing the attenuation factor in dependence of incidence angle (Figure 5.42).
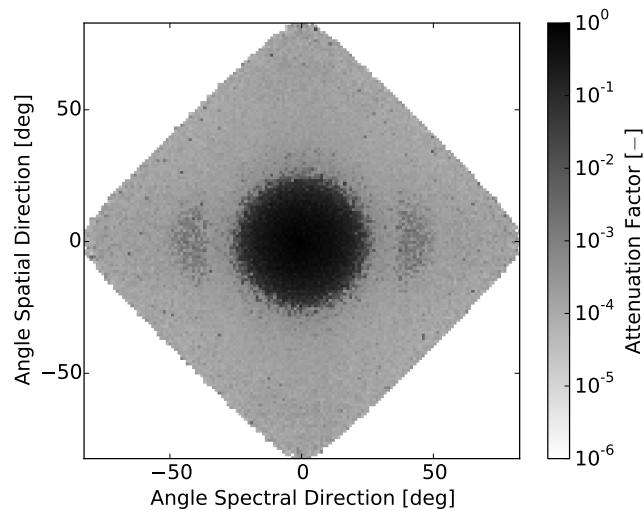
Figure 5.41.: Baffle attenuation factor in dependence of vertical (spatial) and horizontal (spectral) incidence angle.
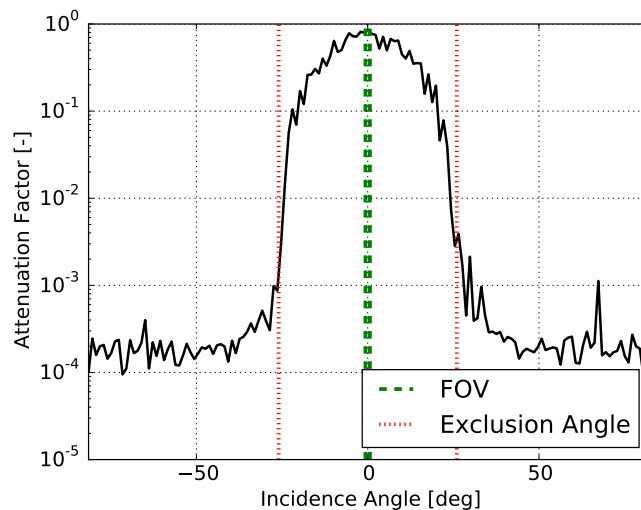
Figure 5.42.: Baffle attenuation factor in dependence of incidence angle (along vertical direction in Figure 5.41). The red dotted lines show the exclusion angle of the baffle and the green dashed line the Field of View (FOV).

Ghost Reflections   The ghost analysis was performed with a single field point. Figure 5.43 shows the radiance at the detector for the field point in the center of the detector in a logarithmic scale.
Multiple ghost mechanisms can be detected. The circular structures have cut of edges from the field-stops on the SHS gratings. The not point-symmetric ghosts are created by reflections between field-widening prisms, gratings, and beamsplitter. Quantitative analysis of the data shows that the relative total intensity of the ghosts is 3.5%, with 1.2% belong to ghosts due to the detector window and 1.9% are created by the SHS. The remaining 0.4% are created by other elements. The ghosts do not focus on the detector.

Thus, their influence is distributed over the detector image for an extended scene and they do not provide sharp features.
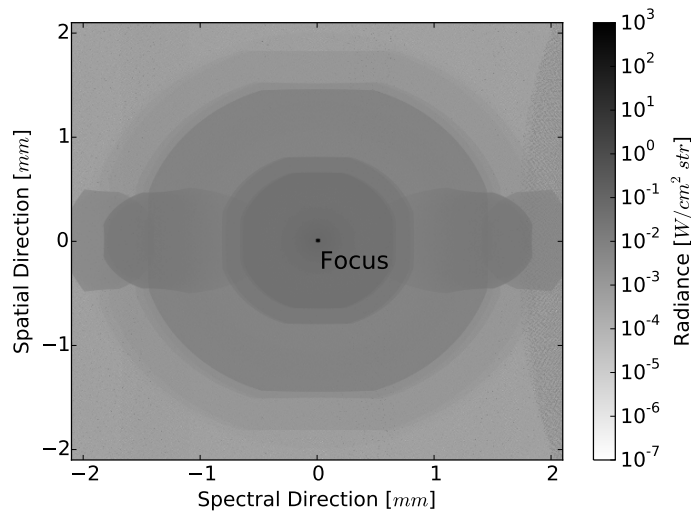
Figure 5.43.: Detector image of the ghost analysis. The center point shows the focus of the center field.

Aperture Diffraction   The aperture diffraction is included in the straylight analysis with a BDDF for the first lens surface. This influence is not independently analyzed through ray tracing and the analytic expression of Chapter 5.2.8.2 is used instead. The Lyot stop is sized in diameter that the undersizing ratios is a bit larger than 95 %, as it is typically optimal (Fest, 2013). Figure 5.44 shows that the fraction of unvignetted rays of the entrance aperture lies between 95 % and 96 % over the FOV, as desired. This fraction is not perfectly constant, because the exit pupil experiences some aberrations. The cutoff of the field stop is also visible in the figure, starting at 0.65°. The finite extent of the focal points on the gratings results in a steep slope instead of a vertical cut.

The performance of the Lyot stop to reduce the aperture diffraction is shown in Figure 5.45. It shows the reduction ratio as a function of undersizing ratio of the entrance aperture due to the Lyot stop. The minimum and maximum undersizing ratios for the Lyot stop of this instrument are shown with two vertical lines. Thereby, a design value of 95 % is chosen and the alignment and manufacturing errors of the Lyot stop are also considered. The figure shows that the aperture diffraction is reduced by more than 1×10^{-5}. Of course, the Lyot stop reduces also other straylight, because it is the only opening to the detector.
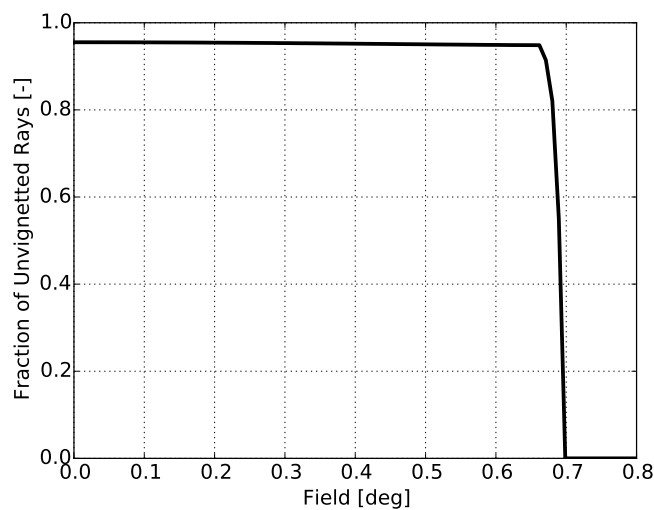
Figure 5.44.: Vignetting by field-stop and Lyot stop for nominal aperture stop positions.
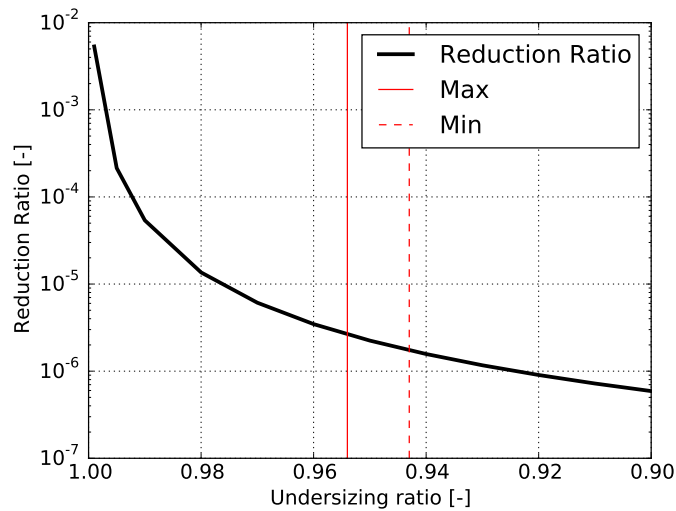
Figure 5.45.: Reduction ratio of aperture diffraction straylight compared to Lyot stop undersizing ratio. The vertical lines show the maximum and minimum undersizing ratio for the chosen Lyot stop with considering its alignment and manufacturing tolerances.

Out-of-field Straylight   Out-of-field straylight is analyzed with the complete optical setup, described above. Thus, it includes the aperture diffraction effects, surface roughness, contamination scatter effects, and the coating of all structural parts. The out-of-field straylight analysis is a time-consuming and resource intense calculation that requires a few million rays to be traced to gain a useful statistics. Thus, the curve shown in Figure 5.46 is not perfectly smooth. The figure shows the straylight attenuation factor as a function of incidence angle. The two vertical lines show also the FOV (green, dashed) and the Earth's surface (red, dotted) as two important angles. The attenuation factor is 0.18 within the FOV and falls off rather fast to 1×10^{-3} at 2°, which is the Earth's surface, due to the field- and Lyot stops. With an angle larger than 6°, straylight is attenuated by a factor larger than 1×10^{-4}. The analysis stops at an angle of 20°, because the number of traced rays needed for useful statistical analysis became to high. However, the baffle analysis shows that the baffle attenuation reaches 1×10^{-3} for angles larger than 28°. With considering that the baffle attenuation is approximately 1×10^{-1} at an angle of 20° and that the total attenuation factor is at 1×10^{-4}, it is argued that the total straylight attenuation for an angle larger than 25° is better than 1×10^{-6} as a conservative estimate.
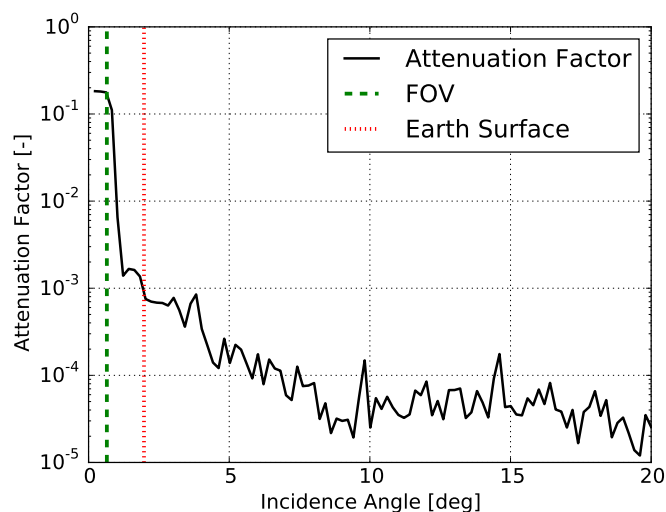
Figure 5.46.: Out-of-field straylight rejection (attenuation factor) of the complete optics in dependence of incidence angle. The two vertical lines show the FOV and the angle of the Earth's surface.

Straylight at Focal Plane Array   The attenuation factor can be used together with knowledge about the strength of different external straylight sources to calculate the radiant flux at the detector in dependence of straylight source. The utilized PST approximates the attenuation factor by using characteristic points and logarithmic interpolation between them. The resulting curves are shown in Figure 5.47. The red curves describe straylight paths active during daytime and the black curves are active during nighttime. Solid lines describe direct illumination by Sun or Moon, dashed lines represent specular reflection on clouds/ the surface and dotted lines show the cloud/ surface reflected contributions.

It is not surprising that the straylight is orders of magnitudes higher during daytime compared to nighttime and that direct Sun illumination is the largest contributor up to approximately 25°. With larger angles, the baffle reduces the direct illumination considerably and the Earth reflected sunlight becomes largest contributor.

During nighttime, direct moon illumination is the strongest contributor and afterwards surface reflected moon light becomes the largest contributor. Overall, the straylight signature is similar to daylight but with a lower order of magnitude.
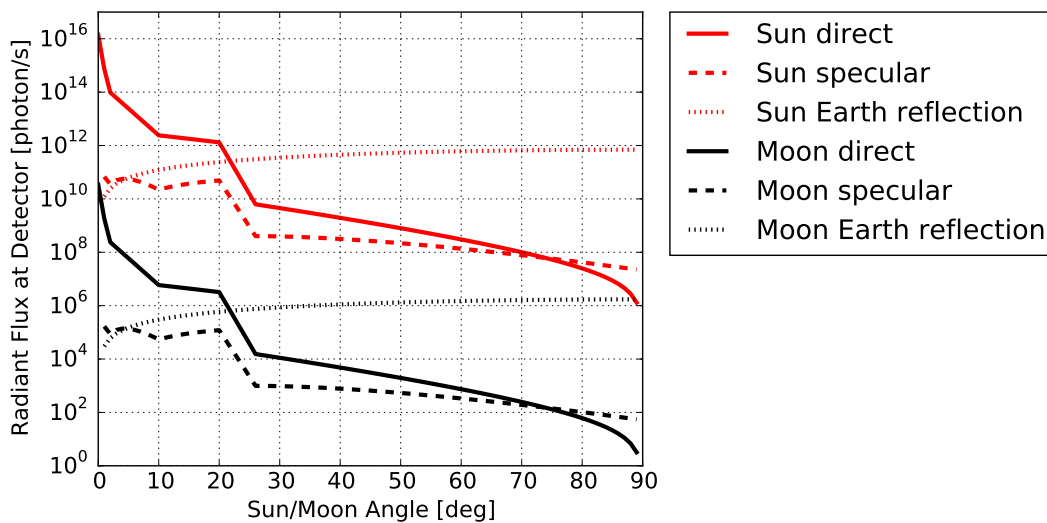
Figure 5.47.: Radiant flux at detector in dependence of incidence angle of Sun or Moon for different external straylight paths during day- and nighttime.

This analysis is conservative in its assumptions. Specifically, the following approximations are worst case estimates. The geometry for view factor calculation is approximated with an half-infinite plane which overestimates the view factor for far extended surface patches, respectively for small incidence angles. As these small incidence angles contribute to most of the cloud/surface reflected straylight, the resulting radiant flux is overestimated.

In addition, the atmosphere is approximated with only an average albedo value and transmission of the atmosphere is set to unity. So, the exitance is assumed to be constant over the spectral bandpass of the filter. However, the transmission of the atmosphere is much weaker in the spectral peaks. If the exitance in an oxygen A-band emission peak is used instead, the radiant flux for Sun and Moon reflected sunlight decreases by 1×10^{-3} to 1×10^{-4}. However, an in-depth analysis of the spectral characteristics of straylight is not within the scope of this work.

5.2.8.5. Summary

The Tether Optical Phenomena Imager used the oxygen A-band to observe gravity waves in a sub-limb configuration. In their paper, Mende et al. (1998) concluded that a $3\,\mathrm{nm}$ bandpass filter together with the absorption of the oxygen in the lower atmosphere was sufficient to suppress most cloud reflected moonlight for full moon conditions and that during low moon conditions, white backscatter is not of significant influence. The analysis here further investigates the influence of direct Moon and albedo reflected moonlight during nighttime and the three corresponding processes during daytime. The largest contributor in both cases is the surface/cloud reflected albedo emission. Hence, the values of 1×10^7 photon/s and

1×10^{12} photon/s for day- and nighttime have already been used in the measurement simulations as worst cases for day- and nighttime, respectively. In turn, this means that the instrument performance may degrade for Sun and Moon angles smaller than 20°, effectively limiting the observational time. However, between 20° and 10°, the straylight radiant flux is only slowly increasing. Thus, the instrument may still operate for these conditions due to the conservative nature of this analysis. Increasing the baffle size is an option to decrease the operational limit further. Therefore, the baffle would need to be extended to at least 30 cm length to have significant influence on the straylight performance. This shows also that the combination of Lyot-stop and field stop are of major importance to keep the straylight at acceptable levels. Especially, the radiant flux at low incidence angles contributes to the majority of straylight, which are efficiently blocked with these two stops. Chapter 7.4 describes how these results fit to the experimental measurements.

5.3. Structural Design

The following sections explain first the basic satellite instrument design, which builds also the baseline design for the AtmoHIT experiment. Thus, this chapter focuses on the conceptual ideas and their implementations. Secondly, the design was further detailed and adopted to the rocket mission requirements within the AtmoHIT experiment. More details about the structural design and specifically about the opto-mechanical mounting for the AtmoHIT experiment can be found in the Bachelor thesis of Rottland (2016) and in Deiml et al. (2017a).

5.3.1. Conceptual AtmoCube-1 Instrument Design

Using a 3U-CubeSat form factor as baseline requires to keep the volume below $34 \times 10 \times 10\,\text{cm}^3$ and the mass below 4 kg. Approximately half of the volume and mass is occupied by the instrument in its stored position. However, the instrument requires a large aperture to have a sufficiently high etendué, but the straylight should also be low. Thus, the instrument is designed to have a deployable baffle, operating similar to the PolarCube satellite (Deiml et al., 2014). The baffle also includes deployable baffle vanes to further reduce the straylight. All movable parts are released with a spring mechanism. The baffle needs to slide over the instrument structure, which requires that the optics and electronics fit within a volume of approximately $15 \times 8 \times 8\,\text{cm}^3$. It also limits the maximum allowable aperture size to approximately 66 mm.

Figure 5.48 shows a cut through the instrument design concept for the AtmoCube-1 satellite. The left part is the baffle with the baffle vanes. The right part is the instrument with fore-optics mounting, spectrometer housing, detector optics mounting, and the detector board (Proximity Electronics (PXE), see Chapter 5.5). An aperture diameter of 66 mm fills out the full front face of the instrument, thus, placing the SHS into the center and reducing the space for the detector optics. This is insofar challenging, because it requires to build a very high performing detector optics within a small volume, increasing the costs considerably. Two options are available for reducing the design complexity. First, the entrance aperture can be decreased to 50 mm, which moves the SHS to the top and increases the maximum length of the detector optics by 8 mm. Second, the requirement to adhere to the CubeSat form factor can be dismissed. The second option is used for the AtmoHIT experiment. However, it is not a viable option for the CubeSat.
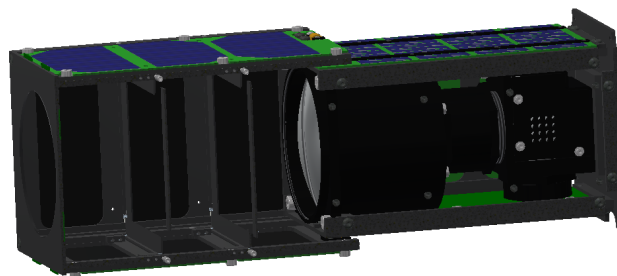
Figure 5.48.: View of the optical assembly for the AtmoCube-1 instrument concept.

5.3.2. AtmoHIT Design

The AtmoHIT experiment is designed to fit within a rocket module with an height of $170\,\mathrm{mm}$ and a diameter of $356\,\mathrm{mm}$. Besides the already discussed CubeSat instrument, the AtmoHIT experiment includes also a camera in the visible range (VisCAM) and a Power Supply Unit (PSU). The VisCAM looks in the same direction as the satellite instrument to simplify data analysis by identifying useful scenes for temperature retrieval. The VisCAM is a commercially available GoPro Hero 3 Black with a custom made extension board for commanding. The PSU acts as the interface to the service module of the rocket. Figure 5.49 shows the assembled experiment. The big window in front is for the spectrometer and the small window next to it is for the VisCAM. The position of the VisCAM next to the spectrometer requires to set the actual camera further back. Thus, the FOV of the VisCAM is vignetted by the window. Figure 5.50 shows a top view of the instrument with labels of the major components.
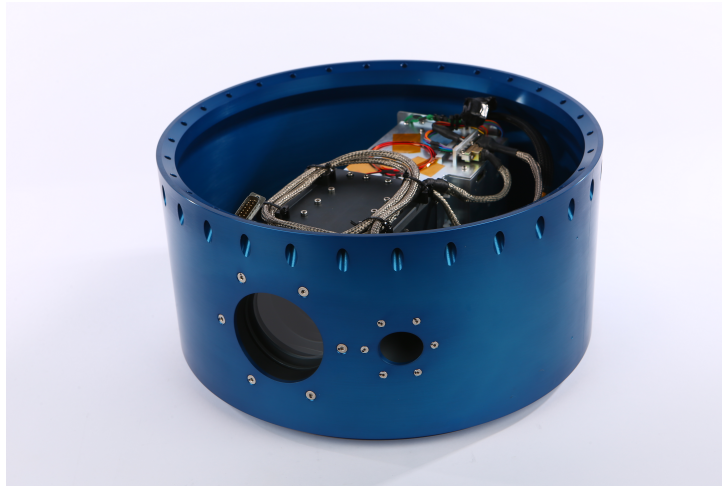
Figure 5.49.: Side view of the assembled AtmoHIT instrument.
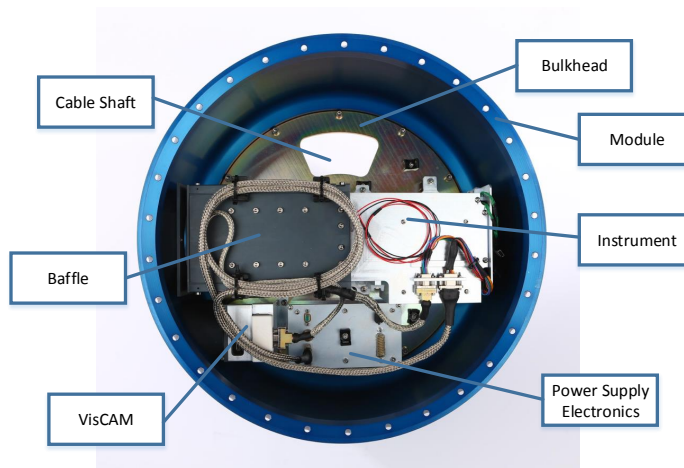
Figure 5.50.: Top view of the AtmoHIT instrument.

5.3.3. AtmoHIT Instrument Design

The spectrometer of AtmoHIT is mounted via wire-rope isolators to the bulkhead. The wire-rope isolators have the function to dampen vibrations from the rocket launch. The instrument is shown in Figure 5.51. Overall, two of these instruments have been assembled with two distinct differences in glueing of the SHS and in the coating of the baffle. The first baffle is black anodized, whereas the second baffle is coated with black velvet paint, as also used in the straylight analysis (Chapter 5.2.8). Visual inspection shows already qualitatively the superior performance of the paint.
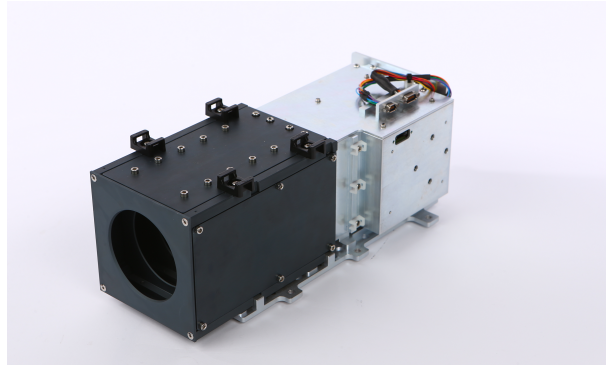
Figure 5.51.: Picture of the AtmoHIT instrument.

The uncoated aluminum of Figure 5.51 houses the optics with spectrometer and the electronics. The optical components themselves are placed in black anodized aluminum houses and held in place by burnished brass rings, see Figure 5.52. The optical mounting is a compromise between complexity and available resources. Sufficient high tolerances are achieved through the direct contact between housing/mounting rings and glass pieces. The mounting torques are calculated such that the lenses stay aligned within the operational temperature range and sufficient gaps between lens sides and housing reduce thermal stresses on the glasses. Alignment turning would have been another alternative to reduce the alignment errors on the lenses while also simplifying the lens housings. However, this technique was not chosen due to its high complexity, requiring specialized tools and extensive knowledge about lens mounting with adhesives.

The SHS is glued into the housing with space-grade silicon to reduce thermal loads from the housing and to reduce structural loads. The housing has an opening on top to gain access to temperature sensors and to block individually each arm of the SHS for flat-field calibration, see Chapter 6.3. The yellow shims in Figure 5.52 are used to align the optical components relative to one another and to the detector for maximum performance.

Figure 5.53 shows the actual optical assembly. The bandpass filter is the first optical element of the fore-optics. It is not included in this picture making the first lens visible. The lens appears blue due to the AR-coating, optimized for the spectral bandpass of the filter.
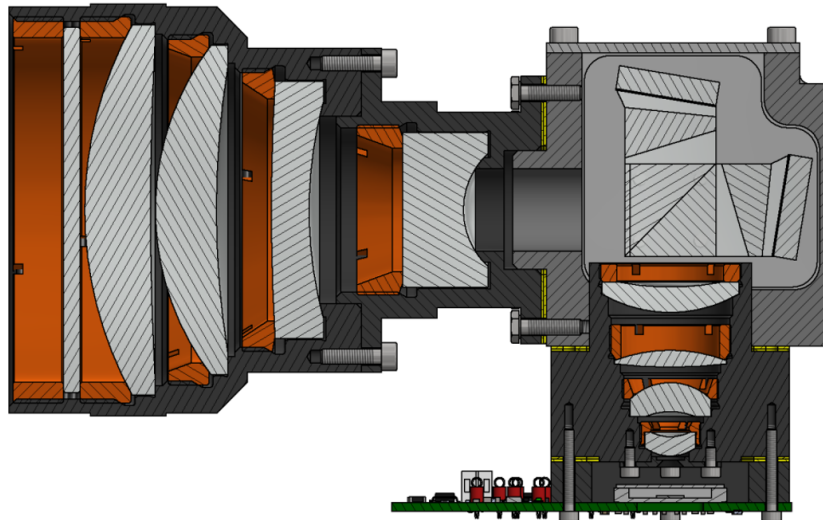
Figure 5.52.: Optical assembly (with PXE) of the AtmoHIT instrument (Rottland, 2016).

Figure 5.53.: Assembled optics (without PXE and filter) of the AtmoHIT instrument.

5.4. Thermal Design

The thermal design of AtmoCube-1 is passive in general and similar to most other CubeSats. The only active component is a heater integrated into the battery pack as a standard component. The reason for the passive thermal design is the limited available power, volume, and mass. This brings also the advantage that many features are common in the thermal design of CubeSats. Thus, design by similarity can be applied at conceptual level, as it is used in this work. The satellite bus is expected to thermally behave similarly to the PolarCube satellite bus, see Deiml (2013). Thus, only special considerations for the AtmoCube-1 thermal design are described, followed by a more detailed description of thermal aspects for the AtmoHIT experiment.

5.4.1. Conceptual Design for the AtmoCube-1 Instrument

These design considerations include the temperature stabilization of the spectrometer and the selection of a thermally highly stable optical filter, with additional information in Chapters 5.2.4 and 5.2.5. The survivability during continuously looking into the Sun and the dimensioning of the radiator plate for passively cooling the detector are two additional aspects that are discussed in the following:

Looking constantly into the Sun would result in a thermal load on the detector of approximately 1.6 W, assuming a solar constant of $1367\,\mathrm{W\,m^{-2}}$ (Wertz and Larson, 1999). However, the optical bandpass filter has an high out-of-band rejection rate with a reflective coating that essentially blocks all radiation. Thus, continuously staring into the Sun can be survived from a thermal standpoint.

The detector needs to be cooled during operations to reduce the dark current. This is especially important during nighttime operations, because the integration time is approximately a factor of 10 higher than during daytime. The detector is cooled passively with a radiator plate directly next to it. The temperature of the radiator can be calculated by Equation 5.26. In the Equation, $\dot{Q}$ is the heat that needs to be dissipated by the radiator, ϵ the emissivity factor of the radiator coating, l and b the length and width of the radiator panel, σ_S the Stefan-Boltzmann-constant, and T_{space} the background temperature of space.

$$T_{radiator} = \left(\frac{\dot{Q}}{\epsilon l b \sigma_S} + T_{space}^4 \right)^{0.25} \tag{5.26}$$

The emissivity of black-velvet coating with $98\,\%$ and the values for width and length from the geometry of the satellite are used to calculate the radiator temperature. Under nominal operations, the detector and PXE dissipate approximately 2.5 W. Then, the radiator panel cools down to approximately $-17\,^{\circ}\mathrm{C}$. The steady-state temperature of the detector is virtually the same as for the radiator because it is only $6\,\mathrm{mm}$ apart from the radiator panel and connected with highly conductive copper. A temperature of $-17\,^{\circ}\mathrm{C}$ is within the operational range of the detector and low enough to be able to neglect the dark current, see Deiml et al. (2017a) for more information. Thus, the measurement simulation (Chapter 4.3.3) uses also a dark current of $0.3\,\mathrm{e^-/s/pixel}$ for a temperature of $-10\,^{\circ}\mathrm{C}$ as a conservative estimate.

5.4.2. AtmoHIT Specific Thermal Analysis and Design

Subsystem specific temperature limits and the thermal environment for different mission phases are briefly described first, because they deviates from the typical CubeSat thermal environment. Aftewards, the AtmoHIT specific thermal design is introduced.

5.4.2.1. Subsystem Temperature Limits

The AtmoHIT experiment is designed to operate in a temperature range between $-10\,°C$ and $50\,°C$. Some subsystems have larger operational temperature ranges, shown in Table 5.12. The temperature limits for the optical components have already been discussed. The lower temperature limit of the VisCAM is factory-set to protect the battery. The temperature limit still stays the same even as the battery is not inserted in the VisCAM for AtmoHIT. The upper and lower temperature limits for the electronics and detector are standard limits for commercial hardware.

Table 5.12.: Survival and operational temperature limits for subsystems of the AtmoHIT experiment.

Component	Operational T (Min/ Max) [°C]		Survival T (Min/ Max) [°C]	
SHS	-10	50	-50	85
Electronics	-40	85	-40	85
Detector	-30	55	-40	85
VisCAM	-10	70	-40	85
Optical Filter	-10	50	-50	85

5.4.2.2. Thermal Analysis

The thermal environment in different mission phases is derived from experience from previous REXUS flight campaigns and is strongly dependent on the local weather.

In the pre-launch phase during transport, the experiment may need to sustain temperatures down to $-30\,°C$ for several hours. The experiment is not expected to operate during these conditions. Thus, this temperature value is within the survival limits of the experiment components. The temperature of the experiment is controlled to approximately $(17 \pm 7)\,°C$ within the launcher housing. This is within the operational temperature range of the experiment and the experiment is expected to also operate under these conditions.

Two major heat sources contribute to warming of the experiment during the flight phase. The rocket motor produces heat which is transported conductively to the service module and experiments. But its influence on the AtmoHIT instrument is deemed negligible, because the experiment is located directly below the nose cone - furthest away from the motor. However, the nosecone and the first module experiences high temperatures with peaks above $200\,°C$, due to air friction. The spectrometer and VisCAM windows might experience such high temperatures and need to be able to cope with them. All temperature critical components are thermally well isolated to the windows and module hull. Thus, these increased temperatures during flight are estimated to be within their operational temperature limits.

Like the pre-launch phase, the experiment may need to endure temperatures of $-30\,°C$ for several hours after the instrument landed in the snow. The experiment is non-operational during this phase and the temperature is within the survival range of all critical components.

5.4.2.3. Thermal Design

The thermal design of AtmoHIT builds upon the design of the AtmoCube-1 satellite. The difference is that the radiator panel for the detector is not useful as it looks to the warm rocket hull instead of to cold space. Therefore, the radiator is also not painted with black color.

The windows will experience high temperatures as discussed before. The selected Borofloat glass for both windows can sustain temperatures up to $500\,°C$ and has also a high thermal shock resistance. Compared to the lenses in the optical assembly, the windows are mounted with o-rings into the structure to allow for larger thermal deformations of the structural parts surrounding them.

The last special aspect for AtmoHIT is the potential water condensation on optical elements. Deiml et al. (2017a) discusses this aspect extensively with the conclusion that water condensation on the outer

windows and on the first optical element of the spectrometer is most unlikely to appear and if it appears that it gets removed before the measurement altitude is reached.

Several sensors are included in the AtmoHIT experiment to monitor the temperature of critical components. More specifically, temperature sensors are attached to the optical filter, to the SHS, and to the detector. In addition, the electronics includes a few internal temperature sensors on the boards and an external sensor measures the temperature in the nose cone.

5.5. Electrical Design

The electronics for the AtmoHIT experiment is the precursor electronics for the AtmoCube-1 experiment. It consists of four parts. The PSU simulates the satellite bus and is used in the AtmoHIT experiment as an interface between rocket service model and the instrument electronics. The instrument electronics consists of the Front-End Electronics (FEE) that is connected to the PXE by a flexible board-to-board connector. The FEE includes an SD-card for data storage and a commercial System-on-a-Chip (SOC)-board with a Field Programmable Gate Array (FPGA) and a dual-core processor for data processing. The PXE houses the Complementary Metal-Oxide-Semiconductor (CMOS) detector and is directly screwed onto the optical assembly. In addition to the actual CubeSat instrument, the AtmoHIT experiment includes a camera in the visible range (VisCAM). This camera is connected to the FEE via an interface board. The interface board is necessary, because the grounding of the satellite instrument is floating to avoid any interferences with other instruments onboard the rocket. Figure 5.54 shows the boards with the connections between them. Detailed information about the electronics can be found in the Master thesis of Denis Fröhlich (Fröhlich, 2016) and in Deiml et al. (2017a).
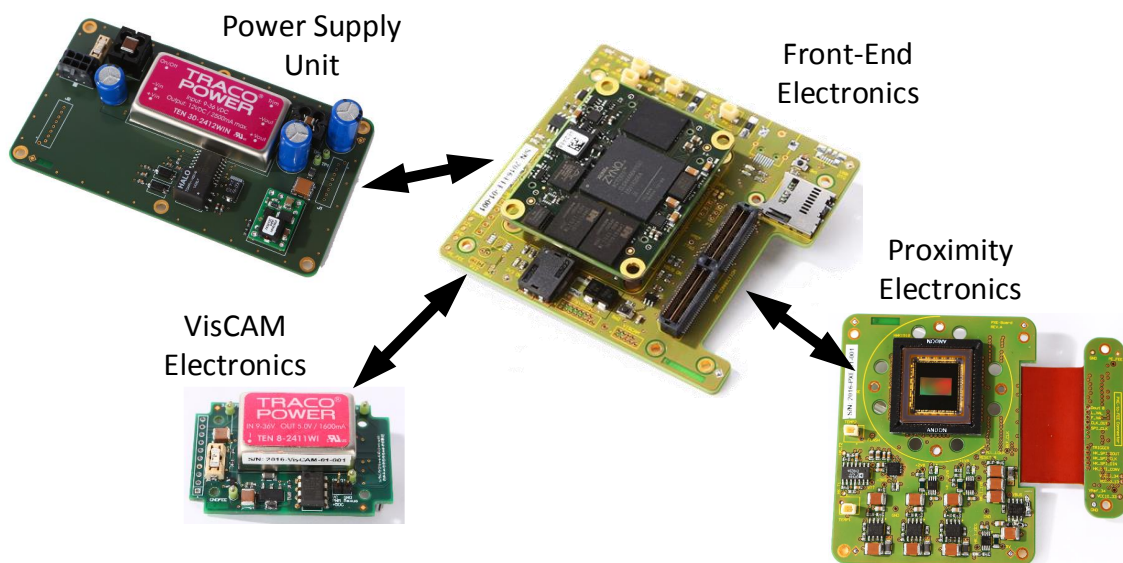
Figure 5.54.: Electronics of the AtmoHIT experiment with power supply electronics, front-end electronics, VisCAM electronics and proximity electronics (Fröhlich, 2016).

6. Characterization and Calibration

The characterization and calibration of the AtmoHIT instrument is not discussed in detail in this work as it is part of another PhD thesis (Liu, 2018, in preparation). The following introduction into this topic describes the different aspects that need to be addressed to derive temperatures from emission spectra. As characterization and calibration is not the focus of this work, the next Chapter 7 shows data which is only "mildly" post-processed and does include artifacts that can be removed with the following corrections and calibrations.

6.1. Pixel Response Non-Uniformity Correction

The name pixel response non-uniformity correction describes already quite precisely the characterization step. Each pixel on the detector has slightly different gains and offsets which need to be corrected to achieve an uniform image. This correction is performed with the detector alone. A clear indicator that the pixel response non-uniformity correction was not performed in the next chapter is the existence of hot pixels in the interferograms.

6.2. Dark Current Removal

The dark current of the detector is a constant offset added to the actual signal and it is pixel and temperature dependent. It can be separated from the signal once it is characterized independently in a dark room for different temperatures and for each pixel. The remaining noise is the shot noise of the dark current which contributes directly to the S/N-ratio. Without removal, the pixel non-uniformity of the dark current reduces the measurement precision.

6.3. Flat-Fielding

Flat-fielding describes the correction of differences in the optical properties of the two arms in the SHS and of the optical path in general. The beamsplitter is not ideally dividing the light in half and also the gratings may have slightly different diffraction efficiencies and imperfections. Also, the overall optics has a varying MTF for different field points which needs to be compensated for. Flat-fielding is a common correction applied to Fourier-transform spectrometer and Englert and Harlander (2006) described multiple approaches to flat-field SHS. The optical and mechanical design of the instrument considers also flat-fielding: Both interferometer arms are accessible in the fully mounted optical assembly and the spacers are hollow. Thus, shutters can be inserted for the correction measurements.

6.4. Phase Correction

The process of phase correction minimizes the phase error of the interferogram. In theory, the SHS interferogram has a constantly increasing phase over the spectral dimension with zero phase in the center for a specific wavenumber. The slope of this line is also constantly increasing with distance from the Littrow wavenumber. It can be described with the planar relation $\phi = a(\sigma - \sigma_L)x$, where ϕ equals the phase, a is a generic slope parameter, σ the emission line wavenumber, σ_L the Littrow wavenumber, and x the position on the detector in spectral direction. In practice, the SHS does not perfectly fulfill this equation. The task of the phase correction is to minimize this error. Englert et al. (2004) described different processes to correct the phase. The largest influence on the phase distortion for the AtmoHIT optics is field-curvature, because it virtually introduces spatial frequency components around the actual

spatial frequency of the emission line. Without phase correction, the spectral resolution is therefore degraded.

6.5. Relative Calibration

The relative calibration has the goal to characterize the intensities of spectral peaks for individual emission lines, because the performance of the instrument is dependent on wavenumber. This dependence needs to be calibrated. Otherwise, it is not possible to retrieve precisely the peak intensities in an A-band interferogram. In this regard, it is also important to characterize the spectral leakage in multi-line interferograms to compensate for unwanted intensity contributions of neighboring peaks. Without a relative calibration, the ratio of peak heights in interferograms are not solely temperature dependent and introduce errors in the temperature retrieval.

6.6. Applied Post-Processing in this Work

Characterization and calibration is a necessary and important step to reach high precision interferograms, useful for temperature retrieval. The characterization and calibration is not performed in detail in this work. The experimental results in the following chapters are not the final products of the AtmoHIT experiment, because only limited post-processing was applied and calibration data was not used. The experimental data are analyzed using the following post-processing procedures for the detector images:

1. Cropping of the detector image
2. Flatfielding with 2nd order 2D-polynomial
3. Apodization with 2D rotational symmetric Hanning function
4. 2D zero-padding
5. 2D-Fourier-transformation
6. Fitting of Gauss-surface on 2D-spectrum
7. Fitting of non-linear SHS equation to data

All operations are performed in the 2-dimensional domain to remove interference effects from not perfectly parallel fringes relative to the spatial direction. Step 6 extracts the spatial frequencies of the spectral peaks in dependence of emission line wavenumber. Applying step 7 retrieves the Littrow wavenumber and the magnification factor of the detector optics with its errors. The fit could be also performed with the Littrow wavenumber and the grating groove density, because the grating groove density and the magnification factor are correlated in this analysis, see Chapter 4.3.2. However, the grating groove density has tight tolerances according to the manufacturer, which cannot explain the experimental data. Nevertheless, the grating groove tolerance introduces a small systematic error in the magnification factor fit result.

7. Verification

The AtmoCube-1 instrument is verified in its version for the AtmoHIT experiment in multiple stages during assembly, calibration, and through a sounding rocket flight campaign. Overall, two AtmoHIT experiments have been built. The assembly procedures have then been tested with and enhanced on the first instrument. Also, most tests have been thoroughly performed for the first instrument. Only the most important verification tests have been performed with the second instrument. Calibration was performed with both instruments. The second instrument was flown on the rocket flight campaign. The following chapters use results from both instruments.

In this chapter, the most important tests are described to demonstrate that the instrument provides the functionality and the performance as designed. The first tests of the first instrument demonstrate the optical performance: Interferograms and spectra of single laser emission lines and a combination of single interferograms to simulate the oxygen A-band emission are used to analyze the spectroscopic quality of the instrument. Their description is followed by a demonstration of the structural stability of the instrument through vibration tests. A discussion of the performed thermal vacuum chamber tests on the first instrument shows the survivability of the instrument in a wide temperature range and under vacuum conditions. This chapter also verifies the temperature stability of the spectrometer. The verification chapter is concluded by a detailed discussion of the sounding rocket flight campaign, where the second instrument was demonstrated in its nominal operational environment.

7.1. Optical Bench Tests

7.1.1. Interferograms from Laser Light Source

The emission of a laser light source provides a narrow band spectral line, resulting in a single spatial frequency and a single spectral peak. The first optical bench tests have used emissions from a tuneable laser light source to verify that the spectrum looks as expected. The absolute laser wavenumber could not be determined accurately and analysis suggests a systematic error of $\pm 0.24 \, \text{cm}^{-1}$ for the laser wavenumber. However, the relative laser wavenumber knowledge is sufficient for all these tests to calculate the relevant properties of the instrument. Figures 7.1a and 7.1b show the interferograms for two different laser wavenumbers ($13\,084.0 \, \text{cm}^{-1}$ and $13\,112.0 \, \text{cm}^{-1}$). The fringe frequency gets higher with increasing distance from the Littrow wavenumber ($13\,127.0 \, \text{cm}^{-1}$). Also, a slight tilt of the fringes is visible in the images. The tilt decreases with increasing spatial frequency. Its origin is a constant spatial frequency in vertical direction, resulting from a relative tilt of the two interferometer arms in this direction.

These images are measurements from the first instrument. It was tested at multiple facilities, which not all have been clean rooms. Thus, a comparatively large amount of particles is visible on the gratings. The gluing process resulted also in unwanted glue in the outer areas of the gratings that moved further inwards through the capillary effect, visible in the darker areas. However, there is still a large glue free area that can be used without considering the glue further.

Specifically, the areas within the black rectangles in Figures 7.1a and 7.1b are used for Fourier-transformation to retrieve the spectra, shown in Figure 7.2. The spectra were obtained with the post-processing, described in Chapter 6.6. Both spectra have small sides peaks towards smaller spatial frequencies next to the main peak. These side peaks stem from the uncorrected field-curvature in the interferogram.

The positions of the laser lines are marked with dashed, green lines. The actual parameters of the SHS could be derived by fitting the spectral peaks to the theoretical peaks, resulting in a Littrow wavenumber of $(13\,128.2 \pm 0.2) \, \text{cm}^{-1}$ and a magnification factor of the detector optics of 0.57 ± 0.01. This magnification factor shows that the SHS is displaced by approximately $1.5 \, \text{mm}$ in vertical direction further away from the detector optics, because no additional shims have been added to the nominal number of shims. Thus, the magnification factor should be 0.6, according to the analysis of Chapter 5.2.7.2. The

assumption of a vertical displacement of the SHS is also confirmed in the thermal vacuum chamber tests (Chapter 7.3).

The bandwidth of the laser emission is small enough that it can be neglected compared to the spectral resolution. The spectral resolution of the instrument is insofar important to analyze, because a sufficient high value is necessary to resolve the fine structure. Thus, the next section explains the simulation of the oxygen atmospheric band spectrum.

(a)   (b)
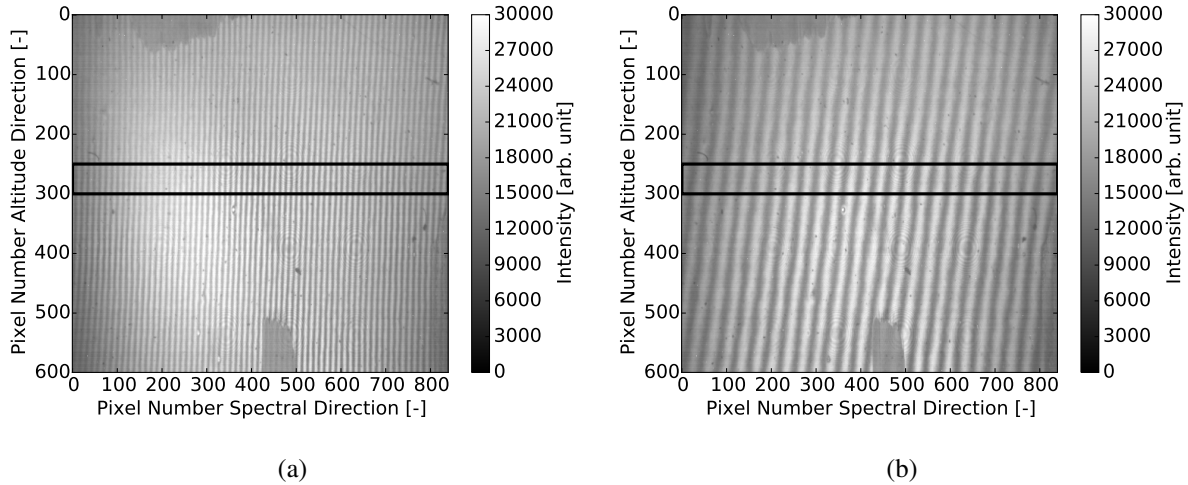
Figure 7.1.: Unprocessed interferograms for laser wavenumbers $13\,084.0\,\mathrm{cm}^{-1}$ (7.1a) and $13\,112.0\,\mathrm{cm}^{-1}$ (7.1b). The black rectangles show the areas that are used for Fourier transformation.

(a)   (b)
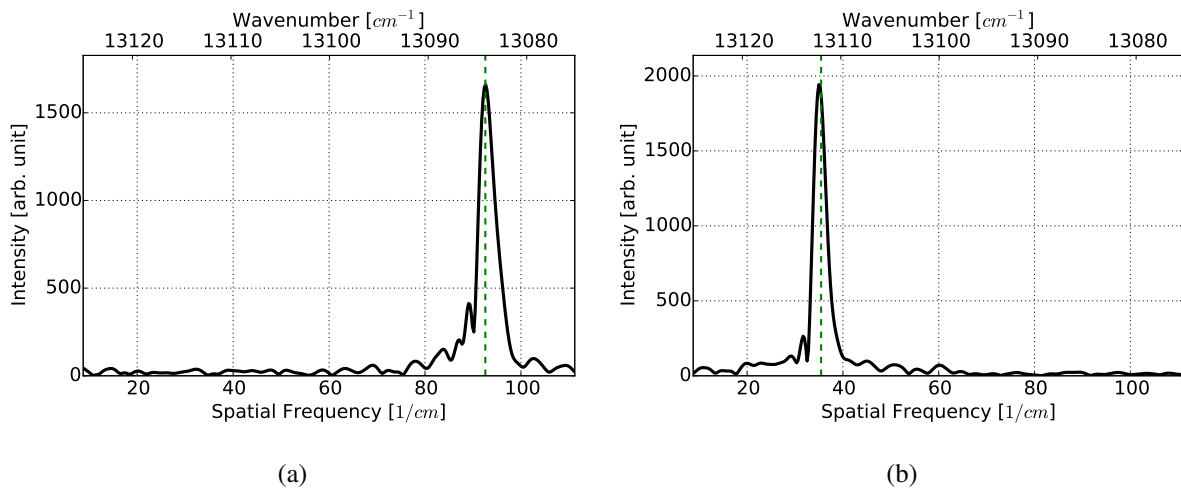
Figure 7.2.: Apodized and zero-padded spectra for laser wavenumbers $13\,084.2\,\mathrm{cm}^{-1}$ (7.2a) and $13\,112.0\,\mathrm{cm}^{-1}$ (7.2b). The vertical green dashed lines show the theoretical positions of the laser lines.

7.1.2. Oxygen A-band Like Spectrum with Laser Light Source

The oxygen A-band spectrum is simulated with a laser light source by tuning the laser to the wavenumber of the emission lines of oxygen, one after the other. Subsequently, interferograms are recorded by the detector and stored on the SD-card. In the post-processing, these individual interferograms are summed up and finally regarded as a single interferogram of the oxygen A-band emission. The data is post-processed as described in Chapter 6.6.

The resulting spectrum is shown in Figure 7.3. As before, the dashed green lines correspond to the theoretical position of the emission lines and the emission peaks overlap very well with these lines for a Littrow wavenumber of $13\,128.2\,\mathrm{cm}^{-1}$ and a magnification factor of the detector optics of 0.57, as before.

The individual fine structure lines can be resolved with the instrument and the spectrum looks similar to the computer-generated oxygen A-band emission spectrum of Figure 4.19a. The two differences

to the simulated image are on the left and right parts of the spectrum. The two emission lines with spatial frequencies of $26 \, \mathrm{cm}^{-1}$ and $30 \, \mathrm{cm}^{-1}$ have not been simulated with laser light and the two highest emission peaks are not very well distinguishable anymore from background noise, which relates to a reduced resolving power.
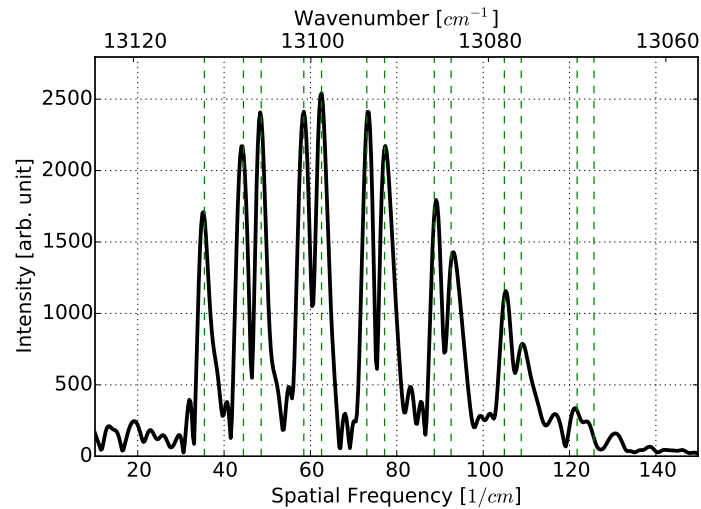
Figure 7.3.: Apodized and zero-padded simulated A-band emission spectrum. The vertical green dashed lines show the theoretical position of the laser lines.

The spectrum is therefore analyzed for resolving power like in Chapter 4.4.3. Each laser emission peak is analyzed separately. The resulting Figure 7.4 shows the resolving power in dependence of spatial frequency and wavenumber, respectively. The included apodization reduces the resolving power compared to the resolving power of an idealized SHS spectrum. It is acceptable as individual peaks are still resolvable and side-lobes are significantly better suppressed. The figure shows that the resolving power decreases approximately linearly with spatial frequency from 8000 to 4000. The resolving power decreases significantly compared to the analytically calculated almost constant resolving power of 9260 ± 253. The difference lies in the not-ideal optics. The MTF of the optics gets worse for higher spatial frequencies, see Figures 5.26 and 5.28. Thus, the contrast decreases and more information leaks to neighboring pixel bins, which broadens the spectral peaks and reduces essentially the resolving power.
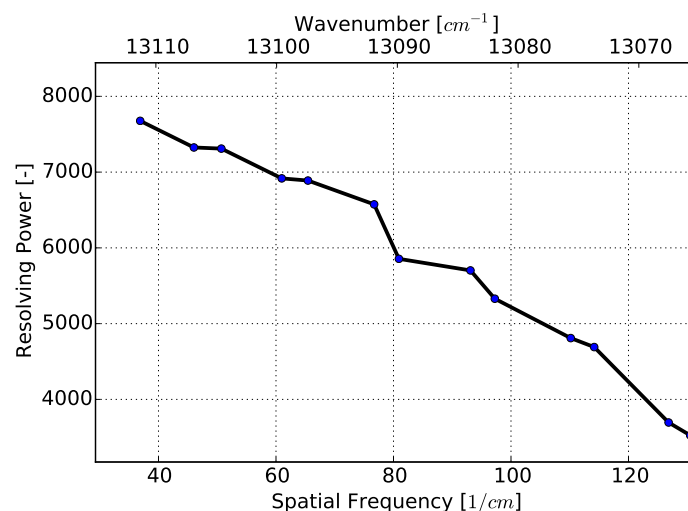
Figure 7.4.: Resolving power in dependence of wavenumber and spatial frequency.

7.2. Vibration Test

A vibration test was performed on each instrument to simulate the conditions of the REXUS rocket launch at acceptance level. The vibration test was divided into a sinusoidal vibration test at $4.0\,g$ between $50\,Hz$ and $2000\,Hz$ and a random vibration test with $6.0\,g$ RMS between $20\,Hz$ and $2000\,Hz$ (Power Spectral Density (PSD) $0.018\,g^2\,Hz^{-1}$). Before and after each test, a low level resonance scan was performed to check for anomalies. Accelerations were applied along the z-axis, corresponding to the roll axis of the rocket, and the instrument was operational during the test. Figure 7.5 shows the test setup for the first vibration test at the Center for Applied Space Technology and Microgravity (ZARM).
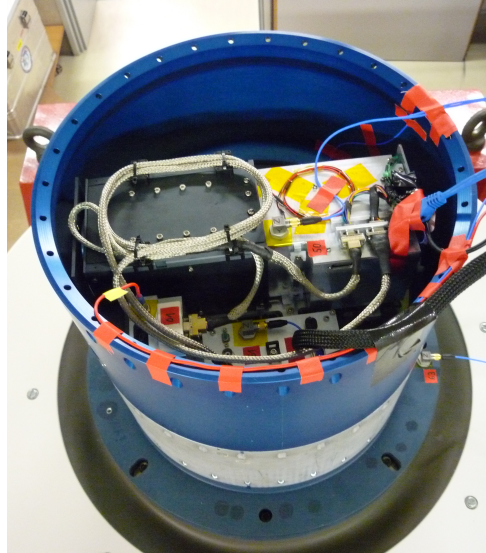
Figure 7.5.: Setup of the vibration test of the AtmoHIT experiment.

Both times, the instruments performed nominal during all stages of the vibration test and major changes in the detector image were not detectable in post-analysis of the data. All mechanical components stayed in place and screws did not loosen. Thus, the vibration test was deemed successful. Detailed test results can be found in test report created by Greif and Kaczmarczik (2016) and Deiml et al. (2017a).

7.3. Thermal Vacuum Chamber Tests

The instrument was tested in a Thermal-Vacuum (T-Vac) chamber at the Research Centre Jülich under various pressure and temperature conditions to verify its survivability and its performance within the designed operating conditions. Specifically, the instrument was tested within a temperature range from $-21.7\,°C$ to $46.7\,°C$ and between a pressure range from $15\,hPa$ to $1013\,hPa$. The instrument was operated continuously during these conditions and all subsystems behaved nominal.

Figure 7.6 shows the setup within the T-Vac chamber. Radiation around $762\,nm$ is provided by a tuneable laser that is located outside the T-Vac chamber. A glass fibre cable from the laser to a collimator introduces light into the chamber. The coherence of the laser beam gets destroyed by a speckle disk and an Ulbricht sphere distributes the light evenly for all exit angles. It is the light source for the instrument. The instrument is connected to the ground station via the standard interface and with an additional Ethernet connection for fast image repetition frequency. The temperature is measured on multiple points of the instrument and the internal chamber temperature is controlled by measurements of an additional temperature sensor.

Figure 7.6.: Setup for the T-Vac tests of the instrument at the Research Centre Jülich.

Three quantitative useful tests were performed in the T-Vac chamber to validate the performance of the SHS. The first test verifies the Littrow wavenumber. The instrument was designed with a Littrow wavenumber of $13\,127\,\mathrm{cm}^{-1}$ in vacuum and a grating groove density of $1200\,\mathrm{lines/mm}$. At a temperature of $-4\,°\mathrm{C}$ and a pressure of $15\,\mathrm{hPa}$, the laser was tuned to simulate the emission lines of the A-band. Figure 7.7 shows the resulting plot of the analysis. The errors of the spatial frequency estimation are below the point size of the plot. The Littrow wavenumber is with $(13\,128.4 \pm 0.2)\,\mathrm{cm}^{-1}$ very close to the design Littrow wavenumber and within the manufacturing tolerance. The magnification factor of the detector optics is calculated to 0.49 ± 0.01. The magnification factor deviates considerably from the design value, which is also expected. The SHS is displaced vertically by $1.5\,\mathrm{mm}$ for the first AtmoHIT experiment, as discussed before. Thus, the magnification factor for the nominal number of shims is 0.57. But in difference to the optical bench tests, seven additional $0.5\,\mathrm{mm}$-shims were added between SHS and detector optics for these T-Vac tests. The optical analysis for a $5\,\mathrm{mm}$ deviation from nominal distance between SHS and detector optics results in a magnification factor of 0.5, which is close to the experimentally derived magnification factor. Overall, these results show that the different magnification factors can be explained by different numbers of shims and a vertical displacement of the SHS by $1.5\,\mathrm{mm}$.
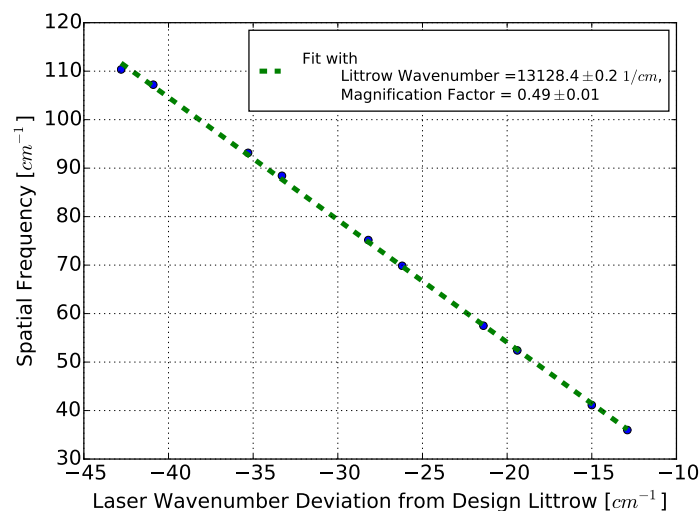
Figure 7.7.: Measured spatial frequencies in dependence of laser emission wavenumber relative to the design Littrow wavenumber.

The second test in the T-Vac chamber was performed to analyze the pressure dependence of the Littrow wavenumber, as discussed in Chapter 5.2.4. The laser was set to $13\,114.1\,\mathrm{cm}^{-1}$ and the SHS had an average temperature of $45\,°\mathrm{C}$. During the test, the pressure was increased from $15\,\mathrm{hPa}$ to $1013\,\mathrm{hPa}$, while keeping the pressure constant for more than 10 measurement samples approximately every $100\,\mathrm{hPa}$. The curve in Figure 7.8 shows a linear correlation, as it is also expected from numerical analysis. The temperature stays almost constant for low pressures and decreases with increasing pressure due to

convection within the T-Vac chamber. The temperature dependence of the Littrow wavenumber can be neglected for this analysis.

The Littrow wavenumber for vacuum conditions fits also reasonably well to the result from above with considering the uncertainty in absolute laser wavenumber determination precision. More importantly, the Littrow wavenumber increases by approximately $1.29\,\text{cm}^{-1}$ from vacuum to ambient air conditions. The trend verifies the analytic model, also with a change of $1.31\,\text{cm}^{-1}$, refer to Chapter 5.2.3.

The third test analyzed the Littrow wavenumber temperature dependence. Chapter 5.2.4 described the Littrow wavenumber temperature stabilization. This test demonstrates that the design goal of low temperature dependence is successfully achieved. Quantitative test data was only taken for the temperature range from $27\,^\circ\text{C}$ to $40\,^\circ\text{C}$. However, qualitative test data with pictures of the interferograms for low temperatures showed also that the fringe frequency changes only very little, like for the upper temperature range. Thus, it is reasonable to extrapolate the data within the operational temperature range. Figure 7.9 shows the result of the analysis. The same post-processing was applied as for the two other tests. The test was performed at ambient pressure and thus the deviation from design Littrow wavenumber is larger compared to test 1 and in alignment with data from test 2. The gradient for the Littrow wavenumber temperature dependence lies between the value from the analytic and numeric solution.
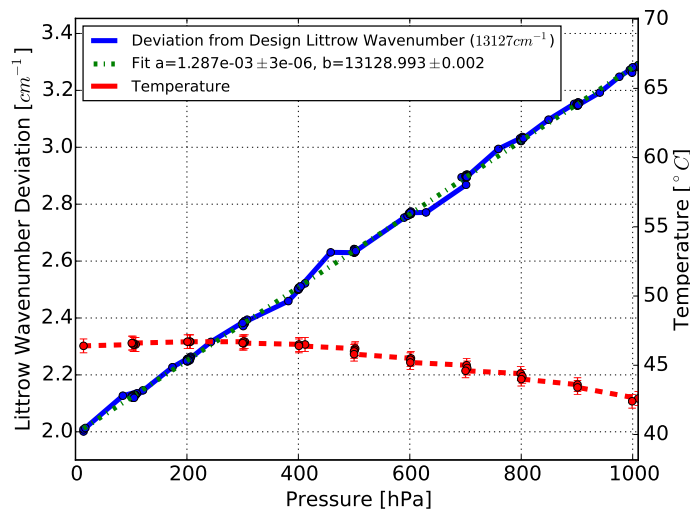
Figure 7.8.: Littrow wavenumber deviation in dependence of pressure with temperature change during test. The laser was tuned to a wavenumber of $13\,114.1\,\text{cm}^{-1}$.
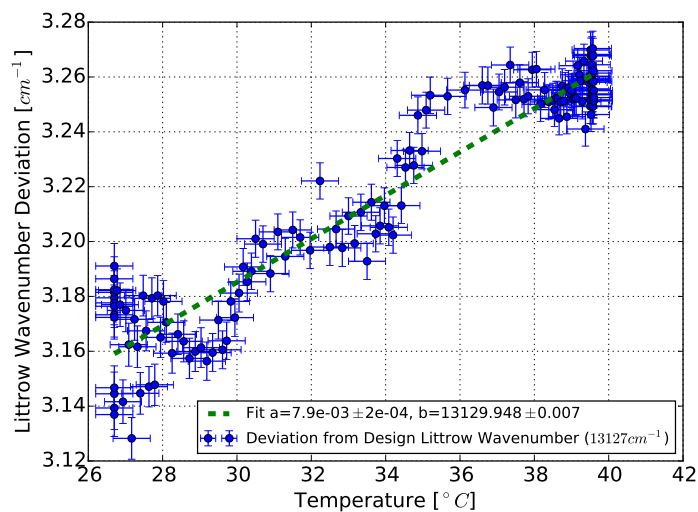
Figure 7.9.: Littrow wavenumber deviation in dependence of temperature for ambient pressure conditions and a laser wavenumber of $13\,114.1\,\text{cm}^{-1}$.

With the T-Vac tests, it was verified that the instrument performs well in its operational temperature range. The maximum operational range of $50\,^\circ\text{C}$ was not fully reached for the SHS (maximum tempera-

ture $46\,°C$), because the electronics got so warm that the test was stopped before reaching its operational temperature range. The lower temperature range was well reached with more than $10\,°C$ lower temperatures than the minimum operational temperature. The filter was not tested during this test and it was relied on the manufacturer specifications. The full survival temperature ranges of the components have not been verified.

7.4. Sounding Rocket Flight Campaign

7.4.1. General Remarks

The final and most important test for the instrument was the sounding rocket launch campaign. The AtmoHIT experiment was launched on a REXUS 22 rocket on 16th of March 2017 at 12:58 UTC. Prior to the launch, both assembled instruments were tested and calibrated to verify that all components work. The instrument was integrated into the REXUS 22 rocket, together with the other experiments, the service module, and the rocket motor. Figure 7.10 shows the fully assembled rocket on its way to the launcher and Figure 7.11 depicts an image taken during the first seconds after lift-off.

Figure 7.10.: Fully integrated REXUS 22 rocket during roll-out before integration into the launcher.

Figure 7.11.: Launch of the REXUS 22 rocket on 16th of March 2017 at 12:58 UTC.

$140\,s$ after lift-off, the rocket reached a ceiling altitude of $84.3\,km$ and landed nominally at its parachute north of Esrange in the snow. It was recovered a few hours later by a helicopter. The flight path of the rocket is shown in Figure 7.12, simulated with the software tool Systems Tool Kit (STK) and with the actual GPS data.
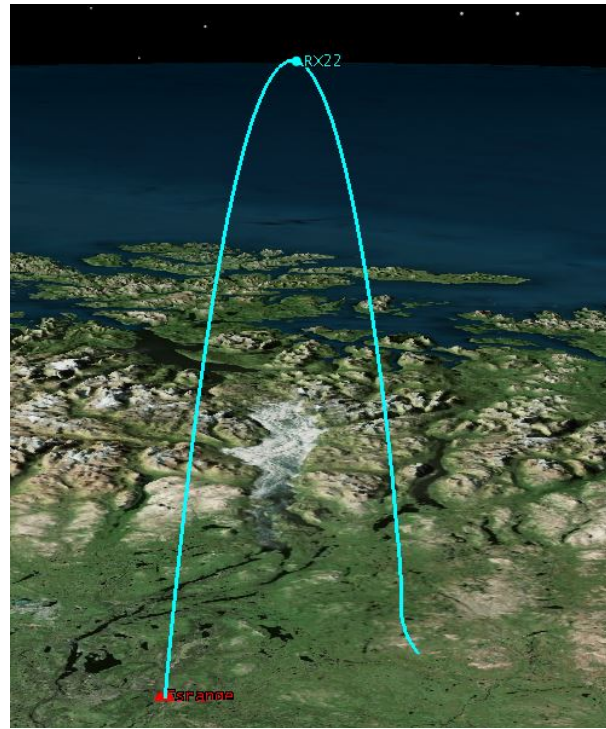
Figure 7.12.: Flight path of REXUS 22 with ceiling altitude of $84.3\,\mathrm{km}$, simulated in STK with GPS data from DLR MORABA with permission.

During the acceleration phase, the rocket spun up to a roll-rate of approximately $1000\,°/\mathrm{s}$. The Yoyo-mechanism to reduce the roll rate after motor burn out was very well balanced, because the roll rate was reduced to only $2\,°/\mathrm{s}$. Unfortunately, an anomaly appeared $68\,\mathrm{second}$ into the flight during motor separation and the payload segment started to tumble quite considerably in all axes. Figures 7.13 show the rotation rate data from the service module during the whole flight (Figure 7.13a) and for the time interval that includes the Yoyo-despin and the motor separation (Figure 7.13b). In Figure 7.13b, the start of the tumbling with motor separation is clearly visible. The rocket rotates in all three axes by more than $100\,°/\mathrm{s}$. The roll rate was reduced to low values again during a $20\,\mathrm{s}$ time interval by another experiment. The other two rotation rates stabilized then. Overall, the strong tumbling of the rocket was detrimental to the AtmoHIT experiment, because it reduced the time the spectrometer looked towards the limb. Subsequently, many images have been saturated and some images had little to no signal.

| (a) | (b) |
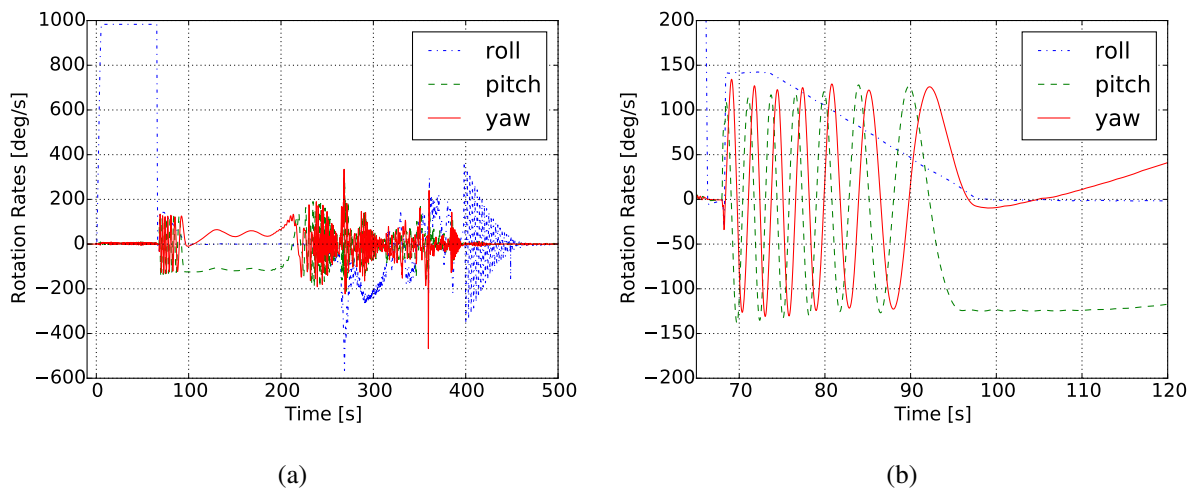
Figure 7.13.: Roll, pitch, yaw rates in $\deg/\mathrm{s}$ from T-10 s to T+500 s (7.13a) and from T+65 s to T+120 s (7.13b). Data from DLR MORABA with permission.

The rocket passed the altitude level of $60\,\mathrm{km}$ between T+69.4 s and T+211.8 s, resulting in a measurement time of $142\,\mathrm{s}$. Of these 142 pictures, approximately $50\,\%$ are saturated (Mean intensity larger than $80\,\%$ of maximum detectable intensity). However, a few images are still useful for analysis and demonstrate

the measurement principle.

7.4.2. Analysis of Example Oxygen A-band Spectrum

Figure 7.14 shows an example interferogram and the corresponding scene at an altitude of $82.6\,\mathrm{km}$. The image shows the timestamp with the convention s.ms with zero at lift-off in the upper left corner. The small rectangle in the middle of the image corresponds to the interferometer FOV of $1.3°$. Its exact position is not known, because an exact alignment of the spectrometer relative to the VisCAM was not possible. The yellow line depicts the altitude range between $60\,\mathrm{km}$ and $120\,\mathrm{km}$ for tangential points. The instrument FOV is just above this altitude range, but it moves through the altitude range during image acquisition. The integration time of $1\,\mathrm{s}$ together with the tumbling of the instrument results in a fairly large altitude range that is covered. The instrument FOV first views the Earth´s surface for approximately $0.25\,\mathrm{s}$, then the limb for approximately $0.03\,\mathrm{s}$, and finally space for this example interferogram.

The interferogram includes the full read-out area of the detector, also with areas that are not further post-processed. On the sides, the glue covered grating area results in peak-like darker areas reaching towards to the center of the image. These areas are excluded in the post-processing. The fringe pattern of overlapping fringe frequencies is clearly visible in the center of the image. It gets less clear towards the corners, because the image has an approximately quadratic envelope that can be removed by flat-fielding. Thus, also the image gets darker towards the corners. The white strips in the image are read-out errors and also some hot pixels are visible in this raw detector image.

Approximately half of the radiometric bandwidth of the detector is used for this measurement. Most of the radiant flux is collected during the first segment viewing towards the Earth´s surface, increasing the background signal. However, because it is only $0.25\,\mathrm{s}$, the detector is not saturated. The limb measurement time is very small, but the instrument itself is still within the emission layer. Thus, some light is collected during space view. The two aspects of space view and Earth´surface view are also further analyzed below. The image series of the VisCAM that corresponds to the here described interferograms is shown in Appendix D.

(a)   (b)
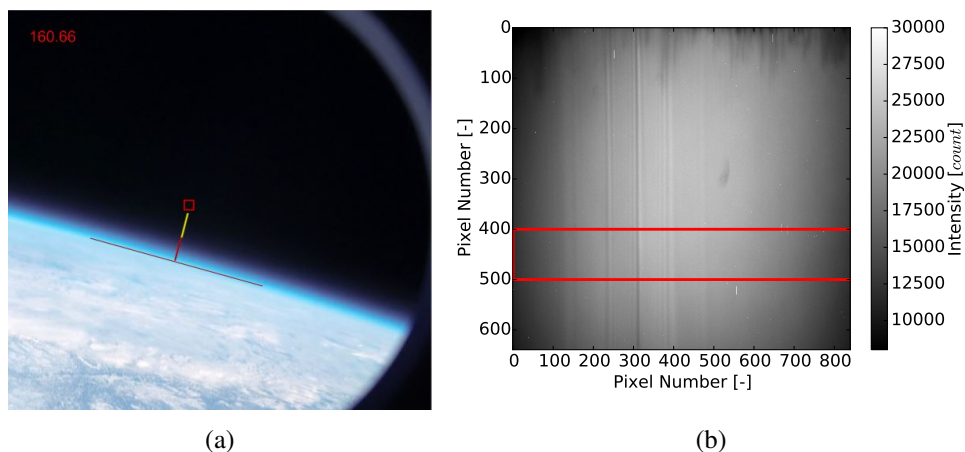
Figure 7.14.: Scene in the atmosphere and corresponding interferogram at an altitude of $82.6\,\mathrm{km}$. The small red rectangle in the left image illustrates the FOV of the instrument and the yellow lines corresponds to the altitude range from $60\,\mathrm{km}$ to $120\,\mathrm{km}$. The red rectangle in the right image shows the area that is Fourier-transformed.

The analysis of the interferogram results in a spectrum without considering the height resolving properties of the instrument. The tumbling of the rocket motor renders it meaningless. The post-processing is similar to the post-processing method described in Chapter 6.6. The interferogram already shows that fringes can be approximated as parallel to the spectral axis. This is also verified in the analysis. Therefore, Figure 7.15 shows the interferogram for zero spatial frequency perpendicular to the spectral direction instead of a two dimensional spectrum. The spectrum was recorded with the second assembled instrument. Thus, the instrument characteristics are different than previously described and needs to be analyzed, again. The same process as in Chapter 7.3 was applied to calculate the Littrow wavenumber to $(13\,129.8 \pm 0.1)\,\mathrm{cm}^{-1}$ (air) and the magnification factor to 0.57 ± 0.01. The magnification factor indicates also that the distance between SHS and detector optics is $1.5\,\mathrm{mm}$ larger than the nominal

distance. The instrument characterization was performed with a tuneable laser in air conditions. Thus, the Littrow wavenumber is corrected for vacuum condition by subtracting $1.29\,\mathrm{cm}^{-1}$, assuming that both instruments have a similar Littrow wavenumber pressure dependence.

Figure 7.15 shows that the oxygen A-band spectrum can be well described with the laboratory calculated instrument characteristics and the simplified post-processing. Each pair of theoretically calculated emission peaks fits to the spectral peaks in the atmosphere. The intensities of the two lines for each pair do not need to be the same. Thus, the exact peak position deviates to the left and to the right for some line pairs. The emission peak with lowest spatial frequency does not very well overlap with the theoretical emission peak position. However, applying the process of phase correction is expected to remove this discrepancy.

The resolving power of the second instrument is larger and almost constant compared to the first instrument. It does not reach the theoretical resolving power of 9260 ± 253, but it is close with 8013 ± 668. The higher resolving power is also visible in the spectrum. The emission peaks at $105\,\mathrm{cm}^{-1}$ are still resolvable and only the last pair within the filter bandwidth cannot be very well resolved anymore. However, the effective resolving power in this image is lower than the laboratory calculated resolving power, because noise on the edges of the detector reduces the practically useful interferogram width. Thereby, the noise is generated by the straylight from Earth view during image acquisition and the higher than estimated dark current due to the warm detector.

The SHS and the detector have a mean temperature of $24.4\,^\circ\mathrm{C}$ and $30\,^\circ\mathrm{C}$ for this example picture, respectively. Overall, the mean temperature of the SHS varies between $24.2\,^\circ\mathrm{C}$ and $24.5\,^\circ\mathrm{C}$ and the detector between $28.1\,^\circ\mathrm{C}$ and $31.0\,^\circ\mathrm{C}$ during the relevant measurement time. Thus, the critical components of the instrument stayed in their operational temperature range. The temperature of the instrument was higher than expected, because the experiment directly below AtmoHIT needed to be heated up before launch through air blowers. The higher temperature increased the dark current of the detector significantly, reducing overall the S/N-ratio of the instrument. It was however accepted to not endanger the other experiment.
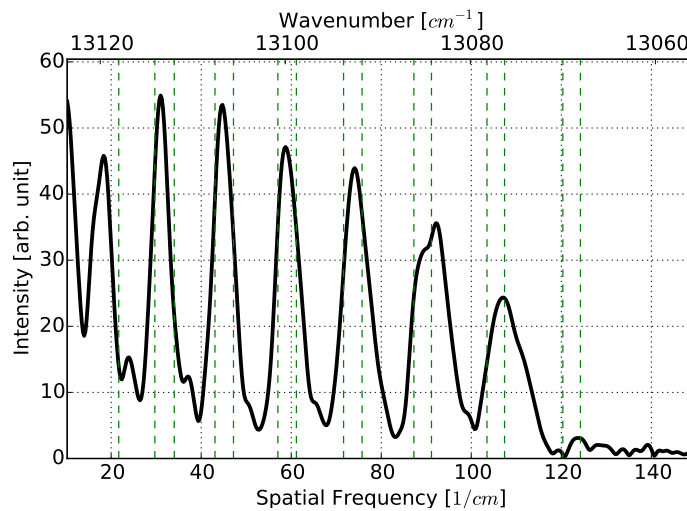
Figure 7.15.: Spectrum at instrument altitude of $82.6\,\mathrm{km}$. The vertical green dashed lines show the theoretical position of the emission lines.

7.4.3. Analysis of Scene between Yoyo-Release and Motor Separation

Figure 7.16 shows the only scene and corresponding detector image, where the instrument was stable while the interferogram was recorded. Appendix D shows the whole VisCAM image series during spectrum acquisition. Unfortunately, the instrument pointed towards deep space and it was at an altitude of $58.3\,\mathrm{km}$, where the oxygen A-band emission is still opaque for tangential emissions. Thus, the straylight from the Sun dominates the image. The incidence angle between Sun and instrument is approximately $20.7°$. The mean intensity of the image is $4.6 \times 10^{10}\,\mathrm{photon/s}$, with considering the mean conversion factor between photons and counts and the number of detector pixels. This mean intensity corresponds to the same radiant flux from the Sun, because the integration time was $1\,\mathrm{s}$.

A radiant flux of 5.3×10^{16} photon/s was calculated in the straylight analysis for the same incidence angle. Thus, the attenuation factor for this angle is 9×10^{-7}. The attenuation factor is two orders of magnitude lower compared to the analytically calculated value. This deviation may also be explained by the uncertainty in the incidence angle estimation. The theoretical value is in alignment with the experimentally calculated one for a $4°$ larger incidence angle. In any case, the straylight analysis overestimates the straylight, which is appropriate for a worst case estimation.

(a)   (b)
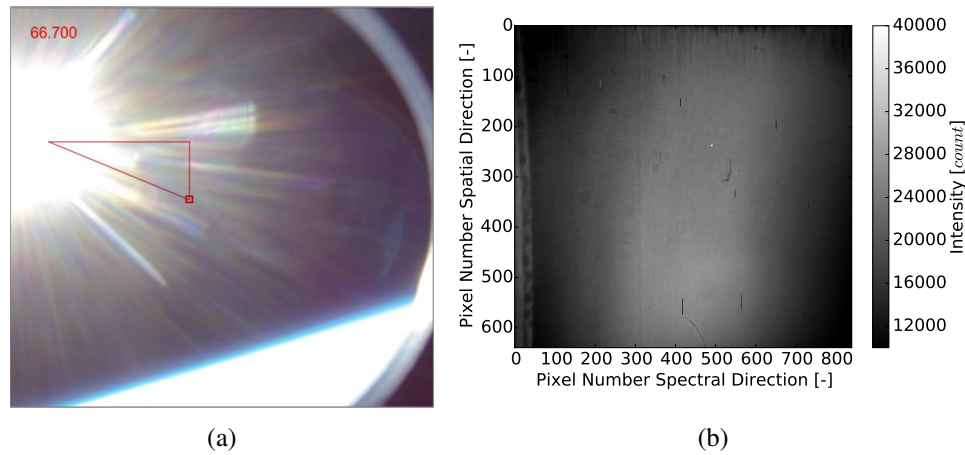
Figure 7.16.: Scene in the atmosphere and corresponding interferogram between Yoyo-release and motor separation at an altitude of $58.3\,\mathrm{km}$.

7.4.4. Analysis of Example Earth Scene

The next scene of an Earth view is analyzed to verify the straylight assumption about the albedo reflected sunlight of Chapter 5.2.8. The tumbling of the instrument results in scenes, where the Earth´s surface is imaged with different fractions of the integration time. The example scene for the oxygen A-band spectrum is used (Figure 7.14a), together with a scene, where the Earth is in view most of the integration time (Figure 7.17a). The Earth is in view for approximately $25\,\%$ and $75\,\%$ for the two scenes, which is estimated from the corresponding VisCAM image series, see Appendix D.

The interferogram for the second Earth view scene is saturated for most parts of the detector area, see Figure 7.17. Thus, the detector intensity in the saturated area is approximated with a 2D-Gaussian fit curve on the unsaturated data. The mean detector intensity is then calculated from this fit curve. The approach is reasonable, because the same method was applied to the first, unsaturated scene, showing that the 2D-Gaussian fit reasonably approximates the detector intensity distribution.

The mean intensity in counts is converted to radiance with the FOV, the aperture area, the number of pixels in the image, and with a mean conversion factor between photons and counts for the corresponding image section. The estimated straylight radiance calculates to 1.8×10^{13} photon/s/cm^2/sr and 1.6×10^{13} photon/s/cm^2/sr for the saturated and unsaturated detector images, respectively. The difference between these two values results in the uncertainty of estimating the fraction of the integration time, when the Earth is within the FOV of the instrument.

The radiance from Earth/cloud reflected sunlight was calculated to 1.2×10^{14} photon/s/cm^2/sr in the straylight analysis. Thereby, the solar elevation angle θ_S was set to $39°$ for the location and time of the rocket launch. This angle is deemed reasonable when it is compared to Figure 7.16a. The experimentally derived radiance is approximately a factor of seven smaller than the value used in the straylight analysis. It is reasonable, because the straylight analysis neglects the absorption in the atmosphere as conservative assumption.

<center>(a)   (b)</center>
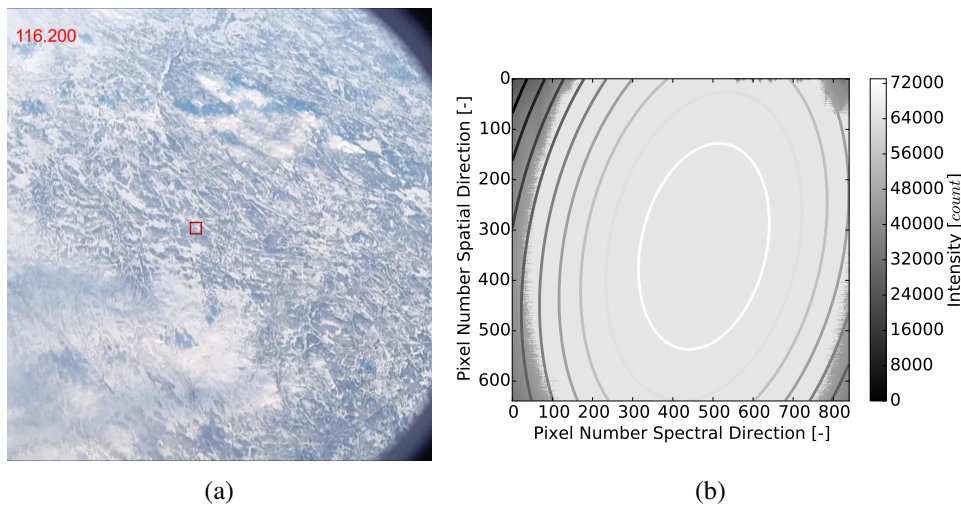
Figure 7.17.: Earthwards looking scene and corresponding interferogram at an altitude of $81.6\,\mathrm{km}$. The saturated area of the interferogram is approximated with a 2D-Gaussian fit.

7.4.5. Analysis of Example Deep Space Scene

The last analyzed scene is an example of a deep space scene. Overall, four of these scenes are recorded during the rocket flight. The interferogram for the scene at time T+116 s after lift-off is shown in Figure 7.18. Noise dominates the image. The only distinct feature is the Barber pole that describes the position of zero-OPD. The barber pole proves that some radiation reaches the detector. Otherwise, only randomly distributed noise would be visible in the image. One explanation for the signal is that the instrument was still within the oxygen A-band emission layer at an altitude of $81.7\,\mathrm{km}$ and thus detected a weak but still measurable signal. However, also other fringes left and right of the barber pole should then be visible. The second explanation contributes the signal to straylight. The image series in Appendix D shows that straylight from the Sun gets larger while the interferogram is recorded. Understanding that the straylight rejection of the VisCAM is much worse than for the spectrometer, this light could still be the explanation for the signal.

The analysis of the scene is insofar important as it shows that the signal during space view is negligible compared to views towards the Earth or in the Earth´s vicinity. Hence, it was justified in the analysis chapter before to neglect the deep space scenes for straylight estimation.
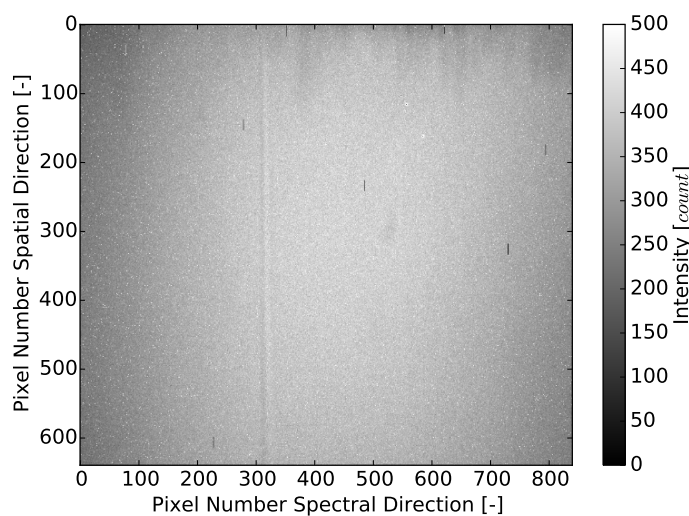
Figure 7.18.: Interferogram of deep space scene at an instrument altitude of $81.7\,\mathrm{km}$.

7.4.6. Summary

The successful measurement of the oxygen A-band spectrum was possible, because of the very well performing instrument. Critical aspects of the mission have been analyzed or tested before the rocket flight. The launch campaign ultimately proved that AtmoHIT could survive the vibrational and static loads, that it could withstand the near-space environment and that it can measure the oxygen A-band spectrum. In addition, water condensation could not be detected after the flight during visual inspection neither in the images of the VisCAM nor the interferograms. The experiment survived the flight without any broken or damaged components. In summary, the sounding rocket flight campaign was fully successful for the AtmoHIT experiment and the main mission objectives could be fulfilled.

8. Discussion

The development of a highly miniaturized, integrated, and high performing spectral Earth observation payload is a challenging topic. It requires a broad understanding of many scientific and engineering disciplines, including know-how in measurement and retrieval, optics/ spectrometers, high precision mechanics, thermal analysis and design, together with a good understanding of systems architectures and engineering for satellite missions. One might say that this is valid for all remote sensing instrument developments. However, for a CubeSat form factor type of instrument, all disciplines are extremely closely linked together, due to the very tight volumetric, mass, and power constraints. In addition, CubeSat projects have usually only fairly limited resources available compared to large satellite missions, resulting in smaller teams. But, the expertise in all these fields still needs to be available within the team. So, exactly the combination of small teams and a large required area of expertise renders these developments a challenging topic.

But it is worth the effort: These small instruments can provide the data that is pressingly needed by researchers in areas where budgetary or timely constraints limit the data available at the moment or in the near future. One of these fields is the characterization of gravity waves in the Mesosphere/ Lower Thermosphere (MLT). Existing satellite missions are close to their end of life and new satellite missions still need to be developed and launched to fill the upcoming data gap. However, characterization of gravity waves is of fundamental importance to better understand the dynamical processes in this region of the atmosphere and to better constrain climate models, which ultimately helps in the fight against global warming.

It is insofar satisfying to be able to state that this work contributes to climate research: A well performing instrument was developed, despite the challenging nature of these instruments. This work started the development of the instrument and ends with its verification on a precursor mission. It was not clear at the beginning which type of spectrometer is best suited to fulfill the challenging requirements. Choosing the SHS is also in retrospective a very sensible decision, because it combines a rigid and fault tolerant design with a very high light sensitivity in a small volume. The instrument was developed for small satellites and a 3U-CubeSat, in particular. The choice for a 3U-CubeSat is a trade-off between science return and mission costs. It is the minimum size for most reasonable scientific missions and is also the minimum for this application. The use of a deployable baffle circumvents the volumetric and power constraints of the 3U formfactor by some degree, but brings again other challenges to the design. The baffle deployment is not a single point of failure, because the instrument can still view the scene in the atmosphere in case of failure. But unsuccessful deployment may increase straylight, may vignette the FOV, and may reduce pointing stability. For maximum performance, the final position of the baffle needs to be met reliably and it needs to be stiffly connected to the structure in its final position to not reduce the pointing accuracy by introducing jitter.

The conceptual satellite bus design shows that commercial off-the-shelf CubeSat subsystems with TRL 9 exist that can be readily adopted for the AtmoCube-1 mission. There are also a variety of fairly recently founded start-up companies that offer complete bus solutions. The recent advances in highly performing miniaturized ADCS are the enablers to actually make such a limb sounding mission feasible. The satellite bus provides enough power for almost continuous scientific operations and can use two different communication systems to send the data to the ground station. Overall, the concept study shows that a feasible bus design exists that can support the instrument.

A software tool for the end-to-end simulation of the instrument was developed in this work to assess the temperature retrieval precision. The oxygen emission model may be the most sophisticated model currently available, because it includes altitude and temperature dependencies where other authors used approximations. Specifically, the photochemical reaction coefficients and the photolysis coefficients are all evaluated in dependence of altitude and temperature. The end-to-end simulation shows that the desired temperature measurement precision can be achieved with the instrument during day- and nighttime conditions. The included noise sources were reiterated with updated values from laboratory tests.

The end-to-end simulation uses an entrance aperture of the optical system of 66 mm diameter. It is the entrance aperture for the AtmoHIT instrument, the precursor mission of the AtmoCube-1 instrument. However, the optics of the AtmoHIT instrument does not fit within the CubeSat form factor, which can be circumvent with an aperture of 50 mm diameter. The smaller diameter reduces the radiant flux by about 45 %. However, the smaller aperture does only slightly reduce the temperature retrieval performance (Retrieval precision daytime: 2.5 K; nighttime: 2.0 K), because the dominating noise sources scale with the aperture diameter. In addition, the smaller entrance aperture increases the baffle performance due to its larger ratio between baffle size and aperture diameter and it increases the optical performance. The F-number of the fore-optics increases for a smaller aperture diameter which reduces optical aberrations. This increases the visibility of the interferograms and the spectral resolution. Overall, the smaller entrance aperture does only slightly reduce the instrument performance for the same integration time and straylight rejection as for the 66 mm aperture diameter. However, the smaller aperture increases the straylight rejection and the optics can be readily adjusted to fit within the available volume for the AtmoCube-1 instrument. Due to the necessary adjustments to optics and structure, the TRL level of the instrument is evaluated to TRL 6 instead of TRL 7 after the successful precursor mission. These required adjustments led also to a less stringent alignment policy of the optical assembly relative to the structural mounting as it needs to be redesigned in any case. In addition, the re-design gives the opportunity to employ the technologies of alignment turning and cementing for the lens mountings, which would decrease alignment errors and widens the operational temperature range. However, it is a challenging topic that requires substantial know-how and experience.

The REXUS/BEXUS student program enabled to verify the instrument as AtmoHIT experiment in a sounding rocket flight campaign. Within the student team, the work packages have been distributed and my role developed towards systems engineer/ project manager. Hence, this work elaborates less details of the design, assembly, and calibration of AtmoHIT. The REXUS program accompanying SED (Deiml et al., 2017a) is a well suited resource for additional information on the topics not covered in this document.

All subsystems of the AtmoHIT experiment have been developed in-house, which includes the spectrometer, the optics, the structure, and the electronics. This development approach resulted in comparatively low development costs for a space instrument and precise control over all instrument features. However, it resulted also in much higher project risks compared to buying subsystems from established industry experts.

Within this work, the first monolithic SHS outside North-America was developed. The development created also SHS simulation and design tools for alignment and tolerance analysis, pressure dependence analysis, filter and aliasing effect analysis, optical performance optimization, and temperature stabilization that can be readily adopted for general SHS designs. In fact, the developed methods and tools are already in use in the follow-on projects AtmoWinds and AtmoShine. The in-depths analysis of the SHS led to an highly optimized and temperature stabilized instrument, suitable for the harsh environment of space. This work showed that it is possible to thermally stabilize a SHS over a wide temperature range of more than 60 K by using specific glass combinations in the spectrometer arms. This is especially useful in aerospace applications, where precise temperature control results in mass, power, and volume penalties.

Prior to the sounding rocket flight campaign, the AtmoHIT experiment was tested on the optical bench, in the T-Vac chamber, and on the shaker. These successful tests showed that the instrument can measure the oxygen A-band spectrum, can withstand launch vibrations/ loads, and can survive in its operational temperature range. The tests were accompanied with flight simulation tests to ensure successful operations. The detailed description of the calibration process for the AtmoHIT project was not further described in this work, because it is part of another PhD thesis. The extensive test and calibration campaign prior to the launch campaign provided already high confidence that the instrument performs well in space.

With the sounding rocket flight campaign, we successfully demonstrated the first monolithic SHS in space conditions. The sounding rocket flight campaign was a full success despite the anomaly in rocket motor separation. The tumbling of the payload segment reduced the number of useful interferograms, but still allowed to retrieve oxygen A-band spectra, verifying and validating the instrument. Within this work, the maturity of the CubeSat instrument was increased from TRL 1 to TRL 6.

9. Summary and Future Applications

A remote sensing instrument in limb sounding configuration for a small satellite has been developed to observe the oxygen atmospheric band emission. Temperatures in the MLT are retrieved from the relative intensity distribution of individual rotational emission lines. The temperature measurements allow to characterize gravity waves, which drive the dynamics in this region of the atmosphere and which need to be better understood and constrained to increase the precision of climate models.

The oxygen A-band emission spectrum in the near infrared is measured with a Spatial Heterodyne Spectrometer (SHS), a Fourier-transform interferometer that combines the advantages of a grating spectrometer and a Michelson interferometer. The instrument is a rigid and temperature stabilized monolithic block, allowing its use on a small satellite. The instrument was successfully verified in its precursor mission AtmoHIT, which enables its use in a multitude of future applications.

The development of a CubeSat form-factor type of instrument renders it well suited for constellation deployment, which increases the scientific return and the fault tolerance of the overall system. The performance of the system could be further enhanced by on-board processing and data compression of the interferograms, because less power and time would be required for communication with the ground station.

In addition, the imaging property of the instrument in horizontal (spectral) direction could be used advantageously in the retrieval process. From a purely temperature retrieval standpoint, the imaging property is detrimental to the performance of the instrument, because atmospheric signatures may overlap with temperature signatures. But as discussed in Chapter 5.2.1.1, the imaging properties are not considered problematic for the AtmoCube-1 instrument. On the contrary, signatures of gravity waves with horizontal wavelengths between $10\,\mathrm{km}$ and $30\,\mathrm{km}$ are visible in the spectra with spatial frequencies between $8.6\,\mathrm{cm}^{-1}$ and $0.7\,\mathrm{cm}^{-1}$. Thus, a well characterized instrument is potentially able to resolve gravity waves with very low horizontal wavelengths not observed at all in this region by current satellite instruments.

The instrument can be further optimized for long mission durations by including slits in the field stops of the SHS arms. These slits need to be positioned such that only light from one arm gets back to a specific area of the detector. An interferogram will not be visible in these areas and the intensity change over time could be used to correct the potential flat-field time dependence of the instrument.

Lastly, the straylight performance of the system can be increased by removing the detector window, or by using a detector window that has an optimized AR coating for the relevant spectral range. However, the removal of the window has the disadvantage that water vapor may directly condensate on the detector pixels. A in-depth analysis of the straylight with its spectral characteristics may provide additional insights and performance enhancements, which could be performed in future development.

SHS instruments can be used for other climate relevant observations, such as the measurement of water vapor in the UTLS, e.g. (Deiml et al., 2017b). More general, the SHS is a versatile technology that can be used in any application that requires high spectral resolution and light sensitivity over a narrow bandwidth in a small formfactor and in harsh environments.

10. Literature

Advanced Optics: Technical Information TIE-26: Homogeneity of Optical Glass, `http://www.schott.com/advanced_optics/english/download/schott_tie-26_homogeneity_of_optical_glass_july_2004_eng.pdf`, 2004.

Advanced Optics: Technical Information TIE-29 Refractive Index and Dispersion, `http://www.schott.com/d/advanced_optics/02ffdb0d-00a6-408f-84a5-19de56652849/1.0/tie_29_refractive_index_and_dispersion_eng.pdf`, 2016.

Alexander, M. J. and Barnet, C.: Using Satellite Observations to Constrain Parameterizations of Gravity Wave Effects for Global Models, Journal of the Atmospheric Sciences, 64, 1652–1665, doi:10.1175/JAS3897.1, 2007.

Alexander, M. J., Geller, M., McLandress, C., Polavarapu, S., Preusse, P., Sassi, F., Sato, K., Eckermann, S., Ern, M., Hertzog, A., Kawatani, Y., Pulido, M., Shaw, T. A., Sigmond, M., Vincent, R., and Watanabe, S.: Recent Developments in Gravity-Wave Effects in Climate Models and the Global Distribution of Gravity-Wave Momentum Flux from Observations and Models, Quarterly Journal of the Royal Meteorological Society, pp. 1103–1124, doi:10.1002/qj.637, 2010.

Allen, S. J. and Vincent, R. A.: Gravity Wave Activity in the Lower Atmosphere: Seasonal and Latitudinal Variations, Journal of Geophysical Research, 100, 1327, 1995.

Barth, C. A.: The 5577-Angstrom Airglow, Science, 134, 1426, 1961.

Blackwell, W., Allen, G., Galbraith, C., Hancock, T., Leslie, R., Osaretin, I., Retherford, L., Scarito, M., Semisch, C., Shields, M., Silver, M., Toher, D., Wight, K., Miller, D., Cahoy, K., and Erickson, N.: Nanosatellites for Earth Environmental Monitoring: The MicroMAS Project, in: 2012 IEEE International Geoscience and Remote Sensing Symposium, pp. 206–209, IEEE, 2012.

Blue Canyon Technologies: Attitude Determination Control System, `http://bluecanyontech.com/wp-content/uploads/2016/08/ADCS_F.pdf`, 2016.

Borgeaud, M., Scheidegger, N., Noca, M., Roethlisberger, G., Jordan, F., Choueiri, T., and Steiner, N.: SwissCube: The First Entirely-Built Swiss Student Satellite with an Earth Observation Payload, in: Small Satellite Missions for Earth Observation, edited by Sandau, R., Roeser, H. P., and Valenzuela, A., pp. 207–213, Springer, Berlin, Heidelberg, 2010.

Boshuizen, C., Mason, J., Klupar, P., and Spanhake, S.: Results from the Planet Labs Flock Constellation, in: 28th Annual AIAA/USU Conference on Small Satellites, 2014.

Bouwmeester, J., Gill, E. K. A., and Verhoeven, C. J. M.: Advancing Nano-Satellite Platforms: The Delfi Program, in: 59th International Astronautical Congress, Glasgow, Scotland, 2008.

Brasseur, G. and Solomon, S.: Aeronomy of the Middle Atmosphere: Chemistry and Physics of the Stratosphere and Mesosphere, Atmospheric sciences library, D. Reidel Pub. Co., Dordrecht ; Boston : Norwell, MA, U.S.A, 2nd rev. ed edn., 1986.

Bucholtz, A., Skinner, W. R., Abreu, V. J., and Hays, P. B.: The Dayglow of the O_2 Atmospheric Band System, Planetary and Space Science, 34, 1031–1035, 1986.

Burch, D. E. and Gryvnak, D. A.: Strengths, Widths, and Shapes of the Oxygen Lines near 13,100 Cm^{-1}, Applied optics, 8, 1493–1499, 1969.

Campbell, I. M. and Gray, C. N.: Rate Constants for O(3P) Recombination and Association with N(4S), Chemical Physics Letters, 18, 607–609, doi:10.1016/0009-2614(73)80479-8, 1973.

Chungu, L., Koch, S., and Wang, N.: Determination of Temporal and Spatial Characteristics of Atmospheric Gravity Waves Combining Cross-Spectral Analysis and Wavelet Transformation, Journal of Geophysical Research, 110, 2005.

Connes, P.: Spectromètre Interférentiel à Sélection Par l'amplitude de Modulation, J. phys. radium, 19, 215–222, 1958.

Deiml, M.: The Thermal-Structure-Optical System Design and Analysis of the Satellite PolarCube, Tech. rep., TU München, Munich, 2013.

Deiml, M., Gasiewski, A. J., Gallaher, D. W., and Sanders, B. T.: PolarCube – A 3-Unit Cubesat for Remote Sensing in the 118 GHz Microwave Frequency, in: IAC-14 Small Earth Observation Missions, Toronto; Ont., Canada, 2014.

Deiml, M., Chen, Q., Fröhlich, D., Liu, J., Loosen, F., Song, R., Wagner, F., Wroblowski, O., and Rottland, B.: Student Experiment Documentation AtmoHIT, Tech. rep., University of Wuppertal, Wuppertal, 2017a.

Deiml, M., Jimenez-Lluva, D., Arago-Higueras, N., Pavesi, S., Rourke, S., Bylund, O., Joblin, J., Karnthaler, A., Klingenberg, T. F., Link, M., Niemela, P., Paraiso, D., Pauna, C., Scheiblaue, S., Al Bitar, A., and Aguirre, M.: WAVE-E: The WAter Vapour European-Explorer Mission, IAA-B11-0603, Berlin, Germany, 2017b.

Doe, R. A., Watchorn, S., Butler, J. J., Xiong, X., and Gu, X.: Climate-Monitoring CubeSat Mission CM2: A Project for Global Mesopause Temperature Sensing, in: SPIE Optical Engineering + Applications, SPIE Proceedings, pp. 81 530Q–81 530Q–12, SPIE, 2011.

Doncaster, B. and Shulman, J.: Nano/Microsatellite Market Forecast, Tech. rep., SpaceWorks Enterprises, Inc. (SEI), Atlanta, GA, 2016.

Englert, C. R. and Harlander, J. M.: Flatfielding in Spatial Heterodyne Spectroscopy, Applied optics, 45, 4583–4590, 2006.

Englert, C. R., Harlander, J. M., Cardon, J. G., and Roesler, F. L.: Correction of Phase Distortion in Spatial Heterodyne Spectroscopy, Applied optics, 43, 6680–6687, 2004.

Englert, C. R., Harlander, J. M., Owrutsky, J. C., and Bays, J. T.: SHIM-Free Breadboard Instrument Design, Integration, and First Measurements, Tech. rep., Naval Research Laboratory, Washington, D. C., 2005.

Englert, C. R., Babcock, D. D., and Harlander, J. M.: Doppler Asymmetric Spatial Heterodyne Spectroscopy (DASH): Concept and Experimental Demonstration, Appl. Opt., 46, 7297–7307, 2007.

Englert, C. R., Harlander, J. M., Brown, C. M., Stephan, A. W., Makela, J. J., Marr, K. D., and Immel, T. J.: The Michelson Interferometer for Global High-Resolution Thermospheric Imaging (MIGHTI): Wind and Temperature Observations from the Ionospheric Connection Explorer (ICON), in: Fourier Transform Spectroscopy, Optical Society of America, 2013.

Englert, C. R., Brown, C. M., Bach, B., Bach, E., Bach, K., Harlander, J. M., Seely, J. F., Marr, K. D., and Miller, I.: High-Efficiency Echelle Gratings for MIGHTI, the Spatial Heterodyne Interferometers for the ICON Mission, Applied Optics, 56, 2090, doi:10.1364/AO.56.002090, 2017.

Ern, M., Preusse, P., Alexander, M. J., and Warner, C. D.: Absolute Values of Gravity Wave Momentum Flux Derived from Satellite Data, Journal of Geophysical Research: Atmospheres, 109, D20 103, 2004.

Ern, M., Hoffmann, L., and Preusse, P.: Directional Gravity Wave Momentum Fluxes in the Stratosphere Derived from High-Resolution AIRS Temperature Data, Geophysical Research Letters, 44, 475–485, doi:10.1002/2016GL072007, 2017.

ESA: ESA's Living Planet Programme: Scientific Achievements and Future Challenges - Scientific Context of the Earth Observation Science Strategy for ESA, no. 1329/1 in ESA SP, ESA Communications, Noordwijk, the Netherlands, 2015.

ESA TEC-SHS: Technology Readiness Levels Handbook for Space Applications, Tech. rep., ESA, 2008.

Fest, E. C.: Stray Light Analysis and Control, SPIE Press, Bellingham, Washington, 2013.

Fetzer, E. J. and Gille, J. C.: Gravity Wave Variance in LIMS Temperatures. Part I: Variability and Comparison with Background Winds, Journal of the Atmospheric Sciences, 51, 2461–2483, doi:10.1175/1520-0469(1994)051<2461:GWVILT>2.0.CO;2, 1994.

Fischer, H., Birk, M., Blom, C., Carli, B., Carlotti, M., von Clarmann, T., Delbouille, L., Dudhia, A., Ehhalt, D., Endemann, M., Flaud, J. M., Gessner, R., Kleinert, A., Koopman, R., Langen, J., López-Puertas, M., Mosner, P., Nett, H., Oelhaf, H., Perron, G., Remedios, J., Ridolfi, M., Stiller, G., and Zander, R.: MIPAS: An Instrument for Atmospheric and Climate Research, Atmospheric Chemistry and Physics, 8, 2151–2188, doi:10.5194/acp-8-2151-2008, 2008.

Fritts, D. C. and Alexander, M. J.: Gravity Wave Dynamics and Effects in the Middle Atmosphere, Reviews of Geophysics, 41, doi:10.1029/2001RG000106, 2003.

Fröhlich, D.: Entwicklung Der sCMOS-Detektor Ausleseelektronik Für Das AtmoHIT-Experiment Zum Einsatz Auf Der REXUS-Höhenforschungsrakete, Tech. rep., Hochschule Düsseldorf, Düsseldorf, 2016.

Fuller, J., Buchen, E., and Olds, J. R.: SpaceWorks Launch Report: 2014 Year in Review, Tech. rep., SpaceWorks Enterprises, Inc. (SEI), Atlanta, GA, 2015.

García-Comas, M., Funke, B., Gardini, A., López-Puertas, M., Jurado-Navarro, A., von Clarmann, T., Stiller, G., Kiefer, M., Boone, C. D., Leblanc, T., Marshall, B. T., Schwartz, M. J., and Sheese, P. E.: MIPAS Temperature from the Stratosphere to the Lower Thermosphere: Comparison of vM21 with ACE-FTS, MLS, OSIRIS, SABER, SOFIE and Lidar Measurements, Atmospheric Measurement Techniques, 7, 3633–3651, doi:10.5194/amt-7-3633-2014, 2014.

Gille, J., Barnett, J., Arter, P., Barker, M., Bernath, P., Boone, C., Cavanaugh, C., Chow, J., Coffey, M., Craft, J., Craig, C., Dials, M., Dean, V., Eden, T., Edwards, D. P., Francis, G., Halvorson, C., Harvey, L., Hepplewhite, C., Khosravi, R., Kinnison, D., Krinsky, C., Lambert, A., Lee, H., Lyjak, L., Loh, J., Mankin, W., Massie, S., McInerney, J., Moorhouse, J., Nardi, B., Packman, D., Randall, C., Reburn, J., Rudolf, W., Schwartz, M., Serafin, J., Stone, K., Torpy, B., Walker, K., Waterfall, A., Watkins, R., Whitney, J., Woodard, D., and Young, G.: High Resolution Dynamics Limb Sounder: Experiment Overview, Recovery, and Validation of Initial Temperature Data, Journal of Geophysical Research, 113, doi:10.1029/2007JD008824, 2008.

Giorgetta, M. A., Roeckner, E., Mauritsen, T., Bader, J., Crueger, T., Esch, M., Rast, S., Kornblueh, L., Schmidt, H., and Kinne, S.: The Atmospheric General Circulation Model ECHAM6-Model Description, 2013.

Green, J. G., Shi, J., and Barker, J. R.: Photochemical Kinetics of Vibrationally Excited Ozone Produced in the 248 Nm Photolysis of O_2/O_3 Mixtures, The Journal of Physical Chemistry A, 104, 6218–6226, doi:10.1021/jp000635k, 2000.

Greif, A. and Kaczmarczik, U.: AtmoHIT Acceptance Test Report, 2016.

Guo, J., Monas, L., and Gill, E.: Statistical Analysis and Modelling of Small Satellite Reliability, Acta Astronautica, 98, 97–110, doi:10.1016/j.actaastro.2014.01.018, 2014.

Hagen, N.: ZemaxGlass 1.0, `https://pypi.python.org/pypi/ZemaxGlass`, 2014.

Hamberg, O. and Shon, E. M.: Particle Size Distribution on Surfaces in Clean Rooms, Tech. rep., The Aerospace Cooperation, El Segundo, California, 1984.

Hand, E.: CubeSats Promise to Fill Weather Data Gap, Science, 350, 1302–1303, 2015a.

Hand, E.: Startup Liftoff, Science, 348, 172–177, doi:10.1126/science.348.6231.172, 2015b.

Harlander, J. M., Reynolds, R. J., and Roesler, F. L.: Spatial Heterodyne Spectroscopy for the Exploration of Diffuse Interstellar Emission Lines at Far-Ultraviolet Wavelengths, The Astrophysical Journal, 396, 730, 1992.

Harlander, J. M., Roesler, F. L., Cardon, J. G., Englert, C. R., and Conway, R. R.: Shimmer: A Spatial Heterodyne Spectrometer for Remote Sensing of Earth' Middle Atmosphere, Applied Optics, 41, 1343, 2002.

Harnisch, F., Healy, S. B., Bauer, P., and English, S. J.: Scaling of GNSS Radio Occultation Impact with Observation Number Using an Ensemble of Data Assimilations, Monthly Weather Review, 141, 4395–4413, doi:10.1175/MWR-D-13-00098.1, 2013.

Harris, F. J.: On the Use of Windows for Harmonic Analysis with the Discrete Fourier Transform, Proceedings of the IEEE, 66, 51–83, 1978.

Harvey, J. E.: Light-Scattering Characteristics of Optical Surfaces, Ph.D. thesis, Arizona Univ., Tucson, 1976.

Herzberg, G.: Molecular Spectra and Molecular Structure: Spectra of Diatomic Molecules, D. van Nostrand, Princeton, 2nd edn., 1950.

Hines, C. O.: Internal Atmospheric Gravity Waves at Ionospheric Heights, Canadian Journal of Physics, 38, 1441–1481, 1960.

Hines, C. O.: Doppler-Spread Parameterization of Gravity-Wave Momentum Deposition in the Middle Atmosphere. Part 1: Basic Formulation, Journal of Atmospheric and Solar-Terrestrial Physics, 59, 371–386, doi:10.1016/S1364-6826(96)00079-X, 1997a.

Hines, C. O.: Doppler-Spread Parameterization of Gravity-Wave Momentum Deposition in the Middle Atmosphere. Part 2: Broad and Quasi Monochromatic Spectra, and Implementation, Journal of Atmospheric and Solar-Terrestrial Physics, 59, 387–400, doi:10.1016/S1364-6826(96)00080-6, 1997b.

Hoffmann, L., Xue, X., and Alexander, M. J.: A Global View of Stratospheric Gravity Wave Hotspots Located with Atmospheric Infrared Sounder Observations: HOTSPOTS OF STRATOSPHERIC GRAVITY WAVES, Journal of Geophysical Research: Atmospheres, 118, 416–434, doi: 10.1029/2012JD018658, 2013.

Hwang, E., Bergman, A., Copeland, R., and Slanger, T. G.: Temperature Dependence of the Collisional Removal of $O_2(b\ ^1\Sigma_g^+,\ V=1\ and\ 2)$ at 110–260 K, and Atmospheric Applications, The Journal of Chemical Physics, 110, 18, doi:10.1063/1.478079, 1999.

IADC Steering Group: IADC Statement on Large Constellations of Satellites in Low Earth Orbit, Tech. rep., Inter-Agency Space Debris Coordination Comittee, 2016.

Incropera, F. P., ed.: Fundamentals of Heat and Mass Transfer, John Wiley, Hoboken, NJ, 6 edn., 2007.

Indranil Sinharoy, xy124, Catherine Holloway, Ville Nummela, ng110, Stuermer, and magro11: Py-ZDDE: Release Version 2.0.2, doi:10.5281/zenodo.44295, 2016.

IPCC: Summary for Policymakers. In: Climate Change 2014: Mitigation of Climate Change. Contribution of Working Group III to the Fifth Assessment Report of the Intergovernmental Panel on Climate Change [Edenhofer, O., R. Pichs-Madruga, Y. Sokona, E. Farahani, S. Kadner, K. Seyboth, A. Adler, I. Baum, S. Brunner, P. Eickemeier, B. Kriemann, J. Savolainen, S. Schlömer, C. von Stechow, T. Zwickel and J.C. Minx (Ed)], Cambridge University Pr, Cambridge, United Kingdom and New York, NY, US, 2014.

Jacquinot, P.: The Luminosity of Spectrometers with Prisms, Gratings, or Fabry-Perot Etalons, JOSA, 44, 761–765, 1954.

Johnson, B. R.: Analysis of Diffraction Reduction by Use of a Lyot Stop, Journal of the Optical Society of America A, 4, 1376, doi:10.1364/JOSAA.4.001376, 1987.

Kernahan, J. A. and Pang, P. H.-L.: Experimental Determination of Absolute *A* Coefficients for 'Forbidden' Atomic Oxygen Lines, Canadian Journal of Physics, 53, 455–458, doi:10.1139/p75-058, 1975.

Kestilä, A., Tikka, T., Peitso, P., Rantanen, J., Näsilä, A., Nordling, K., Saari, H., Vainio, R., Janhunen, P., Praks, J., and Hallikainen, M.: Aalto-1 Nanosatellite - Technical Description and Mission Objectives, Geoscientific Instrumentation, Methods and Data Systems, 2, 121–130, 2013.

Killeen, T. L., Skinner, W. R., Johnson, R. M., Edmonson, C. J., Wu, Q., Niciejewski, R. J., Grassl, H. J., Gell, D. A., Hansen, P. E., Harvey, J. D., and Kafkalidis, J. F.: TIMED Doppler Interferometer (TIDI), vol. SPIE 3756 of *Optical Spectroscopic Techniques and Instrumentation for Atmospheric and Space Research III*, pp. 289–301, doi:10.1117/12.366383, 1999.

Kim, Y.-J., Eckermann, S. D., and Chun, H.-Y.: An Overview of the Past, Present and Future of Gravity-wave Drag Parametrization for Numerical Climate and Weather Prediction Models, Atmosphere-Ocean, 41, 65–98, doi:10.3137/ao.410105, 2003.

Kramer, H. J.: FormoSat-7 / COSMIC-2 (Constellation Observing System for Meteorology, Ionosphere and Climate), https://directory.eoportal.org/web/eoportal/satellite-missions/f/formosat-7, 2015.

Krebs, G.: Flock-1, -1b, -1c, -1d, -1d', -1e, -1f, -2, -2b, -2c, -2d, -2e, -2e', -2k, -2p, http://space.skyrocket.de/doc_sdat/flock-1.htm, 2016.

Krupenie, P. H.: The Spectrum of Molecular Oxygen, J. Phys. Chem. Ref. Data, pp. 423–521, 1972.

Kursinski, E. R., Hajj, G. A., Schofield, J. T., Linfield, R. P., and Hardy, K. R.: Observing Earth's Atmosphere with Radio Occultation Measurements Using the Global Positioning System, Journal of Geophysical Research: Atmospheres, 102, 23 429–23 465, doi:10.1029/97JD01569, 1997.

Lee, L. C., Slanger, T. G., Black, G., and Sharpless, R. L.: Quantum Yields for the Production of O(1D) from Photodissociation of O2 at 1160–1770 A, The Journal of Chemical Physics, 67, 5602, doi:10.1063/1.434759, 1977.

Leovy, C.: Simple Models of Thermally Driven Mesopheric Circulation, Journal of the Atmospheric Sciences, 21, 327–341, doi:10.1175/1520-0469(1964)021<0327:SMOTDM>2.0.CO;2, 1964.

Lindzen, R. S.: Wave-Mean Flow Interactions in the Upper Atmosphere, Boundary-Layer Meteorology, 4, 327–343, 1973.

Lissberger, P. H.: Effective Refractive Index as a Criterion of Performance of Interference Filters, JOSA, 58, 1586–1590, 1968.

Liu, H.-L., Foster, B. T., Hagan, M. E., McInerney, J. M., Maute, A., Qian, L., Richmond, A. D., Roble, R. G., Solomon, S. C., Garcia, R. R., Kinnison, D., Marsh, D. R., Smith, A. K., Richter, J., Sassi, F., and Oberheide, J.: Thermosphere Extension of the Whole Atmosphere Community Climate Model, Journal of Geophysical Research: Space Physics, 115, n/a–n/a, doi:10.1029/2010JA015586, 2010.

Llewellyn, E. J., Lloyd, N. D., Degenstein, D. A., Gattinger, R. L., Petelina, S. V., Bourassa, A. E., Wiensz, J. T., Ivanov, E. V., McDade, I. C., Solheim, B. H., McConnell, J. C., Haley, C. S., von Savigny, C., Sioris, C. E., McLinden, C. A., Griffioen, E., Kaminski, J., Evans, W. F., Puckrin, E., Strong, K., Wehrle, V., Hum, R. H., Kendall, D. J., Matsushita, J., Murtagh, D. P., Brohede, S., Stegman, J., Witt, G., Barnes, G., Payne, W. F., Piché, L., Smith, K., Warshaw, G., Deslauniers, D. L., Marchand, P., Richardson, E. H., King, R. A., Wevers, I., McCreath, W., Kyrölä, E., Oikarinen, L., Leppelmeier, G. W., Auvinen, H., Mégie, G., Hauchecorne, A., Lefèvre, F., de La Nöe, J., Ricaud, P., Frisk, U.,

Sjoberg, F., von Schéele, F., and Nordh, L.: The OSIRIS Instrument on the Odin Spacecraft, Canadian Journal of Physics, 82, 411–422, doi:10.1139/p04-005, 2004.

Lott, F. and Miller, M. J.: A New Subgrid-Scale Orographic Drag Parametrization: Its Formulation and Testing, Quarterly Journal of the Royal Meteorological Society, 123, 101–127, 1997.

Mankiewicz: Nextel Velvet-Coating 811-21, `http://ibzagshop.server1-cms-factory.eu/fileadmin/doc_shop/752_14076_DE_DB.pdf`, 2017.

Marchant, A., Taylor, M., Swenson, C., and Scherlies, L.: Hyperspectral Limb Scanner for the OPAL Mission, in: Small Satellite Conference, vol. SSC14 of *Technical Session VII: Advanced Technologies II*, 2014.

Marsh, D. R., Mills, M. J., Kinnison, D. E., Lamarque, J.-F., Calvo, N., and Polvani, L. M.: Climate Change from 1850 to 2005 Simulated in CESM1(WACCM), Journal of Climate, 26, 7372–7391, doi:10.1175/JCLI-D-12-00558.1, 2013.

Martinez, I.: Radiative View Factors, `http://webserver.dmt.upm.es/~isidoro/tc3/Radiation%20View%20factors.pdf`, 2017.

Mason, J. P., Baumgart, M., Rogler, B., Downs, C., Williams, M., Woods, T. N., Palo, S., Chamberlin, P. C., Solomon, S., Jones, A., and others: MinXSS-1 CubeSat On-Orbit Pointing and Power Performance: The First Flight of the Blue Canyon Technologies XACT 3-Axis Attitude Determination and Control System, arXiv preprint arXiv:1706.06967, 2017.

Massman, W. J.: An Investigation of Gravity Waves on a Global Scale Using TWERLE Data, Journal of Geophysical Research, 86, 4072, doi:10.1029/JC086iC05p04072, 1981.

McDade, I. C., Murtagh, D. P., Greer, R. G. H., Dickinson, P. H. G., Witt, G., Stegman, J., Llewellyn, E. J., Thomas, L., and Jenkins, D. B.: ETON 2: Quenching Parameters for the Proposed Precursors of $O_2(b^1\Sigma_g{}^+)$ and $O(^1S)$ in the Terrestrial Nightglow, Planetary and Space Science, 34, 789–800, doi:10.1016/0032-0633(86)90075-9, 1986.

McLandress, C.: On the Importance of Gravity Waves in the Middle Atmosphere and Their Parameterization in General Circulation Models, Journal of Atmospheric and Solar-Terrestrial Physics, 60, 1357–1383, 1998.

Mehrparvar, A.: CubeSat Design Specification, Tech. rep., California Polytechnic State University, California, 2014.

Mende, S. B., Frey, H., Geller, S. P., and Swenson, G. R.: Gravity Wave Modulated Airglow Observation from Spacecraft, Geophysical Research Letters, 25, 757–760, 1998.

Mlynczak, M. G., Solomon, S., and Zaras, D. S.: An Updated Model for $O_2(a^1\Delta_g)$ Concentrations in the Mesosphere and Lower Thermosphere and Implications for Remote Sensing of Ozone at 1.27 Um, Journal of Geophysical Research, 98, 18 639, doi:10.1029/93JD01478, 1993.

Murgatroyd, R. J. and Goody, R. M.: Sources and Sinks of Radiative Energy from 30 to 90 Km, Quarterly Journal of the Royal Meteorological Society, 84, 225–234, doi:10.1002/qj.49708436103, 1958.

Murgatroyd, R. J. and Singleton, F.: Possible Meridional Circulations in the Stratosphere and Mesosphere, Quarterly Journal of the Royal Meteorological Society, 87, 125–135, 1961.

Murtagh, D., Frisk, U., Merino, F., Ridal, M., Jonsson, A., Stegman, J., Witt, G., Eriksson, P., Jiménez, C., Megie, G., de la Noë, J., Ricaud, P., Baron, P., Pardo, J. R., Hauchcorne, A., Llewellyn, E. J., Degenstein, D. A., Gattinger, R. L., Lloyd, N. D., Evans, W. F., McDade, I. C., Haley, C. S., Sioris, C., von Savigny, C., Solheim, B. H., McConnell, J. C., Strong, K., Richardson, E. H., Leppelmeier, G. W., Kyrölä, E., Auvinen, H., and Oikarinen, L.: An Overview of the Odin Atmospheric Mission, Canadian Journal of Physics, 80, 309–319, doi:10.1139/p01-157, 2002.

Nakamura, T., Tsuda, T., Fukao, S., Manson, A. H., Meek, C. E., Vincent, R. A., and Reid, I. M.: Mesospheric Gravity Waves at Saskatoon (52 Deg N), Kyoto (35 Deg N), and Adelaide (35 Deg S), Journal of Geophysical Research, 101, 7005, 1996.

Nicholls, R. W.: Franck-Condon Factors to High Vibrational Quantum Numbers V: O_2 Band Systems, J. Res. Natl. Bur. Stand. Sect. A, 69, 369, 1965.

Nishida, S., Taketani, F., Takahashi, K., and Matsumi, Y.: Quantum Yield for $O(^1D)$ Production from Ozone Photolysis in the Wavelength Range of 193-225 Nm, The Journal of Physical Chemistry A, 108, 2710–2714, doi:10.1021/jp049979r, 2004.

Noll, R. J.: Reduction of Diffraction of Use of a Lyot Stop, JOSA, 63, 1399–1402, 1973.

Offermann, D., Grossmann, K.-U., Barthol, P., Knieling, P., Riese, M., and Trant, R.: Cryogenic Infrared Spectrometers and Telescopes for the Atmosphere (CRISTA) Experiment and Middle Atmosphere Variability, Journal of Geophysical Research: Atmospheres, 104, 16 311–16 325, doi:10.1029/1998JD100047, 1999.

Palmer, C.: Diffraction Grating Handbook, Newport Corporation, New York, 7 edn., 2014.

Pejaković, D. A.: Collisional Removal of $O_2(b^1\Sigma_g^+, \upsilon = 1)$ by O_2 at Thermospheric Temperatures, Journal of Geophysical Research, 110, doi:10.1029/2004JA010860, 2005.

Pejaković, D. A., Copeland, R. A., Slanger, T. G., and Kalogerakis, K. S.: Collisional Removal of $O_2(b^1\Sigma_g^+, \upsilon = 1)$ by $O(^3P)$, Chemical Physics Letters, 403, 372–377, doi:10.1016/j.cplett.2005.01.038, 2005.

Preusse, P., Dörnbrack, A., Eckermann, S. D., Riese, M., Schaeler, B., Bacmeister, J. T., Broutman, D., and Grossmann, K. U.: Space-Based Measurements of Stratospheric Mountain Waves by CRISTA 1. Sensitivity, Analysis Method, and a Case Study, Journal of Geophysical Research: Atmospheres, 107, 8178, 2002.

Preusse, P., Ern, M., Eckermann, S. D., Warner, C. D., Picard, R. H., Knieling, P., Krebsbach, M., Russell, J. M., Mlynczak, M. G., Mertens, C. J., and Riese, M.: Tropopause to Mesopause Gravity Waves in August: Measurement and Modeling, Journal of Atmospheric and Solar-Terrestrial Physics, 68, 1730–1751, doi:10.1016/j.jastp.2005.10.019, 2006.

Preusse, P., Eckermann, S. D., and Ern, M.: Transparency of the Atmosphere to Short Horizontal Wavelength Gravity Waves, Journal of Geophysical Research, 113, 2008.

Preusse, P., Schroeder, S., Hoffmann, L., Ern, M., Friedl-Vallon, F., Ungermann, J., Oelhaf, H., Fischer, H., and Riese, M.: New Perspectives on Gravity Wave Remote Sensing by Spaceborne Infrared Limb Imaging, Atmospheric Measurement Techniques, 2, 299–311, 2009.

Reddmann, T. and Uhl, R.: The H Lyman-α Actinic Flux in the Middle Atmosphere, Atmospheric Chemistry and Physics, 3, 225–231, 2003.

Remsberg, E. E., Marshall, B. T., Garcia-Comas, M., Krueger, D., Lingenfelser, G. S., Martin-Torres, J., Mlynczak, M. G., Russell, J. M., Smith, A. K., Zhao, Y., Brown, C., Gordley, L. L., Lopez-Gonzalez, M. J., Lopez-Puertas, M., She, C.-Y., Taylor, M. J., and Thompson, R. E.: Assessment of the Quality of the Version 1.07 Temperature-versus-Pressure Profiles of the Middle Atmosphere from TIMED/SABER, Journal of Geophysical Research, 113, doi:10.1029/2008JD010013, 2008.

Richter, J. H., Sassi, F., and Garcia, R. R.: Toward a Physically Based Gravity Wave Source Parameterization in a General Circulation Model, J. Atmos. Sci., 67, 136–156, 2010.

Riese, M., Spang, R., Preusse, P., Ern, M., Jarisch, M., Offermann, D., and Grossmann, K. U.: Cryogenic Infrared Spectrometers and Telescopes for the Atmosphere (CRISTA) Data Processing and Atmospheric Temperature and Trace Gas Retrieval, Journal of Geophysical Research: Atmospheres, 104, 16 349–16 367, doi:10.1029/1998JD100057, 1999.

Riese, M., Oelhaf, H., Preusse, P., Blank, J., Ern, M., Friedl-Vallon, F., Fischer, H., Guggenmoser, T., Höpfner, M., Hoor, P., Kaufmann, M., Orphal, J., Plöger, F., Spang, R., Suminska-Ebersoldt, O., Ungermann, J., Vogel, B., and Woiwode, W.: Gimballed Limb Observer for Radiance Imaging of the Atmosphere (GLORIA) Scientific Objectives, Atmospheric Measurement Techniques, 7, 1915–1928, doi:10.5194/amt-7-1915-2014, 2014.

Rothman, L., Gordon, I., Babikov, Y., Barbe, A., Chris Benner, D., Bernath, P., Birk, M., Bizzocchi, L., Boudon, V., Brown, L., Campargue, A., Chance, K., Cohen, E., Coudert, L., Devi, V., Drouin, B., Fayt, A., Flaud, J.-M., Gamache, R., Harrison, J., Hartmann, J.-M., Hill, C., Hodges, J., Jacquemart, D., Jolly, A., Lamouroux, J., Le Roy, R., Li, G., Long, D., Lyulin, O., Mackie, C., Massie, S., Mikhailenko, S., Müller, H., Naumenko, O., Nikitin, A., Orphal, J., Perevalov, V., Perrin, A., Polovtseva, E., Richard, C., Smith, M., Starikova, E., Sung, K., Tashkun, S., Tennyson, J., Toon, G., Tyuterev, V., and Wagner, G.: The HITRAN2012 Molecular Spectroscopic Database, Journal of Quantitative Spectroscopy and Radiative Transfer, 130, 4–50, doi:10.1016/j.jqsrt.2013.07.002, 2013.

Rottland, B.: Mechanische Konstruktion Zur Halterung Der Optischen Komponenten Eines Spektrometers Und Deren Anbindung an Eine Rakete, Tech. rep., Fachhochschule Aachen, 2016.

Rottman, G. J., Woods, T. N., and McClintock, W.: SORCE Solar UV Irradiance Results, Thermospheric-Ionospheric-Geospheric (TIGER) Symposium, 37, 201–208, doi:10.1016/j.asr.2005.02.072, 2006.

Russell III, J. M., Mlynczak, M. G., Gordley, L. L., Tansock, J., and Esplin, R.: An Overview of the SABER Experiment and Preliminary Calibration Results, in: Proceedings of SPIE, p. 277, 1999.

Sander, S. P., Golden, D. M., Kurylo, M. J., Moortgat, G. K., Ravishankara, A. R., Kolb, C. E., Molina, M. J., Wine, P. H., Finlayson-Pitts, B. J., Huie, R. E., and Orkin, V. L.: Chemical Kinetics and Photochemical Data for Use in Atmospheric Studies, Jet Propulsion Laboratory, 2006.

Schirber, S., Manzini, E., Krismer, T., and Giorgetta, M.: The Quasi-Biennial Oscillation in a Warmer Climate: Sensitivity to Different Gravity Wave Parameterizations, Climate Dynamics, 45, 825–836, doi:10.1007/s00382-014-2314-2, 2015.

Schmidt, H., Brasseur, G. P., Charron, M., Manzini, E., Giorgetta, M. A., Diehl, T., Fomichev, V. I., Kinnison, D., Marsh, D., and Walters, S.: The HAMMONIA Chemistry Climate Model: Sensitivity of the Mesopause Region to the 11-Year Solar Cycle and CO_2 Doubling, Journal of Climate, 19, 3903–3931, 2006.

Schöch, A., Baumgarten, G., Fritts, D. C., Hoffmann, P., Serafimovich, A., Wang, L., Dalin, P., Müllermann, A., and Schmidlin, F. J.: Gravity Waves in the Troposphere and Stratosphere during the MaCWAVE/MIDAS Summer Rocket Program, Geophysical Research Letters, 31, 2004.

Schroeder, S., Preusse, P., Ern, M., and Riese, M.: Gravity Waves Resolved in ECMWF and Measured by SABER, Geophysical Research Letters, 36, doi:10.1029/2008GL037054, 2009.

Schüttauf, K., Schmidt, A., Markgraf, M., Drescher, O., Krämer, S., Kinnaird, A., Bischoff, D., Mawn, S., Kaczmarczik, U., Pinzer, M., Stamminger, A., Newie, N., Inga, M., Fittock, M., Siegl, M., Persson, O., Page, H., Inga, M., and Hellmann, H.: REXUS User Manual, `http://rexusbexus.net/wp-content/uploads/2016/12/RX_UserManual_v7-14_21Dec16.pdf`, 2016.

Selva, D. and Krejci, D.: A Survey and Assessment of the Capabilities of Cubesats for Earth Observation, Acta Astronautica, 74, 50–68, doi:10.1016/j.actaastro.2011.12.014, 2012.

Shannon, C. E.: Communication in the Presence of Noise, Proceedings of the IEEE, 86, 447–457, 1998.

Sheese, P.: Mesospheric Ozone Densities Retrieved from OSIRIS Observations of the O_2 A-Band Dayglow, York Univ., Toronto; Ont., Canada, 2009.

Shepherd, G. G.: Spectral Imaging of the Atmosphere, Academic Press, San Diego, Calif, 2002.

Shepherd, G. G., Thuillier, G., Gault, W. A., Solheim, B. H., Hersom, C., Alunni, J. M., Brun, J.-F., Brune, S., Charlot, P., Cogger, L. L., Desaulniers, D.-L., Evans, W. F. J., Gattinger, R. L., Girod, F., Harvie, D., Hum, R. H., Kendall, D. J. W., Llewellyn, E. J., Lowe, R. P., Ohrt, J., Pasternak, F., Peillet, O., Powell, I., Rochon, Y., Ward, W. E., Wiens, R. H., and Wimperis, J.: WINDII, the Wind Imaging Interferometer on the Upper Atmosphere Research Satellite, Journal of Geophysical Research, 98, 10 725, doi:10.1029/93JD00227, 1993.

Slanger, T. G. and Black, G.: Interactions of $O_2(b^1\Sigma_g^+)$ with $O(^3P)$ and O_3, The Journal of Chemical Physics, 70, 3434, doi:10.1063/1.437877, 1979.

Smith, F. L. and Smith, C.: Numerical Evaluation of Chapman's Grazing Incidence Integral, Journal of Geophysical Research, 77, 3592–3597, doi:10.1029/JA077i019p03592, 1972.

Sofieva, V. F., Gurvich, A. S., Dalaudier, F., and Kan, V.: Reconstruction of Internal Gravity Wave and Turbulence Parameters in the Stratosphere Using GOMOS Scintillation Measurements, Journal of Geophysical Research, 112, doi:10.1029/2006JD007483, 2007.

Solheim, B., Brown, S., Sioris, C., and Shepherd, G.: SWIFT-DASH: Spatial Heterodyne Spectroscopy Approach to Stratospheric Wind and Ozone Measurement, Atmosphere-Ocean, 53, 50–57, doi:10.1080/07055900.2013.855160, 2015.

Song, R., Kaufmann, M., Ungermann, J., Ern, M., Liu, G., and Riese, M.: Tomographic Reconstruction of Atmospheric Gravity Wave Parameters from Airglow Observations, Atmospheric Measurement Techniques Discussions, pp. 1–18, doi:10.5194/amt-2017-118, 2017.

Steck, T., Höpfner, M., von Clarmann, T., and Grabowski, U.: Tomographic Retrieval of Atmospheric Parameters from Infrared Limb Emission Observations, Applied Optics, 44, 3291, doi:10.1364/AO.44.003291, 2005.

Stevens, B., Giorgetta, M., Esch, M., Mauritsen, T., Crueger, T., Rast, S., Salzmann, M., Schmidt, H., Bader, J., Block, K., Brokopf, R., Fast, I., Kinne, S., Kornblueh, L., Lohmann, U., Pincus, R., Reichler, T., and Roeckner, E.: Atmospheric Component of the MPI-M Earth System Model: ECHAM6, Journal of Advances in Modeling Earth Systems, 5, 146–172, doi:10.1002/jame.20015, 2013.

Swartwout, M.: The First One Hundred Cubesats: A Statistical Look, Journal of Small Satellites, 2, 213–233, 2013.

Swartwout, M.: Secondary Spacecraft in 2016: Why Some Succeed (And Too Many Do Not), in: 2016 IEEE Aerospace Conference, pp. 1–13, IEEE, 2016.

Takahashi, K.: Quantum Yields of $O(^1D)$ Formation in the Photolysis of Ozone between 230 and 308 Nm, Journal of Geophysical Research, 107, doi:10.1029/2001JD002048, 2002.

Talukdar, R. K., Longfellow, C. A., Gilles, M. K., and Ravishankara, A. R.: Quantum Yields of $O(^1D)$ in the Photolysis of Ozone between 289 and 329 Nm as a Function of Temperature, Geophysical Research Letters, 25, 143–146, doi:10.1029/97GL03354, 1998.

Tang-Kwor, E. and Matteï, S.: Emissivity Measurements for Nextel Velvet Coating 811-21 between -36 °C and 82 °C, High Temperatures-High Pressures, 33, 551–556, doi:10.1068/htwu385, 2001.

Touzeau, M., Vialle, M., Zellagui, A., Gousset, G., Lefebvre, M., and Pealat, M.: Spectroscopic Temperature Measurements in Oxygen Discharges, Journal of Physics D: Applied Physics, 24, 41, 1991.

Vincent, R. A.: The Dynamics of the Mesosphere and Lower Thermosphere: A Brief Review, Progress in Earth and Planetary Science, 2, doi:10.1186/s40645-015-0035-8, 2015.

Vincent, R. A., Hertzog, A., Boccara, G., and Vial, F.: Quasi-Lagrangian Superpressure Balloon Measurements of Gravity-Wave Momentum Fluxes in the Polar Stratosphere of Both Hemispheres, Geophysical Research Letters, 34, 2007.

Wagner, F.: Entwickeln Und Testen Eines „Spatial Heterodyne Spectrometer" Für Das AtmoHIT-Experiment, Tech. rep., Friedrich-Alexander-Universität, Erlangen-Nürnberg, 2017.

Walter, U.: Formelsammlung Raumfahrttechnik, Tech. rep., Lehrstuhl für Raumfahrttechnik, TUM, Munich, 2008.

Wang, L. and Geller, M. A.: Morphology of Gravity-Wave Energy as Observed from 4 Years (1998–2001) of High Vertical Resolution U.S. Radiosonde Data, Journal of Geophysical Research, 108, ACL 1–1–ACL 1–12, 2003.

Watanabe, S. and Miyahara, S.: Quantification of the Gravity Wave Forcing of the Migrating Diurnal Tide in a Gravity Wave–resolving General Circulation Model, Journal of Geophysical Research, 114, doi:10.1029/2008JD011218, 2009.

Wertz, J. R. and Larson, W. J.: Space Mission Analysis and Design, Microcosm; Kluwer, Torrance, California, 3rd edition edn., 1999.

Wu, D. L.: Horizontal Wavenumber Spectra of MLS Radiance Fluctuations, Journal of Atmospheric and Solar-Terrestrial Physics, 63, 1465–1477, 2001.

Wu, D. L.: Mesoscale Gravity Wave Variances from AMSU-A Radiances, Geophysical Research Letters, 31, L12 114, doi:10.1029/2004GL019562, 2004.

Wu, D. L. and Eckermann, S. D.: Global Gravity Wave Variances from *Aura* MLS: Characteristics and Interpretation, Journal of the Atmospheric Sciences, 65, 3695–3718, doi:10.1175/2008JAS2489.1, 2008.

Wu, D. L., Preusse, P., Eckermann, S. D., Jiang, J. H., Juarez, M. d. l. T., Coy, L., and Wang, D. Y.: Remote Sounding of Atmospheric Gravity Waves with Satellite Limb and Nadir Techniques, Advances in Space Research, 37, 2269–2277, doi:10.1016/j.asr.2005.07.031, 2006.

Yankovsky, V. A.: Electronic-Vibrational Relaxation of $O_2(b^1\Sigma_g^+, \upsilon = 1,2)$ at Collisions with Ozone and Molecular and Atomic Oxygen, (in Russian), Khim. Fiz., pp. 291–306, 1991.

Yankovsky, V. A. and Manuilova, R. O.: Model of Daytime Emissions of Electronically-Vibrationally Excited Products of O_3 and O_2 Photolysis: Application to Ozone Retrieval, Annales Geophysicae, pp. 2823–2839, 2006.

Yoshino, K., Parkinson, W. H., Ito, K., and Matsui, T.: Absolute Absorption Cross-Section Measurements of Schumann-Runge Continuum of O_2 at 90 and 295 K, Journal of Molecular Spectroscopy, 229, 238–243, 2005.

Abbreviations

ADCS Attitude Determination and Control System

AIRS Atmospheric Infrared Sounder

AMSU-A Advanced Microwave Sounding Unit-A

AOI Angle of Incidence

AR Anti-Reflection

AtmoHIT Atmospheric Heterodyne Interferometer Test

BDDF Bi-Directional Diffraction Distribution Function

BSDF Bi-Directional Scatter Distribution Function

CAD Computer Aided Design

CDH Command and Data Handling

CL Cleanliness Level

CMOS Complementary Metal-Oxide-Semiconductor

ConOps Concept of Operations

CVCM Collected Volatile Condensable Material

DASH Doppler Asymmetric Spatial Heterodyne Spectrometer

DLR Deutsches Zentrum für Luft- und Raumfahrttechnik

DOF Degree of Freedom

ECWMF European Centre for Medium-Range Weather Forecasts

ELANA Educational Launch of Nanosatellites

EPS Electrical Power Subsystem

ESA European Space Agency

FEE Front-End Electronics

FEM Finite Element Method

FFT Fast Fourier Transformation

FOV Field of View

FPA Focal Plane Array

FPGA Field Programmable Gate Array

FPS Fabry-Perot Spectrometer

FTS Fourier Transform Spectrometer

FWHM Full-Width Half-Maximum

GCM General Circulation Model

GLORIA Gimballed Limb Observer for Radiance Imaging of the Atmosphere

GNSS Global Navigation Satellite System

GOMOS Global Ozone Monitoring by Occultation of Star

GPS Global Positioning System

GS Ground Station

HAMMONIA Hamburg Model of the Neutral and Ionized Atmosphere

HIRDLS High Resolution Dynamics Limb Sounder

HITRAN HIgh Resolution TRANsmission

ICON Ionospheric Connection Explorer

IPCC Intergovernmental Panel on Climate Change

IR Infra-Red

ISS International Space Station

LEO Low Earth Orbit

LIMS Limb Infrared Monitor of the Stratosphere

LOS Line-of-Sight

MATS Mesospheric Airglow/ Aerosol Tomography and Spectroscopy

MI Michelson Interferometer

MIGHTI Michelson Interferometer for Global High-resolution Thermospheric Imaging

MIPAS Michelson Interferometer for Passive Atmospheric Sounding

MLS Microwave Limb Sounder

MLT Mesosphere/ Lower Thermosphere

MSX Midcourse Space Experiment

MTF Modulation Transfer Function

NIR near-infrared

NOA 88 Norland Optical Adhesive 88

NRL National Research Laboratory (US)

OPAL Optical Profiling of the Atmospheric Limb

OPD Optical Path Difference

OSIRIS Optical Spectrograph and Infrared Imager System

OTF Optical Transfer Function

PAC Percent Area Coverage

PSD   Power Spectral Density

PST   Point Source Transmittance

PSU   Power Supply Unit

PTFE Polytetrafluorethylen

PXE   Proximity Electronics

QBO   Quasi-Biennial Oscillation

QTDW Quasi-Two Day Wave

RAAN Right Ascension of the Ascending Node

REXUS/BEXUS Rocket/ Balloon Experiments for University Students

RF   Radio Frequency

RMS   Root-Mean-Square

RO   Radio Occultation

S/N   Signal-to-Noise

SABER Sounding the Atmosphere using Broadband Emission Radiometry

SED   Student Experiment Documentation

SHS   Spatial Heterodyne Spectrometer

SIM   Spectral Irradiance Monitor

SMR   Submillimeterwave Radiometer

SNSB   Swedish National Space Board

SOC   System-on-a-Chip

SOLSTICE Solar Stellar Irradiance Comparison Experiment

SORCE Solar Radiation and Climate Experiment

SPI   Serial Peripheral Interface

SRC   Schumann Runge Continuum

SSO   Sun-Synchronous Orbit

STK   Systems Tool Kit

SVD   Singular Value Decomposition

SZA   Solar Zenith Angle

TID   Total Ionizing Dose

TIDI   TIMED Doppler Interferometer

TIMED Thermosphere Ionosphere Mesosphere Energetics and Dynamics

TIS   Total Integrated Scatter

TML   Total Mass Loss

TRL   Technology Readiness Level

T-Vac Thermal-Vacuum

UARS Upper Atmosphere Research Satellite

UARS-MLS Upper Atmosphere Research Satellite Microwave Limb Sounder

UHF Ultra-High Frequency

UTLS Upper Troposphere/ Lower Stratosphere

UV   Ultra Violet

VHF Very-High Frequency

VIS   visible

WACCM Whole Atmosphere Community Climate Model

WINDII WIND Imaging Interferometer

ZARM Center for Applied Space Technology and Microgravity

List of Figures

List of Tables

Acknowledgment

A. Appendix AtmoCube-1 Mission Overview

This appendix provides additional information about the CubeSat concept, which includes a detailed power budget for an SSO and an ISS orbit, followed by the power distribution and communication architecture. Afterwards, the data generation and communication budgets are described in more detail. This chapter ends with stating the mass budget and the TRL levels of all components. Data provided in this chapter is not described in detail and only the most important aspects are discussed.

A.1. Electrical Power Subsystem

The electrical power subsystem provides energy to the electrical components of the satellite. Table A.1 shows the required power of each subsystem in each mode. The most power hungry mode is the communication mode to transfer scientific and telemetry data, because the S-band and the UHF/VHF radios are switched on. However, this mode is only operational for $2\,\%$ of the time. Hence, the highest contribution to the average required power of $6.9\,\mathrm{W}$ is attributed to the operational mode. This also means that the overall power consumption can be adjusted by changing the time sampling interval of the instrument. The average power consumption and the required battery capacity are used in the following power budget to determine if the power demand of the subsystems can be fulfilled.

Table A.1.: Power consumption of AtmoCube-1 subsystems.

	Operational Mode	Com Control Mode	Com Data Mode	Com Control and Data Mode	Safe Mode	Idle Mode	Antenna Deployment
Instrument [W]	2.03	0.00	0.00	0.00	0.00	0.00	0.00
UHF/VHF Board [W]	0.20	1.55	0.20	1.55	0.20	0.20	0.20
ADCS [W]	2.00	2.00	2.00	2.00	0.85	1.05	1.05
GPS [W]	1.00	1.00	1.00	1.00	1.00	1.00	1.00
OBDH [W]	0.55	0.55	0.55	0.55	0.55	0.55	0.55
S-Band Board [W]	0.70	0.70	6.00	6.00	0.00	0.70	0.70
EPS [W]	0.34	0.31	0.51	0.58	0.14	0.18	0.18
UHF/VHF Antenna [W]	0.02	0.02	0.02	0.02	0.02	0.02	2.00
Sum [W]	6.84	6.13	10.28	11.70	2.76	3.70	5.68
Mode Duration/Orbit	98.00%	0.80%	1.20%	0.00%	0.00%	0.00%	0.00%
Required Power [W]	6.88						

The eclipse time determines how much energy needs to be stored in batteries and how much energy can be produced in the remaining time during sunlight. Using Equations A.1 and A.2, the eclipse time T_E for the SSO and ISS orbits are calculated in dependence of angle between Sun and equinox γ,

$$\sin \beta = \cos \gamma \sin \Omega \sin i - \sin \gamma \cos \Omega \sin i + sin\gamma \cos i \sin 23.4° \tag{A.1}$$

$$T_e = \frac{T}{\pi} \arccos \left(\frac{\sqrt{(R_E + H)^2 - R_E^2}}{(R_E + H) \cos \beta} \right) \tag{A.2}$$

with the angle between Sun and orbital plane β, the inclination i, the RAAN angle Ω, the orbital period T, the Earth radius R_E, and the orbit altitude H (Walter, 2008). It describes the dynamical evolution of the eclipse time over a year. The RAAN is set to zero, because it only phase shifts the oscillations. The results are shown in Figure A.1. The SSO orbit is not in eclipse for two periods per year and the power generation is at a maximum. The eclipse time stays fairly constant for the ISS orbit. For both orbits, the longest eclipse times are used in the power budget and describe the worst case during the year.
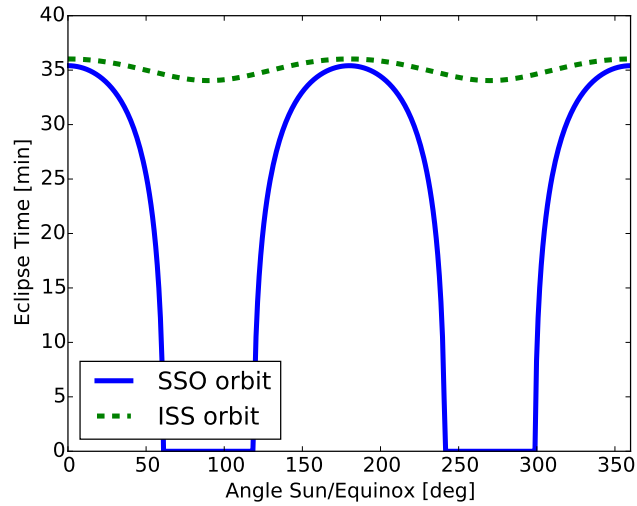
Figure A.1.: Eclipse time $[min]$ as a function of the angle between the Sun and the equinox [°] for the SSO and ISS orbits.

Tables A.2 and A.3 show the detailed power budgets for the SSO and the ISS orbits, respectively. Besides the orbital parameters, standard values from the datasheets are used to calculate the constant available power and the required battery capacity to store this energy. The analysis is performed for two illumination cases. Maximum power generation is achieved, when two sides of the satellite are illuminated with an angle of 45°. Illuminating a single side with a sun angle perpendicular to the solar panel surface results in minimum power generation. Both of these cases are calculated in the two tables. The analysis shows that the power is sufficient for the maximum illumination in the worst eclipse time cases for the both orbits. For minimum illuminated solar panel area, the power is not completely sufficient for 98 % of instrument operations and a more diversified operational scheme needs to be developed in latter stages of the design.

Table A.2.: AtmoCube-1 power budget for SSO.

Item	Value		Unit
Orbit Altitude	600		km
RAAN	0		°
Inclination	98		°
Incoming Radiation	1340		W/m^2
Efficiency Solar Cells	0.28		—
Efficiency BCRs	0.9		—
Efficiency EPS power lines	0.95		—
Orbit duration	5790		s
Daylight Time Worst Case	3665		s
Max. Depth of Discharge	0.2		—
	Average Two Sides	**Single Side**	
Solar Panel Area	0.036	0.026	m^2
Generated Power During Daylight	11.6	8.2	W
Available Energy During Orbit	11.8	8.4	Wh
Required Battery Capacity	21.7	15.4	Wh
Constantly Available Power	7.4	5.2	W

Table A.3.: AtmoCube-1 power budget for ISS orbit.

Item	Value		Unit
Orbit Altitude	400		km
RAAN	0		$°$
Inclination	51.6		$°$
Incoming Radiation	1340		W/m^2
Efficiency Solar Cells	0.28		–
Efficiency BCRs	0.9		–
Efficiency EPS power lines	0.95		–
Orbit duration	5543		s
Daylight Time Worst Case	3381		s
Max. Depth of Discharge	0.2		–
	Average Two Sides	**Single Side**	
Solar Panel Area	0.036	0.026	m^2
Generated Power During Daylight	11.6	8.2	W
Available Energy During Orbit	10.9	7.7	Wh
Required Battery Capacity	21.3	15.1	Wh
Constantly Available Power	7.1	5.0	W

A.2. Communication and Power Distribution Architecture

The bus consists of off-the-shelf components and the main interface between the components is established with the PC/104 standard. It provides communication and power distribution structures to most of the subsystems. Figure A.2 shows this architecture. The power is provided by solar cells and is transferred to the batteries by the EPS, using the battery voltage line with $8.2\,V$. Besides the $8.2\,V$ battery voltage, the EPS provides also $3.3\,V$, $5\,V$, and $12\,V$ lines. The $12\,V$ line is used by the instrument and by the ADCS for its reaction wheels. The ADCS uses also the $5\,V$ line for powering its electronics. The battery pack relies on the $3.3\,V$ or the $5\,V$ line for internal electronics and to power the heater. The CDH board is running on $3.3\,V$, whereas the GPS board uses $5\,V$. The S-band transmitter can cope with multiple available voltages and the $8.2\,V$ battery voltage line was selected. The UHF/VHF-board and its antenna use $5\,V$.

From a communication perspective, a I2C bus is used to connect all subsystems for commanding, except the ADCS. It relies solely on the second available bus, the Serial Peripheral Interface (SPI) bus. This bus is also used to transmit science data from the instrument to the S-band transmitter via the CDH due to its higher datarate of up to 10 Mbit/s. The antennas are connected via standard $50\,\Omega$ RF cables to their respective radios. For ground testing, the instrument communicates its data via an Ethernet interface and the CDH is programmable with a JTAG interface.
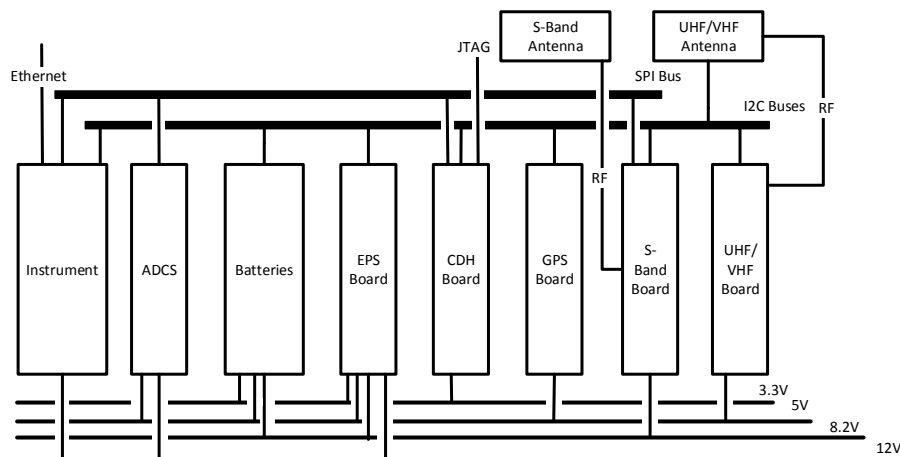

Figure A.2.: Schematic of concept for power and information flow within AtmoCube-1.

A.3. Datarate and Communication Budget

The datarate analysis of table A.4 describes the amount of generated data per orbit. Thereby, the housekeeping data can be neglected, because it is only a small fraction of the generated science data. For science data, the generation needs to be divided between day- and nighttime observations. Daytime observations generate significantly more data, because the atmosphere is sampled with 41 levels instead of 7 levels as for the nighttime observation. The sampling period is set to $10\,\mathrm{s}$ for daytime and $20\,\mathrm{s}$ for nighttime. It does not necessarily be equal the integration time. The generated raw data per orbit calculates to 8.7 Mbyte and 13.6 Mbyte for the two extreme illumination conditions, described above.

Table A.4.: AtmoCube-1 data rate analysis.

Item	Min	Max	Unit
Orbit Duration	5790		s
Eclipse Duration	2258	0	s
Radiometric Resolution	12		bit
Number Bins Spectral	400		—
Daytime Observation			
Number Bins Vertical Day	42		—
Sampling Period Day	10		s
Datarate Day	19.2		$kbit/s$
Nightime Observation			
Number Bins Vertical Night	7		—
Sampling Period Night	20		s
Datarate Night	0.6		$kbit/s$
Measurement Ratio Day/Night	0.63	1	—
Effective Datarate	12.3	19.2	$kbit/s$
Generated Raw Data per Orbit	8.7	13.6	$Mbyte$

The generated science data needs to be sent down to the GS via the S-band communication subsystem. Assuming a factor of safety of 1.9 and by using the downlink data rate from the datasheet of this system, the amount of data transferred per orbit can be estimated. The mean communication duration per orbit is calculated in STK, with assuming a stable link connection if the satellite is $10°$ above the horizon. A detailed link budget was not generated, because the S-band system is designed specifically for the purpose of transmitting up to 2 Mbps on CubeSats in LEO orbits.

For the two analyzed orbits, the transferable data per orbit is larger than 13.7 Mbyte, which means that all science data can be transmitted with a temporal resolution better than $97\,\mathrm{min}$ even during continuous daylight operations, with a significant factor of safety, and without considering any image data reduction schemes. In other words, the current conservative analysis of the communication budget allows to potentially increase the sampling time during daylight conditions.

Table A.5.: AtmoCube-1 communication time analysis.

Item	SSO Orbit	ISS Orbit	Unit
Factor of Safety Communication Datarate	1.9	1.9	—
Downlink Datarate S-band	2	2	$Mbps$
Orbit Altitude	600	400	km
Orbit Duration	5790	5543	s
Mean Communication Duration per Orbit	1746	1657	s
Number of Orbits per Day	14.9	15.6	—
Transferred Data per Orbit S-Band	15.4	14.0	$Mbyte$
Data Transfer Mode per Orbit	1.1	1.2	$\%$
Control Mode per Orbit	0.9	0.8	$\%$

A.4. Mass Budget

The budget of table A.6 shows the mass of all subsystems/components as calculated in the CAD model. It shows that the mass of $3.5\,\mathrm{kg}$ is below the $4\,\mathrm{kg}$ limit of an 3U CubeSat with $14\,\%$ margin.

Table A.6.: Mass budget for the AtmoCube-1 satellite concept.

Component	Mass [g]
Optics	164
Fore-Optics Mounting	429
SHS Mounting	105
Detector Optics Mounting	34
Electronic Boards	125
Solar Panels Instrument	58
Structure Instrument	313
Structure Baffle	307
Solar Panels Baffle	90
Misc (without harness)	21
Total Instrument	**1646**
EPS	86
Batteries	260
ADCS	850
CDH	94
GPS	106
S-Band Board	80
S-Band Antenna	50
UHF/VHF Board	85
UHF/VHF Antenna	100
Solar Panels	84
Structure	99
Misc (without harness)	51
Total Bus	**1894**
Harness	180
Margin (7 %)	260
Total Satellite	**3980**

A.5. Technology Readiness Levels (TRLs) of Subsystems

The TRLs of the subsystems allow to estimate the maturity of the overall system (ESA TEC-SHS, 2008). The reliability of the bus subsystems was an important selection criteria. Thus, subsystems with high TRL level have been preferred. Indeed, the satellite bus consists only of subsystems with successful flight heritage (TRL 9). The TRL level of the instrument subsystems was deemed lower. However, the flight heritage through the REXUS/BEXUS campaign increased it significantly.

Table A.7.: The TRL of all AtmoCube-1 subsystems according to ESA TEC-SHS (2008). *Including successful REXUS/BEXUS campaign.

Component	TRL
Instrument	
SHS	6*
Fore-Optic	6*
Detector Optic	6*
Detector	6*
Baffle	4
Bus	
Electrical Power Subsystem (EPS)	9
Batteries	9
Attitude Determination and Control System (ADCS)	9
Command and Data Handling (CDH)	9
Com S-Band Board	9
Com S-Band Antenna	9
Com UHF/VHF Board	9
Com UHF/VHF Antenna	9
GPS Board	9

B. Appendix Measurement Simulation

B.1. Oxygen Emission Model: Parameter and Errors

Table B.1 summarizes all parameters used in the oxygen emission model. Each parameter is defined by its name, as it is also used in the main part of the document. Errors could not be found for some values and these errors are estimated by the author. These values are marked with an asterix.

Parameters taken from Sander et al. (2006) have temperature dependencies, which are described by the Arrhenius relation in Equation B.1. The error itself is temperature dependent and an upper or lower limit for the error can be derived by multiplying or dividing the Arrhenius equation by Equation B.2. The error increases with larger distance from room temperature. In this work, the error calculation is simplified by calculating the error for a temperature of $150\,\mathrm{K}$ as worst case and distribution of the error on the constant term A and the activation energy term E/R by transformation of the equation.

$$k_{,i} = A \exp\left(-\frac{E/R}{T_{,i}}\right) \tag{B.1}$$

$$f_{,i} = f(298K) \exp\left\|g(\frac{1}{T_{,i}} - \frac{1}{298K})\right\| \tag{B.2}$$

Pejaković et al. (2005) use a slightly modified Arrhenius equation for the quenching factor k_{O_2b}, which fits better to the data. It includes the product term $(T/T_0)^n$. In Table B.1, the three error values refer to the error of A, n and E/R in this order.

$$k_{O_2b,i} = A \left(\frac{T_{,i}}{T_0}\right)^n \exp\left(-\frac{E/R}{T_{,i}}\right) \tag{B.3}$$

The recombination parameter k_5 has a quadratic temperature dependence, described by Equation B.4. It is derived by McDade et al. (1986) and two data points come from Campbell and Gray (1973). Campbell and Gray (1973) reported a value of $k_5 = (11.17 \pm 0.47) \times 10^{-33}\,cm^6/s$ for a temperature of $196\,\mathrm{K}$ and a value of $k_5 = (4.80 \pm 0.36) \times 10^{-33}\,cm^6/s$ for a temperature of $298\,\mathrm{K}$. The error at $298\,\mathrm{K}$ is used as error for the factor A and the error of the temperature dependence factor of $300\,\mathrm{K}$ is approximated with $20\,\%$.

$$k_{5,i} = A \left(\frac{300K}{T}\right)^2 \tag{B.4}$$

Table B.1.: Parameter for volume emission rate calculation. The error column states the worst-case absolute error for this application. Temperature dependent parameters have two error components, separated by a semicolon, corresponding with constant and exponential value. (*Errors are estimated. **Originally from Yankovsky (1991), paper in Russian from same author.)

Parameter	Value	Unit	Error	Source
g_A	6.0×10^{-9}	$1/s$	6.0×10^{-09}	Sheese (2009)
g_B	3.5×10^{-10}	$1/s$	3.5×10^{-11}	Sheese (2009)
k_{Ob}	4.5×10^{-12}	cm^3/s	1.3×10^{-12}	Pejaković et al. (2005)
k_{O_2b}	$2.2 \times 10^{-11}(T/292K)^{1.0}\exp^{\left(\frac{-115K}{T}\right)}$	cm^3/s	$(0.4 \times 10^{-11}; 0.15; 52.5)$	Pejaković (2005)
k_{N_2b}	5.0×10^{-13}	cm^3/s	$5 \times 10^{-14}*$	Hwang et al. (1999)
k_{O_3b}	3.0×10^{-10}	cm^3/s	$3.0 \times 10^{-11}*$	Yankovsky and Manuilova (2006)**
k_{O_2}	$3.3 \times 10^{-11}\exp^{\left(\frac{55K}{T}\right)}$	cm^3/s	$(3.3 \times 10^{-12}; 4.26)$	Sander et al. (2006)
k_{N_2}	$2.15 \times 10^{-11}\exp^{\left(\frac{110K}{T}\right)}$	cm^3/s	$(2.15 \times 10^{-12}; 8.59)$	Sander et al. (2006)
k_5	$4.7 \times 10^{-33}(\frac{300K}{T})^2$	cm^6/s	$(0.36 \times 10^{-33}; 30)*$	Campbell and Gray (1973); McDade et al. (1986)
k_0	$1.8 \times 10^{-15}\exp^{\left(\frac{45K}{T}\right)}$	cm^3/s	$(1.8 \times 10^{-16}; 42.95)$	Sander et al. (2006)
k_3	$3.5 \times 10^{-11}\exp^{\left(\frac{135K}{T}\right)}$	cm^3/s	$(5.25 \times 10^{-12}; 21.47)$	Sander et al. (2006)
k_4	3.9×10^{-17}	cm^3/s	1.95×10^{-17}	Sander et al. (2006)
k_6	8.0×10^{-14}	cm^3/s	2×10^{-14}	Slanger and Black (1979)
k_7	4.3×10^{-13}	cm^3/s	0.84×10^{-13}	Sander et al. (2006)
C^{O_2}	7.5	$-$	0.5	McDade et al. (1986)
C^O	33.0	$-$	4.0	McDade et al. (1986)
A_{771}	7.04×10^{-2}	$1/s$	0.42×10^{-2}	Krupenie (1972, p.486)
A_{1D}	6.81×10^{-3}	$1/s$	1.3×10^{-3}	Kernahan and Pang (1975)
A_{762}	8.5×10^{-2}	$1/s$	0.51×10^{-2}	Burch and Gryvnak (1969)
F_c	0.93	$-$	$9.3 \times 10^{-3}*$	Nicholls (1965)
φ	0.95	$-$	0.13	Green et al. (2000)

B.2. SHS Principles

B.2.1. The Basic Concept

Consider a wave with its electric field $E(t, \vec{r})$ arriving at a beamsplitter. It is divided into two waves $i = 1, 2$ (Equation B.5). Each wave has an amplitude $E_{0,i}$, a wave vector $\vec{k}_i$, an initial phase shift Φ_i and travels through time with the angular frequency ω. In the following, the wave is considered as time averaged. The position vector $\vec{r}$ describes the wave's position in space. Both waves arrive at gratings and are diffracted at an angle described by the grating Equation B.6.

$$E_i(t, \vec{r}) = E_{0,i} \exp j(2\pi\omega t + \vec{r} \cdot \vec{k}_i + \Phi_i) \tag{B.5}$$

The first grating is rotated with an angle θ_L around the y-axis, as in figure B.1. The wave vector of the arriving wave is parallel to the z-axis, which means that the grating "sees" the incoming wave at an angle θ_L. The second wave can be described like the first wave by virtually mirroring the grating along the beamsplitter. The difference to the first grating is that it is rotated with the angle θ_L in the other direction. The wave still arrives along the z-axis, but the grating reflects it in the other direction. The reflection angle γ is calculated by the grating Equation B.6. The parameter m describes the order of diffraction and $1/d$ is the groove density of the grating. The incoming wave is characterized by its wavenumber σ_i.
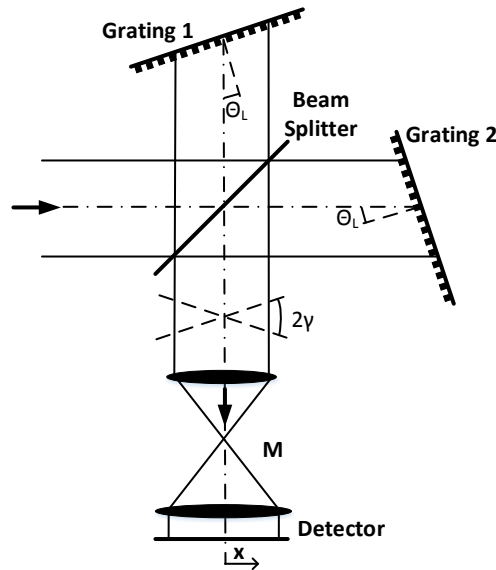
Figure B.1.: SHS schematic with beam splitter, gratings with Littrow angle θ_L, detector optics with magnification M, and detector.

$$\sigma_i[\sin\theta_L + \sin(\theta_L - \gamma_i)] = m/d \tag{B.6}$$

For a specific wavenumber, the so called Littrow wavenumber, the gratings diffract the waves in the same direction as the incoming waves. The angle γ has to be zero and these waves enter and exit the gratings at the same angle θ_L. This Littrow angle θ_L is calculated by Equation B.7.

$$\sin\theta_L = \frac{m}{2d\sigma_L} \tag{B.7}$$

The grating equation is described by the Littrow angle and wavenumber by expressing the ratio m/d with these parameters, see Equation B.7. Inserting the result in Equation B.6 results in Equation B.9, respectively Equation B.10.

$$m/d = 2\sigma_L \sin\theta_L \tag{B.8}$$

$$\sin\theta_L + \sin(\theta_L - \gamma_i) = \frac{2\sigma_L \sin\theta_L}{\sigma_i} \tag{B.9}$$

$$\sin(\theta_L - \gamma_i) = \frac{2\sigma_L \sin\theta_L}{\sigma_i} - \sin\theta_L \tag{B.10}$$

With the addition theorem (Equation B.11), the equation is transformed and the small angle approximations of $\cos\theta_L \approx 1$ is used. It is later identified as the approximately equal cosines of the input and exit angles. The Equation B.12 is further simplified to Equation B.13. It describes the angle with which the waves leave the gratings. The difference in diffraction direction is accounted for by including a $\pm$ sign.

$$\sin(x \pm y) = \sin x \cos y \pm \cos x \sin y \tag{B.11}$$

$$\sin\theta_L \underbrace{\cos\gamma_i}_{\approx 1} - \cos\theta_L \sin\gamma_i = \frac{2\sigma_L \sin\theta_L}{\sigma_i} - \sin\theta_L \tag{B.12}$$

$$\sin\gamma_i = \pm 2\tan\theta_L \frac{\sigma_i - \sigma_L}{\sigma_i} \tag{B.13}$$

The detector plane is normal to the z-direction and the spectrum shall be collected along the x-axis. Thus, the wave vector components in x-direction define the interference between the two waves. The wave vector components depend on the exit angles γ_i in this two dimensional problem. The y-components are zero

by definition and the x-components have different signs, because of the reflection in opposite directions. The z-components are irrelevant, because the detector pixels are perpendicular to them. Equation B.14 describes the wave vector components. The x-components of both waves are expressed with Equation B.15 and B.16, by inserting Equation B.13. The difference between the two expressions is the sign. It is further simplified for small values of γ.

$$\vec{k}_i = \begin{bmatrix} k_{ix} \\ k_{iy} \\ k_{iz} \end{bmatrix} = \begin{bmatrix} 2\pi\sigma \sin\gamma_i \\ 0 \\ 2\pi\sigma \cos\gamma_i \end{bmatrix} \tag{B.14}$$

$$k_{1x} = 4\pi\sigma \tan\theta_L \frac{\sigma - \sigma_L}{\sigma} \tag{B.15}$$

$$k_{2x} = -4\pi\sigma \tan\theta_L \frac{\sigma - \sigma_L}{\sigma} \tag{B.16}$$

With these expressions for the wave vectors, the interference at the detector is calculated. The interference is described by Equation B.17, where the electric field of the two phases are summed up. The intensity at the detector is calculated by the electric field multiplied with its complex conjugate by Equation B.18.

$$E_g(\vec{r}) = E_1(\vec{r}) + E_2(\vec{r})$$
$$E_g(\vec{r}) = E_{0,1} \exp j(\vec{r}\vec{k}_1 + \Phi_1) + E_{0,2} \exp j(\vec{r}\vec{k}_2 + \Phi_2) \tag{B.17}$$

$$E_g(\vec{r})^2 = E_{0,1}^2 + E_{0,2}^2 + E_{0,1}E_{0,2}(\exp(j(\vec{r}(\vec{k}_1 - \vec{k}_2) + (\Phi_1 - \Phi_2)) + \exp(-j(\vec{r}(\vec{k}_1 - \vec{k}_2) + (\Phi_1 - \Phi_2))) \tag{B.18}$$

The sum of the exponential terms can be identified as the cosine ($2\cos x = \exp(-jx) + \exp(jx)$). The cosine argument contains the initial phase difference and the difference in wavenumber. For an ideal SHS, the radiation at the detector has the same initial phase, but the wave vectors are different. Thus, the phase difference term cancels out. The intensity of a wave is proportional to the square of the electric field. Thus, the overall intensity of the interference pattern is expressed by the individual contributions, Equation B.19.

$$I_g = I_{0,1} + I_{0,2} + 2\sqrt{I_{0,1}I_{0,2}} \cos(\vec{r} \cdot (\vec{k}_1 - \vec{k}_2)) \tag{B.19}$$

With assuming the detector at $z = 0$ and pixels along the x-axis, the pointing vector for interference at the detector is described by $\vec{r} = [x\ 0\ 0]^T$. Furthermore, the wavenumber is the same for both waves, $\sigma_1 = \sigma_2 = \sigma$ and with a perfectly dividing beamsplitter, the amplitude of both waves is the same, $I_{0,1} = I_{0,2} = I_0$. Equation B.19 simplifies to Equation B.20.

$$I_g(x, \sigma) = 2I_0(1 + \cos(8\pi \tan\theta_L x(\sigma - \sigma_L))) \tag{B.20}$$

The total incoming radiation at a specific location on the detector is the integral over all wavenumbers of the incoming radiation. Typically, a filter limits the incoming radiation, but it can be described by an integral from 0 to ∞, in general. The intensity of one beam I_0 is a quarter of the incoming radiation L, because the beamsplitter divides the incoming radiation into two beams and half of the radiation is emitted back to the entrance by the beamsplitter. Furthermore, the incoming radiation is dependent on wavenumber, thus $L = L(\sigma)$. The result is Equation B.21, which is the real part of the Fourier transformed incoming radiation intensity. Thereby, the spatial frequency ν_F (Equation B.22) at the detector correlates with light of a specific wavenumber.

$$I_g(x) = \int_0^\infty 0.5L(\sigma)(1 + \cos(8\pi \tan\theta_L x(\sigma - \sigma_L))d\sigma \tag{B.21}$$

$$\nu_F = 4\tan\theta_L(\sigma - \sigma_L) \tag{B.22}$$

B.2.2. Resolving Power

Resolving power is defined as $R = \sigma/d\sigma$. The resolving power of an SHS is derived similar to a Fourier-transform interferometer (Shepherd, 2002). It is defined by the maximum phase difference between two waves, which can still be distinguished. The phase difference is the argument of the cosinus interference term. Its value is dependent on the position on the detector and increases linearly from the middle of the detector to the outer edge. The maximum extension of the beam perpendicular to the optical axis in one side is defined by the width of the grating. It is calculated to $x_{max} = 0.5W \cos(\theta_L)$, where W describes the width of the grating. In Fourier-space, the theoretically infinitely propagating fringes are limited by the maximum phase difference. It is described by a rectangular function folded with the phase difference. The rectangular function is centered around zero phase at σ_L and has the extension to both sides of x_{max}. In the spectral space, this transforms to a sinc-function $D(\sigma)$, see Equation B.23.

$$D(\sigma) = sinc(2\pi(\sigma - \sigma_L)4\tan\theta_L x_{max}) \tag{B.23}$$

The smallest difference in wavenumber $d\sigma$, which can still be resolved is limited by the width of the sinc-function. The first root of the sinc-function is at a distance $d\sigma = 1/(8\tan\theta_L x_{max})$ from the Littrow wavenumber σ_L. However, two peaks at this distance appear as a single broad peak. Thus, the smallest resolvable wavenumber is typically defined as $d\sigma = 1/(4\tan\theta_L x_{max})$. The resolving power of the SHS can now by expressed by Equation B.24. It depends on the width of the grating, the Littrow angle, and the wavenumber.

$$R = \frac{\sigma}{d\sigma} = 4W\sigma \sin\theta_L \tag{B.24}$$

The resolving power equation can be simplified to a useful approximation for fast evaluation of the performance of the SHS. Assuming that the wavenumber σ equals the Littrow wavenumber σ_L, by expressing the term $\sin\theta_L$ with Equation B.7 and setting the diffraction order to one, the resolving power can be simplified to Equation B.25: The resolving power is the number of rulings on both gratings.

$$R = 2W\frac{1}{d} \tag{B.25}$$

B.2.3. Off-Axis Analysis and Superiority

In the previous analysis, it was assumed that light enters the SHS parallel to the optical axis. In the following, the equations are generalized to account for non-paraxial rays. This off-axis analysis determines the maximum allowable FOV and the superiority of the system. Superiority is a performance indicator of spectrometers for comparison of different instrument types, as defined by Jacquinot (1954). Light arrives at the gratings with an off-axis angle i relative to the optical axis, as in Equation B.26. The minus and plus signs depend on the grating, because each grating is tilted in opposite direction relative to the optical axis. The Littrow wavenumber is defined by Equation B.27 with the same condition as before that input and ouput angles are the same ($\gamma = i$).

$$\sigma[\sin(\theta_L \mp \gamma) + \sin(\theta_L \mp i)] = m/d \tag{B.26}$$

$$2\sigma_L \sin(\theta_L \mp i) = m/d \tag{B.27}$$

With substituting the term of the diffraction order and the grating groove density, the grating equation becomes Equation B.28. This equation has to be solved for the exit angle γ, because the angle defines the OPD for interference. By transformation of the Equation B.29 and with using the addition theorem for both sin terms, the grating equation can be solved for $\sin(\gamma)$ (Equations B.30 and B.31).

$$\sigma[\sin(\theta_L \mp \gamma) + \sin(\theta_L \mp i)] = 2\sigma_L \sin(\theta_L \mp i) \tag{B.28}$$

$$\sin(\theta_L \mp \gamma) = \frac{2\sigma_L - \sigma}{\sigma}\sin(\theta_L \mp i) \tag{B.29}$$

$$\mp \sin(\gamma) = \frac{2\sigma_L - \sigma}{\sigma}[\tan(\theta_L)\cos(i) \mp \tan(\theta_L)\sin(i)] - \frac{\sigma}{\sigma}\tan(\theta)\tan(\gamma) \tag{B.30}$$

$$\sin(\gamma) = \mp\frac{2\sigma_L\cos(i) - \sigma(\cos(i) + \cos(\gamma))}{\sigma}\tan(\theta_L) + \frac{2\sigma_L - \sigma}{\sigma}\tan(\theta_L)\sin(i) \tag{B.31}$$

As above, the exit angle γ defines the wave vector (Equation B.14), which in turn defines the measured intensity at the detector (Equation B.19). Equation B.32 describes the overall intensity along the detector x-axis. It shows that the intensity also depends on the input and exit angles at the gratings. With assuming that both angles (i and γ) are relatively small, their cosines are approximately equal, Equation B.33. Then, the equation simplifies that it differs only from the intensity equation derived above (Equation B.20) by a cosine term of the input angle.

$$I_g = 2I_{0,1}[1 + \cos(2x(-2\pi\sigma\frac{2\sigma_L\cos(i) - \sigma(\cos(i) + \cos(\gamma))}{\sigma}\tan(\theta_L))] \tag{B.32}$$

$$\cos(i) \simeq \cos(\gamma) \tag{B.33}$$

$$I_g = 2I_{0,1}[1 + \cos(8\pi\tan(\theta_L)(\sigma - \sigma_L)\cos(i))] \tag{B.34}$$

The off-axis analysis determines that interference relevant OPD has a cosine dependence on the input angle. In addition, the geometrically induced OPD from the tilt of the gratings has also a cosine dependence on the input angle. Equation B.35 shows the overall OPD angle in dependence of input angle. The first term describes the interference relevant optical path difference and the second term the geometric inherent OPD. The interference relevant OPD is much smaller than the geometric inherent term. Thus, it is neglected in the following. Overall, the OPD for a specific location on the detector should be constant. The dependence on input angle influences the contrast of the fringes, because rays from different angles interfere in general not constructively. With increasing input angle, the phase difference increases till it gets intolerable. The threshold for the maximum allowable phase difference is typically defined as one half of a wavelength, Equation B.36, because for larger OPD the waves start to interfere destructively.

$$OPD(x,i) = 4x\tan(\theta_L)\frac{\sigma - \sigma_L}{\sigma}\cos(i) + 4x\tan(\theta_L)\cos(i) \tag{B.35}$$

$$|OPD(x,i) - OPD(x,i=0)| \leq \frac{1}{2}\lambda = \frac{1}{2\sigma} \tag{B.36}$$

Equation B.35 is used to substitute the OPD difference in B.36, resulting in Equation B.37. The cosinus term is approximated by its Taylor-series, which provides Equation B.38. The constant term cancels out and of the remaining terms, the second order term with $\frac{i^4}{24} \ll \frac{i^2}{2}$ has highest influence on the path difference.

$$|4x\tan(\theta_L)(\cos(i) - 1)| \leq \frac{1}{2\sigma} \tag{B.37}$$

$$|4x\tan(\theta_L)(1 - \frac{i^2}{2} + \frac{i^4}{24} \mp ... - 1)| \leq \frac{1}{2\sigma} \tag{B.38}$$

Thus, the resulting Equation B.39 can be solved for the input angle, Equation B.40. This means that for a maximum allowable OPD the input angle is restricted. The minimum allowable value for the input angle is achieved when the numerator is maximal, which is at one edge of the detector. The worst case is thus defined by $x = x_{max} = \frac{1}{2}W\cos(\theta_L)$. Substituting x with x_{max} results in the expression for the maximal allowable input angle, Equation B.41.

$$|-4x\tan(\theta_L)\frac{i^2}{2}| \leq \frac{1}{2\sigma} \tag{B.39}$$

$$i^2 \leq \frac{1}{4x \tan(\theta_L)\sigma} \tag{B.40}$$

$$i_{max}^2 \leq \frac{1}{2 \sin(\theta_L)\sigma W} \tag{B.41}$$

Superiority is a key characteristic of spectrometers. It is defined by the product of resolution R and FOV Ω. Specifically for the SHS, these values can be substituted by the expressions of Equations B.24 and B.41. The final result shows that the superiority of the SHS is 2π (Equation B.42), which is equal to the superiority of the Michelson spectrometer or the Fabry-Perot Interferometer, see also (Harlander et al., 1992).

$$R\Omega = \frac{\sigma}{d\sigma}\pi i^2 = 4W\sigma \sin(\theta_L)\pi\frac{1}{2 \sin(\theta_L)\sigma W} = 2\pi \tag{B.42}$$

B.2.4. Field Widening

The off-axis analysis provided the first insight how the FOV of an SHS is restricted. Similar to an MI, an SHS can be field-widened. From a geometrical perspective, the virtual images of the two gratings need to be rotated perpendicular to the optical axis. Then, off-axis rays form similar rectangles (Shepherd, 2002). Mathematically speaking, field widening tries to minimize the OPD between paraxial and non-paraxial rays over a range of input angles as large as possible. Field-widening is useful because it increases the etendué of the system, making it more responsive. In this chapter, the field-widening approach is derived. Similar to Michelson spectrometers, field-widening can be achieved by adding prisms between beamsplitter and gratings in each arm, the field-widening prisms. These prisms rotate the virtual image perpendicular to the optical axis. Fig B.2 shows the geometry of an SHS with field-widening prisms. According to Harlander et al. (2002), field-widening is either restricted by spherical aberration or astigmatism for small and large prism apex angles, respectively. In any case, the angle between beamsplitter and field-widening prism β, the field-widening prism apex angle α, and the angle between field-widening prism and grating η need to fulfill Equation B.43.
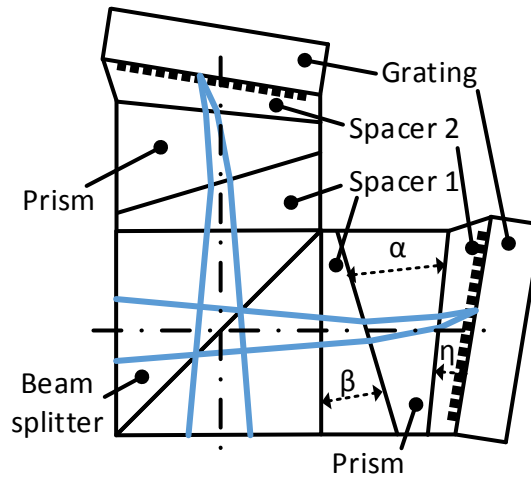

Figure B.2.: Schematic of a field-widenend SHS with beam splitter, spacers, field-widening prisms and gratings. The blue lines represent rays for the center field.

$$\sin(\theta_L - \eta) - n \sin\left(\alpha - \arcsin\left(n^{-1}\sin(\beta)\right)\right) = 0 \tag{B.43}$$

Together with the glass type for the field-widening prism, there are three independent parameter, e.g. α and η, which can be selected with a ray trace program to achieve the best possible field-widening

performance. In practice, it is possible to remove the squared order dependence of the OPD in input angle in the power expansion, as discussed in Chapter B.2.3. Thus, the dependence changes to a power of four dependence on the input angle, Equation B.44. As above, the maximum input angle can be expressed in dependence of Littrow angle, wavenumber and grating width, Equation B.45.

$$4x \tan(\theta_L) \frac{i^4}{24} \leq \frac{1}{2\sigma} \tag{B.44}$$

$$i_{max,w}^4 \leq \frac{24}{4 \sin(\theta_L)\sigma W} \tag{B.45}$$

Field widening has a large influence on the superiority of the SHS. The superiority $R\Omega$ can be expressed as in Equation B.46. Compared to a non-field-widened SHS, a FPS or an MI, the field-widened SHS has a superiority advantage of $\sqrt{6R}$. It makes the SHS especially useful for high spectral resolution measurements. The superiority advantage compared to a grating spectrometer is even larger as discussed by Shepherd (2002).

$$R\Omega = \frac{\sigma}{d\sigma} \pi i_w^2 = 4W\sigma \sin(\theta_L)\pi \sqrt{\frac{24}{4\sin(\theta_L)\sigma W}} = 2\pi\sqrt{6R} \tag{B.46}$$

B.3. Optimal SHS Parameter

For optimization of the SHS parameters, the measurement lines need to be selected. These are selected based on their temperature dependence differences. Furthermore, the lines need to be on a continuous wavenumber interval and the number of lines is restricted. The more lines are measured, the higher the maximum spatial frequency range gets, which increases the required number of pixels in spectral direction on the detector, or increases the physical size of the SHS. The first implication reduces the S/N-ratio and the second is constrained by the size of the instrument. As shown in Figure B.3, the lines of the P-branch can be divided into an increasing regime (Figure B.3a), where the volume emission rate increases with increasing temperature, a transition regime (Figure B.3b), and a decreasing regime (Figure B.3c). The largest differences in the temperature dependence exist in the transition regime. Thus, these lines are selected for the measurement. A subset of these lines has also been selected by Doe et al. (2011) for their satellite instrument.
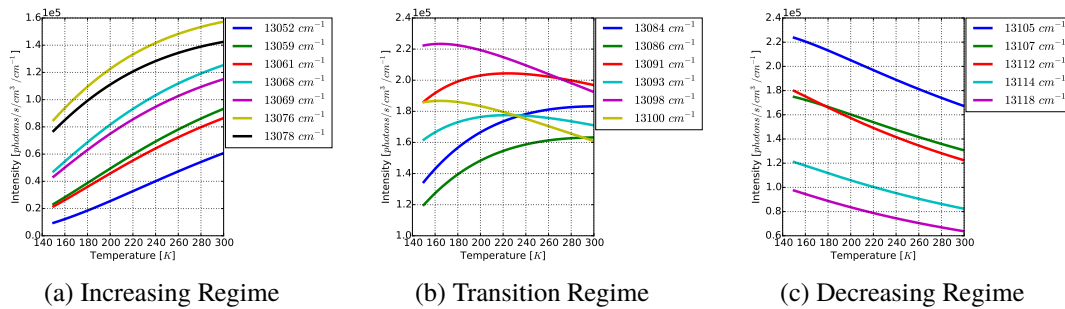

(a) Increasing Regime   (b) Transition Regime   (c) Decreasing Regime

Figure B.3.: Change of volume emission rate in $\mathrm{photons/cm^3/s/cm^{-1}}$ in dependence of temperature between $150\,\mathrm{K}$ and $300\,\mathrm{K}$ for increasing, transition, and decreasing regime of the P-branch in the rotational fine structure distribution.

Overall, six lines are selected, because two lines have increasing volume emission rates for increasing temperature, two stay relatively constant and two decrease. Including more lines to either side provides similar dependencies with less additional information. The information content of the line-temperature-dependence matrix can be analyzed with a Singular Value Decomposition (SVD). The matrix contains the volume emission rate in $\mathrm{photons/cm^3/s}$ in dependence of temperature from $150\,\mathrm{K}$ to $300\,\mathrm{K}$ for eighteen lines of the P-branch between $13\,051\,\mathrm{cm^{-1}}$ and $13\,120\,\mathrm{cm^{-1}}$. An SVD on the line-temperature-dependence matrix shows that most of the information in the matrix can be described by six principal axes of overall 18 axes, as all other axis have singular values smaller than zero. Figure B.4 shows the logarithm of the singular values descending with singular value index for the lines of the P-branch. It also

includes the singular values of a restricted set of six lines from $13\,081\,\mathrm{cm}^{-1}$ and $13\,101\,\mathrm{cm}^{-1}$. Here, three singular values contain approximately $70\,\%$ of the information (sum over singular values) and adding two further lines on either side or two further lines on both sides, increases the information content to $77\,\%$, $81\,\%$ and $88\,\%$, respectively.
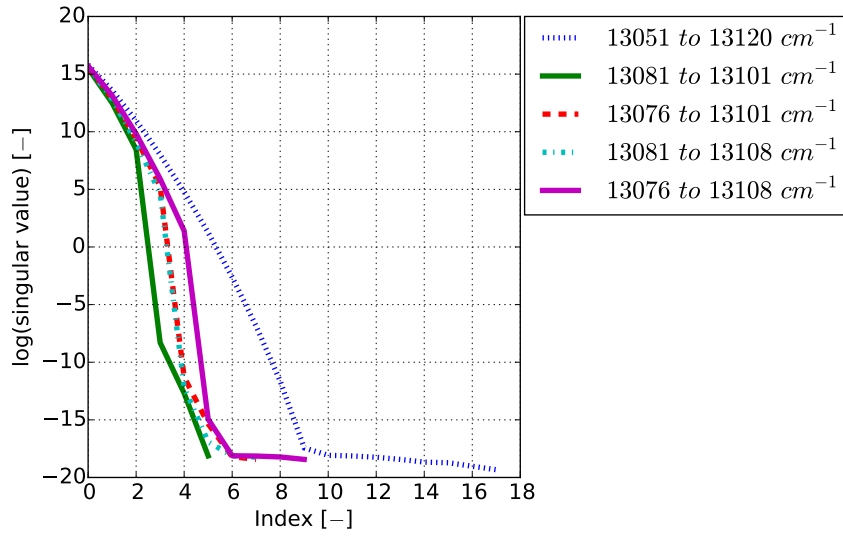

Figure B.4.: Information content in volume emission temperature dependence matrix described by the logarithm of the singular values of the line-temperature-dependence matrix descending with singular value index for the whole P-branch of oxygen A-band emission and selections thereof.

C. Appendix Instrument Design

C.1. Instrument Design Parameter

Requirements specifically implemented for the REXUS launch campaign of the precursor instrument are marked with an asterisk (*).

C.1.1. Functional Requirements

Table C.1.: Functional requirements for the AtmoHIT experiment.

F1	The experiment shall retrieve temperatures in the middle atmosphere.
F2	The experiment shall measure relative spectral flux in the oxygen atmospheric emission band.
F3	The experiment shall provide temperature housekeeping data of the instrument with each measurement.
F4	The experiment shall provide integration time housekeeping data of the instrument with each measurement.
F5	The experiment shall provide U-I housekeeping data of the electronics.
F6	The experiment shall store its scientific data on the mission computer at the ground station.*
F7	The experiment shall store its scientific data on-board.*
F8	The experiment should record an image of the observed scene in the atmosphere.*
F9	The experiment shall measure the temperature at the Spatial Heterodyne Spectrometer.
F10	The experiment shall measure the temperature at the detector.
F11	The experiment shall measure the temperature at the optical filter.

C.1.2. Performance Requirements

Table C.2.: Performance requirements for the AtmoHIT experiment.

P1	The experiment shall retrieve temperatures with a precision better than 2.5 K for the nominal limb viewing scenario.
P2	The experiment shall retrieve temperatures within the altitude range from 60 to 120 km for the nominal limb viewing scenario.
P3	The experiment shall retrieve temperature data with a FWHM spatial resolution in vertical direction of 1.5 km for the nominal limb viewing scenario.
P4	The experiment shall retrieve temperature data with a FWHM spatial resolution in horizontal direction of 60 km for the nominal limb viewing scenario.
P5	The experiment shall retrieve temperatures between 130 K and 500 K.
P6	The experiment shall retrieve temperatures with a geolocation precision lower than 1.5 km for the nominal limb viewing scenario at tangential altitudes.
P7	The experiment shall retrieve temperatures with a geolocation accuracy lower than 1.0 km for the nominal limb viewing scenario at tangential altitudes.
P8	The experiment shall provide temperature housekeeping data of the instrument with a precision better than 0.5 K.
P9	The experiment shall provide temperature housekeeping data of the instrument within a temperature range between 233 K and 333 K.
P10	The experiment shall provide temperature housekeeping data of the instrument with an accuracy better than 0.5 K.
P11	The experiment shall provide temperature housekeeping data of the instrument with a frequency of 1 Hz.
P12	The experiment shall have U-I housekeeping data of the electronics with a frequency of 1 Hz.
P13	The experiment shall have U-I housekeeping data of the electronics with a resolution of 12 bit.
P14	The experiment should image the observation scene with a pixel resolution better than 0.03° in vertical direction.*
P15	The experiment should image the observation scene with a framerate of at least 24 fps.*
P16	The experiment shall provide temperature data with a radiometric resolution of at least 12 bit.
P17	The experiment shall provide temperature housekeeping data with a resolution of at least 12 bit.

C.1.3. Design Requirements

Table C.3.: Design requirements for the AtmoHIT experiment.

D1	The experiment shall have a relative spectral flux calibration.
D2	The experiment shall be protected against dust contamination.
D3	The experiment shall withstand the structural loads during flight.
D4	The experiment shall be compatible with the REXUS electrical interfaces according to the REXUS user manual v7.13.*
D5	The experiment shall not draw a current larger than 3 A.*
D6	The experiment shall be able to deal with voltage steps.*
D7	The experiment shall be able to handle input voltage in a range of 24V to 36V.*
D8	The experiment shall not send a voltage ripple feedback over the power line to the REXUS service module larger than 100 mV.*
D9	The experiment shall not mechanically interfere with other experiments.*
D10	The experiment shall adhere to the mechanical interfaces specified in the REXUS user manual v7.13.*
D11	The experiment shall withstand the temperature conditions according to the REXUS user manual v7.13.*
D12	The experiment shall withstand the pressure conditions according to the REXUS user manual v7.13.*
D13	The experiment shall withstand dynamic and static loads according to the REXUS user manual v7.13.*
D14	The experiment shall provide a global timestamp synchronized with the LO signal.*
D15	The CubeSat Instrument part of the experiment should not exceed 2 kg.
D16	The experiment shall fit within a 170mm REXUS module.*
D17	The experiment shall not disturb the REXUS flight mechanics.*
D18	The experiment´s internal thermal dissipation shall not heat up the outer structure more than 10 K above the ambient temperature.*
D19	The experiment´s internal thermal dissipation shall not heat up the parts close to or in contact with the feed-through cable to more than +70 °C.*
D20	The experiment´s internal thermal dissipation shall not heat up parts facing other modules to more than +50 °C.*
D21	The experiment systems shall be able of withstand centrifugal forces due to the spin of the rocket.*
D22	The experiment, without REXUS interface and additional camera, should fit within a 1.5 unit CubeSat form factor defined in the CubeSat Design Specification rev. 12.
D23	The experiment shall store its scientific data on the mission computer with double redundancy.*
D24	The experiment shall be able to store its scientific data on the mission computer in real time.*
D25	The experiment shall store its scientific data on-board with single redundancy.*
D26	The experiment should store the observation scene image data on-board with single redundancy.*
D27	The experiment shall withstand the structural loads during landing.*

C.1.4. Operational Requirements

Table C.4.: Operational requirements for the AtmoHIT experiment.

O1	The experiment shall operate under variable settings of the detector.
O2	The experiment shall operate completely autonomously during flight.
O3	The experiment shall accept a request for radio silence at any time.
O4	The experiment shall survive several power-on-off cycles.

C.1.5. Constraints

Table C.5.: Constraints for the AtmoHIT experiment.

C1	The experiment shall comply to the experiment requirements as specified in the REXUS user manual v7.13.*
C2	The experiment shall use a Spatial Heterodyne Spectrometer.
C3	The experiment shall adhere to the deadlines set by the REXUS campaign.*
C4	The entrance aperture of the instrument shall have a diameter of at least 66 mm.*

C.2. Optical Bandpass Filter Properties

Table C.6.: Specification of the optical bandpass filter.

Spectral Filter Values		
Material	Fused Silica	
Center Wavenlength	$763.6^{+0.30}_{-0.00}$	$[nm]$
FWHM	4 ± 0.06	$[nm]$
Peak Transmittance	$> 0.93(762.6 - 764.6nm)$	[-]
Number of Cavities	6	[-]
Blocking Range	$300 - 1200$	$[nm]$
Blocking Quality	$> OD4_{average}, > OD3_{abs}$	
Angle of Incidence (AOI)	0.65	$[°]$
Surface Flatness	$0.25 wavelengths$	
Surface Quality	$60/40$	
Parallelity	$< 1 arcsec$	
Temperature Coefficient	$< 0.005nm/°C$	
Dimensions		
External Diameter	71.0 ± 0.1	$[mm]$
Size of utilizable Area	> 67	$[mm]$
Thickness	2.98 ± 0.1	$[mm]$
Miscellaneous		
Beam type	Imaging Beam	
Polarization State	unpolarized	
Operational Temperature Range	-10 to $+50$	$[°C]$

C.3. Grating Diffraction Equation

The pressure dependence analysis of the Littrow wavenumber includes a pressure dependence of the grating diffraction Equation B.6. In literature, the grating diffraction equation is commonly only stated for a refractive index of unity for the surrounding. This is not sufficient for the pressure dependence analysis of the Littrow wavenumber. Hence, the grating diffraction equation with considering the refractive index of the surrounding is derived for convenience in the following. The derivation is based on the explanation of Palmer (2014) and Figure C.1 reproduces the illustrative figure in his text.

Consider the plane wavefront A that hits the grating with a specific incidence angle α. The wavefront is reflected by the angle β relative to the grating normal. The two rays 1 and 2 of the wavefront A have a distance projected on the grating of d, where $1/d$ is the grating groove density. Then, the geometric

path difference between the two rays after the grating is $d\sin(\alpha) + d\sin(\beta)$, with β being negative. The two rays interfere positively, if the OPD is a multiple m of the wavelength of the light λ. The difference between OPD and geometric path difference is the refractive index n_{air} of the surrounding.
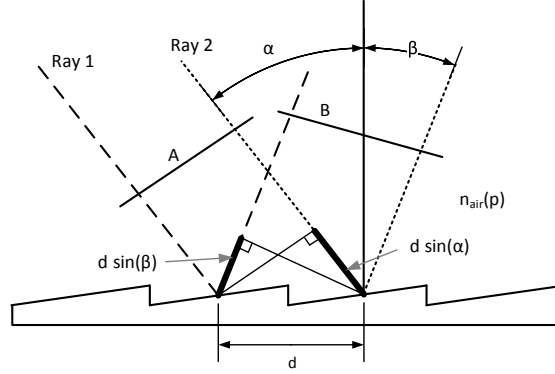

Figure C.1.: Schematics for illustrating the derivation of the diffraction grating equation after Palmer (2014).

Thus, Equation C.1 describes the positive interference of wavefronts with a specific incidence and exit angle of the grating. Compared to the "standard" grating equation, this equation includes also the refractive index of the surrounding.

$$m\lambda = n_{air}d\left(\sin(\alpha) + \sin(\beta)\right) \tag{C.1}$$

C.4. SHS Field-Widening Prism Angle Temperature Dependence

The derivation of Equation 5.16 is described in the following. The coordinate system and all variable names are based on Figure 5.15. First, the coordinates of the corners B and C are derived (Equations C.2 to C.4).

$$y = -\tan\gamma x + b \tag{C.2}$$

$$0 = -\tan\gamma t + b \tag{C.3}$$

$$y = -\tan\gamma(x - t) \tag{C.4}$$

The corners C and B have the following coordinates: $C(\frac{-d}{2\tan\gamma} + t, d/2)$, $B(\frac{d}{2\tan\gamma} + t, -d/2)$. Including the deformations of C and B, the displaced corners C' and B' are described by $C'(\frac{-d}{2\tan\gamma} + t + u_1, d/2 + v_1)$ and $D'(\frac{d}{2\tan\gamma} + t + u_2, -d/2 + v_2)$. With these coordinates, the gradient of the edge can be calculated by Equations C.5 to C.6.

$$m = \frac{(-d/2 + v_2) - (d/2 + v_1)}{(\frac{d}{2\tan\gamma} + t + u_2) - (\frac{-d}{2\tan\gamma} + t + u_1)} \tag{C.5}$$

$$m = \frac{-d + v_2 - v_1}{\frac{d}{\tan\gamma} + u_2 - u_1} \tag{C.6}$$

The angle is expressed by $\beta = \pi/2 - \gamma$ and the gradient is expressed by $m = -\tan\gamma$. Hence, the apex angle in dependence of displacements, prism height, and reference apex angle is calculated by C.7.

$$\beta' = \pi/2 - \arctan\left(\frac{d - v_2 + v_1}{d\tan\beta + u_2 - u_1}\right) \tag{C.7}$$

C.5. SHS Design

The following chapters provide more detailed information about the SHS design by providing a summary for its properties and tolerances. The technical drawings of all individual parts show these again in pictorial form.

C.5.1. Summary Properties and Tolerances

Table C.7.: Summary of dimensions and tolerances for the SHS

Materials		N-BK7	
	Refractive Index Absolute	$n_a = 1.5168 \pm 5 \times 10^{-4}$ (Step 3)	[-]
	Refractive Index Glass Variation	$n_v = \pm 2 \times 10^{-5}$ (S1)	[-]
	Refractive Index Homogeneity	$\Delta n_h = \pm 2 \times 10^{-6}$ (H4)	[-]
	Abbe Number Absolute	$\Delta \nu_a = \pm 0.5$	[%]
	Abbe Number Glass Variation	$\Delta \nu_v = \pm 0.05$	[%]
	N-SF11		
	Refractive Index Absolute	$n_a = 1.7847 \pm 3 \times 10^{-5}$	[-]
	Refractive Index Homogeneity	$\Delta n_h = \pm 4 \times 10^{-6}$ (H3)	[-]
	Abbe Number	$\Delta \nu_d = \pm 0.5\%$	[%]
Angles	Spacer 1	$\beta = 16.6332° \pm 15 arcsec$	
	Field-Widening Prism	$\alpha = 22.4318° \pm 15 arcsec$	
	Spacer 2	$\eta = 3.5598° \pm 15 arcsec$	
	Beamsplitter 2	$45° \pm 15 arcsec$	
Dimensions	Beamsplitter Size	$18 \pm 0.1 \times 18 \pm 0.1 \times 27 \pm 0.1$	$[mm^3]$
	Spacer 1	3.80 ± 0.05	$[mm]$
	Field-Widening Prism	6.70 ± 0.05	$[mm]$
	Spacer 2	2.78 ± 0.05	$[mm]$
Gratings	Grating Groove Density	$1/d = 1200 lines/mm < 0.05\%$	
	Grating Groove Tilt Tolerance	± 60	$[arcsec]$
Misc.	Surface Flatness	$\lambda/10$ @ $763 nm$	[-]
	Striae Class	Standard (SCHOTT)	
	Stress Birefringence	≤ 10	$[nm/cm]$

C.5.2. Technical Drawings

Elements
A: Beamsplitter (2x)
B: Spacer 1 (4x)
C: Prism (2x)
D: Spacer 2 (4x)
E: Grating (2x)

SHS Characteristics
Littrow Wavenumber (in Vaccum): 13127 1/cm
Diffraction Order: 1
Grating Groove Density: 1200 lines/mm ± 0.05%
Reference Temperature: 293.15 K

Misc
Surface Flatness: lambda/10 @763nm
Striae Class: Standard (Schott)
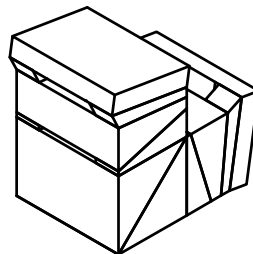Stress Birefringence: < 10 nm/cm

Grating Direction

(38,78)

2,78 ± 0,05

4,5 ± 0,1

(37,78)

18,0 ± 0,1

20,0 ± 0,1

6,70 ± 0,05

3,80 ± 0,05

18,0 ± 0,1

E
D
C
B

A

C
B
D
E

D
B

E
D
C
B
A
A

3,5598° ± 0,0041°

22,4318° ± 0,0041°

45,00° ± 0,05°

16,6332° ± 0,0041°

Materials

B
N-SF11

C
N-SF11
Refractive Index Absolute: 1.50348 ± 3e-5
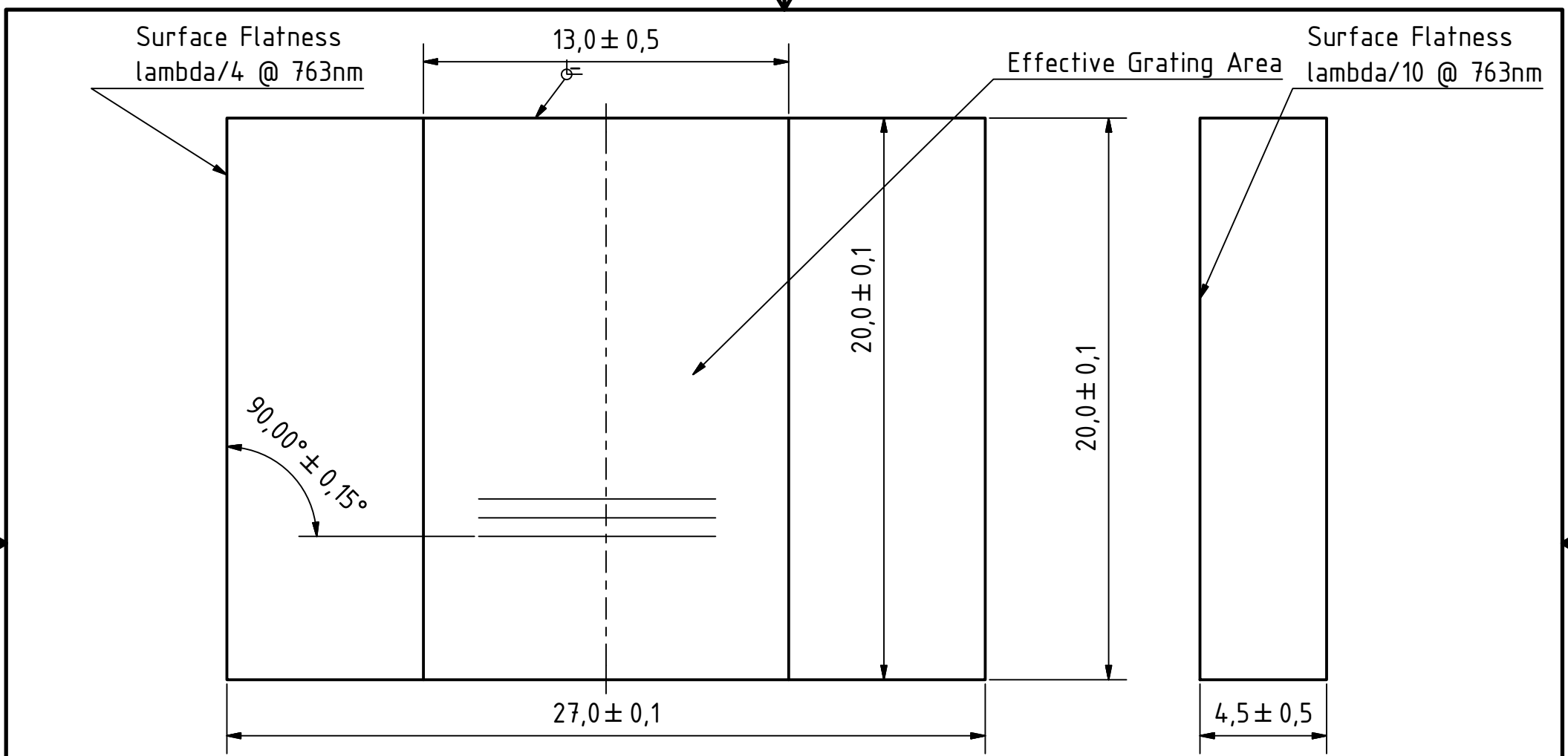Refractive Index Homogeneity: ± 4e-6
Abbe Number: ± 0.5%

D, E
Fused Silica

A
N-BK7
Refractive Index Absolute: 1.5168 ± 5e-4
Refractive Index Variation
between Glass Parts: ± 2e-5
Refractive Index Homogeneity: ± 2e-6
Abbe Number Absolute: ± 0.5%
Abbe Number Variation
between Glass Parts: ± 0.05%

Scale 1:1

Scale 2 : 1

ISO 2768-fH

Dimensions: mm

					Date	Name
				Drawn	25.5.2016	M. Deiml
				Checked		
				Standard		

Spatial Heterodyne
Spectrometer (SHS)

1

A3

State	Changes	Date	Name	

Rz 0.001

AR Coating: R_abs < 0.5%
for lambda in [763 nm; 765 nm]

Coating

50%/50% (± 5%)

@763 nm

45,00° ± 0,05°

45,00° ± 0,05°

90,00° ± 0,05°

90,00° ± 0,05°

18,00 ± 0,05

18,00 ± 0,05

27,0 ± 0,1

N-BK7

Refractive Index Absolute: 1.5168 ± 5e-4
Refractive Index Variation
between Glass Parts: ± 2e-5
Refractive Index Homogeneity: ± 2e-6
Abbe Number Absolute: ± 0.5%
Abbe Number Variation
between Glass Parts: ± 0.05%

Surface Flatness: lambda/10 @763nm
Striae Class: Standard (Schott)
Stress Birefringence: < 10 nm/cm

Scale 5 : 1							ISO 2768-fH	Material: N-BK7
							Dimensions: mm	
					Date	Name		
				Drawn	25.5.2016	M. Deiml	**Beamsplitter**	
				Checked				
				Standard				
							This design and print shall not be distributed without the written permission of University of Wuppertal, Atmospheric Physics Group or Research Centre Juelich, IEK-7	1
								A4
State	Changes	Date	Name					

22,4318° ± 0,0041°

9,83 ± 0,08

73,37° ± 0,17°

9,00

(6,70)

90°

Surfaces (#1)

(2,62)

27,0 ± 0,1

90,00° ± 0,17°

18,00 ± 0,05

Surface (#2)

N-SF11
Refractive Index Absolute: 1.50348 ± 3e-5
Refractive Index Homogeneity: ± 4e-6
Abbe Number: ± 0.5%

Surface Flatness surface (#1): lambda/10 @763nm
Surface Flatness surface (#2): lambda/4
Striae Class: Standard (Schott)
Stress Birefringence: < 10 nm/cm
Polishing Surfaces (#1): Rz 0.001
Polishing Surfaces (other): standard
AR Coating (*): R_abs < 0.5% for lambda in [763 nm; 765 nm]
Pyramidial Error surfaces (#1): < 0.0041°
Tilt Error surfaces (#1) relative to (#2): < 0.0041°

Scale 5 : 1							ISO 2768-fH	Material: N-SF11
							Dimensions: mm	
					Date	Name		
				Drawn	25.5.2016	M. Deiml		
				Checked			Field-Widening Prism	
				Standard				
							This design and print shall not be distributed without the written permission of University of Wuppertal, Atmospheric Physics Group or Research Centre Juelich, IEK-7	1
								A4
State	Changes	Date	Name					

Surface Flatness
lambda/4 @ 763nm

13,0 ± 0,5

Effective Grating Area

Surface Flatness
lambda/10 @ 763nm

20,0 ± 0,1
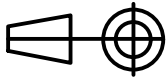
20,0 ± 0,1

90,00° ± 0,15°

27,0 ± 0,1

4,5 ± 0,5

Striae Class: Standard (Schott)
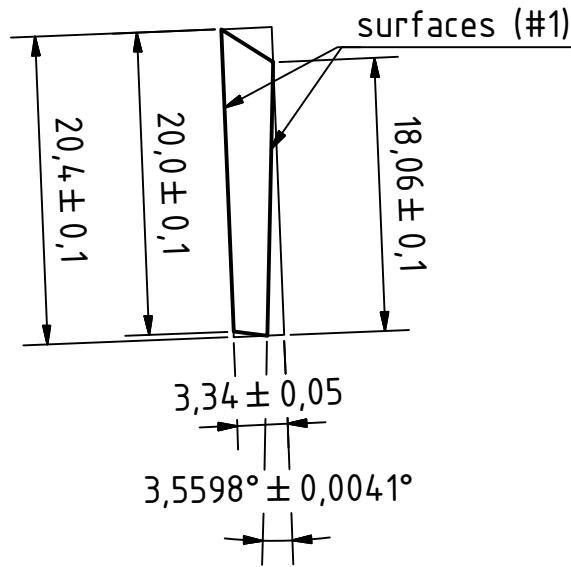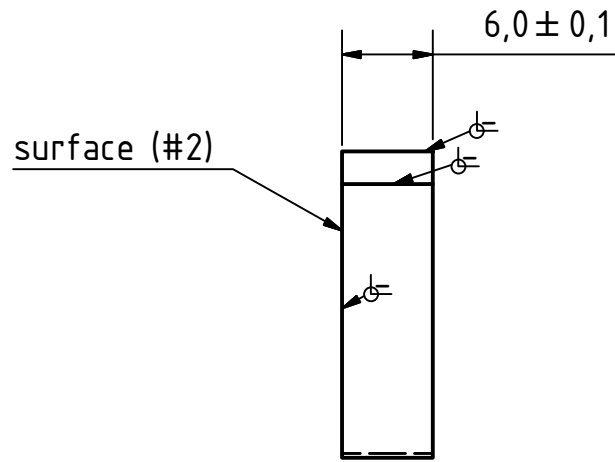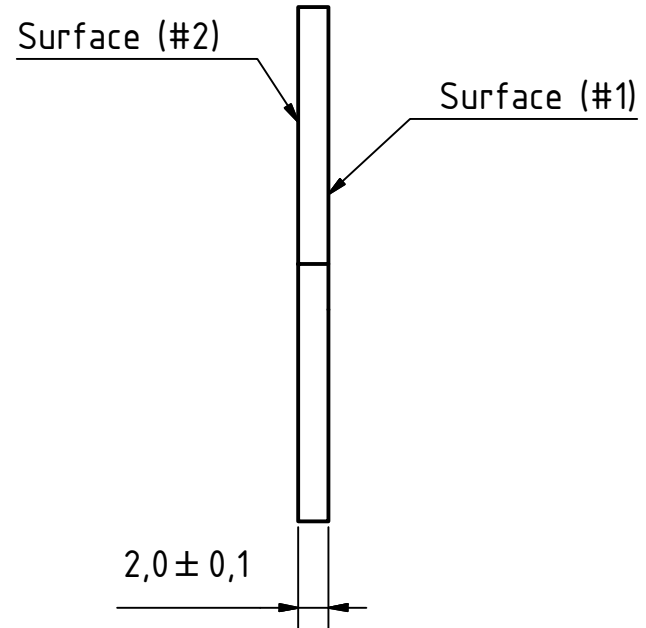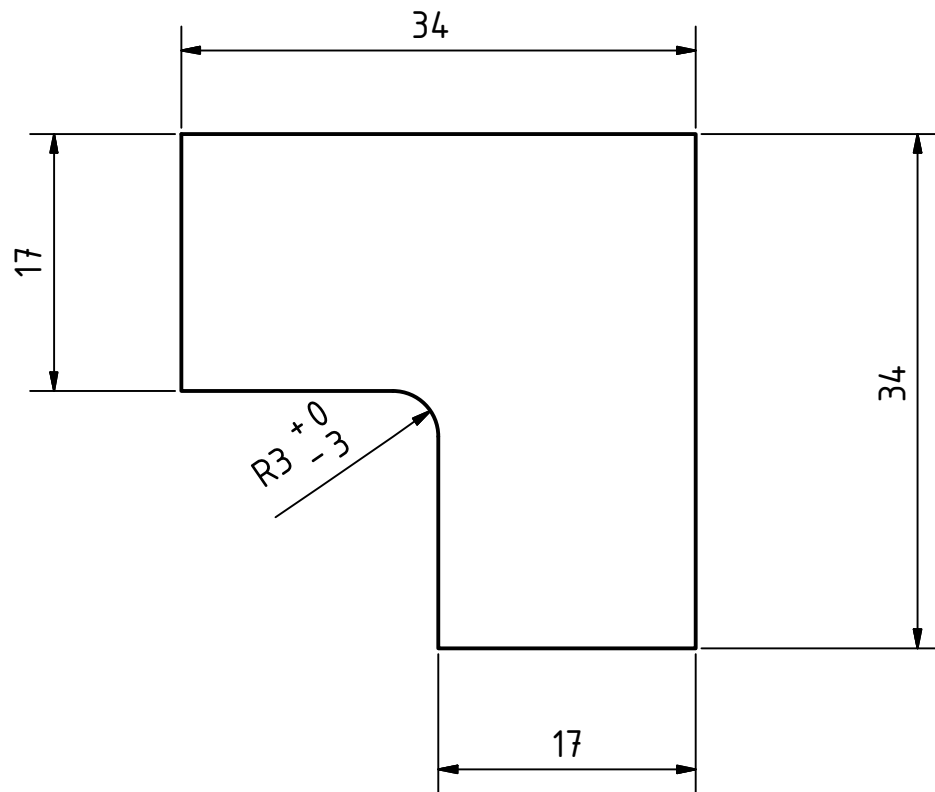Stress Birefingence: < 10 nm/cm

Grating Groove Density: 1200 lines/mm <0.05%
Blaze Wavelength: 800nm
All Surfaces Polished (standard)
No AR Coating

Scale 5 : 1

ISO 2768-fH	Material: F-Silica

Dimensions: mm

					Date	Name
				Drawn	25.5.2016	M. Deiml
				Checked		
				Standard		

Grating

1

A4

State	Changes	Date	Name

surface (#2)

$6,0 \pm 0,1$

surfaces (#1)

$18,00 \pm 0,05$

$6,49 \pm 0,05$

$16,6332° \pm 0,0041°$

Surface Flatness surface (#1): lambda/10 @763nm
Surface Flatness surface (#2): lambda/4
Striae Class: Standard (Schott)
Stress Birefringence: < 10 nm/cm
All Surfaces polished (standard)
Pyramidial error surfaces (#1): < 0.0041°
Tilt error surfaces (#1) relative to (#2): < 0.0041°

Scale 2 : 1

					Date	Name
				Drawn	25.5.2016	M. Deiml
				Checked		
				Standard		

ISO 2768-fH | Material: N-SF11

Dimensions: mm

SHS Spacer 1

1

A4

State	Changes	Date	Name

surface (#2)

6,0 ± 0,1

surfaces (#1)

20,4 ± 0,1

20,0 ± 0,1

18,06 ± 0,1

3,34 ± 0,05

3,5598° ± 0,0041°

Surface Flatness surface (#1): lambda/10 @763nm
Surface Flattness surface (#2): lambda/4
Striae Class: Standard (Schott)
Stress Birefringence: < 10 nm/cm
All Surfaces polished (standard)
Pyramidial error surfaces (#1): < 0.0041°
Tilt Error surfaces (#1) relative to (#2): < 0.0041°

Scale 2 : 1

ISO 2768-fH | Material: F-Silica

Dimensions: mm

					Date	Name
				Drawn	25.5.2016	M. Deiml
				Checked		
				Standard		

Spacer 2

1

A4

State	Changes	Date	Name

34

17

34

17

R3 $^{+0}_{-3}$

Surface (#2)

Surface (#1)

2,0 ± 0,1

Material: N-BK7
Flatness Surface (#1) < lambda/4
Surface (#1), (#2): Polished (standard)

Scale 2 : 1

ISO 2768-mK

Dimensions: mm

					Date	Name	
				Drawn	25.5.2016	M. Deiml	Alignment Plate
				Checked			
				Standard			

1

A4

State	Changes	Date	Name

C.6. View Factor Calculation for Straylight Analysis

The radiative transfer between the Earth´s surface and the entrance aperture requires to calculate the view factor between these entities directly. Thereby, the Earth´s surface (and the cloud layer) is approximated with a half infinite plate. This approximation is a worst case assumption, because the curvature restricts the view between instrument and surface at larger distances, effectively reducing the radiative transfer. The entrance aperture with its area A_1 is approximated with an infinitesimal element, which is reasonable compared to the surface area of the Earth. Figure C.2 shows the configuration for the calculation of the view factor. Thereby, the view factor of a surface patch is calculated for a range $\Delta\theta$ around the incidence angle θ, resulting in an edge length of L in x-direction. A large value for B appropriately approximates the infinite plan in y-direction.
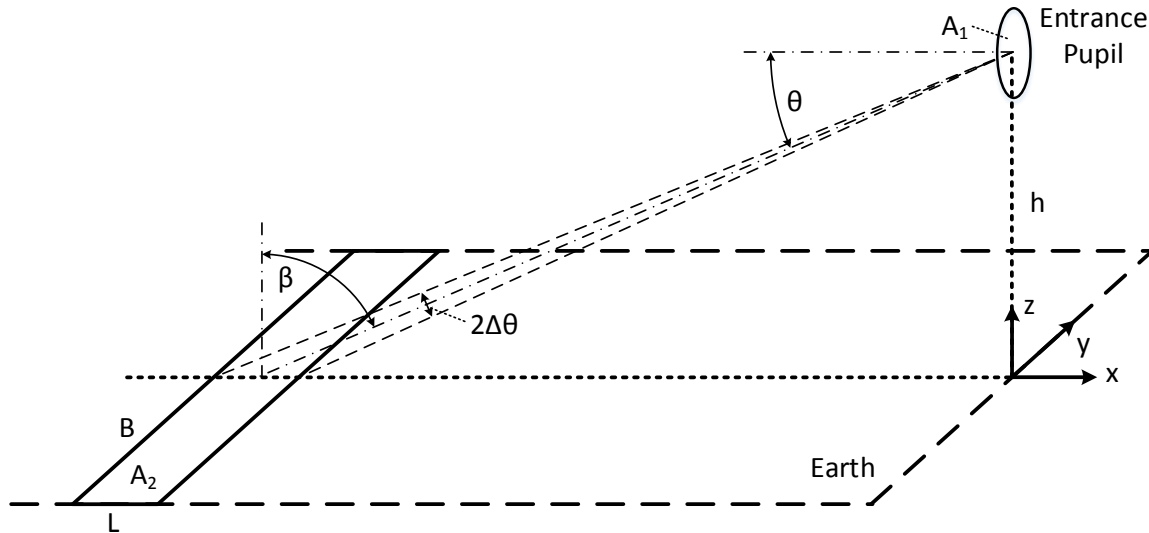

Figure C.2.: Schematics for view factor calculation.

The view factor F_{12} is defined by Equation C.8. It describes the radiative transfer from surface 1 to surface 2, defined by the radiative flux $\Phi_{12} = M A_1 F_{12}$ with M being the exitance. This definition is reverse to the actual radiative transfer and the reason will become apparent in the following. Without dividing the half-infinite plan into individual segments, the view factor approaches 0.5, which is intuitively correct as the plane divides the horizon equally into an absorbing and non-absorbing part. Thus, also the sum of all individual view factors between plane segments and entrance aperture needs to approach 0.5.

$$F_{12} = \frac{1}{A_1} \int_{A_1} \int_{A_2} \left[\frac{\cos(\theta)\cos(\beta)}{\pi r_{12}^2} \right] dA_2 dA_1 \tag{C.8}$$

The view factor between plane segment and entrance aperture is calculated with a Monte-Carlo simulation. Thereby, the two integrals are approximated with the sum over randomly selected points on surface A_2, see Equation C.9. Area A_1 is not randomized, because it is approximated as infinitesimal element. Considering also the geometry of the problem, the equation can be expressed only in dependence of the incidence angle θ_i and the y_i for a point P_i. The resulting Equation C.10 is evaluated on 1×10^7 randomly sampled points for every 1° interval between 2° and 90° incidence angle.

$$F_{12} = \frac{A_2}{N} \sum_i^N \left[\frac{\cos(\theta_i)\cos(\beta_i)}{\pi r_{12,i}^2} \right] \tag{C.9}$$

$$F_{12} = \frac{A_2}{N} \sum_i^N \left[\frac{\cos(\theta_i)\sin(\theta_i)}{\pi \left(\frac{h^2}{\sin^2(\theta_i)} + y_i^2 \right)} \right] \tag{C.10}$$

The resulting view factor in dependence of incidence angle is plotted in Figure C.3. It shows that the largest contribution to the total radiation comes from small incidence angles and decreases with increasing incidence angle. The view factor F_{12} is calculated, because it can be used with the constant area of the

entrance aperture A_1 to calculate the radiative flux and because the reciprocity $F_{12}A_1 = F_{21}A_2$ exists. Using instead F_{21} would result in an incidence angle dependent area A_2 (Equation C.11). Further information about view factor calculations can be found in e.g. Martinez (2017).

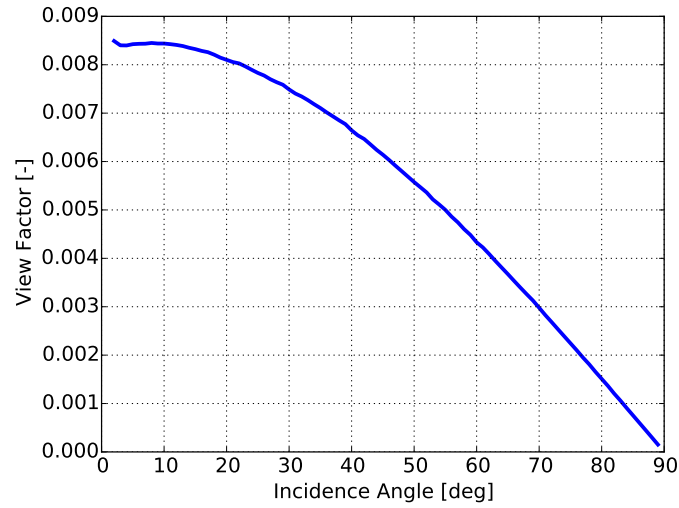$$A_2 = Bh \left(\frac{1}{\tan(\theta + \Delta\theta)} - \frac{1}{\tan(\theta - \Delta\theta)} \right) \tag{C.11}$$

Figure C.3.: View factor F_{12} as a function of incidence angle. The sum of all view factors equals 0.48 for the Monte Carlo simulation.

D. Appendix Verification

D.1. Images during YoYo-Despin

Figure D.1.: Series of VisCAM images after Yoyo-despin and before rocket separation anomaly with the corresponding interferogram. The time stamp in the left upper corner of each image shows the time after lift-off in [s].
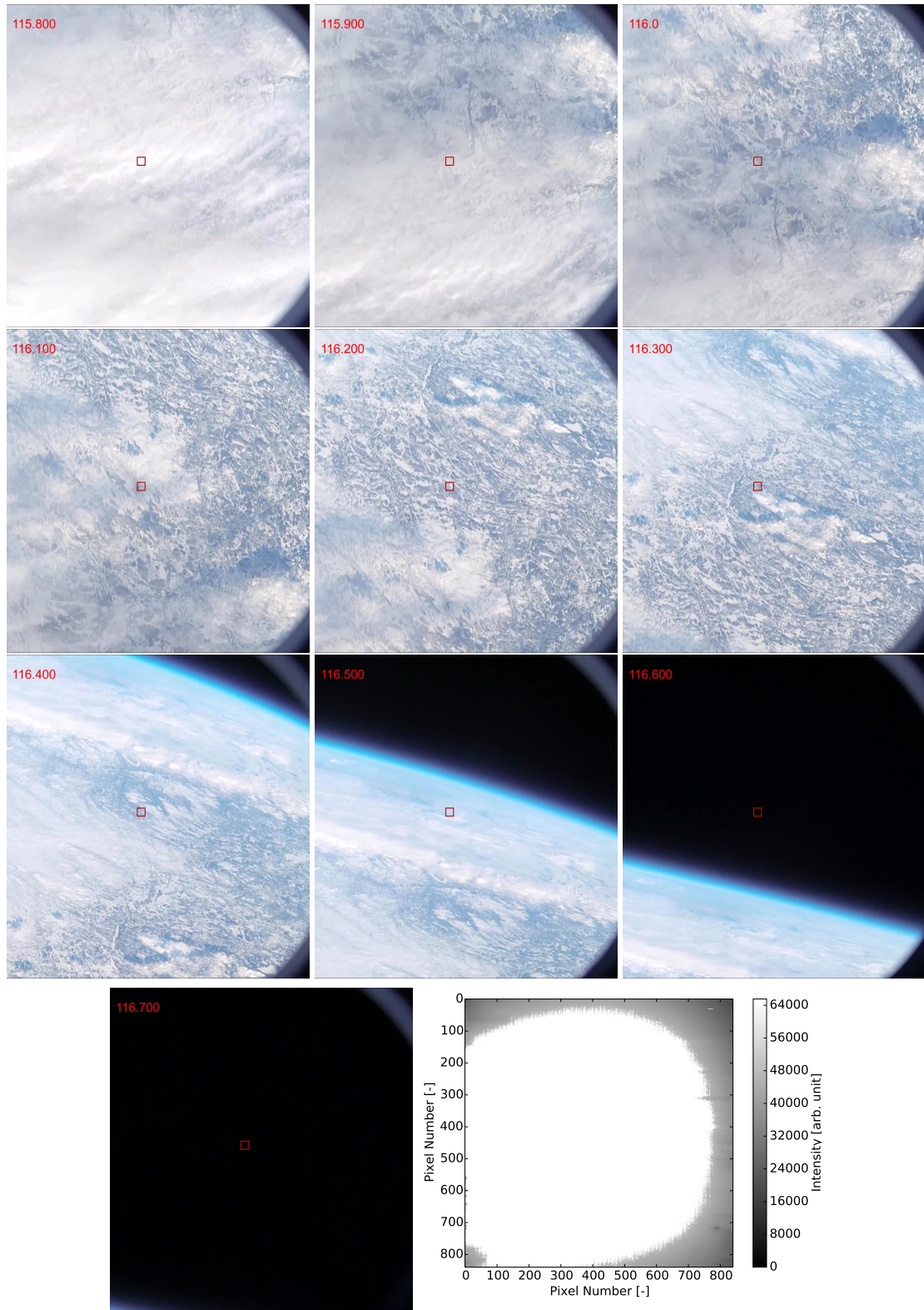
D.2. Images with View to Earth

Figure D.2.: Series of VisCAM images with view to Earth with the corresponding interferogram. The time stamp in the left upper corner of each image shows the time after lift-off in [s].
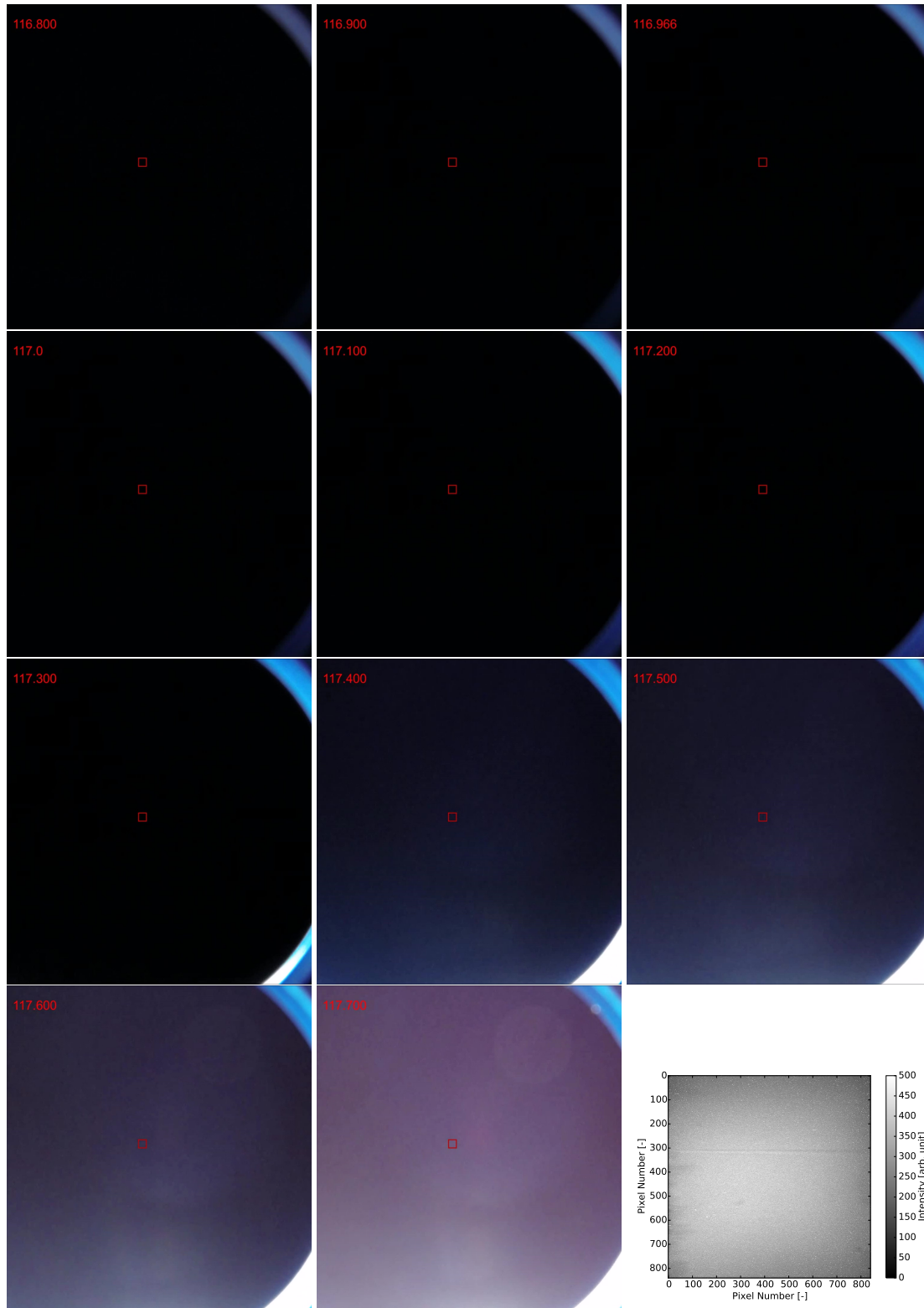
D.3. Images with View to Space

Figure D.3.: Series of VisCAM images with view to space with the corresponding interferogram. The time stamp in the left upper corner of each image shows the time after lift-off in [s].

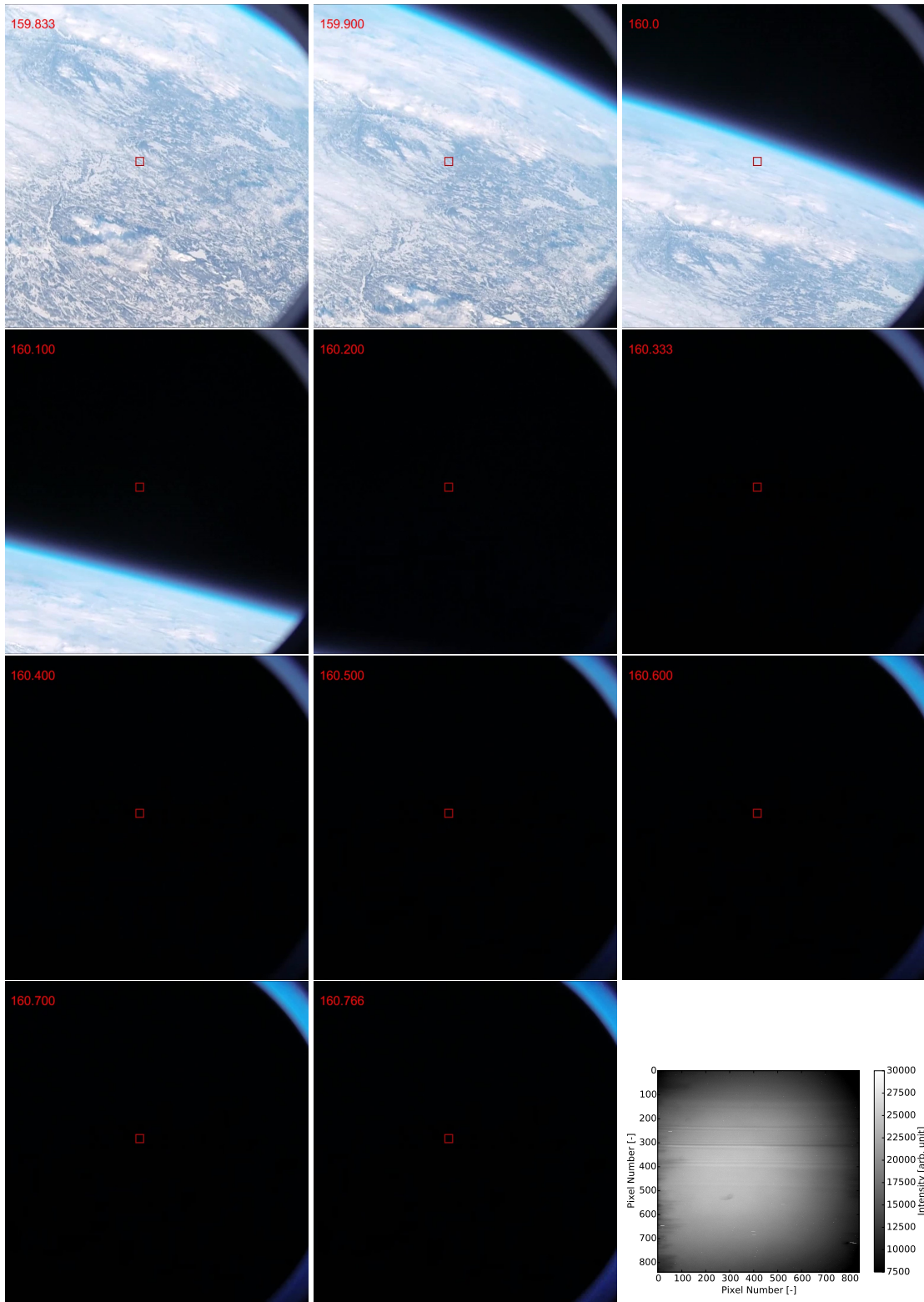# D.4. Images of Atmospheric Limb

Figure D.4.: Series of VisCAM images with view to the limb with corresponding interferogram. The time stamp in the left upper corner of each image shows the time after lift-off in [s].